Statistical Analysis of the results of numerical simulations of accidental situations in Pressurized Water Reactors

Alvaro Rollon de Pinedo

THÈSE

Pour obtenir le grade de

DOCTEUR DE L'UNIVERSITE GRENOBLE ALPES

Spécialité : MEP : Mécanique des fluides Energétique, Procédés

Arrêté ministériel : 25 mai 2016

Présentée par

ÁLVARO ROLLÓN DE PINEDO

Thèse dirigée par **Elsa Merle,** Professeure des universités, Université Grenoble-Alpes, et codirigée par **Nathalie Seiler**, Ingénieure de recherche, CEA

préparée au sein du **Laboratoire de Physique Subatomique et Cosmologie** dans **l'École Doctorale I-MEP2 - Ingénierie - Matériaux, Mécanique, Environnement, Énergétique, Procédés, Production**

Statistical Analysis of the results of numerical simulations of accidental situations in Pressurized Water Reactors

Thèse soutenue publiquement le **20 Décembre 2021,**
devant le jury composé de :

M. Julien Jacques
Professeur des universités, Université Lumière Lyon 2, Rapporteur

M. Tomasz Kozlowski
Associate Professor, University of Illinois, Rapporteur

M. Nicola Pedroni
Associate Professor, Politecnico di Torino, Examinateur

Mme. Amandine Marrel
Ingénieure de recherche, CEA, Examinatrice

Mme. Clémentine Prieur
Professeure des universités, Université Grenoble-Alpes, Présidente du jury

M. Pierre Gaillard
Ingénieur, Framatome, Invité

M. Bertrand Iooss
Ingénieur de recherche senior, EDF R&D, Encadrant

Mme. Elsa Merle
Professeur des universités, INP/PHELMA , Directrice

Mme. Nathalie Seiler
Ingénieure de recherche, CEA, Co-directrice

M. Roman Sueur
Ingénieur de recherche, EDF R&D, Co-encadrant

This page is intentionally left blank

Acknowledgements

It seems unbelievable, but writing this section is also complicated, even though the rest of the manuscript is already finished and all the milestones of the doctorate are already behind me. This work is the end of a long and tortuous road, but it has also given me so many things, both professionally and personally, and since *es de bien nacido ser agradecido*, I will try to express in a few paragraphs my heartfelt thanks to all the people who in one way or another have made it possible for me to successfully complete this journey.

To begin with, I would like to dedicate a few lines to the participants of my thesis committee. Thank you very much for having accepted the invitation to participate in my defense and for your goodwill throughout the whole process. I would especially like to mention my two rapporteurs, Julien and Tomasz, whose very accurate and fair comments have only improved the quality of my manuscript. I would also like to take this opportunity to thank the examiners, Nicola, Amandine, and Clémentine, who also kindly agreed to chair my panel. Thank you for your comments and pertinent questions that made clear the value of my thesis. Finally, thank you very much Pierre, not only for having accepted to be part of my thesis jury, but also for your infinite kindness and for having followed my thesis work from the beginning, participating in my annual supervision committees.

Je ne veux pas laisser passer l'opportunité de remercier ma superbe équipe encadrante.

- Je tiens à remercier très sincèrement ma directrice de thèse, Elsa, qui ne sait faire rien d'autre que donner des conseils pertinents, aider à tout le monde, et débloquer n'importe quel problème administratif que j'ai pu avoir pendant la thèse. Merci d'avoir toujours été aussi réceptive, à l'écoute, et gentille avec moi, je suis très fier d'avoir pu compter sur toi pendant toute la durée de ce projet.
- Nathalie, je ne pourrai jamais te remercier suffisamment pour ta patience, ton soutien et ton encouragement tout au long du chemin. Ton aide et ton travail ont été inestimables et tu as toujours réussi à être présente malgré la distance physique qui nous séparait pendant la thèse. Je pense que la façon dont tu as encadré mon travail est un exemple de la façon dont les choses devraient être faites, et je ne peux que me réjouir de la chance qu'auront les prochains doctorants que tu vas encadrer.
- Roman, merci de m'avoir enlevé un poids de mes épaules pendant ces trois années, que ce soit par tes mots d'encouragement, par tes conseils scientifiques, et surtout, par ces cafés autour desquels on pouvait parler de tout. Discuter avec toi le matin autour d'un café, que ce soit d'histoire, de philosophie ou de politique, était le moyen idéal

de commencer la journée du bon pied. Merci de m'avoir fait comprendre dès le début qu'en plus d'être mon encadrant, tu es mon ami.

- Bertrand, je pense que le mot qui décrit le mieux le fait de travailler avec toi est : amusant. Merci pour ta façon d'être, qui à la fois me maintenait dans une tension constante et me détendait avec tes blagues et ton badinage. Travailler avec toi a été une expérience extrêmement enrichissante qui m'a permis d'apprendre beaucoup. Merci d'avoir été un roc sur lequel s'appuyer dans tous les moments difficiles de la thèse.

- Mathieu, bien que tu n'aies pas pu être avec moi tout au long de la thèse, tu as toujours proposé de nous aider quand nous en avions besoin, et tes commentaires ont toujours été extrêmement utiles. Merci pour ton efficacité et ta prédisposition jusqu'au dernier jour, même lorsque mener à bien ce projet n'était plus ta responsabilité.

Amandine, bien que tu n'aies jamais été officiellement mon encadrante, je veux que tu saches que je considère que chaque seconde où j'ai travaillé avec toi était de l'or pur. L'intensité avec laquelle tu travailles, la qualité de tes idées, ta bonne humeur constante... Travailler avec toi est aussi intense qu'enrichissant, et tu es un idéal auquel il faut aspirer. Merci beaucoup pour tout ce que tu as fait et pour m'avoir tant appris.

Por supuesto, no puedo olvidarme de mencionar a mi familia. A mis padres, Eduardo y Myriam, y a mi hermanita, Ángela. Sé que estos años han sido duros para todos, y creedme cuando os digo que no hay un solo día en el que no os haya echado de menos. Gracias por estar siempre ahí para apoyarme, darme ánimos, y darme la seguridad de que si fijo mi mente en un objetivo, lo conseguiré sin duda alguna. Si por algo soy un privilegiado en este mundo, es por teneros como familia.

Merci également à tous mes collègues d'EDF qui m'ont accompagné pendant ces trois années. Me gustaría hacer primero una mención especial a Pablo, gracias por todas esas conversaciones en castellano que me hacían sentir estar un poquito más cerca de casa. Tenemos un poco de efecto túnel ideológico, pero lo que me he divertido hablando contigo no me lo podrá quitar nadie. Merci également à toute la formidable équipe de doctorants de l'EDF, en particulier Paul et Thomas, avec qui j'ai partagé un bureau pendant si longtemps. On nous a dit que trois personnes, c'était peut-être trop pour un seul bureau, mais la dynamique que nous avions est l'une des choses qui me manqueront le plus dans cette expérience. Je ne veux pas oublier non plus cette fantastique génération de doctorants, merci à Jérôme, qui m'a si bien accueilli à mon arrivée à EDF, merci à Antoine, Sami, Théo, Azénor et Noor (j'aurais aimé te rencontrer plus tôt !).

Merci à tous les ingénieurs et collègues du département PRISME et de toute la R&D d'EDF, en particulier mes collègues de P17. Merci à Pauline, Sanaa, Vanessa et Laura, Thibault (merci de la part d'Àlvar), Claire, Michaël, Emmanuel Ardillon, Emmanuel Remy (merci pour ton sourire le matin quand je venais travailler), Emilie, Jérôme Lonchampt. Monsieur Chabridon, comme nos conversations sur tant de sujets vont me manquer ! Merci Pierre-Yves pour tes blagues tous les matins, et merci à François de m'avoir parlé de la politique française des années 80, j'en sais maintenant un peu plus sur mon petit pays d'accueil.

En bref, un grand merci à toutes les personnes du d'EDF R&D avec lesquelles j'ai partagé ce voyage d'une manière ou d'une autre.

Y bueno, por supuesto, no podía terminar sin mencionar a todos mis amigos de R de Rick's. Lo decimos siempre, pero a pesar de que la mitad del grupo esté esparcido por el mundo, siempre tengo la sensación de que estamos cerca. Muchas gracias por vuestro apoyo inquebrantable, por vuestras palabras de aliento (no voy a olvidar nunca los aplausos en la casa rural al ir a la piscina a descansar de escribir), y por hacer que solo de pensar en volver a Madrid me aparezca una sonrisa enorme en la cara.

Al empezar a escribir estos agradecimientos me dije que intentaría ser breve, pero parece que mi verborrea oral se me ha contagiado a los dedos.

Gracias / Merci / Thank you

Contents

List of Figures

List of Tables

Table of Acronyms

ANOVA ANalysis Of VAriance.

ASN Autorité de Sûreté Nucléaire.

ASTRID Advanced Sodium Technological Reactor for Industrial Demonstration.

BD Band Depth.

BE Best Estimate.

BEPU Best Estimate Plus Uncertainty.

BIC Bayesian Information Criterion.

CATHARE Code Avancé de THermohydraulique pour les Accidents de Réacteurs à Eau.

CCF Common Cause Failure.

CDF Cumulative Distribution Function.

CEA Commissariat à l'Energie Atomique et aux énergies alternatives.

CHF Critical Heat Flux.

CVCS Chemical and Volume Control System.

DTW Dynamic Time Warping.

ECCS Emergency Core Cooling System.

ECR Effective Cladding Reacted.

EDF Electrictié de France.

EDG Emergency Diesel Generators.

EFWS Emergency FeedWater System.

EM Expectation Maximization.

ERF Enthalpy Rise Factor.

FAST Fourier Amplitude Sensitivity Testing.

FDA Functional Data Analysis.

FOD Functional Outlier Detection.

FPCA Functional Principal Component Analysis.

GMM Gaussian Mixture Model.

GSA Global Sensitivity Analysis.

HA Hot Assembly.

HDR High Density Regions.

HPC High Performance Computing.

HR Hot Rod / Half Region.

HS Host Spot.

HSIC Hilbert-Schmidt Independence Criterion.

HTC Heat Transfer Coefficient.

IBLOCA Intermediate Break Loss of Coolant Accident.

IRSN Institut de Radioprotection et de Sûreté Nucléaire.

ISS Important System for Safety.

KL Karhunen-Loève.

LHS Latin Hypercube Sampling.

LOCA Loss of Coolant Accident.

LOOP Loss Of Offsite Power.

LP Low Pressure.

LSA Local Sensitivity Analysis.

MA Mean Assembly.

MBD Modified Band Depth.

MC Monte Carlo.

MCMC Markov Chain Monte Carlo.

MEI Modified Epigraph Index.

MPLS Multivariate Partial Least Squares.

MR Mean Rod.

NPP Nuclear Power Plant.

PCA Principal Component Analysis.

PCT Peak Cladding Temperature.

PIRT Phenomena Identification and Ranking Table.

PLS Partial Least Squares.

PTS Pressurized Thermal Shock.

PWR Pressurized Water Reactor.

QoI Quantity of Interest.

RKHS Reproducing Kernel Hilbert Space.

RPV Reactor Pressure Vessel.

SA Sensitivity Analysis.

SFC Single Failure Criterion.

SG Steam Generator.

SIS Safety Injection System.

TSA Target Sensitivity Analysis.

UQ Uncertainty Quantification.

VLL Very Low Level.

1 Introduction

Contents

This introductory chapter presents the fundamental aspects of the works developed in the document. We present some contributions to the domain of functional data analysis, particularly concerning the domain of functional outlier detection and global analysis of nuclear transients.

In particular, our contributions relate to the link between Uncertainty Quantification (UQ) mathematical methods and the physical analysis of accidental nuclear transients. This is done through the research of outliers (i.e., abnormal data in an existing sample that deviate from an expected "normal" behavior) in the set of functional outputs of a systems code simulator, *CATHARE*, and relating them to specific physical phenomena and events that occur during the transient.

This chapter is introductory, and it firstly aims at providing the necessary elements to understand the industrial and scientific context of the works in section 1.1, also giving the main elements of the necessary framework adopted hereafter. Section 1.2 provides a general description of the two main application cases concerning Pressurized Water Reactors (PWR) that have been treated and which have also motivated these works, finishing in Section 1.3 with a brief description of recent works that have been developed in the same context. Section

1.4 describes the organization of the document and a brief description of the treated subjects in each chapter.

1.1 Context

These research activities are motivated by the need for constant improvement of techniques and methods as requested by the safety authorities to the nuclear industry.

The history of nuclear science and nuclear energy in France is a vast subject both from a historical and scientific point of view. The contributions of this country to the development of nuclear science dated back to the late 19th century, after the discovery of the first evidence of radioactivity by Henri Becquerel, which launched a whole scientific field that lasts until today. From a purely industrial point of view, several historical landmarks were achieved during the 20th century for the French nuclear industry. For instance, in the French case, one can mention the creation of one of the main research institutions in nuclear energy of the world, the CEA, which was created in 1945. The following decades saw the rising of a dynamic industry with the opening of the first nuclear power plant by EDF in the year 1962, which was followed by the construction of several dozens of new reactors in the country.

Nowadays, EDF operates 56 nuclear reactors, which produced a total of 379.5TWh in 2019 (RTE, 2019), which constituted 70.6% of the total electricity production in the country. These nuclear reactors may be classified into three categories according to their output power (see table 1.1). The strategic, industrial, and environmental importance of this industry cannot be understated.

Table 1.1: Number of nuclear reactors in France and their corresponding electrical power outputs.

Nominal output power	**Number of reactors**
900 MW	32
1300 MW	20
1450 MW	4

The relevance of this industry results in the close collaboration of all the most important actors that participate in it. Regarding the safety of the NPP, an independent administrative entity, the ASN (*Autorité de Sûreté Nucléaire*) ensures the control of nuclear safety and radiation protection in the country, providing the regulatory grounds on which the NPP may be opened, operated and decommissioned in France. It is also charged with the inspection of the installations, being capable of shutting down any one of them whenever the safety conditions are considered not to be fulfilled, also assisting the government in the event of a crisis. Finally, this institution is also responsible for guaranteeing the availability of information to the public regarding its activities and the state of nuclear safety and radiation protection.

In this context, EDF and other major actors of the industry are held accountable for the safety in the operation of their nuclear reactors and must fulfill the regulatory requirements imposed by the ASN, proving the safety of their installations. Originally, engineering studies made use of simplified physical models that were based on penalizing assumptions that provided conservative margins to the safety criteria imposed by the authorities. The advances in the computational modeling of nuclear systems and the increasing availability of data resulted in the development of more realistic numerical simulators that were more representative of the actual behavior of nuclear installations, and this resulted in the widespread use of these Best Estimate (BE) physical models. The use of this kind of tools is nowadays encouraged by the regulatory authorities as a complementary tool in safety studies and safety assessment (IAEA, 2001), and in the French case resulted in the development of the BE code *CATHARE (Code Avancé de ThermoHydraulique pour les Accidents de Réacteurs à Eau)* started its development in 1979, by the CEA, EDF, Framatome and the IRSN (Institut de Radioprotection et de Sûreté Nucléaire), the French public institute that acts as the technical advisor of the ASN in the radiological protection domain.

These codes allow the simulation of a wide variety of accidental nuclear transients and thermal-hydraulic systems and have opened whole fields of research regarding the use of numerical simulators in the nuclear safety context.

1.1.1 Nuclear transient simulation

The works developed in this document have been largely motivated by its application cases (presented in the next section). Generally speaking, a computer model (*CATHARE*) is available and capable of simulating specific accidental nuclear transients, i.e., sudden dynamic modifications of the physical state of a NPP that may occur during accidents or abnormal transients. In this case, the nuclear reactor in the NPP deviates from its safe operation domain, and the accidental transient progresses up until a new safe state is reached for the installation.

The *CATHARE* code, which is in constant improvement, has been developed and validated for a large variety of accidental situations (Geffraye et al., 2012) and constitutes a state of the art computer code that allows the estimation of the physical thermal-hydraulic parameters of interest (temperatures, pressures, flows...) during the course of the accident.

In practice, the complexity of the code imposes several limitations when estimating associated mathematical magnitudes. This is why *CATHARE2* is frequently treated as a black-box computer model and represented by a mathematical function (in our case, $\mathcal{M}$). The mathematical formulation is then:

$$\begin{aligned} \mathcal{X} \subset \mathbb{R}^d &\mapsto \mathcal{F}^* \subset \mathcal{F} \\ X &\to Z = \mathcal{M}(X) \end{aligned} \tag{1.1}$$

where $\mathcal{X} \subset \mathbb{R}^d$ is the space of variation of the input variables. In many practical cases, and in our context, $\mathcal{X}$ may be written as the Cartesian product of the support of the marginal laws of every uncertain input, $\mathcal{X} = \prod_{k=1}^{d} \mathcal{X}_k, \forall \mathcal{X}_k \subset \mathbb{R}$. The outputs are defined as functional objects $Z \in \mathcal{F}$, where $\mathcal{F}$ represents a functional space that appropriately models the outputs of the code and $\mathcal{F}^*$ is the functional subspace on which they are defined. Frequently, $\mathcal{F}$ is taken as the space of continuous functions $\mathcal{F} = \mathcal{C}([\mathcal{T}])$, or a Hilbertian space, where $\mathcal{T} \subset \mathbb{R}$ represents the time frame of definition of the simulated transient. Nuclear transients may showcase extremely different time frames, ranging from several minutes to hours and even days. Some examples of the kind of outputs that this code produces are provided in Figure 1.1.

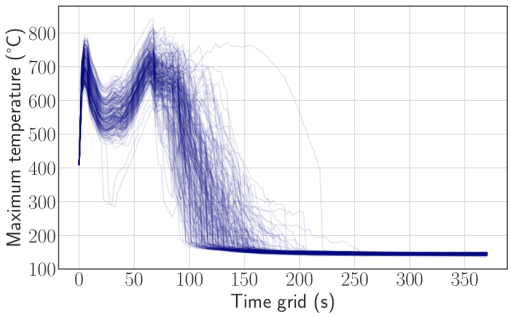

(a) Examples of the evolution of the fuel temperature in a set of nuclear transients.

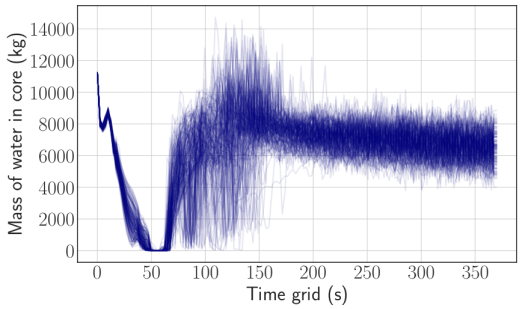

(b) Examples of the evolution of two physical parameters in a set of nuclear transients.

Figure 1.1: Examples of the evolution of two physical parameters in a set of nuclear transients.

Every input variable $X_k \in \mathcal{X}_k$ is representative of an uncertain physical parameter susceptible of being relevant for the considered nuclear transient. They model a wide variety of possible parameters, such as the initial pressure and temperature of specific components, constants of physical correlations and models, or certain parameters that define the specific analyzed scenario.

The treatment and physical analysis of the aforementioned output of the *CATHARE* code is difficult due to their large number and wide variety of shapes, which demands the development of specific techniques related to the Functional Data Analysis (FDA) mathematical framework, presented in detail in the next chapter. Indeed, the outputs generated by the code can be considered to take the form of univariate functions (in the mentioned cases, as functions of time), and thus they are modeled as objects that belong to infinite-dimensional vector spaces. The study of these mathematical objects was originated by the works of Grenander (1950) and was widely popularized in recent years thanks to the works of Ramsay and Silverman (2005) as well as other authors such as Ferraty and Vieu (2006) and Horváth and Kokoszka (2012).

1.1.2 Uncertainty quantification

As it was mentioned, the use of numerical models or simulators that allow the modeling of complex physical systems is increasingly popular. In certain contexts, the nature (i.e., their economic cost, difficulty to create exact replicas, etc.) of the considered physical problems largely motivates the use of these simulators due to their complexity, their economic cost, or their hazardous nature.

In the specific context of the nuclear industry, real physical experimentation is severely limited by safety regulations, economic costs, and technical difficulties, which has encouraged engineers and researchers to develop Best Estimate (BE) codes such as the aforementioned *CATHARE*. For instance, an accidental nuclear transient is extremely complex in the sense that it entails the use of hundreds of components, single-phase and two-phase thermal-hydraulic phenomena, also coupled with neutronic phenomena during potentially long periods of time (even days). All of these factors cannot be known and described, which implies that the knowledge and quantification of their associated uncertainty are essential in order to reliably use the mentioned numerical simulators, providing the grounds for the Best Estimate Plus Uncertainty (BEPU) framework.

Recalling the notations introduced in the previous section, the followin elements are considered: a numerical simulator $\mathcal{M}$, a set of inputs $X \in \mathcal{X} \subset \mathbb{R}^d$, and a set of outputs $Z \in \mathcal{F}^* \subset \mathcal{F}$ shown in (1.1).

As it was introduced, the uncertainty of each one of the inputs $(X_1, ..., X_d)$, and the associated uncertainty of the computer model $\mathcal{M}$ entail an imperfect knowledge of the outputs provided by $\mathcal{M}$. These uncertainties can have many origins, and there is no indisputable classification available for them. However, it is common practice in engineering studies to consider two main sources of uncertainty (Kiureghian and Ditlevsen, 2009):

- **Aleatory uncertainty**. It is related to the actual nature of the studied phenomenon. If a phenomenon is intrinsically random, one cannot expect to know its actual value with precision at all times. For instance, air temperature surrounding a nuclear power plant can play a role in the progression of a nuclear transient. This temperature may present different values that can be modeled as a random variable, which is at the origin of its associated uncertainty. This source of uncertainty is related to the inputs of the computer code but not to the code itself.
- **Epistemic uncertainty**. This type of uncertainty is related to the limited existing knowledge of a particular phenomenon and may be reduced if it is increased (through research, simulations, or experimentation, for instance). As mentioned above, the temperature in a particular nuclear site may evolve with time (for instance, due to climate change), and a better knowledge of this climatic process through research can help better model the considered random variable.

All in all, regardless of the sources, the fact remains that uncertainty presents itself in

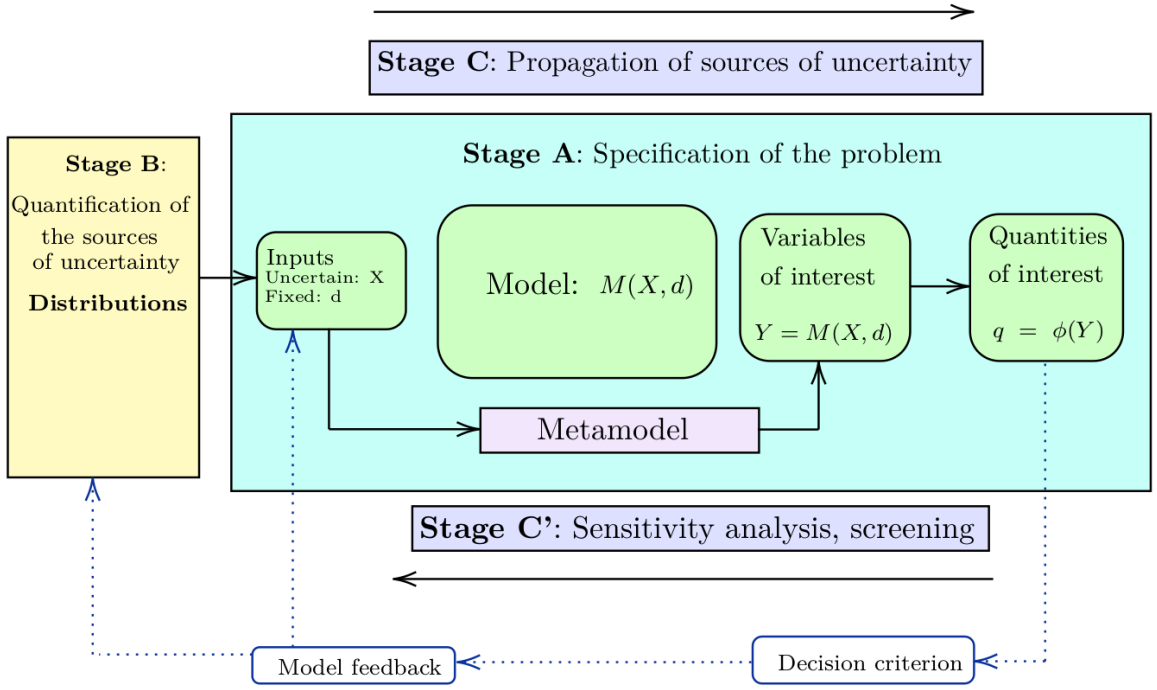

Figure 1.2: General scheme for uncertainty propagation

any given numerical simulator that aims at modeling real data or physical phenomena. The reader can refer to de Rocquigny et al. (2008) or, more recently to Sullivan (2015) for complete reviews on uncertainty quantification.

In practice, in the BEPU context these codes are usually considered as black-box models, i.e., their analytic form is unknown or too complex to be used, and they are known through their inputs and outputs. Associating the uncertainties of specific outputs of the considered model $\mathcal{M}$ as functions of the uncertainties of the inputs X is generally known as uncertainty propagation. The general scheme for uncertainty propagation is presented in Figure 1.2.

Accepting this framework, the inputs of the computer code, the random vector X, belongs to a topological space $\mathcal{X} \subset \mathbb{R}^d$. Let $\mathcal{A}$ be the Borel σ-algebra on $\mathcal{X}$, and let $\mathcal{P}(\mathcal{X})$ be the set of all probability measures defined on $\mathcal{X}$. Then, any element $\mathbb{P} \in \mathcal{P}(\mathcal{X})$ induces the probability space formed by $(\mathcal{X}, \mathcal{A}, \mathbb{P})$, and the inputs of the code may be modeled as the multivariate random vector $X = (X_1, ..., X_d)$, which is the measurable function:

$$\begin{aligned} X : \mathcal{A} &\mapsto \mathbb{R}^d \\ \omega &\to X(\omega) \end{aligned} \tag{1.2}$$

This probabilistic formalism allows accounting for the associated uncertainty of the inputs via the use of Probability Density Functions (PDF) or their respective Cumulative Density

Function (CDF). This way, for any given probability measure $\mathbb{P} \in \mathcal{P}(X)$, and for any given element $a \in \mathcal{X}, a = (a_1, ..., a_d)$, the CDF of the random vector X, F_X, is expressed as:

$$F_X(a) = \mathbb{P}(X \leq a) = \mathbb{P}(X_1 \leq a_1, ..., X_d \leq a_d) \tag{1.3}$$

In practice, the real distribution of the inputs is unknown, and it must be estimated through a model. Engineers may make use of experience, conservative hypotheses, numerical studies, real experiments etc. In order to quantify the uncertainty associated to the elements of $(X_1, ..., X_d)$. By making use of these pieces of information, they are able to determine estimators of the distributions through parametric models and well known distributions such as the normal or uniform ones. Their respective parameters may be estimated through many different methods such as maximum likelihood (Eliason, 1993). It would also be possible to adjust a non-parametric model to the distributions through kernel methods.

Since the considered code $\mathcal{M}$ is deterministic, modeling its inputs as random variables implies that its outputs will also be (functional) random variables. In Figure 1.2, however, the output variable of interest $Y \in \mathcal{Y} \subset \mathbb{R}$ is scalar (e.g., the maximum value of temperature of the nuclear fuel during the transient), or in certain cases, a random vector. The CDF of the output Y, F_Y, which can be estimated via Monte Carlo methods, allows the estimation of the desired derived quantities from Y.

This corresponds to the general methodology of uncertainty propagation, where the uncertainty associated to the inputs translates into an uncertainty of a scalar output variable (or several ones) representative of the physical phenomenon under study. For instance, in the aforementioned nuclear simulators, Y may represent the maximum temperature attained by the cladding of the nuclear fuel, where the actual corresponding output of $\mathcal{M}$ would then be the evolution of this parameter during the transient. This way, for the considered functional random variable Z whose support is the set $\mathcal{T} \subset \mathbb{R}, \mathcal{T} = [t_1, t_2]$, where t_1, t_2 are instants of time of physical simulation, the relationship between both random variables would be $Y = \max_{t \in \mathcal{T}}(Z(t))$ (where $Z(t)$ does not necessarily always account for the temperature at the same point in the fuel).

This is just an example of the kind of data that Y may represent in real applications. However, in practice, the actual object of study in UQ studies is often a derived magnitude from Y, which are called *Quantities of Interest* (QoI). Indeed, the analyst may often be more interested in specific quantities that may be obtained from Y, such as an expectation or a quantile. Following the previous example, an engineer might be more interested in quantifying the number of transients whose maximum temperature surpasses a threshold (i.e., a quantile).

These Ph.D. works are concerned with the set of original functional outputs of $\mathcal{M}$, Z, aiming at developing a general methodology that can be applied to nuclear transients regarless of the specifi characteristics of the scenario.

1.1.3 Functional data

The already introduced uncertainty propagation scheme of Figure 1.2 is concerned with specific scalar outputs Y of the numerical code $\mathcal{M}$, as well as a certain number of associated quantities of interest. However, if the direct outputs of $\mathcal{M}$ are a set of functional random variables, then the available information that can be provided by the code is much larger than the scalar variable of interest Y.

Naturally, the analysis of outputs such as those presented in Figure 1.1, pertains information concerning the progression of the analyzed transient.

The main difficulty that arises in the UQ context related to functional data is due to their intrinsically infinite-dimensional nature (Ramsay and Silverman, 2005). Indeed, if $\mathcal{F}$ is a Hilbert space, any functional random variable $Z : \mathcal{A} \mapsto \mathcal{F}$ of $\mathcal{M}$ can be expressed as a linear combination of the functions that span $\mathcal{F}$:

$$\forall Z \in \mathcal{F}, Z = \sum_{j \in \mathbb{N}} \langle Z, \phi_j \rangle \phi_j \tag{1.4}$$

where $\{\phi_j\}_{j \in \mathbb{N}}$ is an orthonormal basis that generates the Hilbert space $\mathcal{F}$.

In this case, a major problem that arises when considering the functional outputs of the computer code is that, contrary to the scheme shown in Figure 1.2, the cumulative distribution function of Z, F_Z, cannot be uniquely defined, and no available estimator for this notion exists (Gasser et al., 1998; Delaigle and Hall, 2010).

These challenges motivate the use of an alternative approach through the development of dimensionality reduction methods. These methods are reviewed in Chapter 2. Regarding this subject, the seminal works of Ferraty and Vieu (2006) propose a wide framework of dimensionality reduction methods based on semimetrics.

In summary, the totality of UQ methods applied to functional data rely on techniques of dimensionality reduction that provide a set of lower dimensional scores in order to be able to profit from the well developed framework proposed in Figure 1.2.

We shall interest ourselves to the detection of outliers in the sets of functional outputs of *CATHARE2*. The main hypothesis being that the detection of outliers through techniques that take into account the whole transient can prove to be useful in order to automatically detect penalizing accidental situations, detect unexpected physical events or phenomena, or perform code validation and debugging. The main objective of these works is to be able to perform the aforementioned analysis of the transients on the basis of the found outliers.

The detection of outliers in sets of functional data does however present difficulties that are not present in the multivariate framework, and whose origin is mostly linked to the fact that functional spaces are intrinsically infinite-dimensional. on top of that, the taxonomy of said outliers is quite large (see Figure 1.3), and the development of general methodologies

capable of treating a wide diversity of outliers represents a real scientific challenge.

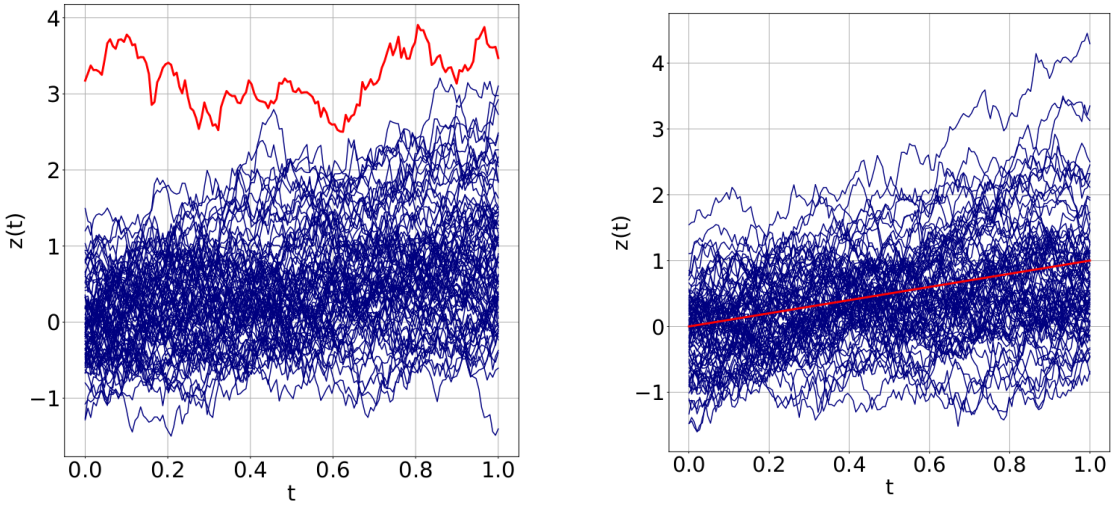

(a) Example of a pure magnitude outlier.

(b) Example of a pure shape outlier.

Figure 1.3: Examples of functional outliers (in color Red).

1.2 Application cases

The work presented in this document was largely influenced by the nature of the considered application cases. Two main applications have been considered and are presented in this document. Their study will constitute the object of Chapters 4 and 5.

Both applications correspond to accidental nuclear transients that are modeled through the *CATHARE* code. The two transients are originated by a similar initiating event, i.e., a break in the cooling system of the primary circuit of a NPP, which entails a sudden loss of coolant (water in this case), that may represent a risk for nuclear safety. The specific nature of this risk depends on the use-case, and involves very different physical phenomena in each case. In order to understand these use-cases, the main elements of a nuclear power plant are briefly explained here.

The most relevant parts of a NPP of Pressurized Water Reactor (PWR) design are showcased in Figure 1.4. An in-depth explanation of the main systems can be found in Chapter 3 whereas here we will just provide the most basic notions. A PWR nuclear power plant involved in the considered transients consists of two main thermal-hydraulic circuits. Firstly, the primary circuit (I), also sometimes referred to as *boiler*, is the part of the installation in charge of taking the thermal energy produced in the nuclear core, mostly through convection between the fuel and the coolant fluid, water. The coolant remains in liquid state even at high temperatures due to the high pressure of the boiler, which remains at approximately 155bar and 320°C. This thermal energy is exchanged with the secondary circuit through a set of large heat exchangers called Steam Generators (SG) (3) . The primary side of these

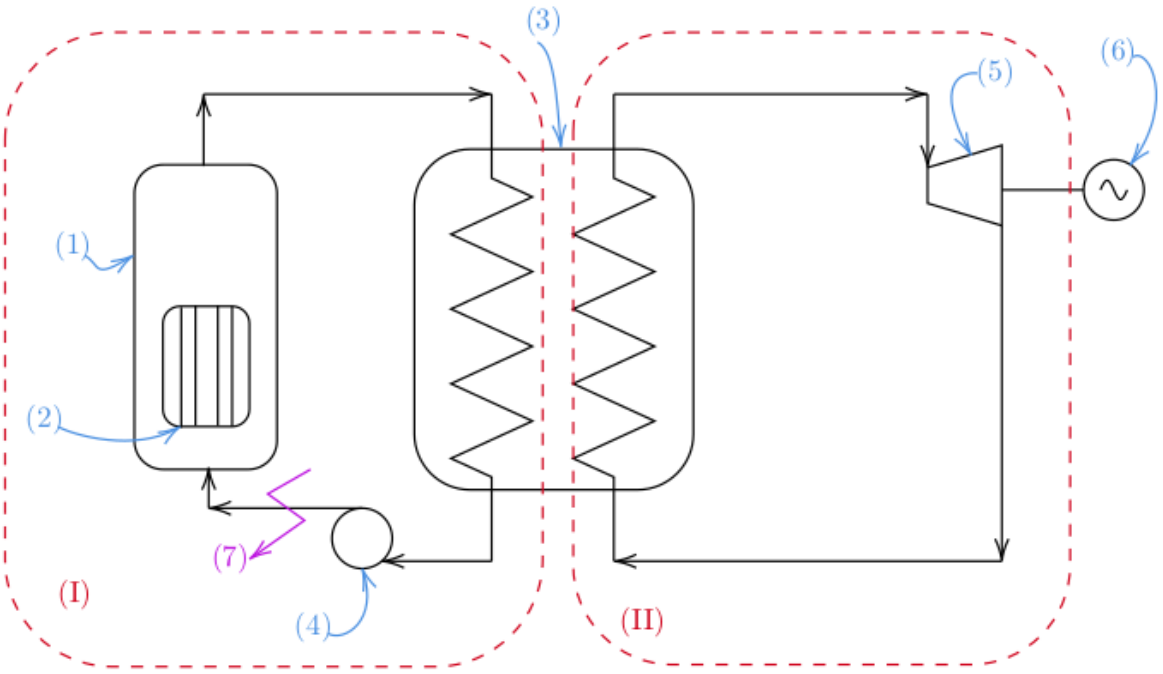

Figure 1.4: Basic thermal-hydraulic diagram of a NPP. I: Primary circuit; II: Secondary circuit. (1): Reactor pressure vessel (RPV); (2): Nuclear core; (3): Steam Generator (SG); (4): Primary pump; (5): Steam turbine; (6): Electrical generator (alternator). (7): Possible break in the primary circuit.

elements is formed by thousands of small tubes that exchange heat with the secondary side, which contains large amounts of pressurized water, which boils in contact with the tubes of the SG through which the primary coolant flows. The generated steam is then sent to the steam turbine (5), where the mechanical energy is transformed into electrical energy sent into the grid.

As it was mentioned, the two considered application cases share the same initiating event, which is a break in the piping system of the primary circuit. This event entails a depressurization of the primary to the surrounding environment's pressure, as well as a loss of coolant through the break that depends on several parameters but which is largely affected by the size of the break. The consequences of the subsequent may largely differ between the cases. These accidents are classified as Loss of Coolant Accidents (LOCA, Joyce (2018)).

We consider in the following two accidental transients which can be modeled with the *CATHARE2* code.

1. **Intermediate Break Loss of Coolant Accident (IBLOCA)**. Firstly, we consider the case of a break of $15.4''$(inches) $= 39.1$cm. A break of this size is frequently considered an intermediate or large one (Tarride, 2013). The considered Intermediate Break LOCA (IBLOCA) transient is characterized by the rapid depressurization of the primary circuit and the loss of a large mass of the water inventory in the boiler. Once

the pressure in the primary becomes too low, the nuclear fission reactions in the core are automatically stopped thanks to the safety systems. However, the nuclear core continues to generate thermal power even after the shutdown phase, mainly due to the radioactive decays of the fission products that remain in the fuel. This source of heat is non-negligible, reaching several dozens of MW in the moments after the shutdown of the core.

In this situation, if the loss of water at the break is not compensated through the Emergency Core Cooling Systems (ECCS), a saturation state can be reached in the primary water through the combined effect of the loss of coolant at the break and the heat release by the fuel. In this situation, if the cooling of the fuel is degraded, its temperature may rise and the main risk of the transient is the possibility of fusion of the nuclear core if a certain threshold of temperature is reached. This transient is analyzed in detail in Chapter 4. An example of several evolutions of the temperature of the fuel and the primary pressure is provided in Figure 1.5. We can appreciate how fast the depressurization is, and the effect of the ECCS once they start injecting cold water into the primary circuit (after about one minute of transient duration).

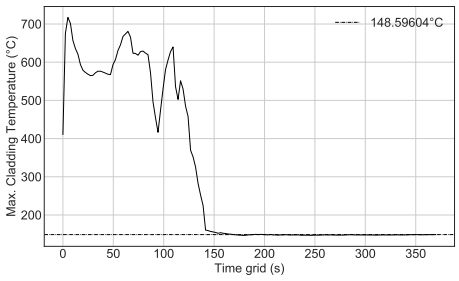

(a) Evolution of the Peak Cladding Temperature (PCT) in a nuclear transient

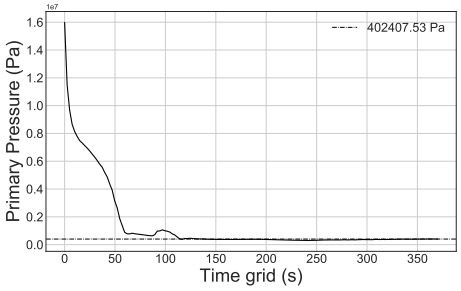

(b) Evolution of the primary pressure in a nuclear transient

Figure 1.5: Examples of different possible evolutions of the maximum temperature of the nuclear fuel and the primary pressure in the case of an IBLOCA.

2. **Pressurized Thermal Shock (PTS)**. The lifespan of NPP can last up to several decades if proper care and maintenance are ensured during its life cycle. In the United States, NPP are allowed by the authorities to extend their life for a total of 80 years (Amano, 2018). In France, the current maximum limit is set to 60 years. Since the RPV (c.f.Figure 1.4) is the only component in a nuclear installation that cannot be substituted during its whole lifespan. It is a component that surrounds the nuclear core and also acts as a confinement barrier for the radioactive material and suffers a constant irradiation (in particular, neutron fluence, measured in neutrons/m^2, of neutrons coming from the core) that entails a progressive modification of its mechanical properties with time. Most notably, this may induce an embrittlement of alloyed steel that composes the RPV, and thus makes it more vulnerable when facing sudden changes in temperature. In particular, an embrittled RPV may be sensitive to an overcooling of the material that can be caused when the ECCS of a nuclear power plant is activated during a LOCA

transient. If this is the case, an existing flaw in the material may become a fracture that can propagate through the component depends on the fracture toughness of the material K_{IC}, which is lowered during the course of the life of the component through the process of radiation embrittlement. The stress intensity at the level of the fracture depends on a number of parameters such as the temperature of the injected water or the pressure. The total stress suffered in this position is assembled into a parameter called stress intensity factor (K_I), such that if $K_I > K_{IC}$, the fracture propagates along the material. If this fracture compromises the integrity of the RPV, the safety of the nuclear installation may also be compromised, which justifies the necessity of the study of this transient.

On a side note, it is relevant to note that this transient becomes particularly severe for small break LOCA transients, and therefore the dynamic of the accident and its physical parameters differ greatly with respect to the previously mentioned IBLOCA. In this case, the analysis requires the use of two chained codes, the system code *CATHARE* and thermal-mechanical one, *CUVE1D*. The latter provides the necessary thermal-hydraulic functional outputs of interest (i.e. the water temperature of the safety injection coolant, the primary pressure and the water flow in the entrance of the RPV), and former allows the calculation of the safety criteria. An example of one of the three thermal-hydraulic functional outputs of the code *CATHARE* that allow the mechanical calculation for the PTS case is displayed in Figure 1.6.

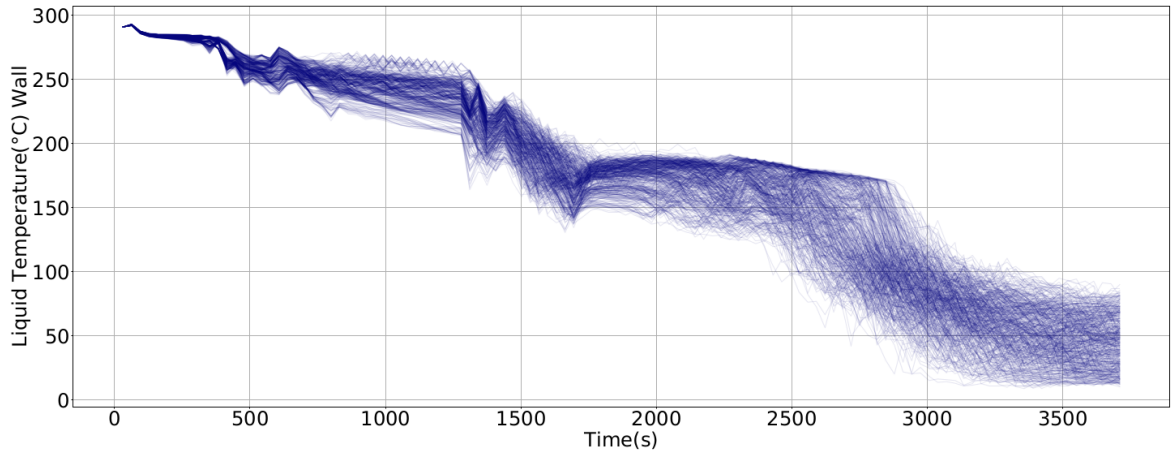

Figure 1.6: Examples of outputs of *CATHARE2* that allow the calculation of safety margins in a PTS transient through the use of a chained mechanical code, *CUVE1D*.

1.3 Some related works

Having provided this Ph.D.'s industrial and scientific context, some related research works developed in recent years which represent significant contributions to the UQ domain applied to nuclear transient simulation are included here. More in-depth reviews of the main literature related to each chapter are included in the first sections of each chapter.

As it was mentioned, the functional outlier detection domain is quite recent, and most contributions were made after 2007, with the works of Febrero-Bande et al. (2008) probably being the most impactful. The domain has been highly influenced by the development of depth functions applicable to functional data (Cuevas et al., 2007; López-Pintado and Romo, 2009; Nagy, 2016) and non-parametric methods (Ferraty and Vieu, 2006), useful to reduce the dimensionality of the problem. There have also been notable contributions that provide visualization tools (Hyndman, 2009; Arribas-Gil and Romo, 2014; Dai and Genton, 2018) and, more recently, some work has also been consecrated to the development of methods applicable to multivariate functional data (Hubert et al., 2015).

A considerable amount of work has been consecrated to the sensitivity analysis domain, aiming at quantifying how the variability of the output variables of interest Y and quantities of interest may be apportioned to the inputs (Saltelli et al., 2008). Some examples are the works of Iooss and Marrel (2019); Marrel and Chabridon (2021) pertaining nuclear applications, as well as the construction of appropriate metamodels for the considered computer code. In Stenger (2020), the author is concerned with the assessment, bounding and optimization of a QoI in a nuclear industrial setting. Accounting for the uncertainty related to the choice of input distributions of the computer model is a subject that has been recently treated in the works of Iooss et al. (2021); Sueur et al. (2017); Gauchy et al. (2021). Regarding the particular subject of FDA, in Auder (2011), the author developed a clustering method for functional outputs of the computer code *CATHARE*, and in Nanty (2015), the author contributes to the framework of sensitivity analysis for functional data linked to scalar covariables.

1.4 Organization of the document

To summarize, this dissertation serves to support engineering studies in the context of nuclear safety assessment. The use of complex numerical simulators requires specialized knowledge of the codes, their inputs, and their outputs, and even then, a vast number of related tasks remain industrially challenging. It is the case, for instance, when functional variables are implicated or when a workflow of chained industrial codes is necessary.

Our contributions aim at facilitating the task of analyzing nuclear transient simulations, dealing with the functional data that may be involved, and providing physical interpretations of the results of the simulations in industrial use-cases, as well as insights regarding penalizing scenarios in a safety assessment context. To do so, we propose to develop the field of functional outlier detection, relating the results of the developed methodology with the inputs of the considered numerical simulator through sensitivity analysis techniques and establishing a general methodology of physical analysis of nuclear transients. The developed methods are confronted with industrial use-cases representative of a wide variety of industrial issues.

The organization of the document is as follows:

Chapter 2, provides an overview of both the domain of functional data analysis, treating the subject of their representation and their reduction of dimension. The subject of outlier

detection is presented in a generic manner, in order to particularize the framework to the particular case of functional data. A general review of the existing methods to perform functional outlier detection is given, highlighting the main scientific challenges. The chapter finishes with the proposition of a methodology to perform this task, testing it against a number of toy examples and state of the art methods.

Chapter 3 particularizes the aforementioned functional data to the context of nuclear transient simulation. We provide here the essential notions in the analysis of these simulations, as well as an overview of the main components of a NPP, how they are modeled through the *CATHARE* code, and how the Best Estimate Plus Uncertainty framework can be used to complement the analysis of nuclear transients. Secondly, the chapter deals with the subject of sensitivity analysis and the available methods that can be used in the context of complex black-box industrial codes (such as *CATHARE*), capable of handling high-dimensional inputs and complex non-linear physical phenomena. Finally, we propose a generic nuclear transient methodology that allows the detection of functional outliers in a particular design of experiments, relates them to the inputs of the code and other physical parameters relevant for the comprehension of the transient through sensitivity analysis techniques and statistical testing, and allows the comparison of the inlying and outlying samples of functional data.

Chapter 4 presents the first relevant use-case, the Intermediate Break Loss of Coolant Accident (IBLOCA). This accidental transient constitutes one of the most commonly analyzed transients in Pressurized Water Reactors, as they constitute one of the dimensioning transients of NPP. Here, the main phases of the accident are presented, as well as how the safety systems of the NPP manage it, including also the *CATHARE* modeling of both the main components of the NPP and the progression of the transient. We showcase how the methodology of transient analysis is capable of identifying outlying transients in a particular design of experiments, and provided a posterior physical interpretation of the results.

Chapter 5. This chapter constitutes a more exploratory application of the methodology to the PTS transient, and serves a twofold objective. Firstly, it showcases the generality of the methodology and how it may serve as a generic tool of analysis several different nuclear transients; and secondly, it constitutes an example of how outliers may be interpreted in real industrial settings as extreme values of a considered distribution of data, and not only samples that have been generated from a different underlying distribution as the majority of the considered sample of data. Finally, it allows to showcase how the generic score of outlyingness presented in Chapter 2 has statistical and physical significance which can be used to provide an interpretation of the inputs and outputs of both the code $\mathcal{M}_1$ (*CATHARE*), and the chained code $\mathcal{M}_2$ (CUVE1D).

Finally, Chapter 6 presents the main conclusions of the developed works, assembles the contributions and provides a set of possible perspectives of these works.

2 Functional Outlier Detection

Contents

2.1 Introduction

In this chapter, we will introduce the main mathematical framework of the manuscript. In the previous chapter we gave the main notions of the uncertainty quantification domain, in particular in the context of industrial numerical simulators. Specifically, in the context of nuclear transient simulators we showcased how the domain is closely related to other mathematical and statistical disciplines, including sensitivity analysis (Iooss and Lemaître, 2015), quantile estimation (Stenger et al., 2020) or metamodeling (Iooss and Marrel, 2019).

In particular, we are interested in the study of numerical simulators that produce one dimensional functional outputs, i.e., unidimensional curves that are functions of a unique variable (namely, the time). The study of these mathematical objects has been widely researched in recent years, and is part of a larger domain usually called *Functional Data Analysis*, term coined by Ramsay (Ramsay, 1982). The study of these objects presents a considerable amount of challenges derived from their intrinsically high (or infinite) dimensional nature.

Let us note that, even though these works are largely motivated by their industrial application, as physical time dependent outputs of the system code *CATHARE2* (Geffraye et al., 2011), we shall remain as general as possible in this chapter and not make reference to the specific physical nature of our data. The reasoning behind this is that the nature of the use-cases that will be analyzed through the document may differ greatly between them even if all of the applications fall into the umbrella of numerical transient simulations. Therefore, it is of great importance to remain as general as possible in the development of the methodologies and conclusions that are extracted from these works, so that they may be applied without adaptations to a wide variety of conceivable use-cases.

The chapter is organized as follows: Section 2.2 details the main mathematical framework of Functional Data Analysis, characterizing the analyzed objects and showcasing the interest of the field. Section 2.3 provides the main elements of the field of outlier detection, with an introduction in the context of multivariate data and the proposed extensions to functional

data, showcasing the main challenges and difficulties that arise in this context. Sections 2.3 and 2.4 provide a brief review of the main existing methods in the context of outlier detection, their deficiencies and advantages, as well as the proposed methodology of Functional Outlier Detection (FOD) that we have developed. We finally confront the proposed methodology against analytical toy-examples and other competitors in Section 2.5, and finish with the conclusions of the chapter in Section 2.6.

2.2 Basic elements of functional data analysis

First of all, we shall recall the notations of the main mathematical objects that will be relevant throughout the whole manuscript. Let us consider a numerical simulator $\mathcal{M}$ (in practice, this will be the aforementioned code *CATHARE2*), which takes a set of uncertain input parameters and provides in turn a functional output:

$$\begin{aligned} \mathcal{M} : \mathcal{X} \subset \mathbb{R}^d &\mapsto \mathcal{F}^* \subset \mathcal{F} \\ X &\to Z = \mathcal{M}(X) \end{aligned} \tag{2.1}$$

where $X = (X_1, X_2, ..., X_d)$ is a set of scalar input variables in $\mathbb{R}^d$, and Z the functional output defined in a functional space $\mathcal{F}$. To be more specific, we will be interested in one-dimensional functional outputs, i.e., functions of one variable that in practice will represent the physical time of simulation in each experiment.

2.2.1 Functional data

The Functional Data Analysis (FDA) framework deals with objects that present themselves in the form of functions. Although the treatment of this kind of mathematical objects can be dated to the works of Grenander (1950) and Rao (1958), it was through the works of Ramsay (1982) and Ramsay and Dalzell (1991) that the term was coined and started gaining considerable interest in industrial settings.

A considerable research effort in the treatment of functional data has been developed in recent years, partially motivated by the wide variety of fields in which this kind of data are present, as well as the increasing measuring and storing capacities of high-dimensional data. The groundbreaking works of Ramsay and Silverman (2005) must be mentioned as a major contributor in the popularization of FDA, also providing practical and real life examples and tools for the treatment of functional data. An alternative vision of the subject was presented in the works of Ferraty and Vieu (2006) through the use of semimetrics that better describe the data. Horváth and Kokoszka (2012) provide several theoretical insights in functional data inference, as well as useful software and practical examples. Some reviews on FDA can be found in Cuevas (2014) and Goia and Vieu (2016).

Functional data serves as a term that describes objects of very different natures. In general, we speak of functions, which may represent one-dimensional or multivariate curves,

spatial data, etc. It is possible to make use of the probabilistic framework to model this kind of objects. In our case, let us consider the probability measurable space $(\Omega, \mathcal{A}, \mathbb{P})$ where Ω represents the sample space, $\mathcal{A}$ is the event space, and $\mathbb{P}$ is a the probability measure over the possible events.

Definition 2.1
Functional random variable. A random variable is called *functional* if it takes its values in an infinite-dimensional vector space. It is then a measurable application $Z : \Omega \mapsto \mathcal{F}$.

In the case of this manuscript, we will consider the output Z, consisting of real-valued functions defined in a set $\mathcal{T} \subset \mathbb{R}$, they may be written:

$$Z_1, ..., Z_S : \Omega \times \mathcal{T} \mapsto \mathbb{R} \tag{2.2}$$

In that case, any function $Z_s(\omega, \cdot) : \mathcal{T} \mapsto \mathbb{R}, \forall \omega \in \Omega$ is called a *trajectory* of Z_s, and any variable $Z_s(\cdot, t) : \Omega \times \mathbb{R}, \forall t \in \mathcal{T}$ is a real-valued random variable.

Let us mention that, in practice, the abundant literature dedicated to this domain makes use of several terms that refer in essence to the same type of mathematical objects. In particular, the notions of *functional data* and *functional random variable* are widely used as synonyms (Ferraty and Vieu, 2006; Chagny et al., 2017) although sometimes the term *functional data* is used in order to refer to specific realizations (samples) of a *functional random variable*. In similar fashion, the term *stochastic process* is commonly used to describe the exact same type of objects, as well as the term *random function* (Gusak et al., 2010). On the other hand, some authors refer to the *functional data* as the realizations of the underlying *stochastic process*, which would then be the random physical process that generates the data (Ordóñez et al., 2011). Finally, if we restrict ourselves to the case where $\mathcal{T} \subset \mathbb{R}$, i.e., one-dimensional functional data, then the previously explained mathematical formalism overlaps with the time series domain. For instance, in Hamilton (1994), the author refers to the time series as a realization of an underlying *stochastic process*.

As we can see, any of these terms can be interchanged with the others and may be used as synonyms for the most part. In our case, since the functional objects that will be analyzed are generated as outputs of a deterministic physical model $\mathcal{M}$ that takes scalar random variables as inputs, it seems appropriate to refer to them as functional random variables or functional data. For the sake of uniformity and clarity, these are the two terms that will be consistently used throughout the manuscript.

As in many industrial cases, we are interested in the framework of these works in functional data whose domain of definition is $\mathcal{T} \subset \mathbb{R}$, i.e., one-dimensional functional data (also called random curves in this case). If the variations of the analyzed physical process can be rightfully considered to do so in a continuous manner, the functional data can be assumed to belong to the space of continuous functions $\mathcal{C}(\mathcal{T})$. Commonly, the analyzed functional data are assumed to belong to a particular Hilbert space (complete metric space with respect

to an inner product) $\mathcal{F}$ which are *normed*, i.e., where $\forall f \in \mathcal{F}, ||f|| = \sqrt{\langle f, f \rangle}$. A frequent example is the $L^2(\mathcal{T})$ space of square-integrable measurable functions. This formalism allows a representation of any element of $\mathcal{F}$ in terms of its inner product such that:

Theorem 2.1
Let $(H, \langle \cdot, \cdot \rangle)$ be a separable Hilbert space. Then H admits a countable hilbertian basis $\{\phi_j, j \in \mathbb{N}\}$ of orthonormal elements, such that any element $f \in H$ can be uniquely decomposed in the form:

$$\forall f \in H, f = \sum_{j \in \mathbb{N}} \langle f, \phi_j \rangle \phi_j$$

This framework allows the definition of exploratory statistics for functional random variables such as their expectation and their covariance operator and covariance function.

Definition 2.2
Let Z be a functional random variable defined in a functional space $\mathcal{F}$. If $\mathbb{E}[||Z||] < \infty$, it is possible to define the **expectation** of Z as:

$$\mathbb{E}[Z] = \int_{\Omega} Z(\omega) d\mathbb{P}(\omega)$$

where the integral is the Bochner integral (Dunford and Schwartz, 1988) of Z, and $|| \cdot ||$ is a norm in $\mathcal{F}$. If $\mathcal{F}$ is a Hilbert space, we can also express the expectation as: $\mathbb{E}[\langle Z, \mathcal{F} \rangle] = \langle \mathbb{E}[Z], f \rangle$.

Conversely, the notion of covariance may be represented in the functional case by an operator. Again, if we consider that $\mathcal{F}$ is a Hilbert space:

Definition 2.3
Assuming that $\mathbb{E}[||Z||^2] < \infty$. Then the **covariance operator** κ of Z is defined as:

$$\kappa : f \in \mathcal{F} \mapsto \kappa f = \mathbb{E}[\langle Z - \mathbb{E}[Z], f \rangle (Z - \mathbb{E}[Z])]$$

If these hypotheses are verified, κ is autoadjoint, and diagonalizable in an orthonormal basis. This result yields useful expansions such as the one presented in 2.2.2.

From a practical point of view, it is common to see and express the functional data as a family of real random variables, since it is impossible to dispose of a perfect representation of $Z(t), t \in \mathcal{T}$, and functional objects are observed in a discrete grid $\tau = \{t_g\}_{g=1}^{p}$. For the rest of the chapter, we will assume that a sample of functional variables z_i (in minuscule for easiness to the reader) of size N indexed by i is available in a discretization grid τ:

$$z_i : \mathcal{T} \mapsto \mathbb{R}, \forall i \in \{1, ..., N\} \tag{2.3}$$

whereas specific values of z_i in each point of the discretization grid are noted $z_{i,g} = z_i(t_g)$.

If the functional data are sampled with a uniform time step, i.e., $t_g - t_{g-1} = C, \forall g \geq 1$, where C is a constant (which will be the usual case in this manuscript), empirical estimates for both the mean and covariance function exist such that: $\hat{\mu}(t_g) = \frac{1}{N}\sum_{i=1}^{N} z_{i,g}$, where $\hat{\mu} = \{\hat{\mu}(t_1), ..., \hat{\mu}(t_p)\}$ is the empirical functional mean; and $\hat{\Sigma}(t_l, t_v) = \frac{1}{N}\sum_{i=1}^{N}(z_{i,l}, \hat{\mu}(t_l))(z_{i,v}, \hat{\mu}(t_v))$. For some insight on the case where data is missing and heterogeneous grids are used the reader can refer to Little and Rubin (2019).

A natural question that arises concerning the grid is the quality of the representation of functional data that can be made depending on the size p of the grid. We usually speak about the *density* of the data, but no formal definition of this notion exists yet in the literature. A somewhat unified approach is provided in Zhang and Wang (2016), where they classify functional data into three categories: *dense*, *ultra-dense* and *sparse* functional data. This classification is influenced by the asymptotic properties of certain statistical estimators from the sample of functional data. Anyhow, it is common practice to consider that the considered sample of functional data is dense if the convergence rate of the empirical estimator of the mean $\mu(t) = \mathbb{E}[Z]$ attains a rate of $\sqrt{n}$ according to a standard metric (namely, the L^2 norm) when the increase in size of the time grid p diverges to infinity fast enough (Wang et al., 2016).

2.2.2 Representation of functional data on a basis

As we have seen, functional data are generally observed in a finite set. This arises the question of how to find an appropriate representation of the data. This representation depends mainly on the nature of the data, and how they are observed. For instance, if the functional data are observed without error, an appropriate representation of the data should be interpolatory, i.e., the reconstructed functional data must take the exact observed values in the available grid. Otherwise, if they are observed with an error or the data are subject to random noise, then smoothing techniques become necessary. Regarding the nature of the analyzed functional data, if they present specific patterns, are oscillatory. or present some kind of specific characteristic, this should be taken into account when performing the reconstruction.

In practice, the main objective is to find a useful representation of the available functional data that best represents the underlying physical process that generates them. Representing functional data as a linear combination of elemental functions is a practical and valuable way of simulating these data.

Let us consider a sample $\{z_i\}_{i=1}^{N}$of a functional random variable defined in $\mathcal{F} = L^2(\mathcal{T})$, where $\mathcal{T} \subset \mathbb{R}$. The idea is to approximate any observation z_i as a linear combination of functions that form a basis of $\mathcal{F}$. If Z is a functional random variable in $\mathcal{F} = L^2(\mathcal{T})$, we can express it as:

$$Z = \sum_{k=1}^{\infty} c_k \phi_k(t) \tag{2.4}$$

This representation can be implemented in practice by truncating this expansion and estimate the corresponding coefficients. It is then possible to approximate Z by $\hat{Z}(t) = \sum_{k=1}^{D} \hat{c}_k \phi_k(t), t \in \mathcal{T}$. This procedure allows the obtention of a lower dimensional subspace of dimension D.

We show some of the main approximation basis that are commonly used. It should be noted that they can be classified into two main groups. Firstly, those which are *fixed*, i.e., they do not depend on the actual data that will be modeled (for instance, the Fourier and wavelet bases), and those which adapt to the specific sample of available data. These representations are also widely used in the FOD domain (see for instance Barreyre et al. (2019)).

2.2.2.1 Fourier basis

The Fourier basis, also called trigonometric basis is one of the most well known possible bases used to represent random curves with a periodic behavior.

Definition 2.4
Fourier basis. The Fourier basis is defined as:

$$\phi_0(t) = 1; \phi_{2k-1}(t) = \sin(kwt); \phi_{2k} = \cos(k\omega t), k \in \mathbb{N}^+$$

where ω is the period. The mathematical theory on the use of the Fourier basis is largely developed, and numerous results on the convergence of this representation exist for functional data.

2.2.2.2 B-spline basis

Given a set of knots $\{t_1, ..., t_p\} \in \mathcal{T} \subset \mathbb{R}$, let us define two supplementary boundary knots $t_0 < t_1$ and $t_{p+1} > t_p$ in which we shall evaluate the spline functions. Let us also define the knot sequence of points τ:

- $\tau_1 \leq \tau_2 \leq ... \leq \tau_M \leq t_0$
- $\tau_{j+M} = t_j, j \in \{1, ..., p\}$
- $t_{p+1} \leq \tau_{p+M+1} \leq \tau_{p+M+2} \leq ... \leq \tau_{p+2M}$

the additional knots outside of $\mathcal{T} + \{t_0\} + \{t_{p+1}\}$ can have arbitrary values assigned, and are commonly set equal to the values of t_0 and t_{p+1}. Let $B_{l,m}(t)$ denote the lth B-spline function

of order m for the knot sequence τ, with $m \leq M$. These basis functions can be recursively defined in terms of divided differences:

$$B_{l,1}(t) = \begin{cases} 1 \text{ if } \tau_l \leq t \leq \tau_{l+1} \\ 0 \text{ otherwise} \end{cases}$$

for $l = 1, ..., p + 2M - 1$

$$B_{l,m} = \frac{t - \tau_l}{\tau_{l+m-1}} B_{l,m-1}(t) + \frac{\tau_{l+m} - t}{\tau_{l+m} - \tau_{l+1}} B_{l+1,m-1}(t)$$

for $l \in \{1, ..., p + 2M - m\}$.

2.2.2.3 Wavelet bases. The Haar basis

More recent bases that combine some of the characteristics of the already presented bases can be mentioned. In particular, those based in wavelet systems (Daubechies, 1992; Härdle et al., 1998).

A wavelet system in $\mathcal{F} = L^2(\mathcal{T})$ is a collection of functions with the form:

$$\{2^{l/2}\psi(2^l t - v)\}_{l,v \in \mathbb{Z}} = \{\psi_{l,v}\}_{l,v \in \mathbb{Z}} \tag{2.5}$$

where $\psi \in L^2(\mathcal{T})$ is a fixed function. Any wavelet system that forms an orthonormal basis in $L^2(\mathcal{T})$ is called a *wavelet orthonormal basis* for $L^2(\mathcal{T})$.

There is a particular type of wavelet basis called the Haar (Mitteilung, 1910) basis of $L^2(\mathcal{T})$. By setting $\phi_0 = \mathbb{1}_{\mathcal{T}}$ and $\psi = \mathbb{1}_{[\inf(\mathcal{T}),\sup(\mathcal{T})/2[} - \mathbb{1}_{[\sup(\mathcal{T})/2,\sup(\mathcal{T})[}$, for all $l \geq 0, v \in \Theta(l) = \{0, 1, ..., 2^l - 1\}$ we write $\phi_{l,v}(t) = 2^{l/2}\psi(2^l t - v)$. This way, the set of functions $(\phi_0, \phi_{l,v})$ forms the orthonormal Haar basis of $\mathcal{F}$.

This way, any function $z \in \mathcal{F}$ can be represented by an expansion in the Haar basis:

$$z(t) = \phi_0(t) + \sum_{l \geq 0} \sum_{v \in \Theta(l)} c_{l,v}\phi_{l,v}(t) \tag{2.6}$$

2.2.2.4 Karhunen-Loève expansion

In the multivariate framework, the Principal Component Analysis (PCA) (Pearson, 1901; Hotelling, 1933) has proven to be a powerful tool in order to perform dimensionality reduction tasks. It allows to find the orthogonal directions which maximize the projected variance of a sample of points in a space $\mathbb{R}^q$.

In the functional case, Ramsay and Silverman (2005) proposed an evolution of this method called Functional Principal Component Analysis (FPCA).

Recalling the notations used in 2.2.1, we have seen that, given a Hilbert space $(\mathcal{F}, \langle\cdot,\cdot\rangle)$ with covariance operator κ, this operator is diagonalizable such that there exists a basis for $\mathcal{F}$ formed by the eigenvectors $\{\psi_j\}_{j\in\mathbb{N}}$ of κ, associated to the set of eigenvalues $\{\lambda_j\}_{j\in\mathbb{N}}$, solutions to the problem $\kappa\psi_j = \lambda_j\psi_j$. In this case, any functional random variable Z can be developed in this hilbertian basis.

Definition 2.5
Karhunen-Loève (KL) expansion. We call KL expansion of a functional random variable Z in a given Hilbert space $\mathcal{F}$ such that $\mathbb{E}[||Z||^2] < \infty$ to its projection into the basis of eigenfunctions of its corresponding covariance operator κ:

$$Z = \mathbb{E}[Z] + \sum_{j=1}^{\infty}\langle Z, \psi_j\rangle\psi_j = \mathbb{E}[Z] + \sum_{j=1}^{\infty}\sqrt{\lambda_j}\xi_j\psi_j$$

where $\xi_j = \langle Z, \psi_j\rangle\sqrt{\lambda_j}$.

2.3 Outlier Detection

Detecting outliers in datasets is a generic statistical task that lacks a rigorous framework based on mathematical grounds. First of all, there is some uncertainty regarding the terminology. Hawkins (1980) defines an outlier as an *observation which deviates so much from the other observations as to arouse suspicions that it was generated by a different mechanism.* This could be regarded as the most indisputable definition of what constitutes an outlier in a set of data, regarding outliers as realizations of a spurious data generation process different from the one that generates the *majority* of data.

Outliers may be found in the literature among different names, such as *abnormalities*, *deviants* or *anomalies*, and their detection is often important as a previous step in the analysis of the expected data so as to avoid working with *contaminated* datasets that may pollute the interpretations that may be extracted from them (Aggarwal, 2017). Naturally, the main problem that arises in this context is the definition of what constitutes "normal behavior, and how to ensure that the chosen measure (or measures) that quantify this notion can be universally accepted as such.

To add another layer of complexity to the problem, some authors (Aggarwal and Yu, 2001; Knorr and Ng, 1999) make the distinction between *weak* and *strong* outliers. Weak outliers would be those data points which present a deviation from the normal behavior sufficiently important so as to classify them as outliers, but whose presence may be of no interest to the analyst since it is regarded as *noise*. On the other hand, strong outliers would be those whose deviation is sufficient, and also may be representative of an important underlying process of

interest for the analyst. An example of this situation is presented in Figure 2.1.

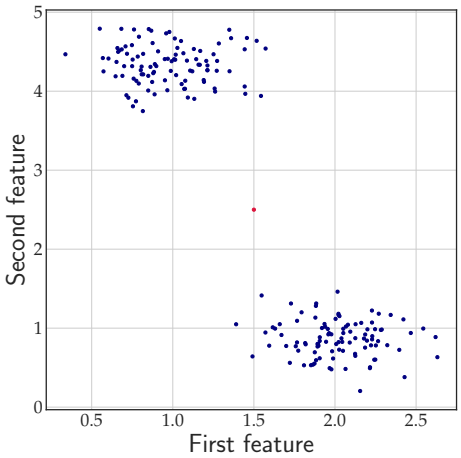

(a) Example of strong outlier (in red). We can appreciate the existence of two distinct clusters and an isolated point that can be rightfully be considered an anomaly.

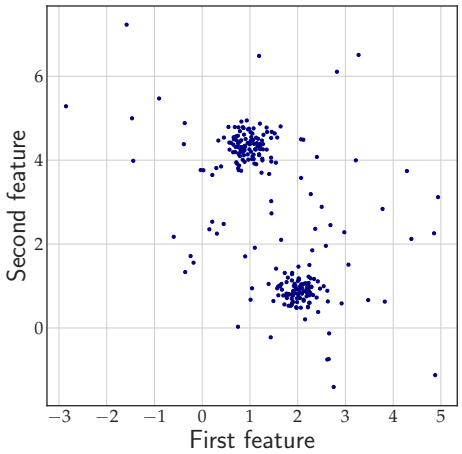

(b) Example of weak outliers. Amongst the two main groups of samples, we can see a set of points whose nature is much more subjective.

Figure 2.1: Examples of strong and weak outliers.

In other real life situations, outliers can be conceived as extreme values of a unique underlying process. Indeed, it is impossible in practice to differentiate an outlier from an extreme value, even if both data had been generated by different processes. In this setting, detecting strong outliers, weak outliers or extreme values becomes only a matter of semantics. If this is the case, in the univariate setting these extreme values may be identified through well-known statistical tail confidence tests (t-value test, or the sum of squares deviations, which follow a χ^2 distribution), as well as graphical tools such as the boxplot (Savage et al., 1962). In higher dimensional contexts, it is indeed possible to apply these techniques over scores that allow to perform a dimension reduction. As an example, one could apply these techniques over each individual principal component score shown in 2.2.2.4 in order to identify outliers.

Another important matter to discuss is the fact that, in essence, the domain of outlier detection can be interpreted as purely *unsupervised*, if we have no prior knowledge of the nature that the outliers may adopt; or *supervised*, if some prior knowledge exists. As usual, the detection of outliers in the supervised setting becomes a much more simple task, since even though the nature of the outliers may differ considerably in a dataset, the prior knowledge of the existence of outliers largely facilitates the task of rigorously defining the "normal" behavior. In order to remain as general as possible, we will consider in our setting that only a sample of data is available, and no prior knowledge of them exists.

In a very general sense, all (or most) outlier detection techniques aim at modeling a

standard or normal pattern in the available data, and estimate outlyingness scores based on the divergence between each individual observation and this pattern. Naturally, modeling the standard nature of the observations is much easier in the supervised setting, but similar techniques may be applied in the unsupervised setting. From Aggarwal (2017), a basic classification of outlier methods in both the supervised and unsupervised context may be established, and is showcased in Table 2.1.

Table 2.1: Basic classification of outlier detection methods for both the supervised and unsupervised setting.

Supervised model	**Unsupervised equivalent**	**Type of model**
k-nearest neighbor	k-NN distance, LOF, LOCI	Instance based
Linear Regression	Principal Component Analysis	Explicit generalization
Naive Bayes	Expectation-maximization	Explicit generalization
Rocchio	Mahalanobis method, Clustering	Explicit generalization
Decision Trees, Random Forests	Isolation Trees, Isolation Forests	Explicit generalization
Rule-based	FP-Outlier	Explicit generalization
Support Vector Machines	One-class support-vector machines	Explicit generalization
Neural Networks	Replicator neural networks	Explicit generalization
Matrix factorization	Principal component analysis, Matrix factorization	Explicit generalization

As shown in Table 2.1, detection methods may be separated into *explicit generalization* and *instance-based* ones. The former makes reference to models, in which the underlying model that is supposed to represent the normal patterns has to be generated as a previous step to the detection of the desired outliers; whereas the latter simply computes the desired test instances through the available data.

Finally, the subject of the rigorous validation of detection algorithms remains a complex task without a real solution in current literature. Firstly, due to the intrinsic low probability of occurrence of an outlier (they are rare by definition), it is not trivial to evaluate the detection capabilities of any given algorithm over a wide variety of situations so as to estimate reliable false positive and detection rates. On top of that, when applied to real examples, no "indisputable" label of outlier or *inlier* (i.e. not outlier) can be obtained, and so the results

are open for interpretation in an unsupervised scenario. Therefore, most of the research on this field relies on simple toy examples as validation tools to compare these rates of interest. The obvious downside of this procedure is that it is difficult to generalize and extrapolate the results to real examples, and seems to imply that the quality of the procedures can only be evaluated on a case-by-case basis.

2.3.1 Notion of outlier in a functional context

In the functional setting, the detection of outliers becomes even more complex due to the intrinsic infinite-dimensional nature of the data. The first works regarding the FOD domain date from the works of Fraiman and Muniz (2001), where they introduced the notion of functional depth as an extension to the same notion of functions in the multivariate setting (Mozharovskyi, 2016; Oja, 1983), aiming at providing an ordering in spaces of large dimension. This ordering could be used in order to quantify the centrality of a particular observation in a sample of functional data or, conversely, how extreme it is, providing a center-outward ordering of the sample (Febrero-Bande et al., 2008). This idea also serves as a FOD tool.

The detection of functional outliers presents the same difficulties as in the multivariate setting, plus certain difficulties of its own. Since no natural ordering exists in any given space $\mathbb{R}^d, d \geq 2$, most multivariate methods must rely on notions of distance or density of data in their respective spaces, which are sensitive to the *curse of dimensionality*. This problem becomes even more relevant in infinite-dimensional vector spaces that model functional data, but other challenges exist. Another very relevant challenge is the broad nature or *taxonomy* (Dai et al., 2020) of possible outliers that may arise when analyzing functional data.

Most authors make the distinction between two main types of functional outliers. Hyndman (2009) defines *magnitude* outliers as those which are *distant from the mean curve*, whereas *shape* outliers would be those which present *a different pattern* from the bulk of curves. Dai et al. (2020) very generally describes a magnitude outlier as an observation which *is outlying in some part or across the whole design domain*, whereas shape outliers are those which *present a different shape from the bulk of data, even though it may not be outlying throughout the whole domain*. In Hubert et al. (2015), the authors prefer the terminology *amplitude* outliers to refer to magnitude ones, describing them as *curves that may have the same shape as the majority but its scale (range, amplitude) differs*, and shape outliers being those *whose shape differs from the majority without necessarily standing out at any time point*. Finally, Dai and Genton (2018) propose a division of shape outliers between *shifted*, *isolated* and pure *shape* outliers, plus the *magnitude* ones.

An example of all of these types of outliers can be seen in Figure 2.2. For the remainder of the document, we shall adhere to the classical terminology of the field and consider that shifted and isolated outliers can be seen as combination of magnitude and shape ones, such that we will consider that the outliers may only be considered as such in the magnitude sense, the shape sense, or as a combination of both.

No exhaustive review of functional outlier detection methods has been published up until

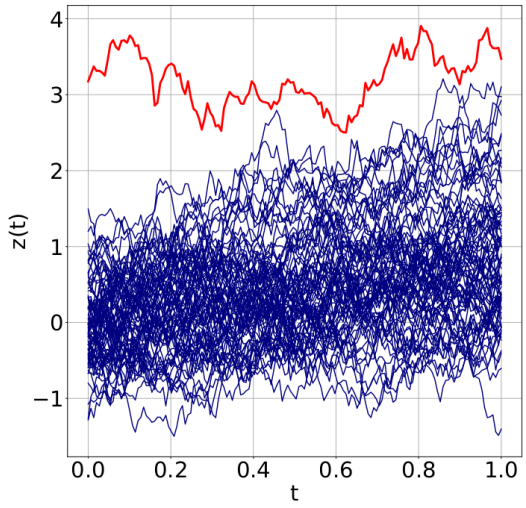

(a) Example of a pure magnitude outlier.

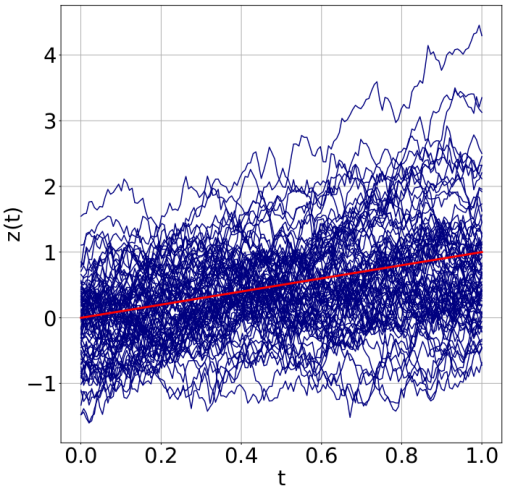

(b) Example of a pure shape outlier.

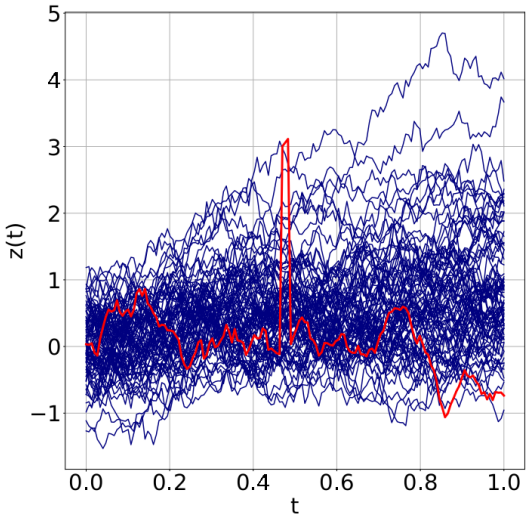

(c) Example of an isolated outlier.

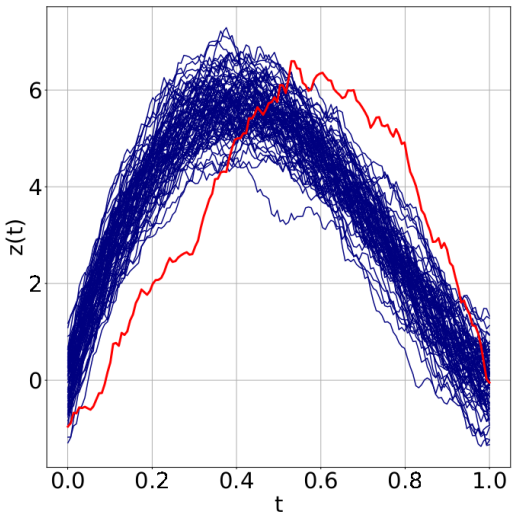

(d) Example of a shifted outlier .

Figure 2.2: Main types of outliers. Red: outlying observation in the sample of functional data, generated by a different underlying process. Blue: bulk of normal curves generated by the standard underlying process.

today. This is due to the fact that the domain is quite recent, with most published methodologies dating after the paper by Febrero-Bande et al. (2008), and presenting a wide diversity and heterogeneity between them. There exists however some work that has been published in the domain of functional data clustering, the reader may refer to the works of Jacques and Preda (2014) and the Ph.D. works of Auder (2011). As we introduced before, there is a degree of overlapping between the outlier detection domain and the clustering one. If we assume that a sample of functional data $\{z_i\}_{i=1}^N, z_i \in \mathcal{F}$, where $\mathcal{F}$ is a Hilbert space, the clustering task consists in assigning each observation z_i to one specific subspace $\mathcal{F}_s$ in the set

$\{\mathcal{F}_s\}_{s=1}^{S}, \mathcal{F}_s \subset \mathcal{F}$. In this case, if we establish $S = 2$, where one of the subspaces is formed by the samples that present an inlying behavior, and the other is formed by the outliers, both problems (clustering and outlier detection) become equivalent.

In practice, a similar distinction between the existing methods can be made for the FOD domain and the clustering one. From Jacques and Preda (2014), four main families exist:

1. Raw curve classification. If any z_i is observed in a discretized grid $\tau = \{t_g\}_{g=1}^{p}$, it can be considered as a random vector $(z_i(t_1), z_i(t_2), ..., z_i(t_p)) \in \mathbb{R}^p$. In that case, classical multivariate techniques may be used (Bouveyron and Brunet, 2013) without taking into account the functional nature of the sample. This approach is the most simple one, and among its main drawbacks, we can mention the *curse of dimensionality* problem, since the sample of curves can easily be of the same order of magnitude than the grid size ($N \leq p$)), and the fact that it does not take into account the functional nature of the data. In practice, these methods are mostly sensitive to basic types of magnitude outliers.

2. Two-stage approaches (*filtering methods*). The sample $\{z_i\}_{i=1}^{N}$ is projected onto a basis of functions of $\mathcal{F}$ (for instance, one of those presented in 2.2.2), and a second clustering step is performed on the lower dimensional multivariate space of coefficients (Abraham et al., 2003; Peng and Müller, 2008). See Barreyre et al. (2019) for an example using the Haar basis (2.2.2.3) based on statistical tests.

3. Non-parametric approaches (see Ferraty and Vieu (2006)). They rely on notions of distance and ordering (ranking) between the data, in order to apply a clustering technique on these selected features. For instance, they may rely on depth measures (see 2.3.2) on non-parametric notions of proximity (see 2.3.2.1) such as :

$$d_l(z_i, z_j) = \Big(\int_{\mathcal{T}} (z_i^{(l)}(t) - z_j^{(l)}(t))^2 dt \Big)^{\frac{1}{2}} \tag{2.7}$$

   where $z^{(l)}$ represents the lth derivative of the observation z. Examples of this procedure can be found in Ieva et al. (2013); Tokushige et al. (2007).

4. Model-based approaches. These methods rely on the estimation of the underlying probabilistic structure that generates the sample of functional data. Since the notion of density function cannot be uniquely defined in infinite-dimensional spaces, this objective is unfeasible, and in practice this is done by estimating the desired model over a lower-dimensional representation of the data. Regarding this group of methods, in the context of clustering both tasks (the projection and the estimation of the model) are usually made simultaneously, whereas in the outlier detection framework this is not necessarily the case (Hyndman, 2009).

We will dedicate the next section to explaining several techniques that allow to perform a reduction of the dimensionality of the sample of functional data.

2.3.2 Dimension Reduction

The vast majority of explanatory tools for functional data are based on techniques that allow a lower-dimensional representation of the considered set of functional data, so as to avoid the difficulties that arise when working with infinite-dimensional spaces. The methods that allow a lower-dimensional representation of functional data are diverse and based on very different kinds of measures. We provide in the following sections a comprehensive review of the main possibilities available to perform dimensionality reduction on functional data.

It should be noted that the representation through functional bases presented in Section 2.2.1 could also be included here, since they are also methods that allow to perform dimensionality reduction of the problem. We focus here however in measures aiming at detecting specific features of the analyzed functional data, and not necessarily reconstruct the sample.

2.3.2.1 Semimetrics

Ferraty and Vieu (2006) provide wide overview of non-parametric methods as exploratory tools for functional data. The authors make the case as to how normed metric spaces can be too restrictive as modeling tools for functional data if the objective is to extract statistical information from them. They briefly showcase how the use of semimetrics can aid in the extraction of information from functional data.

Definition 2.6
Pseudometrics (Arkhangel'skii and Pontryagin, 1990). Let $\mathcal{F}$ be some vector space, then any mapping $d : \mathcal{F} \times \mathcal{F} \mapsto \mathcal{I}, \mathcal{I} \subset \mathbb{R}^+$ is a pseudometric on $\mathcal{F}$ as soon as:

1. $\forall z \in \mathcal{F}, d(z, z) = 0$
2. $\forall (z_1, z_2) \in \mathcal{F} \times \mathcal{F}, d(z_1, z_2) = d(z_2, z_1)$ *(*symmetry *condition)*
3. $\forall (z_1, z_2, z_3) \in \mathcal{F} \times \mathcal{F} \times \mathcal{F}, d(z_1, z_2) \leq d(z_1, z_3) + d(z_3, z_2)$

In other words, a pseudometric can be seen as a metric that does not satisfy the *separation* condition, i.e., $d(z_1, z_2) = 0 \implies z_1 = z_2$. To be precise, the notion of semimetric is relatively ambiguous in the literature, so we shall adhere to the definition provided by Ferraty and Vieu (2006), where a semimetric can be seen as a pseudometric which does not satisfy the *symmetry* condition:

Definition 2.7
Semimetric. Let $\mathcal{F}$ be some vector space, then any mapping $d : \mathcal{F} \times \mathcal{F} \mapsto \mathcal{I}, \mathcal{I} \subset \mathbb{R}^+$ is a semimetric on $\mathcal{F}$ as soon as:

1. $\forall z \in \mathcal{F}, d(z, z) = 0$
2. $\forall (z_1, z_2, z_3) \in \mathcal{F} \times \mathcal{F} \times \mathcal{F}, d(z_1, z_2) \leq d(z_1, z_3) + d(z_3, z_2)$

They are actually defined in analogy to seminormed spaces.

Three main families of semimetrics are proposed, although no universal classification exists, since there is an infinity of possibilities when it comes to building semimetrics that will be applied to functional data. Let us consider a finite sample of independent and identically distributed observations of functional data $\{z_i\}_{i=1}^N$ from a functional random variable Z in $\mathcal{T} \subset \mathbb{R}$. The first class of semimetrics are those based in the FPCA presented in 2.2.2.4. Considering that $\mathcal{F} \subset L^2(\mathcal{T})$, and the corresponding functional random variable Z:

$$Z = \sum_{j=1}^{\infty} \langle Z, \psi_j \rangle \psi_j = \sum_{j=1}^{\infty} \sqrt{\lambda_j} \xi_j \psi_j = \sum_{j=1}^{\infty} \Big(\int Z(t)\psi_j(t)dt \Big) \psi_j \tag{2.8}$$

where $\{\psi_j\}_{j=1}^{\infty}$ are the orthonormal eigenfunctions of the covariance operator κ. By truncating the previously defined expansion, we consider: $\tilde{Z}^{(q)} = \sum_{j=1}^{q} \Big(\int Z(t)\psi_j(t)dt \Big) \psi_j$, we have an optimal representation of the data in a lower dimensional space in the sense of the L^2 norm. This expansion minimizes $\mathbb{E}[\int (Z(t) - P_q Z(t))^2 dt)]$ over any given projection P_q of Z into this space. It is thus possible to define a whole family of semimetrics based on the norm L^2:

$$d_q^{FPCA}(z_v, z_l) = \sqrt{\sum_{j=1}^{q} \Big(\int [z_v(t) - z_l(t)]\psi_j(t)dt \Big)^2} \tag{2.9}$$

Since κ is unknown in practice, it may be estimated from its empirical form (for a centered process): $\kappa_Z^N(s,t) = \frac{1}{N} \sum_{i=1}^{N} z_i(s) z_i(t)$, whose eigenfunctions are consistent estimator of the eigenfunctions of κ (Cardot et al., 1999). Considering also the discretized versions of the sample of functional data in the grid τ, each individual integral in (2.3.2.1) can be approximated as (Castro et al., 1986):

$$\int [z_v(t) - z_l(t)]\psi_j(t)dt \approx \sum_{g=1}^{p} w_g (z_v(t_g) - z_l(t_g))\psi_j(t_g) \tag{2.10}$$

where $\{w_g\}_{g=1}^{p}$ are the quadrature weights used to approximate the integral (a standard possibility is to simply choose $w_g = t_g - t_{g-1}$). This way, the empirical version of any semimetric based on a FPCA can be written as:

$$\widetilde{d}_q^{FPCA}(z_v, z_l) = \sqrt{\sum_{j=1}^{q} \Big(\sum_{g=1}^{p} w_g (z_v(t_g) - z_l(t_g))\psi_j(t_g) \Big)^2} \tag{2.11}$$

A second important family of semimetrics can be built in the context where the functional random variable Z is associated to a scalar (or multivariate) response. This case does not apply here, but there exist well adapted constructions of semimetrics based on the Partial Least Squares (PLS) and Multivariate Partial Least Squares (MPLS) decompositions (Wold, 1966; Frank and Friedman, 1993; Helland, 1990).

Finally, Ferraty and Vieu (2006) establish a third family of semimetrics by taking into account notions of distance between derivatives of the observed functions. In general, these semimetrics take the form:

$$d_l(z_i, z_j) = \Big(\int_{\mathcal{T}} (z_i^{(l)}(t) - z_j^{(l)}(t))^2 dt \Big)^{\frac{1}{2}} \tag{2.12}$$

The computation of derivatives (and in particular, those of higher order) can be numerically challenging. It is however possible to circumvent this problem by projecting the set of observations onto an analytic functional basis such as the B-splines one, presented in 2.2.2.2. Since the analytical form of the basis functions is known, each z_i in the sample can be efficiently approximated and its derivatives can be estimated.

2.3.2.2 Depth functionals

Generally speaking, *depth* functions appeared as an attempt to generalize the notions of quantile to multivariate data (Mozharovskyi, 2016), or, equivalently, as tools aiming at providing a center-outward ordering of objects existing in such spaces (Zuo and Sering, 2000). Although attempts at providing a sense of ordering in multivariate and functional spaces have been made, it was Zuo and Sering (2000) who made the first comprehensive review of characteristics that are supposed to define what a depth functional is and what their properties are.

Still in the multivariate setting, let us consider a compact set $\mathcal{E} \subset \mathbb{R}^d$, and consider the functions $d : \mathcal{E} \mapsto \mathbb{R}$. If we denote the set of all Borel probability measures on $\mathcal{E}$ as $\mathcal{P}$, and $(\Omega, \mathcal{A}, \mathbb{P})$ is the probability space on which all multivariate random variables $X : \Omega \mapsto \mathcal{E}$ are defined, a depth function D is a bounded mapping $D : \mathcal{E} \times \mathcal{P} \mapsto \mathbb{R}^+; (x, \mathbb{P}) \to D(x, \mathbb{P})$.

Let F_x be the cumulative distribution of any given random vector x, realization of the random variable X, then the basic properties of a multivariate depth function would be:

1. $D(Ax + b, F_{Ax+b}) = D(x, F_X)$ holds for any random vector X in $\mathbb{R}^d$, where A is any non-singular matrix of dimension $d \times d$, and b is any given vector in $\mathbb{R}^d$. In other words, a depth function D should be affine invariant and not depend on the coordinate system.

2. $D(\xi, F) = \sup_{x \in \mathbb{R}^d} D(x, F)$ hold for any distribution F in the class of distributions on the Borel sets of $\mathbb{R}^d$ whose *center* is ξ. The term center is loosely defined in Zuo and Sering (2000) as a *point of symmetry according with respect to any notion of symmetry* (in $\mathbb{R}^d$), such that D attains its maximum there.

3. For any F whose deepest point is ξ, $D(x, F) \leq D(\xi + \alpha(x - \xi), F), \forall \alpha \in [0, 1]$, i.e., D decreases monotonically with respect to the deepest point in the considered sample.

4. $D(x, F) \to 0$ as $||x|| \to \infty$ for any given F. Depth functions must vanish at infinity.

Naturally, since the actual analytic form F is seldom available, it is common practice to replace $D(x, \mathbb{P})$ by its sample version, i.e., substituting the considered measure of probability by an empirical one $D_N(x) = D(x, \mathbb{P}_N)$.

Analogously to what we have previously presented, the development of depth functionals for functional data is much more recent than the multivariate one, and the field has experienced considerable development in recent years, with the proposition of many depth functionals adapted to functional data (Cuevas and Fraiman, 2009; López-Pintado and Romo, 2009; Cuesta-Albertos and Nieto-Reyes, 2008). A natural idea that arises in the definition of depth functionals in this context would be to simply replace the considered compact set $\mathcal{E}$ for an equivalent functional space $\mathcal{F}$ such that the same aforementioned desired properties are preserved. Some very obvious examples of how this might be challenging can be extracted from looking at the already presented properties. For instance, even in multivariate spaces the notion of symmetry is not uniquely defined, let alone in functional ones, so the actual verification of the second property is almost intractable in practice. Other rather obvious example can be extracted from property number 4. Since there is no equivalence between norms in infinite-dimensional spaces, contrary to finite ones, the extrapolation of this property to the functional setting must be looked upon with attention.

Even though there exist some works in which this approach proves to be of use (see Cuesta-Albertos and Nieto-Reyes (2008) for an example of the generalization of the Tukey depth to infinite-dimensional spaces), a lot of care must be taken in the development of depth functionals and the establishment of their properties in functional spaces. In Nieto-Reyes and Battey (2016) the authors provide a generalization of the desired properties that can be applied to the functional setting.

Following the previous notations, let us consider the probability space $(\Omega, A, \mathbb{P})$ on which all the random variables are defined, and the measurable mapping (functional random variable) $Z : \Omega \mapsto \mathcal{F}$, where $\mathcal{F}$ is a Hilbert space. The set of all Borel probability measures on $\mathcal{F}$ is $\mathcal{P}$, and so any *functional statistical depth functional* is a mapping $D : \mathcal{F} \times \mathcal{P} \mapsto \mathbb{R} : D(z, \mathbb{P}) \to D(z, \mathbb{P})$, where $z \in \mathcal{F}$. The properties of D are:

- **P1: Distance invariance**. $D(f(z_1), \mathbb{P}_{f(Z)}) = D(z_1, \mathbb{P}_Z)$ for any $z_1 \in \mathcal{F}$ and $f : \mathcal{F} \mapsto \mathcal{F}$ such that for any $z_2 \in \mathcal{F}, d(f(z_1), f(z_2)) = a_f d(z_1, z_2)$ with $a_f \in \mathbb{R}/\{0\}$ and where d is any metric defined in $\mathcal{F}$.

- **P2: Maximality at centre**. For any $\mathbb{P} \in \mathcal{P}$ with a unique center of symmetry $\xi \in \mathcal{F}$ with respect to any notion of functional symmetry, $D(\xi, \mathbb{P}) = \sup_{z \in \mathcal{F}} D(z, \mathbb{P})$.

- **P3: Strictly decreasing with respect to the deepest point**. For any $\mathbb{P} \in \mathcal{P}$, if $D(z_3, \mathbb{P}) = \max_{z \in \mathcal{F}} D(z_1, \mathbb{P})$ exists, $D(z_1, \mathbb{P}) < D(z_2, \mathbb{P}) < D(z_3, \mathbb{P})$ holds for any $z_1, z_2 \in \mathcal{F}$ such that $\min\{d(z_2, z_3), d(z_2, z_1)\} > 0$ and $\max\{d(z_2, z_3), d(z_2, z_1)\} < d(z_1, z_3)$.

- **P4: Upper semi-continuity in** z. $D(z, \mathbb{P})$ is upper semi-continuous. $\forall z \in \mathcal{F}$ and $\forall \epsilon > 0, \exists \delta > 0$ such that: $\sup_{d(z_1, z_2) < \delta} D(z_2, \mathbb{P}) \leq D(z_1, \mathbb{P}) + \epsilon$.

- **P5: Receptivity to convex hull width across the domain**. $D(z,\mathbb{P}) < D(f(z),\mathbb{P}_{f(Z)})$ for any $z \in \mathcal{H}(\mathcal{F},\mathbb{P})$, where $\mathcal{H}$ is the convex hull of $\mathcal{F}$ with respect to $\mathbb{P}$.

- **P6: Continuity in** $\mathbb{P}$. $\forall z \in \mathcal{F}$ and $\forall \mathbb{P},\mathbb{Q} \in \mathcal{P}$ and $\forall \epsilon > 0, \exists d(\epsilon) > 0$ such that $|D(z,\mathbb{P}) - D(z,\mathbb{Q})| < \epsilon$ almost surely, with $d_{\mathcal{P}}(\mathbb{Q},\mathbb{P}) < \delta$.

This set of properties is better adapted to the functional context and constitutes the first major attempt at developing a general framework for depth functions in functional data, jointly with the works of Nagy (2016). There exist several nuances regarding the actual applicability of all these properties in real functional depths, which are discussed in Gijbels and Nagy (2017). In the FOD setting, let us remark that **P2** and **P3** are particularly problematic. In both cases, the possible existence of more than one mode in the distribution of Z may imply that a suitable functional depth for FOD may be forced to *not* verify these conditions in order to be sensitive to possible multimodalities in the distribution.

We shall now define the main depth functionals that will be considered in these works and which will be used further in the document (see section 2.5).

Definition 2.8
Let $(\mathcal{F},d) = (L^2, ||\cdot||_{L^2})$. The **h-mode** depth (Cuevas et al., 2007) of $z \in \mathcal{F}$ with respect to $\mathbb{P}$ is:

$$D_h(z,\mathbb{P}) \coloneqq \mathbb{E}[||K_h(z-Z)||_{L^2}] \tag{2.13}$$

where, for any fixed $h > 0$, $K_h(\cdot) = \frac{1}{h}K(\frac{\cdot}{h})$ *with* $K(\cdot)$ *being a Gaussian kernel.*

Definition 2.9
Let $(\mathcal{F},d) = (\mathcal{C}(\mathcal{T}), ||\cdot||_\infty)$, for a given $J = 2,3,...$ a band delimited by $z_1,...,z_J \in \mathcal{C}(\mathcal{T})$ is defined as*:*

$$B(z_1,...,z_J) = \Big\{(t,z(t))^T \in \mathbb{R}^2 : t \in \mathcal{T}, \min_{i=1,...,J} z_i(t) \leq z(t) \leq \max_{i=1,...,J} z_i(t)\Big\} \tag{2.14}$$

This way, for $J = 2,3,...$ and $\mathbb{P} \in \mathcal{P}(\mathcal{C}(\mathcal{T})$, the **Band Depth (BD)** (López-Pintado and Romo, 2009) of order J of $z \in \mathcal{C}(\mathcal{T})$ with respect to $\mathbb{P}$ is given by:

$$D_{BD}(z,\mathbb{P}) \coloneqq \frac{1}{J-1}\sum_{j=2}^{J} \mathbb{P}(G(z) \subset B(z_1,...,z_j)) \tag{2.15}$$

where $G(z) = \{(t,z(t))^T \in \mathbb{R}^2 : t \in \mathcal{T}\}$.

Definition 2.10
Let $(\mathcal{F},d) = (\mathcal{C}(\mathcal{T}), ||\cdot||_\infty)$, by considering the Lebesgue measure λ of the set $\Big\{t \in \mathcal{T} : (t,z(t))^T \in B(z_1,...,z_j)\Big\}$. The **Modified Band Depth (MBD)** of order J of $z \in \mathcal{F}$ is:

$$D_{MBD}(z,\mathbb{P}) \coloneqq \frac{1}{J-1}\sum_{j=2}^{J} \mathbb{E}[\lambda\Big(\Big\{t \in \mathcal{T} : (t,z(t))^T \in B(z_1,...,z_j)\Big\}\Big)] \tag{2.16}$$

Definition 2.11
Let $(\mathcal{F}, d) = (\mathcal{C}(\mathcal{T}), ||\cdot||_\infty)$, the **Half-Region (HR)** depth (López Pintado and Romo, 2011) of $z \in \mathcal{F}$ with respect to the measure $\mathbb{P}$ is:

$$D_{HR}(z, \mathbb{P}) \coloneqq \min\{\mathbb{P}(Z \in H_z), \mathbb{P}(Z \in E_z)\} \tag{2.17}$$

where $H_z \coloneqq \{y \in \mathcal{F} : y(t) \leq z(t), t \in \mathcal{T}\}$ i.e. H_z is the hypograph of z; and $E_z \coloneqq \{y \in \mathcal{F} : y(t) \geq z(t), t \in \mathcal{T}\}$, i.e., E_z is the epigraph of z. In other words, the HR corresponds to the minimum between the proportion of curves in the hypograph and the epigraph of the functional observation z.

Definition 2.12
Let $(\mathcal{F}, d) = (L^2(\mathcal{T}), ||\cdot||_\infty)$. The **spatial** depth of $z \in \mathcal{F}$ with respect to $\mathbb{P} \in \mathcal{P}$ is:

$$D_S(z, \mathbb{P}) \coloneqq 1 - \Big|\Big|\mathbb{E}\Big[\frac{z - Z}{||z - Z||_{L^2}}\Big]\Big|\Big| \tag{2.18}$$

where the convention $\frac{0}{0} = 0$ is adopted.

All in all, all these definitions of functional depth may be used as measures that provide a center-outward ordering of $\mathcal{F}$. Basic criteria or estimations of cutoff values for the set of depths assigned to a set of functional data may be used in order to provide an outlyingness criterion.

2.3.2.3 Measures from the times series domain

As we have already mentioned, the time series domain is highly related to the FDA one, which is the main reason why it makes sense to consider possible measures coming from this domain in order to perform an efficient dimensionality reduction on the data.

In particular, the Dynamic Time Warping (DTW) (Müller, 2007) is a technique that has been proven to be useful when comparing time series. It provides measures of similarity and, most of all, correspondence between two sequences of data.

It has been vastly explored in the time-series domain, even though most of the efforts of the scientific community seem to have been focused on improving the computational cost of the algorithm, rather than improving its precision or way of working (Ratanamahatana and Keogh, 2004).

In the following section we will explain the general algorithm of DTW, which is mostly taken from Müller (2007), and which will be of use in Section 2.4.

2.3.2.3.1 General Algorithm As it has been said, the general idea behind the DTW algorithm is to be able to compare two sequences of data which are observed in discretized

points of a certain grid, which is why most of the modifications of the method have been developed in the time series domain. Fixing two sequences $X \coloneqq (x_1, x_2, ..., x_N); N \in \mathbb{N}$ and $Y \coloneqq (y_1, y_2, ..., y_M); M \in \mathbb{N}$, as well as a feature space $\mathcal{S}$ and $x_n, y_m \in \mathcal{S}$ for $n \in [1 : N]$ and $m \in [1 : M]$. Let us also define a local cost measure (sometimes also called local distance measure), which is a function:

$$c : \mathcal{S} \times \mathcal{S} \mapsto \mathbb{R}_{\geq 0}$$

In general, it is considered that $c(x, y)$ is low if x and y are similar to each other, and otherwise (high cost), $c(x, y)$ is large. By evaluating each pair of elements of each of the sequences, we obtain the *cost matrix* $C \in N \times M$, $C(n, m) \coloneqq c(x_n, y_m)$.

The idea is to find the alignment between the points in both sequences which has the lowest overall cost. As it is stated in Müller (2007), this alignment runs along a “valley" of low cost within the cost matrix C.

The notion of alignment is (more formally) defined a (N, M)-warping path (or warping path if both values of (N, M) are clear by context), which is a sequence $p = (p_1, ..., p_L)$ with $p_l = (n_l, m_l) \in [1 : N] \times [1 : M]; \forall l \in [1 : L]$ which also satisfies the following conditions:

- Boundary condition: $p_1 = (1, 1)$ and $p_L = (N, M)$
- Monotonicity condition: $n_1 \leq n_2 \leq ... \leq n_L$ and $m_1 \leq m_2 \leq ... \leq m_L$
- Step size condition: $p_{l+1} - p_l \in \{(1, 0), (0, 1), (1, 1)\}$ for $l \in [1 : L - 1]$

The third condition implies the second, but normally both are shown for the sake of clarity. A warping path $p = (p_1, ..., p_L)$ defines an alignment between two sequences by assigning the element x_{n_l} of X to the element y_{m_l} of Y.

Going beyond the formalism, the first condition guarantees that the first and last elements of both sequences will be aligned, whereas the second condition (monotonicity) ensures that if any element of the first sequence comes before another, this will also be true for the corresponding points in the other sequences. Finally, the third condition serves to ensure that all the points in both sequences are aligned with some other element in the other sequence, as well as to ensure that there shall not be any replications of the same alignment.

The total cost $c_p(X, Y)$ of a given warping path is:

$$c_p(X, Y) \coloneqq \sum_{l=1}^{L} c(x_{n_l}, y_{n_l})$$

Finally, an *optimal warping path* between X and Y is a warping path p^* having minimal total cost among all possible warping paths. Having defined this path, *DTW distance* $DTW(X, Y)$ between X and Y is defined as the total cost of the optimal warping path.

$$DTW(X,Y) = c_{p^*}(X,Y) = \min\{c_p(X,Y)\}|p \text{ is an}(N,M)\text{warping path}\}$$

There are several remarks to make concerning this measure. Firstly, in general, the optimal warping path is not unique, which means that it is up to the user to define which one of the found paths is the optimal depending on the problem. Secondly, the results given by the algorithm depend on the chosen cost function, which is not unique or defined in general when applying the algorithm. Finally, it must also be noted that even if the chosen cost function c is positive definite, this is not necessarily true in general for the DTW distance.

The computation time of the algorithm would be exponential with the sizes of the analyzed sequences if one wanted to test each possible path between X and Y. However, making use of the *dynamic programming* the overall cost of the algorithm could be reduced to $O(NM)$.

2.3.2.3.2 Computation of the algorithm. In order to simplify the computation of the optimal path, we can define the sequences $X(1:n) \coloneqq (x_1, ..., x_n)$ for $n \in [1:N]$ and $Y(1:m) \coloneqq (y_1, ..., y_n)$ for $m \in [1:M]$ and set the value:

$$D(n,m) \coloneqq DTW(X(1:n), Y(1:m))$$

The corresponding values $D(n,m)$ define a matrix called the *accumulated cost matrix* (obviously, $D(N,M) = DTW(X,Y)$). It can be demonstrated that the matrix D satisfies the identities:

$$\begin{cases} D(n,1) = \sum_{k=1}^{n} c(x_k, y_1); \forall n \in [1:N] \\ D(1,m) = \sum_{k=1}^{m} c(x_1, y_k); \forall m \in [1:M] \\ D(n,m) = \min\left\{D(n-1,m-1), D(n-1,m), D(n,m-1)\right\} + c(x_n, y_m); \end{cases}$$

In the last case, the calculations are made for the values $1 < n \leq N$ & $1 < m \leq M$.

In particular, $DTW(X,Y) = D(N,M)$ can be computed with $O(NM)$ operations. Finally, the optimal warping path algorithm makes use of this matrix to calculate the optimal path $p^* = (p_1, ..., p_L)$, which is computed in reverse of the indices, i.e., by starting in $p_L = (N,M)$. Supposing that we have already computed $p_l = (n,m)$, if $(n,m) = (1,1)$, we then have $l = 1$ and the procedure is finished. In any other case:

$$p_{l-1} \coloneqq \begin{cases} (1, m-1) & \text{if } n = 1 \\ (n-1, 1) & \text{if } m = 1 \\ \arg\min\left\{D(n-1,m-1), D(n-1,m), D(n,m-1)\right\} & otherwise \end{cases}$$

Even though it is true that by proceeding this way the whole process is accelerated, it is nonetheless true that the computational cost is still of order $O(MN)$, which is still quite elevated for some applications (when there is a great number of points to be analyzed).

This is the reason why there are some quite well known propositions of acceleration methods for the DTW algorithm.

2.3.2.3.3 DTW variations These methods can be explained in depth but here we shall content ourselves with an explanation of the general methodology for each of the modifications.

- Step size condition. The step size conditions assure that each point of every sequence is assigned to one of the other. The main drawback of this condition is the possibility of degeneration, i.e., one point may be assigned many times to a large number of points of the other sequence, which translates by a big horizontal or vertical line in the cost matrix. In order to avoid this problem, it is possible to modify the step condition to constrain the slope of the warping path. For instance, the step condition could be written as:

$$p_{l+1} - p_l \in \{D(n-1, m-1), D(n-2, m-1), D(n-1, m-2)\} + c(x_n, y_m)$$

- Local Weights. It can sometimes be interesting (due to prior knowledge of the data that is compared) or to avoid degenerations as in the previous case, to favor the horizontal, vertical, or diagonal paths in the alignment. To accomplish this, it is possible to introduce a weight vector $(w_d, w_h, w_v) \in \mathbb{R}^3$, so that:

$$D(n, m) = \min \begin{cases} D(n-1, m-1) + w_d c(x_n, y_m) \\ D(n-1, m) + w_h c(x_n, y_m) \\ D(n, m-1) + w_v c(x_n, y_m) \end{cases}$$

- Global constraints. It is one of the most common variants. The idea is to constrain the possible warping paths to a certain region in the cost matrix, normally a closed region near the diagonal of the matrix. More precisely, $R \subseteq [1:N] \times [1:M]$, then a warping path relative to R is a warping path that runs entirely on the chosen region R, and the optimal warping path relative to R is denoted p_R^*. It is the cost-minimizing warping path among all warping paths relative to R.

- Approximations. A very basic idea, it consists in performing the alignment on coarsened versions of the sequences X and Y, effectively reducing the lengths of the sequences. The obvious drawback of this methodology is that information is lost, and the optimal warping path that is ultimately found may not exactly correspond to the true optimal path that could have been found if we had kept all of the values.

  However, there is an interesting modification of this idea called Multiscale DTW, where this approach is taken in order to generate a basic global region which serves to establish

a global constraint (described previously) and where in the following step the actual optimal warping path will be searched.

2.3.3 Review of functional outlier detection methods

The development of techniques capable of dealing with outliers in sets of functional data has experienced an important growth since the works of Febrero-Bande et al. (2008), where a technique based on functional depths was successfully used in order to identify anomalous concentrations of pollutants. Since then, considerable work has been consecrated to the study of the nature, taxonomy, identification and explanation of functional data outliers. Nonetheless, no formal review of methods has been made on the subject and the existing techniques remain scattered and diverse.

For instance, Spear and Hornberger (1980) propose a methodology based on several different notions of depth by estimating the cutoff value of depth by smooth bootstrapping. In López-Pintado and Romo (2009) the authors presented the notion of band depth and MBD to show how it could be used as tool to identify if different sets of functional data can be considered to have originated from the same distribution. There exist graphical tools such as the *rainbow plots*, the *functional bagplots* and *HDR* boxplots (Hyndman, 2009), based on the adjustment of probabilistic models over the two main FPCA components. Similarly, Sun and Genton (2011) proposed a non-trivial extension of the univariate boxplot for functional data without relying on the classical boxplots in each of the individual points in the sampling grid thanks to the notions of BD and MBD. In Gervini (2012), the author compared the performances of a number of trimmed estimators in order to capture the outlyingness of more general forms of functional data (not necessarily univariate curves).

After these early attempts, considerable research effort was made in order to improve some of the main problems of the aforementioned methodologies. Most of them were only sensitive to very specific types of outliers, and those which relied on depth notions could not provide robust estimators for the cutoff values from which outliers are considered since its actual distribution impossible to estimate. In Arribas-Gil and Romo (2014), the authors present one of the earliest efficient attempts at detecting shape outliers through the use of both graphical tools and two different depth notions, the MBD and the modified epigraph index (López Pintado and Romo, 2011). In Hubert et al. (2015), the authors developed a new graphical and analytical technique based on depth functionals for multivariate functional data, whereas in Kuhnt and Rehage (2016), the authors focus on shape outliers in the same framework through angle-based data depths (*pesudo-depths* according to them, since they do not fulfill the criteria presented in 2.3.2.2). Nagy et al. (2017) showcased how derivative-based depth functions may be used to better identify shape outliers. In Dai and Genton (2018) the authors make use of the work presented in Dai and Genton (2019), where an outlyingness estimator is developed aiming at quantifying the outlyingness both in magnitude and shape sense. They also provided a visualization tool that facilitates the interpretation.

Finally, in more recent years, novel methodologies have continued to arise, still trying to

improve the explicability of the methodologies, and also simplifying them without harming their detection capabilities, while also improving the theoretical framework of the field (Nieto-Reyes and Battey, 2016; Gijbels and Nagy, 2017). We can mention the works of Barreyre et al. (2019), where statistical tests are performed on the coefficients of the projections into the Haar basis (2.2.2.3) of the set of functional data. Dai et al. (2020) proposes another methodology based in rankings of estimators obtained from derivatives for smooth sets of functional data.

Classifying all these methodologies (as well as others that have not been mentioned) can prove to be a complicated task, due to the very different natures of all of the methods, although all of them can be classified according to the framework proposed in Section 2.3. It is however possible to classify them according to their sensitivity to the specific types of outliers that they search to identify:

- **Magnitude outliers**: Functional boxplots, functional bagplots, HDR plots, smooth bootstrap depth notions, BD, MBD.
- **Shape outliers**: Angle-based methods, depth notions on derivatives.
- **Magnitude and shape outliers**: Multiple testing on well chosen coefficients in a basis, Magnitude-Shape plot, outliergram, sequential transformations

We provide now a succinct state of the art of the main methods that are used nowadays for FOD.

2.3.3.4 Functional boxplot

Given a sample of functional data $\{z_i\}_{i=1}^N$ defined in a univariate domain $\mathcal{T} \subset \mathbb{R}$ indexed by the variable t, it is possible to compute the any α central region (Liu et al., 1999) by considering the band delimited by the proportion of $\alpha \in (0, 1)$ deepest curves according to the band depth estimate.

Followin the notations of the authors in Sun and Genton (2011), the 50% central region of the sample can then be defined as:

$$C_{0.5} = \left\{(t, z(t)) : \min_{i=1,\dots,\lceil N/2 \rceil} z_{[i]}(t) \leq z(t) \leq \max_{i=1,\dots,\lceil N/2 \rceil} z_{[i]}(t)\right\}. \tag{2.19}$$

where $z_{[i]}(t)$ represents the sample curve associated with the ith largest band depth value.

This region can be interpreted as an analogous of the inter-quartile range for functional data, and it effectively corresponds to it pointwise. The whiskers of the functional boxplot can be computed by extending 1.5 times the pointwise extremes of the central region, such that the outliers are detected if they surpass the frontiers defined by these whiskers. The extended explanation of the method and some applications can be found in Sun and Genton

(2011). An example of the functional boxplot applied to a set of functional data can be found in Figure 2.3.

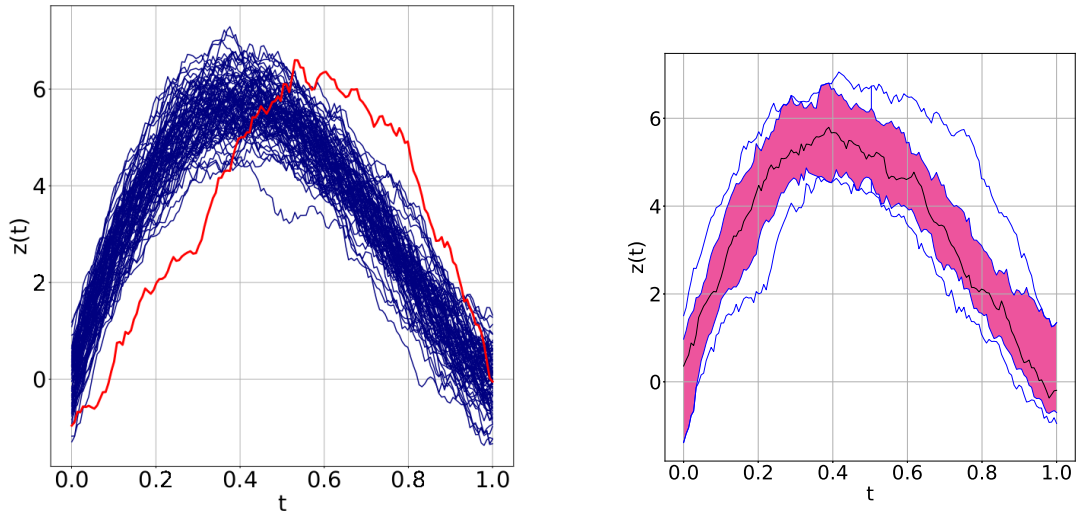

(a) Example of set of functional data with one outlier

(b) Example of functional boxplot showcasing the central envelope $C_{0.5}$ in pink.

Figure 2.3: Example of an application of the functional boxplot.

2.3.3.5 High-Density Regions (HDR)

In order to compute the bivariate HDR plot (Hyndman, 2009), the first two principal component scores are computed for each z_i in the considered sample. A kernel estimator of the underlying probability density function $\hat{f}(C1, C2)$ of set of bivariate scores $\{c_{1,i}, c_{2,i}\}_{i=1}^{N}$ from the bivariate random variable $C : \mathcal{F} \to \mathcal{V} \subset R^2$ can be estimated:

$$\hat{f}(c_1, c_2) = \frac{1}{N} \sum_{i=1}^{N} K_h\big((c_{1,i}, c_{2,i}) - C\big)$$

The bandwidth can be estimated by cross-validation, and $K_h(\cdot) = \frac{1}{h} K(\frac{\cdot}{h})$, where $K(\cdot)$ is a given kernel function. This way, a HDR is the set defined by:

$$R_\alpha \coloneqq \{(c_1, c_2) : \hat{f}(c_1, c_2) \geq f_\alpha\} \tag{2.20}$$

where f_α is chosen such that $\int_{R_\alpha} \hat{f}(c_1, c_2) d(c_1, c_2) = 1 - \alpha$, with $\alpha \in [0, 1]$. Naturally, the detection capabilities of the algorithm depend firstly on the choice of α, and how well variability of the considered functional random variable can be captured by the principal components. An example can be found in Figure 2.4.

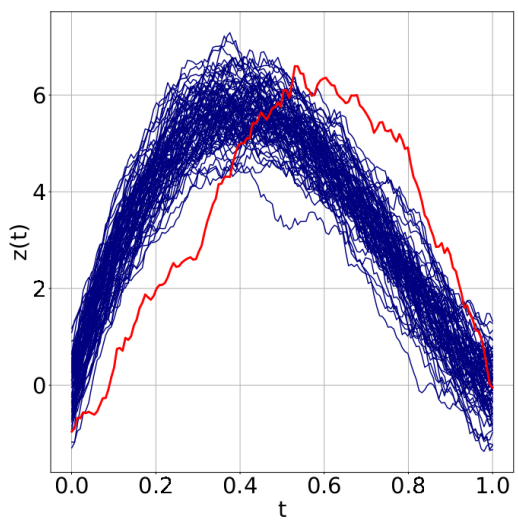

(a) Example of set of functional data with one outlier

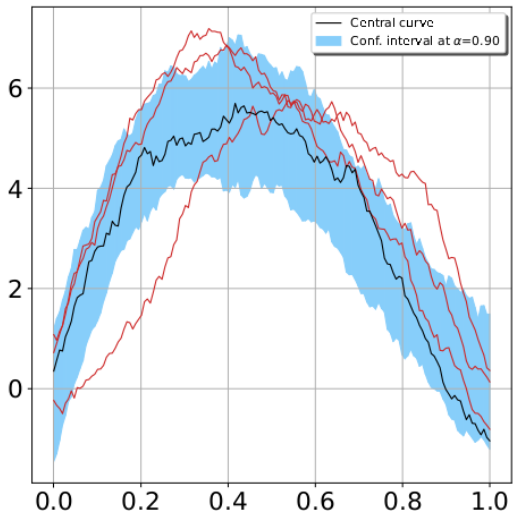

(b) Example of functional HDR plot showcasing the $\alpha = 10\%$ more outlying curves according to this criterion in red.

Figure 2.4: Example of an application of the HDR plot.

2.3.3.6 Outliergram

The outliergram (Arribas-Gil and Romo, 2014) was proposed as a way to tackle the difficulty of identifying shape outliers. It is a graphical tool based on two notions of functional depth, the MBD (see Definition 2.16) and the Modified Epigraph Index (MEI) (López Pintado and Romo, 2011). For the previously defined set of functional data in $\mathcal{F} = \mathcal{C}(\mathcal{T})$ defined in $\mathcal{T} \subset \mathbb{R}$, and let λ be the Lebesgue measure, the MEI is defined as:

$$D_{MEI}(z) = \frac{1}{N} \sum_{i=1}^{N} \frac{\lambda(\{t \in \mathcal{T} | z_i(t) \geq z(t)\})}{\lambda(\mathcal{T})} \tag{2.21}$$

which corresponds to the mean proportion of time that the curve z remains below the curves of the sample. A quadratic inequality between the MBD and the MEI can be established as follows:

$$D_{MBD}(z) \leq a_0 + a_1 D_{MEI}(z) + a_2 N^2 D_{MEI}^2(z) \tag{2.22}$$

where $a_0 = a_1 = \frac{-2}{N(N-1)}$ and $a_1 = \frac{2(N+1)}{N-1}$. This way, it is possible to plot the bivariate plane $(D_{MBD}, D_{MEI}) \in \mathbb{R}^2$ and establish a detection criterion based on the vertical distance of each corresponding point in the bivariate plane to the parabola defined in (2.3.3.6). An example of the results in a simple identification case can be found in Figure 2.5.

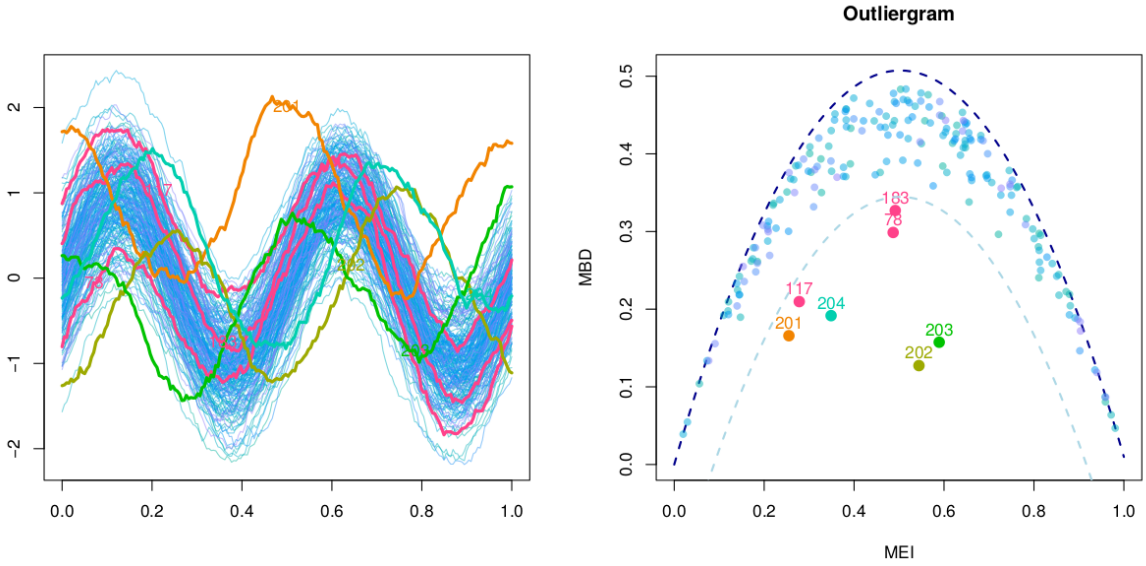

Figure 2.5: Example of an application of the outliergram. The numbers represent the index of the corresponding outlying curves.

2.3.3.7 Magnitude-shape plot

This method (Dai and Genton, 2018) is also based on the decomposition of the sample's outlyingness into different elements that account for the total outlyingness of a single functional object. First of all, in Dai and Genton (2019), the authors define the *directional outlyingness* of any given random variable X defined in $\mathcal{V} \subset \mathbb{R}^d$ as:

$$O(X, F_X) \coloneqq \{\frac{1}{D(X, F_X) - 1} - 1\} \cdot v, D(X, F_X) > 0 \tag{2.23}$$

where F_X represents the distribution of an arbitrary random variable X and D represents any chosen depth notion. The vector $v \in \mathcal{V}$ is a unit vector in pointing from the median (i.e., the deepest point of F_X according to D) to X. If this notion of median (m_X) is unique, the authors propose $v = \frac{(X - m_X)}{||X - m_X||}$. If we consider now the functional random variable Z defined in $\mathcal{T} \in \mathbb{R}$, it is possible to decompose the total outlyingness of any object $z(t)$ in the sample in three components.

Definition 2.13
Mean directional outlyingness M_O:

$$M_O(Z, F_Z) = \int_{\mathcal{T}} O(Z(t), F_Z) w(t) dt \tag{2.24}$$

Definition 2.14

Variation of directional outlyingness V_O:

$$V_O(Z, F_Z) = \int_{\mathcal{T}} ||O(Z(t), F_Z) - M_O(Z, F_Z||^2 w(t)dt \tag{2.25}$$

Definition 2.15
Functional directional outlyingness F_O:

$$F_O(Z, F_Z) = \int_{\mathcal{T}} ||O(Z(t), F(Z)||^2 w(t)dt \tag{2.26}$$

where $w(t)$ is a weight function of $\mathcal{T}$ which can be chosen as a constant or proportionally to a local variation measure of the functions (depending on the derivatives for instance). For outlier detection purposes, the authors choose $w(t) = \{\lambda(\mathcal{T})\}^{-1}$. The three measures can be related through the expression: $F_O = ||M_O||^2 + V_O$. The Magnitude-shape plot is a scatter of points of $(M_O^T, V_O)^T$ for a collection of functional data. The inlying points are supposed to remain close to the lower central region, whereas outliers will scatter through the edges depending on their nature (the predominant values of the vector $(M_O^T, V_O)^T$).

2.3.3.8 Sequential transformations

This algorithm from Dai et al. (2020) relies on the transformation of a wide diversity of shape outliers into magnitude outliers, much easier to detect through standard procedures. Given a sequence of operators defined in $\mathcal{F}$ (the functional space that generates the considered data) $\{\mathcal{G}_k\}, k = 0, 1, 2, .. $, the method consists in sorting the raw and transformed data into vectors of ranks for each observation. The vectors of ranks are sorted according to a one-side depth notion, such as the *extreme rank depth* for instance, and a global envelope is constructed, which allows the outlier identification.

2.4 Proposed Methodology for Outlier Detection

The aforementioned methodologies constitute a solid foundation of the state of the art in what concerns the detection of outliers in sets of functional data. They also provide an insight as to what the main strengths and weaknesses are currently in this diverse field, and how their applicability, although wide, can be limited depending on the chosen methodology and the taxonomy of the analyzed functional data.

We now address the major existing challenges in the FOD domain taking into account the main existing methodologies:

- Most of the methods are only applicable to specific sets of functional data and lack generality. For instance, the functional boxplots (Sun and Genton, 2011) and HDR plots (Hyndman, 2009) are apt for detecting magnitude outliers, but are almost incapable of detecting more complex forms of outlyingness. In a similar way, the outliergram seems to be very capable of detecting a wide spectrum of outliers, but according to the examples presented in Arribas-Gil and Romo (2014), this is only the case if the outliers present a very apparent outlying behavior. Similarly, the methods explored in Dai et al. (2020) are apt for cases where the main source of outlyingness is due to the differences in the derivatives of the analyzed objects, which is not necessarily always the case, even for shape outliers.

- The diversity of the existing methods hinders the comparability of the results. As it was mentioned in Section 2.3, in the non-supervised framework the only valid way of testing the detection capabilities of a detection algorithm is to compare its provided results through a chosen set of toy examples. This problem is rarely addressed in the literature, and most examples of compared methodologies simply rely on the comparison of their detection rates in rather simple models. On top of that, many methodologies (Dai et al., 2020; Arribas-Gil and Romo, 2014; Febrero-Bande et al., 2008; Nagy et al., 2017) but not all, only provide a binary label of *inlier* or *outlier* in a set of data. However, in many contexts (e.g., in sensitivity analysis), a quantifiable score of outlyingness is more useful, since there will always exist data whose outlyingness may be considered to be too small to classify them as outliers, but whose score is still sufficient to be relevant when analyzing the taxonomy of outliers.

- Most methods rely on an arbitrary notion. Frequently, an extension to the functional framework of the commonly used heuristic of $1.5 \times IQR$, where IQR stands for the interquantile range (Sun and Genton, 2011; Arribas-Gil and Romo, 2014; Nagy et al., 2017). These kinds of choices are difficult to justify in practice, and are more of a common practice in the literature than a real methodological and rigorous choice.

Finally, it is worth noting that the methods are rarely or almost never tested on sets of functional data generated by numerical simulations. In most cases, the methodologies are tested against the mentioned toy examples or measured data (common data sets come from the environmental sciences field and climatology), but not sets of functional obtained from computer simulators.

As an example, we showcase a set of temperature curves provided by the code *CATHARE2* in Figure 2.6. These curves correspond to the evolution of the temperature in a particular point of the primary circuit of a nuclear power plant. As we can see, the density of curves is quite large (specifically, there are 996 curves), and none of them can be easily identified as an outlier to the naked eye. The applicability of functional outlier detection methods on this kind of application (set of similar data, large number of observations, difficult interpretation of the possible flagged outliers) remains to be tested, and is the object of Chapters 4 and 5.

We propose at this stage a detection methodology (Rollón de Pinedo et al., 2021) that aims at addressing these considered problems.

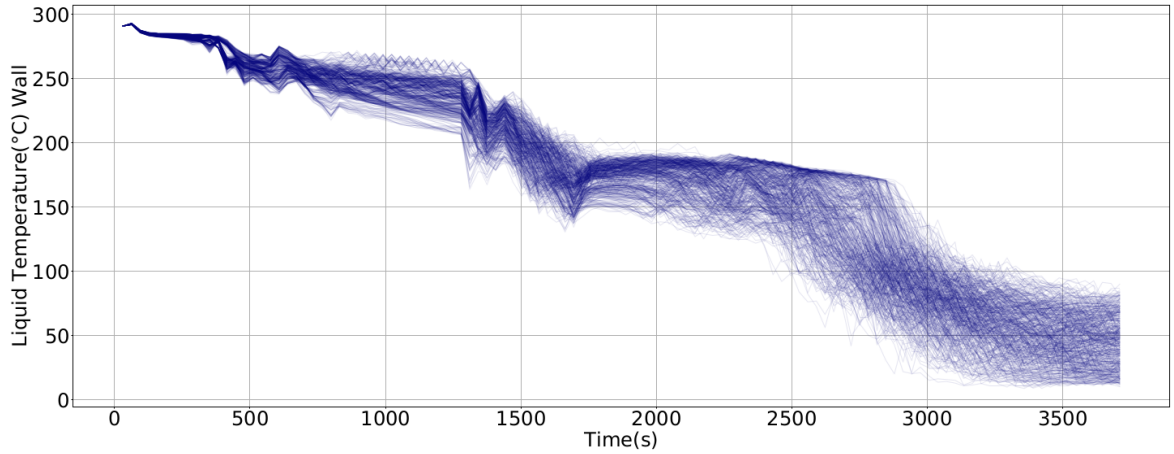

Figure 2.6: Example of a set of curves generated as output of the numerical code *CATHARE2*.

2.4.1 Probabilistic modeling of features

Firstly, we shall consider that a certain number of features is available to model the considered set of functional data and that they are capable of quantifying their outlyingness both in the magnitude and shape sense. Let us consider the probability space $(\Omega, A, \mathbb{P})$ on which all the random variables are defined, and the measurable mapping (functional random variable) $Z : \Omega \mapsto \mathcal{F} \subset \mathcal{F}^*$, where $\mathcal{F}^*$ is a Hilbert space. The set of all Borel probability measures on $\mathcal{F}$ is $\mathcal{P}$.

We can define the multivariate feature random variable $\mathcal{U} \in \mathcal{S} \subset \mathbb{R}^R, \mathcal{U} = \{U_1, ..., U_r, ..., U_R\}$. These functions may take the form of depth functions, or other available semimetrics, and they are mappings $U_r : \mathcal{F} \mapsto \mathbb{R}$.

Let us suppose that a certain number of features are available to describe our functional data and are able to capture the specific characteristics of both central and abnormal observations. If $\mathcal{U} = \{u_1, ..., u_r, ..., u_R\}$ represents this set of features, with no imposed a priori restrictions on its size, such that $\forall u_r \in \mathcal{U}, u_r : \mathcal{F} \mapsto \mathbb{R}$.

The extreme nature of any object in the multivariate feature space $\mathcal{S}$ can be measured in terms of the subsets of $\mathcal{S}$ where U takes its values of higher or lower probability. Let $\theta \in (0, 1)$, a minimum volume set $\mathcal{S}_\theta$ of mass at least θ is the solution of the constrained optimization problem (Polonik, 1997):

$$\min_{\mathcal{S}\ Borelian} \lambda(\mathcal{S}) / \mathbb{P}(U \in \mathcal{S}) \geq \theta \tag{2.27}$$

where the minimum is taken over all measurable subsets of $\mathcal{S} \in \mathbb{R}^R$.

In order to guarantee that this measure is suitable for outlier detection, these sets must be unique. This can be guaranteed as long as the probability density function p with respect to the Lebesgue measure on $\mathbb{R}^R$ of the random variable U respects the following properties:

- $\mathcal{P}.\mathbf{1}$. $||p||_\infty < +\infty$, i.e., the function is bounded.

- $\mathcal{P}.\mathbf{2}$. $\mathbb{P}[p(u_r) = c] = 0, \forall c \in \mathbb{R}$

In this case, as long as p belongs to at least $\mathcal{C}(\mathcal{T})$, the set $\mathcal{S}_\theta$ is unique.

We can then define a general quantile function:

$$\forall \theta \in (0,1), \theta^*(\theta) \coloneqq \lambda(\mathcal{S}_\theta) \tag{2.28}$$

where θ^* is continuous on $(0,1)$ and as long as $\text{supp}(p)$ is compact. Since p is always unknown, this function may be estimated through the empirical version of its cumulative distribution function $P_N = \frac{1}{N}\sum_{i=1}^{N} \delta_{U_i}$ (δ represents the Kroneker delta function), solving the optimization problem over all Borelian subsets of $\mathbb{R}^R$.

We will address the problem of the estimation of p in the following section.

2.4.2 Estimation of the underlying model

As we mentioned, the estimation of the underling probabilistic model may simply be made through the empirical version of p. It is however desirable to represent p by a smooth function that allows a certain level of control over its form from the user, so that it may be adapted for outlier detection.

It is possible to estimate p through a parametric model, such that $p(\cdot, \nu)$ is characterized by the set of parameters $\nu \in \mathcal{V}$. Let us consider the Gaussian Mixture Model (GMM) here (Reynolds, 2009).

Definition 2.16
Gaussian Mixture Model. The probability density function p of a mixture of K Gaussians with individual densities $\{f_1, ..., f_K\}$ in the feature space $\mathcal{S}$ can be written as the linear combination:

$$p(u|\nu_1, ..., \nu_K) = \sum_{k=1}^{K} w_k f_k(u|\nu_k), \forall u \in \mathcal{S} \tag{2.29}$$

where ν_k represents the collection of parameters that describe the kth Gaussian component and $\{w_k\}_{k=1}^K$ are the corresponding weights of each component. They verify as well $\sum_{k=1}^K w_k = 1$, and for any given individual Gaussian f_k, the parameters $\nu_k = \{\mu_k, \Sigma_k\}, \mu_k \in \mathcal{S} \subset \mathbb{R}, \Sigma_k \in \mathbb{R}^R \times \mathbb{R}^R$, where μ_k represents the average and Σ_k is the covariance matrix of f_k.

The analytical form of individual Gaussian is given by:

$$f_k(u|\mu_k, \Sigma_k) = \frac{1}{\sqrt{|2\pi\Sigma_k|}} \exp\Big(- \frac{(u-\mu_k)^T \Sigma_k^{-1} (u-\mu_k)}{2} \Big) \tag{2.30}$$

It is then necessary to estimate the collection of parameters $\{\nu_k\}_{k=1}^K$. This can be achieved via the Expectation Maximization algorithm (EM) presented in the following section.

2.4.2.1 The Expectation Maximization (EM) algorithm

The EM algorithm (Dempster et al., 1977) was introduced as a general method to estimate the parameters of a parametric model by maximum likelihood when the evaluated function is complex, i.e., when the likelihood function of the parameters cannot be computed analytically. It is also an efficient methodology to estimate models which have latent variables. Following the previous notation, if we denote the set of observed multivariate data by u, and the set of latent variables by l, whereas the set of all the parameters of the model is ν, then the log likelihood of the corresponding density function p is given by (Bishop, 2006):

$$\ln p(u|\nu) = \ln \Big\{ \sum_l p(u, l|\nu) \Big\} \tag{2.31}$$

where we have considered that the latent variables are categorical (as will be the case in the GMM). This is equally applicable to continuous latent variables by substituting the summation by an integral in the continuous case. The set $\{u, l\}$ is usually called the *complete* set of data, whereas the set $\{u\}$ is the *incomplete* one. In practice, only the incomplete set is available, and we can consider that all the available information concerning the latent variables is given by $p(l|u, \nu)$. Basically, the EM algorithm will be divided into two steps. In the **E** step, we will consider the expected value of the log likelihood under the posterior distribution of the latent variable, whereas in the **M** step, this quantity will be maximized.

In practice, given an estimated set of parameters ν^{old} a successive set of E and M steps will provide a new set of ν^{new} parameters up until convergence. More formally, both steps can be summarized as:

- E-step. Given ν^{old}, obtain $p(l|u, \nu^{\text{old}})$. This posterior distribution is used in order to evaluate the complete log likelihood evaluated over a generic set of parameters ν. The corresponding expectation $\mathcal{Q}(\nu, \nu^{\text{old}})$ is given by:

$$\mathcal{Q}(\nu, \nu^{\text{old}}) = \sum_l p(l|u, \nu^{\text{old}}) \ln p(u, l|\nu) \tag{2.32}$$

- M-step. We obtain the updated set of parameters ν^{new} by maximizing the obtained expectation:

$$\nu^{\text{new}} = \underset{\nu}{\operatorname{argmax}} \mathcal{Q}(\nu, \nu^{\text{old}}) \tag{2.33}$$

The EM algorithm is summarized in Algorithm 1:

Algorithm 1: Generic EM algorithm

Result: Set of parameters ν^{final}

1. Choose (manually or randomly) a starting set of parameters ν^{old};
2. **E-step**. Evaluate $p(l|u, \nu^{\text{old}})$;
3. **M-step**. Evaluate ν^{new} given by

$$\nu^{\text{new}} = \underset{\nu}{\operatorname{argmax}} \mathcal{Q}(\nu, \nu^{\text{old}})$$

$$\mathcal{Q}(\nu, \nu^{\text{old}}) = \sum_{l} p(l|u, \nu^{\text{old}}) \ln p(u, l|\nu)$$

;
4. Check for convergence of the log likelihood or the set of parameters. If a convergence criterion is not met, then let:

$$\nu^{\text{old}} \leftarrow \nu^{\text{new}}$$

The adaptation of the algorithm for Gaussian mixtures is straightforward, as we will see in the next section.

2.4.2.2 EM for Gaussian Mixtures

If we consider the Gaussian mixture model, we can define the set of latent variables as a K-dimensional binary random variable L such that if any particular element l_k equals 1 then all the other elements are equal to 0, i.e., $l_k \in \{0, 1\}$ and $\sum_{k=1}^{K} l_k = 1$. The marginal distribution of the latent variable may be expressed in terms of the weights (mixing coefficients) of the GMM, such that $p(l_k = 1) = w_k$, and the aforementioned marginal distribution can be written as:

$$p(l) = \prod_{k=1}^{K} w_k^{l_k} \tag{2.34}$$

Conversely, the conditional distribution of U given a value l for the Gaussian case can be written:

$$p(u|l) = \prod_{k=1}^{K} f_k(u|\mu_k, \Sigma_k)^{l_k} \tag{2.35}$$

In this case, the likelihood function of the complete set of data takes the form:

$$p(u, l|\mu, \Sigma, w) = \prod_{i=1}^{N} \prod_{k=1}^{K} w_k^{l_{ik}} f_k(u_i|\mu_k, \Sigma_k)^{l_{ik}} \tag{2.36}$$

where l_{ik} denotes the kth component of l_i (the value of the latent variable for the ith observation). Taking the logarithm of this expression, we obtain the log likelihood function:

$$\ln p(u, l|\mu, \Sigma, w) = \sum_{i=1}^{N} \sum_{k=1}^{K} l_{ik}[\ln w_k + \ln f_k(u_i|\mu_k, \Sigma_k)] \tag{2.37}$$

Finally, analogously to the methodological sequence followed in the previous section, the posterior distribution of the complete data log likelihood is:

$$p(l|u, \mu, \Sigma, w) \propto p(u, l|\mu, \Sigma, w) = \prod_{i=1}^{N} \prod_{k=1}^{K} w_k^{l_{ik}} f_k(u_i|\mu_k, \Sigma_k)^{l_{ik}} \tag{2.38}$$

and hence the expectation of any indicator variable l_{ik} can be written as:

$$\mathbb{E}[l_{ik}] = \frac{\sum_{l_{ik}} l_{ik}[w_k f_k(u_i|\mu_k, \Sigma_k)]^{l_{ik}}}{\sum_{l_{im}} [w_m f_m(u_i|\mu_m, \Sigma_m)]^{l_{im}}} = \frac{w_k f_k(u_i|\mu_k, \Sigma_k)}{\sum_{m=1}^{K} w_m f_m(u_i|\mu_m, \Sigma_m)} = \gamma(l_{ik}) \tag{2.39}$$

where $\gamma(l_{ik})$ is called the responsibility of the component k in the mixture for each point i.

Therefore, the EM algorithm applied to the estimation of the parameters of the Gaussian mixture is finally described in Algorithm 2.

2.4.2.3 Adapting EM for outlier detection

Although the raw form of the EM algorithm can be used in the general context of functional data analysis, there are several issues concerning the adjustment of the considered parameters in the context of outlier detection. Some of them are addressed in Aggarwal (2017), and they can be summarized as follows:

- If the probabilistic model is adjusted taking into account the presence of outliers, they may bias the estimation of the underlying model. This is especially problematic if the outliers are assumed to be generated by a different distribution than the other data and are no only considered to be extreme realizations of the same underlying process than the others. On top of that, if the sample presents a high degree of contamination or the sample size is small, this bias can greatly influence the detection.

Algorithm 2: EM algorithm for GMM estimation

Result: Set of parameters ν^{final}

1. Choose (manually or randomly) a starting set of parameters $\nu^{\text{old}} = \{\mu_k^{\text{old}}, \Sigma_k^{\text{old}}, w_k^{\text{old}}\}_{k=1}^K$;
2. **E-step**. Evaluate the corresponding responsibilities $\gamma(l_{ik})$;
3. **M-step**. Re-estimate the parameters through:

$$\mu_k^{\text{new}} = \frac{1}{N_k} \sum_{i=1}^{N} \gamma(l_{il}) u_i$$

$$\Sigma_k^{\text{new}} = \frac{1}{N_k} \sum_{i=1}^{N} \gamma(l_{ik})(u_i - \mu_k^{\text{new}})(u_i - \mu_k^{\text{new}})^T$$

$$w_k^{\text{new}} = \frac{N_k}{N}$$

where N_k represents the number of observations assigned to the kth Gaussian in the mixture, i.e., $N_k = \sum_{i=1}^{N} \gamma(l_{ik})$;
4. Check for convergence.

- If the multivariate sample can be classified in several different clusters but they number of components is not well-chosen, the possibility of overfitting the probabilistic model to the data becomes a real problem. In this case, some small-sized clusters may appear overly adjusted to the outliers, which will not be identified as such.

In order to tackle these issues, we propose the inclusion of two additional steps in the estimation of the GMM in the feature space once the likelihood function is evaluated.

1. The log likelihood function presented in Equation (2.37) is unbounded. This means that, if at any point the estimated mean vector $\mu_k^{\text{new}} = \frac{1}{N_k} \sum_{i=1}^{N} \gamma(l_{il}) u_i$ of one of the components in the mixture were to be estimated to be equal to one of observed points in the sample of the feature space u_i ($\mu_k^{\text{new}} = u_i$, then the likelihood function diverges. In other words, it attains a singularity and therefore being interpreted by the algorithm as an optimal point in the estimation of ν. Naturally, this leads to spurious results in which the mixture model adjusts a single Gaussian component to individual points in the sample which are not representative of the standard expected behavior of the sample of functional data. In order to circumvent this problem, if at any point $u_i = \mu_k, \forall i, k \in \{1, ..., N\} \times \{1, .., K\}$ then the point is extracted from the sample, as it is an isolated outlier. In practice, the point is extracted if at any point in the procedure $||u_i - \mu_k||_2 < \epsilon$, where $\epsilon = \inf_{\mathcal{S}} ||u_i - u_j||_2, \forall i, j \in \{1, ..., N\} \times \{1, ..., N\}$ and $\mathcal{S} \subset \mathbb{R}^R$ introduced in section 2.4.1 is the lower-dimensional space of features.

2. In each iteration step, w_k can be interpreted as the prior probability of $l_{ik} = 1$, whereas $\gamma(l_{ik})$ is the posterior probability once the sample is observed. If such posterior probability is considered too low (in our applications we shall take a value of 0.1 as the minimum

weight of the mixing coefficients), we will consider that the corresponding component is either overfitting the data, or that it has detected a small subset of points which is not representative of the central trend of the data. In this case, the other calculated parameters of the components are kept and the values of means and covariances of the small cluster are reinitialized to a random value in the space.

This procedure yields the algorithm shown in Algorithm 3.

Algorithm 3: EM algorithm for outlier detector GMM

Result: Set of parameters ν^{final}

1. Choose (manually or randomly) a starting set of parameters $\nu^{\text{old}} = \{\mu_k^{\text{old}}, \Sigma_k^{\text{old}}, w_k^{\text{old}}\}_{k=1}^K$;

2. **E-step**. Evaluate the corresponding responsibilities $\gamma(l_{ik})$;

3. **M-step**. Re-estimate the parameters through:

$$\mu_k^{\text{new}} = \frac{1}{N_k}\sum_{i=1}^{N}\gamma(l_{il})u_i$$

$$\Sigma_k^{\text{new}} = \frac{1}{N_k}\sum_{i=1}^{N}\gamma(l_{ik})(u_i - \mu_k^{\text{new}})(u_i - \mu_k^{\text{new}})^T$$

$$w_k^{\text{new}} = \frac{N_k}{N}$$

where N_k represents the number of observations assigned to the kth Gaussian in the mixture, i.e., $N_k = \sum_{i=1}^{N}\gamma(l_{ik})$;

4. Check for convergence.;

5. Check $||u_i - \mu_k||_2 < \epsilon, \epsilon = \inf_{\mathcal{S}}||u_i - u_j||_2, \forall i, j \in \{1, ..., N\} \times \{1, ..., N\}, \forall k \in \{1, ..., K\}$;

6. For the given level α, check $w_k^{\text{new}} < \alpha, \forall k \in \{1, ..., K\}$

2.4.3 Testing for outlyingness and ordering score

Now that a probabilistic model adapted for outlier detection is available in the R-dimensional space of features $\mathcal{S} \subset \mathbb{R}^R$, a statistical test for outlyingness may be constructed based on the probability that each point has to have been generated by the components of the constructed GMM. This way, for any $u_i \in \mathcal{S}$:

$$\begin{aligned} &H_0 : u_i \text{ has been generated by } f_k \text{ with probability at least } p_{\alpha k} \\ &H_1 : u_i \text{ is an outlier.} \end{aligned} \tag{2.40}$$

Under H_0, $p(u_i|l_k = 1) > p_{\alpha k}$, where $p_{\alpha k} = f_k(u_\alpha|\mu_k, \Sigma_k)$ such that $\mathbb{P}(u_\alpha|z_k = 1) \geq \alpha$.

The set of data points less likely than u_α is determined by the Borelian set in $\mathcal{S}$ that verifies:

$$(u-\mu_k)^T\Sigma^{-1}(u-\mu_k) \geq (u_\alpha-\mu_k)^T\Sigma^{-1}(u_\alpha-\mu_k). \tag{2.41}$$

And therefore, $\mathbb{P}[(u-\mu_k)^T\Sigma^{-1}(u-\mu_k) \geq (u_\alpha-\mu_k)^T\Sigma^{-1}(u_\alpha-\mu_k)] = 1-\mathbb{P}[C^* \leq (u_\alpha-\mu_k)^T\Sigma^{-1}(u_\alpha-\mu_k)]$, where C^* follows a Chi-squared distribution, $C^* \sim \chi^2(k)$. By performing this test over all of the points considered in the feature space, a unique criterion for outlier detection is obtained, such that the outlying points will be the ones presenting p-values under a certain threshold $\alpha, \forall f_k$.

Here we have provided a unique detection criterion that allows the comparison to other detection methods that only provide a binary score. However, the interest in the development of a continuous outlier score that can quantitatively assign a degree of outlyingness in amongst the functional observations was already discussed. This can be estimated by measuring the *probability mass* contained in the corresponding minimum volume level set $\mathcal{S}_\theta$ in $\mathcal{S}$ that corresponds to the ith observation. If the underlying probabilisitc model of the functional data in the feature space is denoted by p, and an available estimator $\hat{p}$ exists, the outlyingness score θ_i of the ith observation can be estimated through the expression:

$$\hat{\theta}_i = \int_{\mathbb{R}^R} \hat{p}(u)\mathbb{1}_{\{\hat{p}(u)\geq\hat{p}(u_i)\}}d^R u \tag{2.42}$$

where $\mathbb{1}$ represents the indicator function.

Finally, let us consider the more realistic case where the availability of data is actually limited, and the sample of functional data is small so that the representation of $\hat{p}$ is not sufficient to guarantee the adequacy of the estimated function to represent the underlying probability model. This could be for instance the case for expensive industrial simulation codes, such as the mechanical or thermal-hydraulic simulators. In this case, a natural extension of this idea for outlier detection can be implemented via bootstrap resampling, (Efron and Tibshirani, 1994). B groups are formed by successively drawn with replacement in the original sample. This way, the absence of data can be mitigated through the re-estimation of the GMM for each bootstrap group. If for B bootstrap groups $p_b(\mathbf{u})$ represents the GMM of the bth group, the form of the (bootstrap) estimator of outlyingness would then be:

$$\hat{\theta}_i = \int_{\mathbb{R}^R} \frac{1}{B}\sum_{b=1}^{B} \hat{p}_b(u)\mathbb{1}_{\{\hat{p}_b(u)\geq\hat{p}_b(u_i)\}}d^R u \tag{2.43}$$

Throughout this reasoning, the hyperparameter K (the number of components of the mixture model) has been supposed to be fixed, but in practice, this is yet another input parameter of the GMM that must be provided *a priori* to the EM algorithm. Indeed, the actual form of the model is significantly different depending on the number of components that are considered. If that is the case, the use of an oversimplified mixture when modeling complex multivariate distributions can induce incorrect conclusions about the distribution of

data, whereas an unnecessary increase in the number of components may lead to overfitting problems, unacceptable computational costs or imprecise conclusions.

This question can be treated as a model-selection problem, and several metrics are available in order to estimate an appropriate number of components depending on the sample. Some examples are the Bayesian Information Criterion (BIC) (Schwarz, 1978) or the Integrated Completed Likelihood (Biernacki et al., 2000). In this paper, the selection of the number of components is performed by means of the Bayesian Information Criterion:

$$BIC = 2\log(\hat{v}) - G\log(N) \tag{2.44}$$

where $\hat{v}$ represents the log-likelihood function for the GMM, G is the chosen number of components and N is the sample size used for the estimation. The second term introduces a penalty which depends on the number of components in order to mitigate overfitting effects.

With these elements, the detection methodology is summarized in Algorithm 4.

In the following section, analytical results for the detection methodology considering several sets of features are presented, comparing the results to some existing methodologies.

2.5 Numerical Tests

The detection capabilities of the algorithms will be assessed via simulation experiments taken from some common examples that can be found in the literature (López-Pintado and Romo, 2009; Long and Huang, 2015; Dai et al., 2020).

Let us consider a sample of $N = 50$ functional observations, in a uniformly distributed grid of 30 points in $\mathcal{T} = [0, 1]$ and $B = 10$ bootstrap groups. Let us consider the following four function generators (see Table 2.2 for the specifics in the notations):

- **Model 1**. $Z(t) = 4t + G(t)$ is the function generator for the reference set of curves. In this case the outliers follow the distribution $Z_o(t) = 4t + G(t) + 2\mathbb{1}_{\{(t_I<t)\}}$.
- **Model 2**. The reference model for the curve generation remains $Z(t) = 4t + G(t)$, whereas the outliers are now generated from the distribution $Z_o(t) = 4t + G(t) + 2\mathbb{1}_{\{(t_I<t<t_I+3)\}}$.
- **Model 3**. Here the reference model becomes $Z(t) = 30t(1-t)^{3/2} + G(t)$. The outliers are generated from $Z_o(t) = 30(1-t)t^{3/2} + G(t)$.
- **Model 4**. For this last case, we keep the reference model as it is for Model 1 and Model 2, but the outliers simply consist of the sole deterministic part $Z_o(t) = 4t$ (the Gaussian component is removed).

Algorithm 4: FOD algorithm

Result: Set of outlyingness scores $\{\theta_i\}_{i=1}^N$, and set of outliers $o \subset \{z_i\}_{i=1}^N$

1. Check if the sample of functional data is uniformly sampled. Otherwise, Project the data onto a basis shown in 2.2.2 until a desired level of error $||\hat{z}_i - z_i||$, where $\hat{z}_i$ are the projected samples, is reached.Uniformly resample in this grid;

2. Choose a family of R semimetrics and project $\{z_i\}_{i=1}^N$ into the feature space $\mathcal{S}$;

3. **for** $K \in \{1, ..., K_{max}\}$ **do**

(a) Choose (manually or randomly) a starting set of parameters $\nu^{\text{old}} = \{\mu_k^{\text{old}}, \Sigma_k^{\text{old}}, w_k^{\text{old}}\}_{k=1}^K$;

(b) **E-step**. Evaluate the corresponding responsibilities $\gamma(l_{ik})$;

(c) **M-step**. Re-estimate the parameters through:

$$\mu_k^{\text{new}} = \frac{1}{N_k} \sum_{i=1}^{N} \gamma(l_{il}) u_i$$

$$\Sigma_k^{\text{new}} = \frac{1}{N_k} \sum_{i=1}^{N} \gamma(l_{ik})(u_i - \mu_k^{\text{new}})(u_i - \mu_k^{\text{new}})^T$$

$$w_k^{\text{new}} = \frac{N_k}{N}$$

where N_k represents the number of observations assigned to the kth Gaussian in the mixture, i.e., $N_k = \sum_{i=1}^N \gamma(l_{ik})$;

(d) Check $||u_i - \mu_k||_2 < \epsilon, \epsilon = \inf_{\mathcal{S}} ||u_i - u_j||_2, \forall i, j \in \{1, ..., N\} \times \{1, ..., N\}, \forall k \in \{1, ..., K\}$;

(e) For the given level α, check $w_k^{\text{new}} < \alpha, \forall k \in \{1, ..., K\}$

(f) Check for convergence.;

(g) $BIC_K = BIC$ associated with the estimated density, $(\hat{p}_K)$ with $\hat{p}_K$ being the estimated GMM model with K components;

end

4. Set $K = \underset{k \in \{1,...,K_{\max}\}}{\text{argmin}} \{(BIC_k)\}_{k=1}^{K_{\max}}$;

5. For a level α, test H_0, H_1 $\forall u_i \in \{u_i\}_{i=1}^N$. Obtain o;

6. Estimate

$$\hat{\theta}_i = \int_{\mathbb{R}^R} \frac{1}{B} \sum_{b=1}^{B} \hat{p}_b(u) \mathbb{1}_{\{\hat{p}_b(u) \geq \hat{p}_b(u_i)\}} d^R u, \theta_i \forall i \in \{1, ..., N\}$$

It is important to note that the coefficients (multiplicative factors) of the indicator functions have been reduced in order to make the outliers less apparent. A summary of the

notations can be found in Table 2.2.

Table 2.2: Description of the common parameters of the models.

Notation	Description
$G(t)$	Centered Gaussian process of covariance function $\Sigma(t_1, t_2) = 0.3 \exp \frac{-\lvert t_1 - t_2 \rvert}{0.3}$
$Z(t)$	Functional random variable generating the main model
Z_0	Functional random variable generating the outliers
t_I	Random point uniformly generated in the definition domain of the function

The corresponding models are plotted in Figure 2.7.

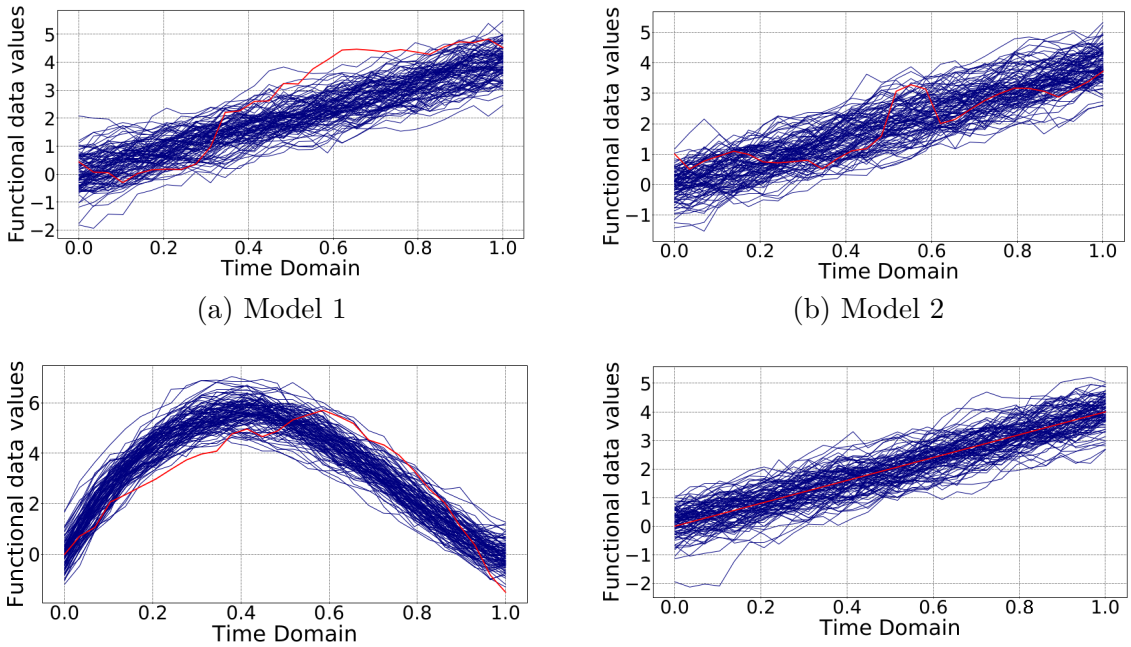

(a) Model 1 (b) Model 2

(c) Model 3 (d) Model 4

Figure 2.7: Toy examples of functional data. Blue: Standard curves. Red: outlier.

Let us now consider a set of features adapted to perform the dimensionality reduction part of the algorithm:

- The h-mode depth, described in the Equation (2.13).
- The Dynamic Time Warping (DTW), found in Section 2.3.2.3.
- The modified band depth (noted BD), which can be found in Equation (2.16).

- The L_2 norm (noted L2) which is one of the most intuitive and widely used metrics that can be applied to functional data. It takes the form: $||z(t)||_2 = \left(\int_{\mathbb{R}} |z(t)|^2 dt \right)^{1/2}$.

The experiments are replicated a total number of $n = 100$, and the feature space is constructed by using a pair of functional measures. Several reasons justify this choice. Firstly, the estimation of the minimum volume level sets can be computationally expensive in higher dimensions, and the addition of measures in the construction of the underlying model is not necessarily useful, since we aim at identifying the two main types of outliers: magnitude and shape. On top of that, the estimation of $\hat{p}$ requires a larger number of parameters, and most notably, the computation of the elements in the covariance matrices can become costly.

Two scores are used in order to measure the detection capabilities of the algorithm. The first one is simply the estimated θ (see Equation 2.42) values of the score of outlyingness, for each observation in each replication. It is directly proportional to the outlying nature of each functional observation in the feature space, and quantifies the probability of finding another observation at least as anomalous. The second score is the average ranking of each observation with respect to the whole population of functional data in each replication according to θ_i. The score θ_i provides a center-outward ordering of the curves according to this metric. In industrial applications, this ranking can be followed by the engineer to analyze particular data (e.g. numerical simulations) from the most suspicious (potentially interesting) observation to less suspicious ones.

The results of these tests are summarized in Figures 2.9 and 2.8, as well as in Table 2.3.

Table 2.3: Average rankings of the outlier for each analytical model and combination of features.

Pairs of features	**Model 1**	**Model 2**	**Model 3**	**Model 4**
BD-DTW	48.663	41.272	49.621	42.376
BD-hM	41.342	39.067	49.833	43.643
DTW-L2	44.551	42.660	**50**	**43.842**
hM-L2	48.937	44.133	49.968	41.929
hM-DTW	**49.225**	**45.154**	49.852	42.343
BD-L2	44.254	41.418	49.944	43.672

As one can see from the Table 2.3 and Figure 2.9, the combination of features that show the highest detection capabilities are the ones that include at least the h-Mode depth or the DTW as component of the considered Gaussian mixture model. In the case of the first two models, it is the combination of both features that yields the best detection results, whereas it remains close to the best result for Model 3 and Model 4.

This result was expected, since the L^2 norm is a very general non-parametric measure

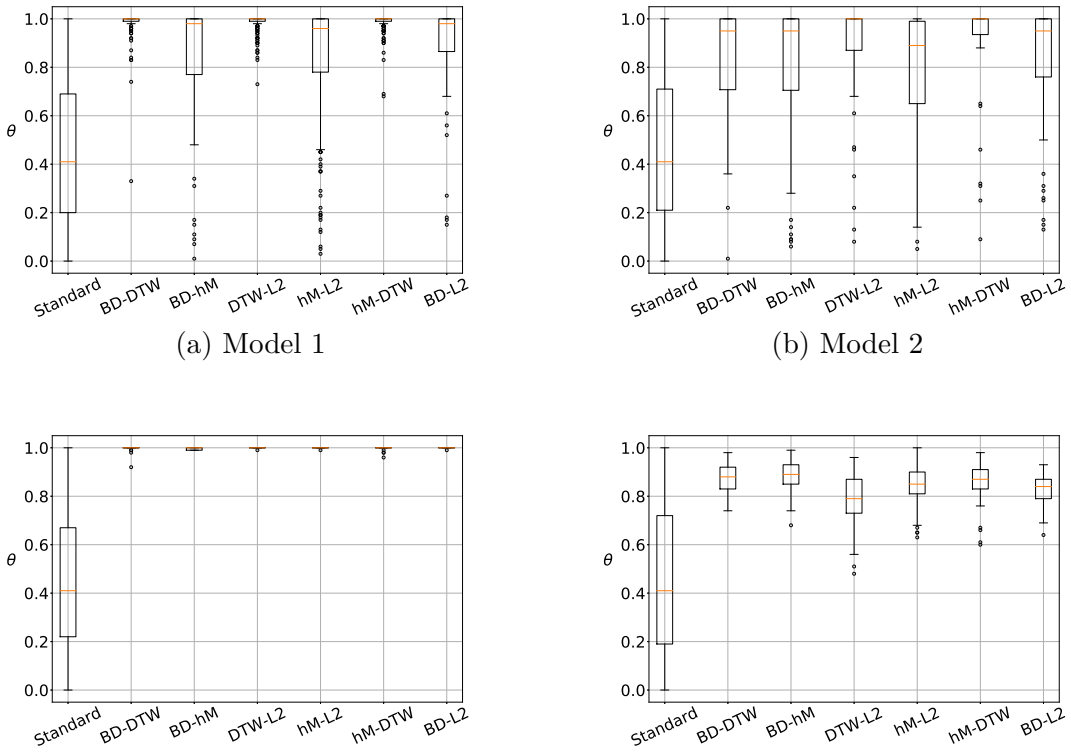

(a) Model 1 (b) Model 2

(c) Model 3 (d) Model 4

Figure 2.8: Boxplots of the outlyingness score for all combinations of features in each model in the $n = 100$ replications. The boxplot takes into account the whole distribution of θ_i for all the replications of each experiment.

which is probably not well suited for the direct application to the detection of anomalies in functional data, in spite of its usefulness for functional data characterization. The Modified Band Depth appears to be adapted for a quick detection of magnitude outliers, but not such a sensitive measure regarding shape outliers, which are far more complicated to define, identify and detect. That also explains why the scores for the third model (magnitude outlier) are so high with respect to the others.

The presented scores can be used in order to compare different detection methods that could be based on identical features (multiple testing, use of level sets, functional boxplots...) as well as a tool to compare the usefulness of different features for a common detection on the basis of a common detection algorithm.

In both cases (for the boxplots of the $\hat{\theta}_i$ and the rankings), it is possible to appreciate not only the absolute detection capabilities that were mentioned before, but also the relative dispersion of the data. This can also be interpreted as an indicator of robustness (which depends on the choice of features). When looking at figures 2.8 and 2.9, several aspects can be noted. The first obvious remark is that the detection capabilities for the third model are

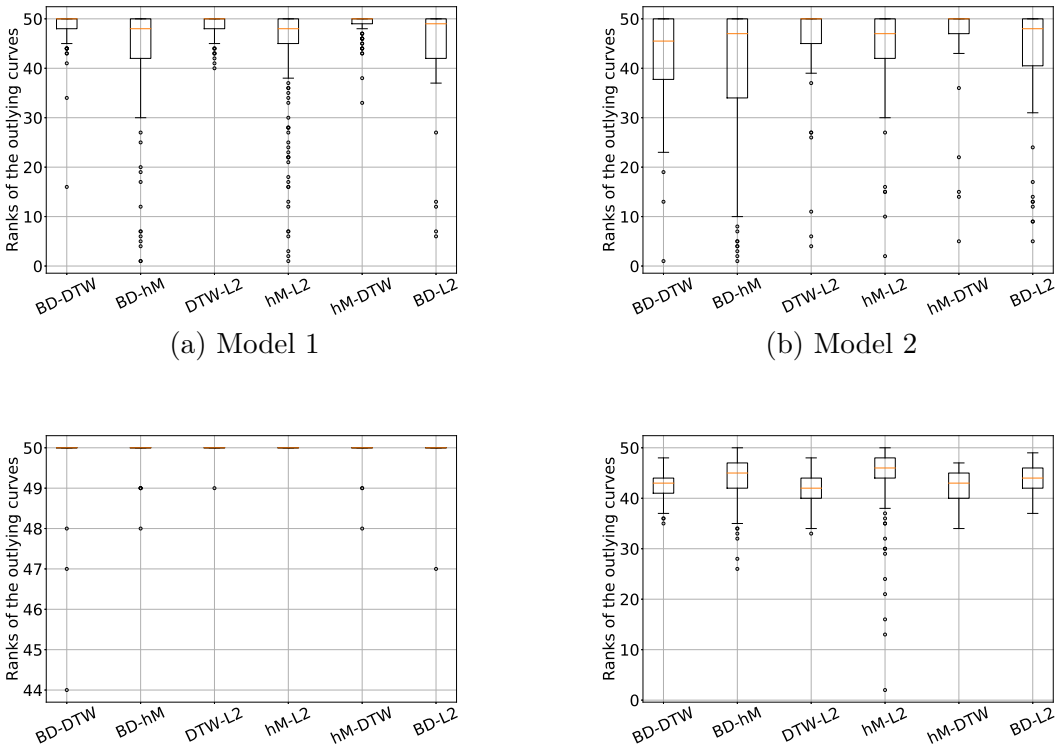

(a) Model 1 (b) Model 2

(c) Model 3 (d) Model 4

Figure 2.9: Boxplots of the ranking score of the outlier for all models over the $n = 100$ replications.

far superior to those of the others. This is explained by the fact that this is the only one that constitutes both a shape and magnitude outliers, which largely facilitates its detection, even for less sensitive measures such as the L^2 distance. Another interesting point is that for the first model, which is contaminated by a shape outlier, all of the best results are obtained by the combinations that employ the DTW metric. This is also coherent, since it is the feature that best takes into account the shape differences between the curves. Finally, when analyzing the results of the experiments, it can be concluded that the use of a joint model through the h-mode depth and the DTW provide not only the highest detection rates in general, but also the smallest dispersion out of all the possible combinations. This is mostly related to the fact that the DTW is the most sensitive feature when it comes to analyzing shape outliers (it is specifically designed to provide a measure of correspondence between sequences). In conclusion, recommended use for general outlier detection is the couple of measures: h-mode depth and DTW.

We can also compare the performance of our algorithm considering these 2 measures against other state of the art methods. For that purpose, we retain the previous 4 presented models as test cases, simulating $n = 500$ replications of the detection experiments with an increased sample of curves $N = 100$ and different degrees of contamination in the models:

1%, 5% and 10% (i.e., 1, 5 and 10 outliers in the samples).

The results are summarized in Table 2.4.

Table 2.4: Performances of the different algorithms on the test models. The results are expressed as a percentage (detection rates). Algorithm: our proposed algorithm; DO: Directional Detector; FB: Functional Boxplots; HDR: High-Density Regions. N: total sample size. p: proportion of outliers in the sample.

N=100, p=1%	**Model 1**	**Model 2**	**Model 3**	**Model 4**
Algorithm	**100.00**	**96.94**	**100.00**	**100.00**
DO	59.26	39.51	100.00	0.00
FB	2.33	0.00	100.00	0.00
HDR	89.47	69.64	100.00	0.00
N=100, p=5%				
Algorithm	**91.14**	**96.79**	99.17	**97.50**
DO	58.23	54.40	**100.00**	0.00
FB	2.53	4.18	11.95	0.00
HDR	48.35	44.8	49.48	0.00
N=100, p=10%				
Algorithm	**81.50**	**75.49**	86.67	**92.37**
DO	47.25	45.97	**99.63**	0.00
FB	0.75	1.71	7.41	0.00
HDR	22.25	23.41	14.07	0.00

Firstly, we must note that the identification capabilities and rates are clearly reduced when the size of the outlying sample is increased. This reduction of the performance of any detection algorithm is logical, since higher degrees of contamination naturally pollute the functional sample, which increases the bias of the score that is used for outlier detection. In the same line, if the size of the outlying sample is considerable (10% of outliers for instance), an argument can be made to defend that this sample might not be outlying, and that it simply corresponds to another mode in a hypothetical multimodal functional sample. This kind of phenomenon, as well as masking effects, is described in detail in Aggarwal (2017).

Looking at the results, we can appreciate that the performance of our proposed algorithm is indeed competitive when compared with existent methods, even for complex sets of functional data, such as Model 4. In this case, we can clearly appreciate how the inclusion of a measure specifically dedicated to the detection of shape differences allows the consistent detection of the outlier. This capability is especially significant when we compare it with the

other methods, which prove to be unable to detect this kind of shape outlier. In the case of the widely used Functional Boxplots, this is to be expected since they are intended to detect magnitude outliers. Regarding the HDR method, its low detection capabilities in this case are due to the fact that the low-dimesional representation through robust Functional Principal Component Analysis is not sufficiently precise to capture the outlying nature of the straight line. It is indeed possible that retaining a higher number of modes in this case could allow better detection capabilities, but this procedure greatly increases the curse of dimensionality problem (even if this subject is not treated in the paper of Hyndman (2009)), and it does not allow visualization purposes.

It is clear that Model 3 (being the only pure magnitude outlier amongst the considered models) is the simplest and easy to detect and most methods can consistently detect this kind of outlier when the sample is not overly polluted. Methods which rely the most on the density of curves are more vulnerable to any introduced bias in the sample by the curves if more than one mode exists, as they tend to identify the proportion of curves that *behave unusually* as belonging to a different modes of curves instead of treating them as genuine outliers. In the case of the functional boxplots, this is to be expected since by construction they are dedicated to the detection of magnitude outliers, which is useful if the contamination of the sample is made by a wide variety of magnitude outliers, but not so much if those outliers have all been generated by a homogeneous family of curves. In the case of the HDR plots, the existence of a homogeneous sample of outliers generates a set of points in their two-dimensional feature space of principal component scores with a high density of data, which prevents them from being identified as outliers.

In Models 1 and 2 the conclusions are similar (both models present a combination of slight magnitude and shape outliers). Most methods do not showcase any robustness for such slight magnitude outliers, contrary our developed algorithm. The main conclusion that can be extracted from these tests is that most methods struggle to find outliers when they are not apparent.

Finally, it must be mentioned that the Directional Detector is the most robust method when it comes to detecting the pure magnitude outlier presented in Model 3, as it is the least sensitive method to more contaminated samples. The main advantage of this methodology is its capability of finding outliers in multivariate functional data sets.

2.6 Conclusions

In this chapter, we have provided an overview of the main elements commonly used in the FDA domain. We have shown which are the main elements necessary to represent functional data and perform basic exploratory analysis in this framework.

We have also provided an extensive review on the main challenges that exist currently in the outlier detection domain, both in a general sense and in the particular case of functional data. This domain presents very specific and particular challenges which are rarely addressed.

The representation of functional data in lower dimensional spaces is also presented in detail, providing a practical framework of this representation through the use of semimetrics. A concise review of current methods for functional outlier detection is also presented, which constitutes a first attempt at classifying the existing methodologies.

Finally, we proposed a novel methodology that is competitive to state of the art algorithms, and whose usefulness in industrial context will be showcased in the following chapters.

3

Global Nuclear Transient Analysis

Contents

In this chapter we will introduce the industrial context of our work, which is the analysis of accidental nuclear transients in nuclear power plants (NPP). Transients that may occur in French Pressurized Water Reactors (PWR) are simulated using the *CATHARE2* code. This requires to model the studied reactor using the functionalities of *CATHARE2*, and run simulations at the end of which the code provides functional outputs that describe the evolution of thermal-hydraulic (TH) quantities during the transient. The outputs, which are functional by nature, are then analyzed with a specific procedure based on the Functional Outlier Detection (FOD) method presented in Chapter 2. Section 3.1 first presents the basic elements upon the design of PWR that motivate the study of transients for these reactors, as well as a description of the *CATHARE2* modeling, and how simulations are conducted with this code. The approach adopted for the analysis of simulation results comes from the domain of Sensitivity Analysis (SA). Section 3.2 provides a brief introduction to SA methods and presents the HSIC indices, which are the main tool used to study the influence of input variables of *CATHARE2* on physical parameters of interest (Variables of Interest). The methodological contribution to the study of nuclear transient analysis is then exposed in section 3.3, including the different steps of a study based on our approach. The chapter concludes in Section 3.4 with a brief summary of the framework both in the theoretical and industrial setting, and what the application of the presented methodology aims to achieve in the context of nuclear transient simulation.

3.1 The *CATHARE2* code in nuclear safety studies

This section gives a general presentation of *CATHARE2* and its role in nuclear safety assessments. Some fundamentals about the design of PWR are first provided as well as about the physics of Loss of Coolant Accident (LOCA), which is the main kind of transient targeted by our approach. These general elements are followed by a more detailed description of the *CATHARE2* modeling, that is, the set of equations on which the *CATHARE2* modeling is based and the basic modeling tools provided by the platform (modules and submodules). Finally the procedure to run *CATHARE2* simulations is briefly explained.

3.1.1 General presentation of Pressurized Water Reactors (PWR)

EDF is operating 56 nuclear reactors (since 2020, after the Fessenheim NPP was closed), all being Pressurized Water Reactors deriving from the same initial design. The French fleet of power reactors is hence characterized by its uniformity when it comes to the conception, operating conditions and safety rules of nuclear power plants. The operating principle on which

PWR are based (illustrated in Figure 3.1) consists in extracting power from the nuclear core, which lies in a thermal-hydraulic circuit called *primary circuit*, and transferring it to another circuit, called *secondary circuit*, to drive the main turbine-generator unit. The nuclear power generated by the core is converted into thermal power of the fluid that flows in the primary circuit. The primary circuit is subdivided into three (or four, depending on the reactor type) cooling loops allowing the primary-secondary power transfer. This power exchange from the core to the secondary circuit through the primary fluid is also essential for safety, as the core keeps on producing power even after a potential emergency shutdown of the reactor. This *residual power* must be evacuated to prevent an overheating of the core with unacceptable consequences. The safety of the operating process is indeed based on the existence of several confinement barriers that prevent radio-active materials from being released in the environment. The fuel cladding is the first one of this confinement barriers, the second one being the primary circuit itself. This circuit includes five main components which are essential for nominal producing conditions and in case of accidental events.

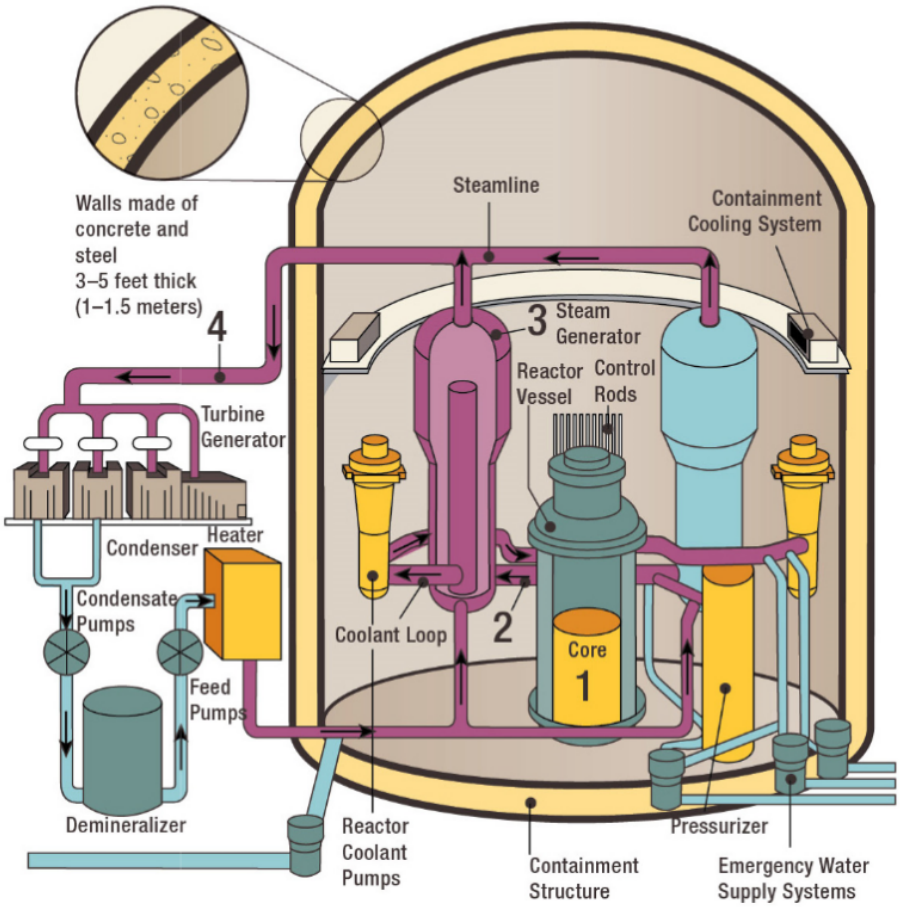

Figure 3.1: Illustration of the main basic elements of a PWR nuclear power plant. Taken from: Nuclear Regulatory Commision (NRC) (2015) (url: `https://www.nrc.gov/reactors/pwrs.html`)

1. **Core**. The nuclear core contains the fuel through which the power is generated. This

fuel is constituted by pellets of Uranium dioxide (UO_2) enriched in the 235 isotope (as opposed to the $^{92}_{238}U$ isotope which is more common), in a proportion that ranges from 3% to 5%. This isotope is a *fissile* material, i.e., it allows the sustained production of energy so long as the amount of available neutrons allowing the fission of the fuel atoms is guaranteed. This phenomenon releases both energy and neutrons, potentially contributing to a chain reaction. Fuel pellets are embedded in rods with a sheath made of Zircalloy (Zirconium-based alloy). These rods are themselves assembled into a component known as Fuel Element (FE) or fuel bundle. This fuel, thanks to the occurrence of nuclear reactions, produces large quantities of power that are transferred from rods to the surrounding coolant fluid. In this process, the coolant fluid also *moderates* the nuclear reaction, which means it slows down the neutrons emitted during the fission of uranium atoms. As neutrons collide with the water molecules of the coolant, their overall energy is lowered, considerably increasing the fission probability of 235− uranium nucleii. This way, water fulfills a double role in PWR: in one hand, it is a coolant which allows the extraction of energy from the fuel, and on the other hand, it is a moderator making possible a sustained and controlled chain reaction in the nuclear core.

2. **Reactor Pressure Vessel (RPV)** (IAEA, 2009). The RPV is the component containing the nuclear core and is thus exposed to a high-energy neutron flux. It is constituted of a cylindrical wall of low-alloy carbon steel, whose internal part is usually coated with an austenitic stainless steel layer in order to minimize corrosion. It is closed by a hemispherical bottom head which is welded to the vessel's body and a bolted upper head that can be opened for refueling operations or maintenance.The vessel also contains the support structures that guarantee the mechanical stability of the core in the demanding pressure and temperature conditions in the primary circuit (respectively around 155 bar and 320 °C), and neutron-absorbing control rods which allow controlling the nuclear reactions in the core. As part of the second confinement barrier the RPV plays a major role in nuclear safety, although the radiation flux coming from the core might alter the vessel material and its mechanical properties during the years of operation.

3. **Pressurizer (PZR)** (NRC, 2004). The pressurizer is the element allowing to control the primary pressure, ensuring this way the pressure value remains within standard operation limits (changes of the pressure value are usually caused by changes in temperature of the core). This control is achieved by maintaining a water-steam equilibrium for the fluid contained by the component. The pressure can be raised if necessary through the use of heaters, whereas it can be lowered thanks to a liquid water spray system, as well as valves (operator-controlled relief valves and safety ones).

4. **Reactor Coolant Pumps (RCP)** (NRC, 2004). The RCP, also called *primary pumps*, provide to the primary coolant the force required to maintain the forced flow of the fluid. This flow is necessary to ensure the extraction of power from the core and the transfer of this power to the secondary circuit. Each loop in the primary circuit is equiped with one pump. Primary pumps are themselves powered by electric generators ranging from 4.5MW to 7.5MW depending on the specific kind of reactor. Their activation at each start of the reactor also provides to the fluid the thermal power required to heat

the coolant up to the nominal operating temperature value. It is to be noted that in accidental situations, primary pumps constitute a non-negligible thermal input to the coolant if they are still in motion once the chain reaction is stopped.

5. **Steam Generators (SG)**. The steam generators are the components through which the primary/secondary power exchange is performed. The water in the SG at the secondary side (feedwater) is heated on contact with large tubes (in commercial PWR the SG can reach a height up to 20m) through which the primary fluid is flowing. The secondary fluid, which is liquid when entering the steam generator, is vaporized due to its power intake, and redirected to the steam turbine. The steam generators are also essential for safety as they ensure the evacuation of the residual power in case of emergency shutdown of the core.

3.1.2 Nuclear transients in PWR

As the operating principle of PWR is based on the extraction of energy from a source (the core) *via* heated water, the primary circuit of PWR (with its auxiliary systems) is often called *boiler*. In normal operating conditions, the reactor is kept in a stable state. To reach such a steady state, for example at the start of a new production cycle, the boiler continuously goes through intermediate states until meeting its nominal operating point. Similarly, the reactor state changes from a nominal power producing state to a cold one when the reactor is stopped (for example to partially renew the fuel in the core). French PWR are also designed to be capable of modulating the produced power level on power grid requirements. This power modulations also impose to operate a transition from a reactor state to another with corresponding power levels to follow the electrical system's demand.

Such dynamical operating phases are called transients as they consist in transitory changes of the reactor's physical parameters. *Transient* also applies to the dynamic modification of the boiler's state which may occur in case of an accident. The accidental transient starts when the reactor, due to some hazardous event, deviates from its safe operating domain, and lasts until reaching a new safe state.

One of the accidental transients which might affect a PWR (although extremely unlikely) is called Loss Of Coolant Accident (LOCA). It is characterized by the opening of a break on the primary circuit, causing a significant diminution of the amount of water available in the boiler to keep cooling the core. A safety injection system is then automatically activated to bring water to the primary circuit and hence compensate the fluid loss. However, some undesirable phenomena, for which regulatory authorities impose strict safety requirements, might also arise during the accident. In particular the coolant loss can cause a partial vaporization of the primary fluid, drastically limiting its cooling power nearby the fuel rods. In all cases the emergency shutdown of the reactor results in a decrease of the coolant flow rate which in turn diminishes its power extraction capacity. Due to this temporary perturbation of the cooling function, fuel rods are subject to a temperature peak (or several ones in some cases). Safety studies are then required to make sure that the fuel rods cladding will resist these

solicitations.

Another undesirable consequence of LOCA events is the solicitation of the reactor pressure vessel caused by the injection of water by safety systems. The injected water is indeed pumped from a tank located outside the reactor building. This water, whose temperature is imposed by meteorological conditions (and kept between limits imposed by operating rules), thus causes a thermal shock on the circuit's steel components close to the injection points. In particular, a crack may initiate in the reactor pressure vessel wall, due to the irradiation embrittlement of the component's steel, and the simultaneous potential presence an undetected flaws in the component's steel, which is also embrittled . The impossibility of such a crack initiation event has to be proved by safety studies and is also subject to strict regulatory requirements.

Although many other transients (accidental or not) might occur in PWR, we will focus on LOCA in the following chapters as the main application of this work. LOCA transients will be described in more details further in this document.

3.1.3 Best Estimate codes in the context of nuclear safety

Most nuclear power operators are confronted to a strict licensing process either to validate the reactor's design before its constructions and start-up or during the plant's life in service with periodic reappraisals. This process aims to ensure nuclear installations will be operated safely up to their decommissioning. In this process, operators have to prove that reactors, and in particular their safety systems, do meet regulatory requirements. Such a demonstration implies the examination the consequences of accidental scenarios on the parts of the boiler that are most essential for safety functions. More precisely, this means estimating the value of critical physical parameters throughout the considered scenario. At all times this quantities must remain within limits fixed by the regulatory authority, justifying the absence of risk of unacceptable events (such as the release of radioactive materials in the environment) even in case of accidental transient.

Engineering studies intended for this justification were first based on penalizing assumptions and simplified physical models, hence enabling conservative estimations of quantities of interest while limiting the complexity of the methodology employed. This however provides little insight on the margins actually existing between safety criteria and values representative of the studied reactors. To account for more realistic evaluations of severity levels associated with accidental situations, the use of Best Estimate (BE) models is now widely spread. BE models are defined so as to obtain results as close as possible to real physical values for a given precision level. They were first used in complement to conservative studies to produce validation arguments for the design of nuclear systems. This first approach, based on deterministic calculations, lead to a first rise in importance of BE models as they improve the knowledge upon uncertain key parameters.

Although this option for the incorporation of BE codes in safety reports is mentioned in the *Safety Guide on Safety Assessment* (IAEA, 2001), this document also stresses on a second possibility. BE codes indeed also support the use of Uncertainty Quantification (UQ) methods

in a probabilistic framework, hence allowing a more accurate assessment of the conservatism level of reference calculations. This approach, which combines *realistic* physical hypothesis (on initial and boundary conditions) and uncertainty treatments is then called *Best Estimate Plus Uncertainties* (BEPU, see IAEA (2008)). It naturally yields less penalizing results, and should be based on statistically likely conditions for both the NPP and the simulator, in such a way that safety requirements are shown to be fulfilled with a sufficiently high probability. In addition to this, probabilistic methods can be used to validate the design of a component with respect to specific probabilistic targets or to search for potential risk outliers.

3.1.4 Nuclear transient analysis with *CATHARE2*

The main actors of the French nuclear industry (*Commissariat à l'Energie Atomique et aux energies alternatives* or CEA, French public body dedicated to the study of nuclear physics as well as the development of nuclear reactors and weapons, *Electricité de France* or EDF, French public company in charge of the operation of nuclear reactors, Framatome, French public company in charge of the design and sale of french PWR and the *Institut de Radioprotection et de Sûreté Nucléaire* or IRSN, French public lab in charge of the monitoring of nuclear activities as regards safety and radiation protection). have historically dedicated a considerable amount of effort to the development of a Best Estimate code called *CATHARE*, which stands for *Code Avancé de ThermoHydraulique pour les Accidents de Réacteurs à Eau*. *CATHARE* is dedicated to simulation of TH phenomena at the scale of a component or the whole boiler, and hence falls into the so-called category of *system* codes.

Thanks to long terms efforts for its experimental validation, the *CATHARE2* code is now considered as a state-of-the-art computer tool for nuclear transient analysis and is licensed by the French regulatory authority (Autorité de Sûreté Nucléaire or ASN) for this application. It is currently at its third major version (Geffraye et al., 2011).

As a multipurpose system code, *CATHARE2* allows simulating TH transients for a large variety of thermal-hydraulic systems and reactor designs. It was initially created as a tool for transient analysis in water-cooled reactors such as PWR or BWR (Boiling Water Reactor). It was also used in more recent research and development works for advanced concepts such as gas-cooled reactors, sodium-cooled reactors, sodium-cooled fast-breeder reactors and supercritical water-cooled reactors. In practice, *CATHARE2* is mainly used nowadays in three particular contexts: In validation studies, as a complementary tool in safety studies and transient analysis, and as an uncertainty quantification tool.

The role of validation studies is to quantify modeling errors coming from the numerical code, in order to find the best possible modeling of specific components in nuclear reactors. As a general rule, they consist in comparing experimental datasets to results obtained with numerical simulations. The validation chain of *CATHARE2* has been the subject of this kind studies by French organizations for the last decades. Nevertheless, a considerable effort is still currently being made in order to further improve the knowledge and capabilities of the code. As an example, the works presented in Carnevali and Bazin (2015), showcase a

comparative study of the 3-D and the previous 1-D/0-D modeling of the RPV of the Japanese experimental installation OECD/ROSA-LSTF (Large Scale Test Facility).This is done to validate the simulated 3-D effects observed in experimental tests. The same kind of work is performed in other tests presented in Mazgaj et al. (2016) and Carnevali and Bazin (2016).

In recent years, similar efforts were made in the context of validation studies for Generation IV Advanced Nuclear Reactors. This new generation of advanced reactors looks to improve upon the more classical designs of Nuclear Power Plants according to specific criteria of safety, sustainability, economy and proliferation Forum (2002). *CATHARE2* has provided satisfactory results in the physical modeling of these systems as well. This is shown in Geffraye et al. (2012), in which the results provided by the code were compared to the experimental ones for the *HE-FUS3* facility in Italy, or to simulations concerning the Oberhausen I and II NPP in Germany (Bentivoglio et al., 2008). The last two examples correspond to gas-cooled GenIV nuclear systems, but as previously mentioned *CATHARE2* has already been tested in other types such as sodium-cooled reactors. In particular, Bertrand and Mauger (2015) applies a *CATHARE2* modeling to the ASTRID (Advanced Sodium Technological Reactor for Industrial Demonstration) demonstrator.

As it was introduced in Chapter 1, *CATHARE2* has also been used as a Best Estimate (BE) code to support uncertainty quantification studies in several contexts, such as in robust quantile estimation Stenger et al. (2020); Stenger (2020), functional outputs clustering Auder (2011), metamodeling Iooss and Marrel (2019) or sensitivity analysis Iooss (2018).

From now on, and unless otherwise specified, all the physical results, interpretations, figures or tables will be coming from *CATHARE* simulations.

3.1.5 The *CATHARE2* modeling

3.1.5.1 Basics of TH systems modeling with *CATHARE2*

As it was previously mentioned, the *CATHARE2* code is conceived as a modular code, which allows to represent of a wide variety of flow configurations at a macroscopic (system) level. Modules and specific submodules (see description in Section 3.1.5.2 below) can be combined to reproduce the TH behavior of both experimental facilities and nuclear systems, whether these are components, loops or a whole boiler. *CATHARE2* implements a two-fluid modeling with six conservation equations (concerning mass, momentum and energy), plus several optional equations accounting for additional non-condensible gases or chemical elements in some components of TH circuits. For the sake of clarity, the system of equations on which the simulation engine is based is presented in its most simple version, which corresponds to a unidimensional (1D or axial) portion of flow.

The code is capable of simulating the mechanical and thermal-hydraulic non-equilibrium phenomena occurring during nuclear transients. All of the main phases LOCA transient (in particular, the blowdown, refill and reflood phases, see chapter 4 and 5) can be reproduced

using a *CATHARE2* modeling. Some mechanical phenomena showing relevance for safety studies can be predicted, such as fuel ballooning or rupture of the fuel rods' cladding, although their specific effect on the coolant flow and TH quantities in general cannot be taken into account. This limits the domain of application of *CATHARE2* to cases that do not include any severe damage to the fuel rods, which is the case in applications considered in this manuscript.

Uncertainties in *CATHARE2* calculations may arise from the lack of knowledge upon physical laws and parameters involved in the system's state equations. Furthermore, several options are usually available to model a same equipment, depending on the targeted realism level and on the phenomena under study. As an example, the core can be modeled using a simple unidimensional module accounting for the overall power discharge in the primary fluid or a three-dimensional one if asymmetrical fluid dynamics and other 3D physical effects within the core have a significant influence on the considered variable of interest. Hence, uncertainties are also induced by user's choices in the modeling of a given system.

3.1.5.2 The Modules of *CATHARE2*

A *CATHARE***module** is a basic numerical model implementing a meshing of the flow geometry, for which a set of conservation equations can be established (see 3.1.5.4). The meshing of the overall model with this set of equation define a numerical scheme for which equations are solved for each module's individual mesh as well as for junctions between modules. *CATHARE2* provides four main kinds of module to represent TH components and systems. These modules are:

1. **1-D** module (also called *pipe* or *axial*). It is adapted to the representation of elements in which one of the three spatial dimensions is preponderant over the others, and is formed by a succession of truncated cones capable of representing evolving flow sections in a duct. The fair use of this module justifies certain simplifying assumptions in the resolution of the conservation equations. For instance, in this elements the axial components of the viscous stress tensor and the work are neglected, as well as the axial heat conduction and the mass diffusion.

2. **0-D** module (also called *volume* or *capacity*). This element aims to represent a capacity with connections to other elements. It is designed to model large volumes (especially compared to the diameters of the connections to other elements, with certain thermal-hydraulic assumptions). It is assumed that all thermal-hydraulic parameters are uniform in any horizontal plane, and velocities inside of the module will be much smaller than those in the junctions. Due to these assumptions, any inertial forces are supposed to be negligible inside **0-D** modules compared to gravity forces, such that the momentum equations finds simplified too, resulting in a usual hydrostatic pressure field.

3. **3-D** module. This module allows the modeling of volumes for which no dimension can be rightfully neglected with regard to the values taken by TH quantities. In general, **3-D** modules are used to model the RPV of Pressurized Water Reactors (where 3D

effects can be of interest for the study of accidental transients), as well as any eventual solid structure.

4. **Boundary Conditions**. This module can be set in the extremity of the previously mentioned modules (1-D, 0-D and 3-D), such that they impose specific values to the considered thermal-hydraulic parameters (flows, pressures, temperatures ...). There are two main ways of implementing such restrictions. *CATHARE2* allows the imposition of the boundary conditions as *internal* variables, i.e., they are defined as functions of time and their values evolve during the transient; or as *external* variables, in which case the the variables are constant over time.

3.1.5.3 The submodules of *CATHARE2*

The **submodules** of *CATHARE2* are more specific and allow the modeling of special components of the reactor. In general, **submodules** are elements that are connected to the main modules and usually modify their thermal-hydraulic behavior such that their variables are coupled with those of neighboring common modules. They can be seen as a set of subroutines that influence the aforementioned conservation equations, calculating supplementary equations or terms.

Some examples of **submodules** are: thermal structures, such as walls, heat exchangers, fuel rods etc.; the *reflood* **submodule**, which models the heat exchange between the fuel and the steam-water mixture in certain transients; or certain modelings of the primary pumps, like the one-node pump or the one-node electromagnetic pump.

3.1.5.4 The *CATHARE2* set of equations

The conservation equations used by *CATHARE2* (Bestion, 1990) to compute the physical state of the overall modeled system are presented below for a **1-D** module:

- **Conservation of mass**:

$$\frac{\partial}{\partial t}(A\alpha_k\rho_k) + \frac{\partial}{\partial z}(A\alpha_k\rho_k V_k) = (-1)^k A\Gamma + S_k \tag{3.1}$$

The index k represents the considered phase in the equation ($k = -1$ for the liquid phase and $k = 1$ for the gas), whereas Γ represents the transfer of mass in the interface between the liquid and the gas. The term S_k is an added term that includes any source or sink of mass that may exist in the considered mesh. The term α_k represents the title of the considered phase in the two-phase mixture, i.e., the proportion of steam contained in the steam-water, $\alpha_k = \frac{u_k}{u_k+(-1)^k u_L}$, where u_k is the volume occupied by phase k. The term ρ_k represents the density of the phase k, $\rho_k = \frac{m_k}{u_k}$, where m_k is the mass of the considered phase. We have included here the one-dimensional representation of the mass transfer equation.

- **Conservation of momentum**

$$\begin{aligned} A\alpha_k\rho_k\Big[\frac{\partial V_k}{\partial t}+V_k\frac{\partial V_k}{\partial z}\Big]+A\alpha_k\frac{\partial P}{\partial z}+AP_i\frac{\partial \alpha_k}{\partial z}+\\ +(-1)^k A\beta\alpha(1-\alpha)\rho_m\Big[\frac{\partial V_G}{\partial t}-\frac{\partial V_L}{\partial t}+V_G\frac{\partial V_G}{\partial z}-V_L\frac{\partial V_L}{\partial z}\Big]=\\ =(-1)^k A\Gamma(W_i-V_G)-(-1)^k A\tau_i-\chi_f C_k\frac{\rho_k}{2}V_k|V_k|-\\ -A\frac{K}{2\Delta Z}\alpha_k\rho_k V_k|V_k|+A\alpha_k\rho_k g_z+\frac{R(1-\alpha_k)}{4}P_i\frac{\partial A}{\partial z} \end{aligned} \tag{3.2}$$

In this equation, τ_i represents the stationary component of the interfacial stress between the two phases (this will also be called interfacial friction during the document). β is an added mass term linked to inertial effects, and the terms $P_i\frac{\partial \alpha_k}{\partial z}$ and $P_i\frac{\partial(1-\alpha_k)}{\partial z}$ are due to the heterogeneity of the pressure field in the transverse direction of the interface, especially relevant in stratified flows. $(-1)^k A\Gamma(W_i-V_G)$ is the interfacial momentum transfer, whereas $\Gamma(W_i-u_G)$ is the momentum transfer due to phase change and the generic term $\chi_f C_k\frac{\rho_k}{2}u_k|u_k|$ models the wall friction. Any singular head losses assemble in the term $-\frac{K}{2\Delta Z}\alpha_k\rho_k u_k|u_k|$,and the final terms $\frac{R\alpha_k}{4}P_i\frac{\partial A}{\partial z}$ and $\frac{R(1-\alpha_k)}{4}P_i\frac{\partial A}{\partial z}$ describe the distribution of pressure if the duct is of variable diameter. This term is usually neglected in the case of non-stratified flows (Bestion, 1990). The term $(-1)^k A\tau_i$ represents the interfacial friction. The terms α_k, A, ρ_k have the same meaning as in Equation (3.1).

- **Conservation of energy**

$$\begin{aligned} A\frac{\partial}{\partial t}\Big(\alpha_k\rho_k\Big[H_k+\frac{V_k^2}{2}\Big]\Big)+\frac{\partial}{\partial z}\Big(A\alpha_k\rho_k V_k\Big[H_k+\frac{V_k^2}{2}\Big]\Big)-A\alpha_k\frac{\partial P}{\partial t}=\\ =Aq_{ke}+\chi_c q_{pk}+(-1)^k A\Gamma\Big[H_k+\frac{W_i^2}{2}\Big]+A\alpha_k\rho_k V_k g_z+SE_k \end{aligned} \tag{3.3}$$

The energy equation is written in with respect to the enthalpy instead of internal energy of the system through the terms h_k, specific enthalpies of phase k. There exist several new terms. q_{ke} () represents the thermal exchange between the liquid and gas phases, whereas q_{pk} represents the thermal exchange between each one of the phases and the corresponding walls. Finally,the term SE_k represents any additional energy source that may be taken into account.

3.1.5.5 Running a *CATHARE2* simulation

As explained above, a *CATHARE2* model is defined by adding together modules and sub-modules with appropriate connections, boundary conditions and parameters settings. It is specified by the user in a input file through a dedicated language derived from FORTRAN. Any *CATHARE2* calculation can be divided into two main steps:

1. **Steady State Calculation**. The calculation of any transient with *CATHARE2* requires the previous establishment of a *steady state* which shall serve as *initial state* from which the transient calculation will start. This state acts as the reference from which all thermal-hydraulic variables will have a particular value. In general, *CATHARE2* provides a state that will be *stationary*, i.e., where the variables are the solutions of the conservation equations without the derivative terms.

2. **Transient Calculation**. This phase can be divided into two main subsets. Firstly, the fluid thermal-hydraulic equations are solved for the primary circuit taking into account the connected **submodules**; in the second step, the same equations are solved for the secondary circuit and their °submodules.

The *CATHARE2* simulation engine computes the values of all the physical parameters that characterize the system during the simulation. It implements an iterative algorithm, which includes the following operations at each time step of the numerical resolution scheme:

1. Determination of the system of equations using the conservation equations of mass, momentum and energy for each mesh in all the different **modules** the overall model comprises. This depends on both the physical properties of the liquid and gas phases, and the closure relations between the fluids and surrounding walls.

2. Determination of additional contributions of **submodules** to this system of equations.

3. Resolution of the whole system of equations.

4. Convergence tests for the solution of the system of equations, i.e., the all the determined thermal-hydraulic values for the variables.

If convergence of the thermal-hydraulic values is reached, then *CATHARE* proceeds to the calculation of parameters belonging to the secondary circuit. If this is not the case, then the last iteration is restarted with a modified time step and all the previously explained stages are calculated again. In the next section, we present some elements regarding the subject of global and target sensitivity analysis, which will be an important step in the analysis of transients with *CATHARE2*.

3.2 Sensitivity Analysis

In Chapter 1, we introduced the framework of uncertainty quantification and propagation of uncertainty in computer models, as well as its interest in the particular context of the nuclear industry and nuclear transient simulation. The field has proved its relevance in recent years through the development of numerous tools that have vastly improved the knowledge of the associated uncertainty of complex physical phenomena that are modeled by the Best

Estimate (BE) computer codes. As a reminder, the general mathematical setting that has been retained for our studies is the following:

$$\begin{aligned} \mathcal{X} \subset \mathbb{R}^d \mapsto \mathcal{F}^* \subset \mathcal{F} \\ X \to Z = \mathcal{M}(X) \end{aligned} \tag{3.4}$$

where, following the notation introduced in 2, Z represents the functional random variable that acts as the outputs of the numerical simulator $\mathcal{M}$, whereas $\mathcal{X}$ represents the measurable space to which the input parameters belong. They are the set of input random variables $X = (X_1, ..., X_d)$ of dimension d such that $\mathcal{X} = \prod_{k=1}^{d} \mathcal{X}_k \subset \mathbb{R}^d$, and modeled by the probability density functions. $\mathcal{F}$ represents the functional space to which the outputs belong, usually a Hilbert space of continuous functions, since in general we can consider that the evolution of the physical parameters vary continuously at the observation scale, so in general $\mathcal{F}^*$ will be at least $\mathcal{C}([0, T])$, where T represents the final physical time of the simulation.

Again, following the notation presented in the first chapter, we consider that the outputs of our computer code ($\mathcal{M}$) are functional random variables defined in the probability space $(\Omega, \mathcal{A}, \mathbb{P})$, where $\mathcal{T} \subset \mathbb{R}$ is time domain of definition of the considered functional random variables:

$$Z_1, ..., Z_S : \Omega \times \mathcal{T} \mapsto \mathbb{R} \tag{3.5}$$

where S represents the total number of possible functional outputs, i.e., the possible time-dependent physical variables that constitute the outputs of *CATHARE2*. This way, a realization $Z_s(\omega, t) = z_s(t) : \mathcal{T} \mapsto \mathbb{R}$, with $s \in \{1, ..., S\}$ is a function of time. In nuclear safety studies, these outputs are linked to a safety criterion via a simple mathematical function (for instance, the maximum value of temperature attained during the transient) or another chained computer code.

As it was previously mentioned, these safety criteria are scalar parameters representative of the severity of a nuclear transient, which justify why most of the research effort in the domain has been dedicated to scalar outputs of code. This way, instead of considering the whole functional space of outputs of *CATHARE2*, researchers focus on these scalar outputs of interest $Y \in \mathcal{Y}$, with $\mathcal{Y}$ being the possible set of values of the variable of interest.

Generally speaking, Sensitivity Analysis (SA) techniques serve as tools to quantify *how uncertainty in the output of a model (numerical or otherwise) can be apportioned to different sources of uncertainty in the model input* (Saltelli et al., 2008; Iooss and Lemaître, 2015). The output of the model (which may or not be numerical), Y, is a variable of interest in the considered study. We may classify SA methods into two main families: **Local Sensitivity Analysis (LSA)** and **Global Sensitivity Analysis (GSA)**.

In the first case, LSA focuses on how small variations (usually around their nominal or purposely penalized values) of the values of the input parameters may affect the output

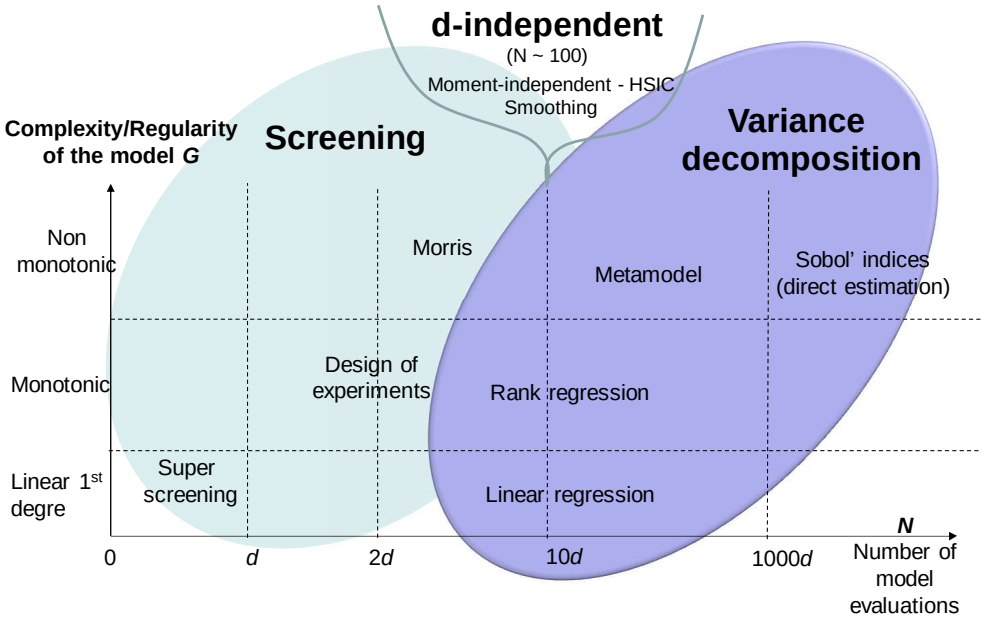

Figure 3.2: Diagram of the main methods available to perform global sensitivity analysis. Taken from Iooss and Saltelli (2017). The showcased *model G* is equivalent to the denoted numerical simulator $\mathcal{M}$ in this document.

quantity of interest. Depending on the nature of the considered model, different approaches can be retained. For instance, in the case where an analytical formulation of the considered model is available, approaches based on adjoint modeling (Cacuci, 1981) can be retained, even in the case of a large number of inputs. In a more industrial setting where the model is treated as a black box, approaches based on *One At a Time* experiments have been developed. In this case, the effect that a single variation of each input has on the output is quantified through individual small variations of the inputs around the nominal values without changing the nominal values of the others. In practice, the variations are made on the partial derivatives of the inputs and outputs, so as to quantify how perturbations of the inputs affect the outputs (Alam et al., 2004).

In numerous real industrial applications, it is necessary to consider the whole domain of variation of the input parameters of the computer model. For instance, in a risk analysis framework, the most penalizing values of the inputs may differ by a large margin from their nominal values, which justifies the interest in GSA.

Figure 3.2 showcases the main families of methods.

In the following sections we will provide the main elements to perform sensitivity analysis, in particular when the analyzed variable of interest is scalar, as well as the main aspects of the issue when the considered data are functional.

3.2.1 Global and Target Sensitivity Analysis

Two main families of methods to perform SA, variance-based methods, and those based on dependence measures will be detailed in this sections. Variance-based ones are included since they constitute one of the main tools available to perform this task, and methods based on dependence measures have already proved their usefulness both in general settings and in the industrial context.

3.2.1.1 Variance-based methods. The Sobol' indices

Quantifying the influence that a set of inputs of a physical model may have on an output of interest may obey to different objectives, such as identifying the most influential inputs on the output uncertainty (**screening**), prioritize the inputs by order of importance or simply fixing the non-influential ones to their nominal values. Since the works of Sobol (1993), variance-based methods have been precious tools in order to analyze complex physical phenomena through numerical simulations.

Saltelli et al. (2008) describes how variance is a legitimate sensitivity measure, and even goes to the extreme of recommending its use whenever the computational cost allows it (this being the main drawback of such methods). Nonetheless, these methods remain independent from the numerical model that is analyzed and their use is allowed in the context of complex black box computer codes.

Sobol' indices (Sobol, 1993) are based on the ANOVA (ANalysis Of VAriance) decomposition of a function (namely, a numerical simulator $\mathcal{M} : \mathbb{R}^d \mapsto \mathbb{R}$) based on the functional decomposition proposed by Hoeffding (1948):

$$\mathcal{M}(x) = Y = \mathcal{M}_0 + \sum_{i=1}^{d} \mathcal{M}_i(x_i) + \sum_{1 \leq i < j < d}^{d} \mathcal{M}_{i,j}(x_i, x_j) + \cdots + \mathcal{M}_{1,\ldots,d}(x) \tag{3.6}$$

which is unique as long as :

$$\int_0^1 \mathcal{M}_{i_1 \ldots i_s}(x_{i_1}, ..., x_{i_s}) dx_{i_k} = 0 \tag{3.7}$$

where $1 \leq k \leq s, \{i_1, ..., i_s\} \subseteq \{1, ..., d\}$, from which we conclude that $\mathcal{M}_0$ is constant, and all the summands in (3.6) are orthogonal. The elements in the form $\mathcal{M}_i : [0, 1] \mapsto \mathbb{R}, i \in \{1, ..., d\}$ are called *main effects* and quantify how the individual variance of one input affects the

variance of the considered output $Y = \mathcal{M}(x)$. On the other hand, the terms in the form $\mathcal{M}_{i,j} : [0,1]^2 \mapsto \mathbb{R}; i,j \in \{1,...,d\}, i \neq j$ are the *second order interactions* or *effects*.

Considering that the input vector $X = (X_1, X_2, ..., X_d)$ is formed by independent random variables, one can express the variance of the output quantity of interest Y as a function of the variance of the inputs and their interactions:

$$\mathrm{Var}(Y) = \sum_{i=1}^{d} \mathrm{Var}(\mathcal{M}_i(x_i)) + \sum_{1\leq i<j\leq d}^{d} \mathrm{Var}(\mathcal{M}_{i,j}(x_i,x_j)) + \cdots + \mathrm{Var}(\mathcal{M}_{1,...,d}(x)) \tag{3.8}$$

The elements of the form $\mathrm{Var}(\mathcal{M}_i(x_i))$ correspond formally to the variance of the conditional expectations of the output Y given x_i, i.e. $\mathrm{Var}[\mathbb{E}(Y|x_i)]$. Analogously, the elements $\mathrm{Var}(\mathcal{M}_{i,j}(x_i,x_j)) = \mathrm{Var}[\mathbb{E}(Y|x_i,x_j)] - \mathrm{Var}[\mathbb{E}(Y|x_i)] - \mathrm{Var}[\mathbb{E}(Y|x_j)]$, as well as for any other interactions. Let $\mathcal{L} = \{1,...,d\}$, and let $\mathcal{P}^{\mathcal{L}}$ denote the powerset (the set of all possible subsets) of $\mathcal{L}$, then:

Definition 3.1
Sobol' Index: The Sobol' index or *variance-based sensitivity index* (Sobol, 1993) associated to $K \in \mathcal{P}^{\mathcal{L}}$ is defined as*:*

$$\begin{aligned} S_K &= \frac{\mathrm{Var}(\mathcal{M}_K(X_K)}{Var(Y)} \\ S_K &= \frac{+\sum_{L\subset K}(-1)^{|K|-|L|}\mathrm{Var}(\mathbb{E}(Y|X_L))}{\mathrm{Var}(Y)} \end{aligned} \tag{3.9}$$

where $|K|$ is the cardinality of K.

Definition 3.2
Order 1 Sobol' Index: Let us consider the singleton $\{l\}$, with $l \in \{1,...,d\}$, then the Sobol' index of order 1 or *main effect* for the input X_l writes:

$$S_l^I = \frac{\mathrm{Var}[\mathbb{E}(Y|X_l)]}{\mathrm{Var}(Y)} \tag{3.10}$$

Definition 3.3
Total Sobol' Index: Let us consider the input parameter X_l of the model $\mathcal{M}$, $l \in \{1,...,d\}$, then the Total Sobol' index or *total effect* for l writes:

$$S_l^T = \frac{\mathbb{E}_{\sim l}[\mathrm{Var}(Y|X_{\sim l})]}{Var(Y)} \tag{3.11}$$

where $\sim l$ represents the set of all inputs of the numerical model $\mathcal{M}$ except the lth input. This

expressions allow to apportion the total variance of Y as a fraction of the variance of each input and their interactions.

Regarding their properties, the Sobol' indices verify:

Proposition 3.1
Let$\mathcal{L} = \{1, ..., d\}$, the Sobol' index S_l verifies*:*

$$\begin{aligned} 0 \leq S_l \leq 1 \\ \sum_{l \in \mathcal{P}^{\mathcal{L}}} S_l = 1 \end{aligned} \tag{3.12}$$

In total, the number of Sobol' indices increases exponentially in a progression of order 2^{d-1} with d, which imposes limitations to the number of indices that are estimated in practice. If d is large, the computational cost of the estimation of the Sobol' indices usually only allows the estimation of the *main effects* and the *total effects* or second order indices.

In practice, if the analytic form of $\mathcal{M}$ is usually unknown, such as in the case of expensive numerical simulators and therefore the estimation of the Sobol' indices relies on the results provided by a design of experiments. Several estimation schemes for the Sobol' indices have been proposed throughout the years. Some relevant methodologies include the *pick-freeze* estimators introduced by Sobol (Sobol, 1993) or Monte-Carlo methods for the first-order indices such as those presented in Monod et al. (2006), and whose asymptotic properties are studied in Janon et al. (2014). Improvements in the definition of the designs of experiments leading to the estimation of the indices through *Random Balance Designs*(RBD) are proposed in Tissot and Prieur (2015). Spectral approaches that allow the estimation of the Sobol' indices at a reduced cost relies on the FAST (Fourier Amplitude Sensitivity Test, Cukier et al. (1978)), which allows the decomposition of the considered computer code into a Fourier basis (if regularity conditions of $\mathcal{M}$ are met). Other alternatives (da Veiga et al., 2021) repose on the use of metamodels, i.e., mathematical approximations of the code $\mathbb{M}$ whose evaluation is cheaper. They allow increasing the size of the designs of experiments and, therefore, better estimations of the indices (albeit they introduce an uncertainty themselves).

3.2.1.2 Sensitivity analysis with dependence measures

The aforementioned limits of more traditional methods to quantify the dependence between random variables has motivated the development of SA techniques more computationally efficient and capable of capturing a wider range of types of dependence. The use of similarity measures between random variables in the context of sensitivity analysis and risk analysis was introduced in Baucells and Borgonovo (2013), where an intuitive framework on the use of dissimilarity measures is proposed. Recalling the previous notation, let us consider a scalar output $Y = \mathcal{M}(X_1, X_2, ..., X_d)$, with $\mathcal{M} : \mathbb{R}^d \mapsto \mathbb{R}$ a continuous numerical simulator, where out objective is to quantify the influence of each input $X_j, j \in \{1, ..., d\}$ on the output Y.

A natural way of quantifying the dependence between X_j and Y is to provide a function capable of measuring the similarity between the distributions of Y and the conditional distribution of the output, i.e., $Y|X_j$. The relationship between these inputs and outputs can be written:

$$S_{X_j} = \mathbb{E}_{X_j}(d(Y, Y|X_j)) \tag{3.13}$$

where $d(\cdot,\cdot)$ represents a similarity measure between the considered variables. More generally, da Veiga, Sébastien (2015) shows how a broad number of common similarity measures between probability measures can be conceived as particular cases of the so called f-divergence (Csiszár, 1967), including the Kullback-Leibler divergence (Kullback and Leibler, 1951) or the Hellinger distance (Hellinger, 1909). They also highlight how there is a link between the f-divergence and other measures coming from the information theory domain, such as the *mutual information* of Shannon (1948).

3.2.1.2.1 The $HSIC$ indices

The research for adequate similarity measures that are tractable from a computer cost point of view, sensitive to a wide range of dependence structures and capable of tackling the *curse of dimensionality* has lead to the consideration of the dependence measure called *distance correlation* or *distance covariance* (Székely et al., 2007) as a tool to construct sensitivity indices. This measure performs well in the context of high-dimensional data (in our case, codes with a large number of inputs, d) and can be seen as a particular case of *characteristic kernels* Sriperumbudur et al. (2010). Amongst these measures, the *Hilbert-Schmidt Independence Criterion* (from now on, $HSIC$) (Gretton et al., 2005) serves as a generalization of the notion of covariance between random variables, which is the reason why a notable amount of work has been developed around them as a sensitivity measure, especially as a suitable competitor to the Sobol' indices in an industrial setting (da Veiga, Sébastien, 2015; de Lozzo and Marrel, 2016a).

The $HSIC$ belong to the family of dependence measures based on *Reproducing Kernel Hilbert Spaces* (RKHS, Aronszajn (1950)). If we consider the random vector $X \in \mathcal{X} = \prod_{j=1}^{d} \mathcal{X}_j$, each X_j having probability distribution P_{X_j}, let us introduce the RKHS $\mathcal{H}_j$ of functions $\mathcal{X}_j \to \mathbb{R}$ with kernel $k_{\mathcal{X}_j}$ and inner product $\langle\cdot,\cdot\rangle_{\mathcal{H}_j}$. Conversely, let us consider a second $RKHS, \mathcal{H}_Y$ of functions $\mathcal{Y} \to \mathbb{R}$ with kernel $k_{\mathcal{Y}}$ associated to $Y \in \mathcal{Y}$ and with distribution P_Y.

Definition 3.4

Cross-covariance operator. The covariance operator $(C_{X_j,Y})$ of the joint distribution of the considered random variables, $P_{X_j,Y}$, is a linear operator between the spaces $\mathcal{H}_j \to \mathcal{H}_Y$ for each function $h_j \in \mathcal{H}_j$ and $h_Y \in \mathcal{H}_Y$ such that:

$$\langle h_j, C_{X_j,Y} h_Y \rangle_{\mathcal{H}_j} = \mathbb{E}_{X_j,Y}[h_j(X_j)h_Y(Y)] - \mathbb{E}_{X_j} h_j(X_j)\mathbb{E}_Y h_Y(Y) \tag{3.14}$$

This is defined as an analogously to the standard notion of covariance through the use of

the *tensor product*:

$$C_{X_j,Y} \coloneqq \mathbb{E}[h_j \otimes h_Y] - \mathbb{E}[h_j] \otimes \mathbb{E}[h_Y] \tag{3.15}$$

The cross-covariance operator generalizes the notion of covariance matrix between random variables (in this case X_j and Y) by making use of nonlinear kernels. The $HSIC$ definition makes use of the notion of the Hilbert-Schmidt norm of the cross-covariance operator (Marrel and Chabridon, 2021):

$$||C||^2_{HS} = \sum_{k,p} \langle u_k, Cv_p \rangle^2_{\mathcal{H}_j} \tag{3.16}$$

where u_k and v_p represent the respective orthonormal bases of the spaces $\mathcal{H}_j$ and $\mathcal{H}_Y$. This notion allows the definition of the $HSIC$ criterion:

Definition 3.5

$$\begin{aligned} HSIC(X_j, Y)_{\mathcal{H}_j,\mathcal{H}_Y} = ||C_{X_j,Y}||^2_{HS} = \mathbb{E}[k_{\mathcal{X}_j}(X_j, X_j^{'}) k_{\mathcal{Y}}(Y, Y^{'})] \\ -\mathbb{E}[k_{\mathcal{X}_j}(X_j, X_j^{'})]\mathbb{E}[k_{\mathcal{Y}}(Y, Y^{'})] - 2\mathbb{E}[\mathbb{E}[k_{\mathcal{X}_j}(X_j, X_j^{'})|X_j]\mathbb{E}[k_{\mathcal{Y}}(Y, Y^{'})|Y]] \end{aligned} \tag{3.17}$$

where all the elements $(X_j^{'}, Y^{'})$ are independently and identically distributed (i.i.d.) copies of (X_j, Y). The main interest of the use of $HSIC$ is that, as long as the considered $RKHS$ spaces are *universal*, i.e., dense within the space of continuous functions with respect to the $||\cdot||_\infty$ norm, the nullity of $HSIC(X_k, Y)$ is equivalent to the independence of the variables (X_j, Y).

Remark 3.1
As it was mentioned, the $HSIC$ serves as a tool to quantify independence between random variables depending on their associated $RKHS$. In practice, the universality condition of the kernels is quite restrictive (for instance, Gaussian kernels are universal only on compact subsets of $\mathbb{R}^d$). To circumvent this problem, weaker assumption may be made over the properties of the kernels that still preserves the condition of independence between (X_j, Y) if and only if $HSIC(X_j, Y) = 0$. From Gretton (2015); Szabo and Sriperumbudur (2018) we see that the condition of universality is not actually required, and that *characteristic kernels* are sufficient to guarantee the desired notion of independence.

Taking this condition into account, the use of Gaussian kernels is common. We recall the expression:

$$k_h(x_1, x_2) = \exp(-\frac{h}{2}||x_1 - x_2||_2^2), \forall (x_1, x_2) \in \mathbb{R}^d \times \mathbb{R}^d \tag{3.18}$$

This expression still relies on the value of h (the *bandwidth parameter*). Although optimal values of h are unknown, since they depend on the joint distribution of (X_j, Y), heuristic approaches exist, as well as estimation methods based on cross-validation methods (Sugiyama and Yamada, 2012), or aggregation tests Meynaoui (2019).

Finally, in the context of global sensitivity analysis, sensitivity indices have been developed based on the aforementioned $HSIC$ measures:

Definition 3.6
HSIC sensitivity indices*(da Veiga, Sébastien, 2015).* For any j in $\{1, ..., d\}$, the sensitivity index that quantifies the influence of the input X_j on the output Y can be expressed by the normalized index*:*

$$R^2_{HSIC,j} = \frac{HSIC(X_j, Y)}{\sqrt{HSIC(X_j, X_j)HSIC(Y, Y)}} \tag{3.19}$$

This index is bounded in the range $[0, 1]$, which allows an easy interpretation of the dependence between each input of the considered computer code $\mathcal{M}$ and the output of interest Y.

The estimation of these indices can be performed through their *plug-in* estimator:

$$\hat{R}^2_{HSIC,k} = \frac{\widehat{HSIC}(X_k, Y)}{\sqrt{\widehat{HSIC}(X_k, X_k)\widehat{HSIC}(Y, Y)}} \tag{3.20}$$

Finally, regarding the estimation of the $HSIC$ indices themselves that appear in Equation (3.20), Gretton et al. (2005) proposes the following estimator when a design of experiments is available:

$$\widehat{HSIC}(X_j, Y) = \frac{1}{n^2} \operatorname{Tr}(L_j H L H) \tag{3.21}$$

where Tr represents the trace of a matrix.

Several elements appear in the equality shown in 3.21. Let us consider the design of experiments $E = \{(X_{i,j}), i \in \{1, ..., n\}, j \in \{1, ..., d\}\}$, with the corresponding outputs $\{(Y_i), i \in \{1, ..., n\}\}$. $H = (\delta_{l,m} - \frac{1}{n})_{1 \leq l,m \leq n}$, where $\delta_{l,m}$ is the Kronecker operator, and the matrices L_j and L correspond to the Gram matrices defined in the following:

$$\begin{aligned} L_j &= (k_{\mathcal{X}_j}(X_{l,j}, X_{m,j}))_{1 \leq l,m \leq n} \\ L &= (k_{\mathcal{Y}}(Y_l, Y_m))_{1 \leq l,m \leq n} \end{aligned} \tag{3.22}$$

3.2.1.2.2 Testing independence through $HSIC$ measures

As it was explained in the previous sections, the $HSIC$ is a dependence measure from which sensitivity indices can be inferred. If used as a ranking tool, the raw indices can serve to rank the influence of every individual input variable of the considered computer code. However, if a cutoff criterion that serves as a decision making tool to separate the set of inputs between influential and non-influential ones is to be defined, a more rigorous approach is necessary.

In this context, the *Statistical Independence Tests* framework is relevant, and provides tools that help quantify the probability of misjudging the influence of each variable on the output, while also serving as screening and ranking tools. Two main cases can be differentiated: First, the case when a large sample (namely, $n \gg 1000$)) of realizations of the inputs and their corresponding outputs is available; and secondly, the case where only a limited sample (in our case, due to the relatively expensive nature of *CATHARE2*).

In any of the cases, several general points can be raised. Firstly, let us consider the input-output vector (X_j, Y), such that the input is characterized by its marginal density p_{X_j} and the outputs by theirs, p_Y. If the joint probability density of the variables can be written as $p_{X_j,Y}$, then testing independence between the considered variables is equivalent to testing that $p_{X_j,Y} \neq p_{X_j} \otimes p_Y$.

Taking this into account it is possible to write the generic test:

$$\begin{aligned} \mathcal{H}_0 &: X_j \text{ and } Y \text{ are independent} \\ \mathcal{H}_1 &: X_j \text{ and } Y \text{ are dependent} \end{aligned} \tag{3.23}$$

where $\mathcal{H}_0$ represents the **null hypothesis** and $\mathcal{H}_1$ is the **alternative hypothesis**. Naturally, the actual densities $p_{X_j}, p_Y, p_{X_j,Y}$ are unknown beforehand in most real applications, and therefore a *test statistic* must be estimated in practice from the available observations. In that case, the $\mathcal{H}_0$ is rejected any time that the statistic belongs to a certain *rejection domain* with a specified probability. More precisely, if an available test statistic $\hat{\tau} = \hat{\tau}\big((X_{1,j}, Y), ..., (X_{n,j}, Y_n)\big), \forall j \in \{1, ..., d\}$ representative of the dependence between (X_j, Y), then a test function Δ can be defined such that:

$$\Delta = \mathbb{1}_{\hat{\tau} > C} \tag{3.24}$$

where C is the critical value from which the dependence (or independence) can be assured with a certain probability. If this is the case $\mathcal{H}_0$ is rejected any time that $\Delta = 1$.

In this case, the independence between the variables can be inferred through the nullity (or lack of) the $HSIC$ measure, such that the test presented in 3.23 is rewritten as:

$$\begin{aligned} \mathcal{H}_0 &: HSIC(X_j, Y) = 0 \\ \mathcal{H}_1 &: HSIC(X_j, Y) > 0 \end{aligned} \tag{3.25}$$

The natural estimator of the statistic of this test would then be $\widehat{HSIC}(X_j, Y)$, such that the null hypothesis is rejected whenever the statistic is sufficiently large. This is equivalent to saying that $\mathcal{H}_0$ is rejected whenever the estimator of the statistic surpasses a specified quantile of its distribution under the null hypothesis.

In practice, if we aim at testing independence between the couple (X_j, Y), the statistic estimator $\hat{\tau}_j = n \times \widehat{HSIC}(X_j, Y)$ is a natural choice, and the aforementioned test can be rewritten in terms of the p-values. The p-value is defined as the probability that the considered test statistic τ_j surpasses the observed value of $\hat{\tau}_j = n \times \widehat{HSIC}(X_j, Y)$, i.e., p-value$= \mathbb{P}_{\mathcal{H}_0}(\tau_j > \hat{\tau}_j)$. If a significance level $\alpha \in [0, 1]$ is chosen, the null hypothesis $\mathcal{H}_0$ is rejected (i.e., there is not sufficient evidence that supports independence between the variables) any time that p-value$< \alpha$.

Having introduced the main elements of independence testing through $HSIC$ measures, two main ways of performing the test are possible depending on the value of n.

Firstly, if n is sufficiently large, it is possible to make use of the **asymptotic framework** in order to estimate the quantile that will serve as threshold of the *acceptance region*, which we will denote q. Gretton et al. (2008) shows how it is possible to approximate the distribution of $\widehat{HSIC}(X, Y)$ under $\mathcal{H}_0$ through a Gamma law, which allows itself the estimation of the desired p-value such that:

$$p\text{-value} \approx 1 - F_\Gamma(n \times \widehat{HSIC}(X_j, Y)) \tag{3.26}$$

where F_Γ is the cumulative distribution function of the Gamma distribution.

Outside of the asymptotic framework, when a more restricted number of observations of (X, Y) is available, the desired quantile may be estimated through **permutation tests** (de Lozzo and Marrel, 2016a). In this case, by making use of the E design of experiments, we can consider $\mathcal{B}$ independent and uniformly distributed permutations of the experiments $(\{1, ..., n\})$, denoted $\{\pi_1, ..., \pi_\mathcal{B}\}$, such that every individual permuted sample is written E^{π_b}. In this case, the test statistic is:

$$\hat{\mathcal{P}}^b = \widehat{HSIC}(E^{\pi_b}), b \in \{1, ..., \mathcal{B}\} \tag{3.27}$$

All the variables $\hat{\mathcal{P}}^b$ have the same original distribution as the $HSIC$ estimator as long as the null hypothesis is acceptable. If this is true, the searched quantile q may be estimated by $\hat{q}$ (with a significance level α) defined as the same quantile of the order statistic of $\hat{\mathcal{P}}^1, ..., \hat{\mathcal{P}}^\mathcal{B}$, or:

$$\hat{q} = \hat{\mathcal{P}}^{\lceil \mathcal{B}(1-\alpha) \rceil} \tag{3.28}$$

Finally, the p-value of the test may be calculated through the expression:

$$p\text{-value} = \frac{1}{\mathcal{B}} \sum_{b=1}^{\mathcal{B}} \mathbb{1}_{\hat{p}^b > \widehat{HSIC}(X_j, Y)} \tag{3.29}$$

There exist further examples of tests of independence through $HSIC$ measures, both in the asymptotic and permutation-based frameworks. In particular, we can mention the works of Meynaoui (2019), where a novel version of the permutations tests is developed such that the level of the test α may be controlled.

3.2.1.2.3 Target Sensitivity Analysis

As it was stated before, the main objective of global sensitivity analysis (as introduced in section 3.2) is to quantify the influence of the inputs of a model onto its output in its whole variation domain (Iooss and Lemaître, 2015)). It is however logical in certain contexts (such as risk analysis) to focus the interest on the influence of said inputs the **occurrence** of specific subsets of the set of possible values of the output. In other words, given the aforementioned set of inputs and outputs (X, Y), with $Y \in \mathcal{Y} \subset \mathbb{R}^d$, one may want to quantify how each individual input X_j affects the probability that the output Y takes values on a specific subset of values $\mathcal{Y}' \subset \mathcal{Y}$.

Generally speaking, this domain is usually referred to as **Target Sensitivity Analysis** (TSA), as opposed to GSA. The strict term of TSA is indeed recent Marrel and Chabridon (2021), but similar work has been performed in other fields, such as environmental science (Spear and Hornberger, 1980), reliability engineering (in particular, structure reliability engineering) such as in Au and Beck (2001); Lemaître (2014); Perrin and Defaux (2019) or in the so called *Quantile-oriented* sensitivity analysis (Fort et al., 2016).

In practice, TSA can be achieved for scalar random variables through indicator functions that allow to transform the output of the considered model to restrict its values to the considered subset of interest (following the previous notation, we could call this subset $\mathcal{Y}' \subset \mathcal{Y}$). To be precise, it is possible to extend the notions presented in the previous sections to the couple $(X, \mathbb{1}_{Y \in \mathcal{Y}'} \cdot Y)$.

This approach, although feasible, presents some major disadvantages, especially in the case where the analyzed model (in our case, $\mathcal{M}$) is expensive and the total simulations budget is limited. For instance, the total available information is not totally exploited when this approach is retained. Indeed, the values of Y close to the domain of interest $\mathcal{Y}'$ can very well be informative of the process that is studied, in particular when the output of interest is represented by a physical variable that may vary continuously. As an example, if we focus on a nuclear transient application and we are interested in analyzing the critical values of temperature of the fuel over a particular threshold, then the simulations that lead to temperatures close to said threshold can also be of use in an eventual analysis methodology of the associated phenomena.

In order to overcome this issue, Marrel and Chabridon (2021) propose to use a transformation that provides a smoother threshold of the frontier of the considered subset of interest

$\mathcal{Y}'$. They propose the use of the weight function:

$$w_{\mathcal{Y}'}(Y) = \exp\Big(-\frac{\max(\hat{q}_{1-\alpha} - Y, 0)}{s\hat{\sigma}_Y}\Big) \tag{3.30}$$

where s represents a tuning parameter that represents the smoothness of the function (which regulates how much close values of Y to $\mathcal{Y}'$ will be taken into account for TSA purposes), and $\hat{\sigma}_Y$ is the estimated standard deviation of the output of interest from the available sample of size N. $\hat{q}_{1-\alpha}$ is an estimator of the empirical α quantile of the distribution of Y. The use of the empirical quantile $\hat{q}_{1-\alpha}$ comes from the fact that the proposed methodology is guided by a nuclear safety application, in which the region of interest $\mathcal{Y}'$ is characterized by the higher values of the safety parameter (The maximum cladding temperature of the fuel attained during the transient).

Finally, consistent estimators for sensitivity indices based on both the Sobol' indices (see 3.2) and the $HSIC$ indices (see 3.2.1.2.1) are proposed in Marrel and Chabridon (2021) based on the weight function $w_{\mathcal{Y}'}(\cdot)$ through the study of the couple $(X_j, w_{\mathcal{Y}'}(Y))$.

The first-order Sobol' indices in the proposed TSA framework take the form:

$$S_{T,w}(X_j, Y) = \frac{\mathrm{Var}[\mathbb{E}[w_{\mathcal{Y}'}(Y)|X_j]]}{\mathrm{Var}[w_{\mathcal{Y}'}(Y)]} \tag{3.31}$$

whereas the target $HSIC$ sensitivity indices (expressed both in terms of the $HSIC$ indices themselves or the associated R^2_{HSIC} from 3.20) can be written:

$$\begin{aligned} HSIC_{T,w_{\mathcal{Y}'}}(X_j, Y) &= HSIC(X_j, w_{\mathcal{Y}'}(Y)) \\ R^2_{HSIC,w_{\mathcal{Y}'}} &= \frac{HSIC(X_j, w_{\mathcal{Y}'}(Y))}{\sqrt{HSIC(X_j, X_j)HSIC(w_{\mathcal{Y}'}(Y), w_{\mathcal{Y}'}(Y))}} \end{aligned} \tag{3.32}$$

3.2.2 Sensitivity analysis with functional outputs

Although we do not aim at making an extensive review of methodologies of sensitivity analysis in the framework of the study of functional data, since the works presented in this manuscript are largely motivated by the study of these mathematical objects, it is worth mentioning some of the most recent and notable works regarding this domain.

The domain of sensitivity analysis, and in particular, of global sensitivity analysis, is quite recent when it comes to functional data Hsieh and Huang (2021). As we have seen, most of the development in the domain of functional data analysis was done from the 1980s (Ramsay, 1982), and the SA domain is also relatively recent.

Let us consider a similar model from the one presented previously, but which provides functional outputs in a finite grid of points: $Y = \mathcal{M}(X), (X, Y) \in \mathcal{X} \times \mathcal{Y}, \mathcal{X} \subset \mathbb{R}^d, \mathcal{Y} \subset \mathbb{R}^q$. If this is the case, two natural families of methods can be mentioned: those which rely on the estimation of sensitivity indices between the input variables of the model and each point in the multivariate output grid; and those which rely on projections of the data into lower-dimensional spaces such that GSA indices may be obtained between the inputs and an appropriate set of features. We speak then of *ubiquitous* or *aggregated* sensitivity indices (da Veiga et al., 2021) (these are sometimes referred to as *point* and *block* sensitivity indices de Lozzo and Marrel (2016b)).

The first approach presents relevant disadvantages when it comes to GSA. Amongst them, we can mention: the computational cost of estimating sensitivity indices for each point in the considered grid; the redundancies in the information that may be extracted from sensitivity indices calculated in adjacent of close points; the loss of information as a consequence of not taking into account the underlying dependence structure of the functional data when they are considered as an output multivariate object without dependence between its elements.

This is the reason why most methodologies rely on functional decompositions of the outputs of the code onto a predefined basis (namely, the mentioned wavelet basis, the Fourier basis, or the Principal Components one mentioned in Chapter 2).

One of the first mentions to this field can be traced back to the works of Yamanishi and Tanaka (2005), in which rather than investigating the impact of input parameters into the output distribution of functional data, they focus on the influence of specific individuals of the population on the chosen coefficients of the basis. The first real mention to the SA domain in computer simulations where the outputs are functions can be found, to the best of our knowledge, in Campbell et al. (2006), where the authors apply GSA techniques between the inputs of their numerical model and the coefficients of a functional PCA basis. Other works that improve upon the same notions are those of Lamboni et al. (2011), and Wicaksono et al. (2015); Perret et al. (2019), where FDA techniques such as landmark registration are applied as a previous step of GSA on the first components of the PCA. da Veiga, Sébastien (2015) also proposes an adaptation for GSA making use of dependence measures by applying semi-metrics to functional data such as those presented in Ferraty and Vieu (2006). This approach is challenging nonetheless, since the universality of the kernels associated to said semi-metrics cannot be guaranteed, which as it was mentioned in Section 3.2.1.2.1 is a necessary (and sufficient) condition of independence.

Other authors propose extensions to the more *classical* variance-based methodologies. For instance, Gamboa et al. (2014) present a rigorous extension of the Sobol' sensitivity indices for multivariate and functional outputs. In de Lozzo and Marrel (2016b), the authors showcase several sensitivity indices adapted to multivariate (spatial) outputs, making use of both the Sobol' indices and the $HSIC$ measures.

Several graphical techniques have also been successfully applied in the context of SA for functional data (Ribés et al., 2020), while Francom et al. (2018) make use of the bayesian framework in order perform this task on one dimensional functional data.

Finally, Hsieh and Huang (2021) made use of the concept of *influence functions* in order to quantify the impact of variations of the inputs of a numerical model into the cumulative distribution of a scalar outputs of interest. In their case, they apply this notion to the functional PCA coefficients of the analyzed curves.

3.3 Methodology for nuclear transient simulations

In this section we propose a methodology of analysis of nuclear transients through the code *CATHARE2*. Making use of the notation presented in Chapter 2, we consider the numerical simulator (representing the code *CATHARE2*) $\mathcal{M}$ in (3.4), that we reproduce here:

$$\begin{aligned} \mathcal{X} \subset \mathbb{R}^d &\mapsto \mathcal{F}^* \subset \mathcal{F} \\ X &\to Z_s = \mathcal{M}(X) \end{aligned} \tag{3.33}$$

We consider that the input space of parameters $\mathcal{X}$ is formed by the product of the individual spaces of each independent input parameter of the computer code $\mathcal{X} = \prod_{k=1}^{d} \mathcal{X}_k$. The condition of independence comes from the fact that the input parameters of the code can each be sampled from independent one dimensional probability density functions, which is not always the case in industrial simulation experiments. The outputs of the code consist of one dimensional functions $\mathcal{F}^*$ living in $\mathcal{C}([0,T])$, where T is the total physical time of simulation. Depending on the analyzed nuclear transient, T can differ by several orders of magnitude, from minutes to several hours. These functional output are represented by functional random variables in the considered probability space of 3.2, such that:

$$Z_1, ..., Z_S : \Omega \times \mathcal{T} \mapsto \mathbb{R} \tag{3.34}$$

In this expression, all the realizations $Z_s(\omega, t), s \in \{1, ..., S\}$ (whose notation is simplified to $Z_s(t)$ to express our outputs only as time-dependent functions) correspond to all the possible outputs of interest provided by the code *CATHARE2*. There are numerous possibilities to the outputs that the code can provide, but frequently these are limited by the actual parameters of interest for nuclear safety. Examples of these output variables can be: Maximum cladding temperatures of the nuclear fuel, cold water injection flows from the safety injection system, swollen level of water in the nuclear core etc. An example of these outputs is provided in Figures 3.3 and 3.4.

As it was introduced in Chapter 1, the main objective of these works is to be able to provide insights and interpretations between the mathematical and statistical analysis of the input/output chain of a nuclear accidental transient modeled with *CATHARE2* and the phenomena that impacts the most nuclear safety. In order to achieve this objective, we have developed a methodology consisting of different steps that allow a synthetic interpretation of

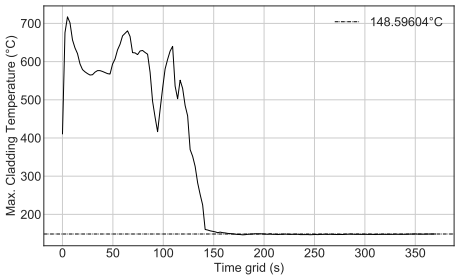

Figure 3.3: Example of the evolution of the PCT in a nuclear transient

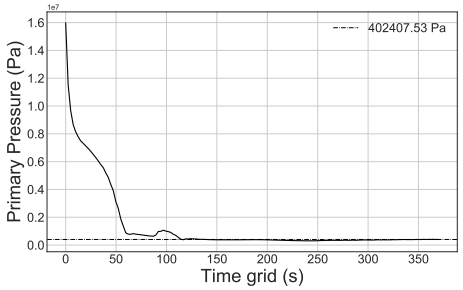

Figure 3.4: Example of the evolution of the primary pressure in a nuclear transient

the outlying simulations of a specific sample of experiments. The methodology is synthetically presented in Figure 3.5.

As it can be seen in Figure 3.5, the methodology may be divided into 4 main parts, which will be further detailed in the subsequent sections. They are:

1. Definition of relevant physical parameters and *breakpoint* events in the analyzed transient.
2. Design of experiments and calculation of the outlying scores θ for each individual functional output in the considered design.
3. Global and Target sensitivity analysis between the inputs and θ.
4. Statistical and graphical analysis between the inlying and outlying samples of inputs variables and intermediate parameters.

3.3.1 Definition of relevant physical parameters

This stage aims at producing a set of relevant outputs from *CATHARE2*, a set of intermediate parameters and a set of breakpoint events that allow a systematic study of the analyzed transient. First of all, let us define these notions; these terms will be consistently mentioned along the manuscript and always make reference to the same notions.

Definition 3.7
CATHARE modeling. *This makes reference to a specific set of modules and submodules (3.1) with their corresponding boundary, scenario and initial conditions that allow the simulation of a particular nuclear accidental transient.*

Definition 3.8
Output of interest. *They consist of the subset of outputs provided by* CATHARE2 *that are relevant to the global progress of the analyzed nuclear transient.*

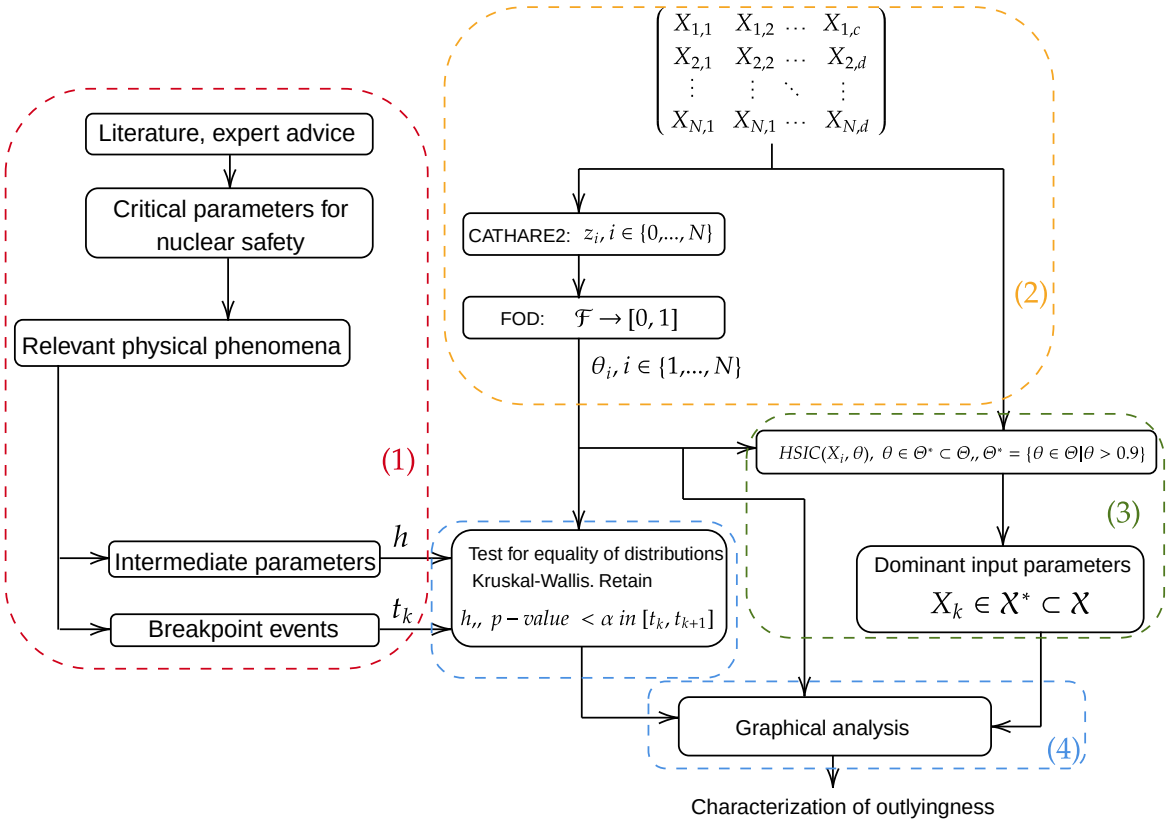

Figure 3.5: Synthetic diagram of the physical analysis methodology of outlying transients with *CATHARE2*.

The variety of possible outputs provided by the code is considerable. One could imagine hundreds of possible physical variables along all the meshes of the specific *CATHARE modeling*, such as temperatures, pressures, void fractions etc. In an in-depth analysis of the unfolding of the transient, it is necessary to identify which time-dependent outputs are relevant to the phenomenology of interest.

Definition 3.9

Intermediate Parameter. *Let $h : \mathcal{F}_s^* \mapsto \mathcal{R} \subset \mathbb{R}$ be an injective application between the functional space of interest of one considered output of the code and $\mathcal{R}$, a real-valued compact subset of possible physical values of Z_s. Then, $h(\cdot)$ is called* ***Intermediate Parameter*** *of the functional output Z_s.*

As an example, $h(\cdot)$ could be $h(z_s) = \max(z_s)$, such that the intermediate parameter would be the maximum value amongst the possible set of values of a particular output of interest. In this example, this could for instance be the maximum of the cladding temperature of the nuclear fuel in a certain time interval of the transient.

Definition 3.10

Breakpoint event. *Event occurring in a specific moment* $t_\tau \in [0, T]$ *susceptible of having a major impact on the progress of the nuclear transient.*

What constitutes a major impact on the progress of the transient is obviously a subjective notion. In practice, the selection of these breakpoint events is chosen on the basis of expert judgement of the specific nuclear transient, previous studies performed on the same or similar *CATHARE modeling*, or simply taking into account the activation of any system classified as relevant for nuclear safety (IAEA, 2014).

All in all, there are three main outputs in this stage that will be used afterwards. Firstly, this study must provide the set of functional outputs of interest, and especially those more closely related to nuclear safety, and on which the FOD methodology shall be applied so as to detect the searched anomalous behavior. The second is the set of intermediate variables which will serve as auxiliary parameters in the physical analysis. Finally, the set of breakpoint events $t_k, k \in \{1, ..., K\}$ is also obtained.

3.3.2 Design experiments and functional outlier detection

The objectives of this stage are: i) to produce design of experiments E presented in 3.2.1.2.1 that will be used along the whole physical study of the considered transient; ii) to launch the simulations corresponding to the considered design of experiments E presented in 3.2; iii) to calculate the outlyingness score $\theta_i \in [0, 1] \forall i \in \{1, ..., N\}$ of the functional outputs of interest.

In the following paragraphs of the section we will focus on stage i). This is because ii) consists in handling the *CATHARE2* simulations launching in High Performance Computing (HPC) systems, which, although crucial in the generation of the data for this Ph.D. and which required considerable effort, is of no specific interest here; iii) the Functional Outlier Detection methodology that has been used here has been extensively explained in Chapter 2.

We present below two common sampling strategies for scalar random variables, which constitute the inputs of our numerical simulator.

Let us assume that we have d input parameters of our computer code whose values may be sampled from an *a priori* defined probability density functions $(p_{X_j}, j \in \{1, ..., d\})$ that verify independence between them, i.e., $p_{X_1, X_2, ..., X_d} = p_{X_1} p_{X_2} \cdots p_{X_d}$. As a general rule, these laws will be bounded so as to guarantee that the variables always vary in the desired domain.

Without loss of generality, let us consider a unitary hypercube that constitutes the sampling space of the input variables $[0, 1]^d$. The main objective here is to produce a sample of points in this space (a design of experiments) that has minimal size but is nonetheless capable of capturing the desired information of the output of interest. In da Veiga et al. (2021), the authors mention the most important properties of a design of experiments. Firstly, the space-filling properties in the d-dimensional space, both upon criteria regarding the uniformity of the distribution of points and the geometrical distance between them. A second requirement

is related to the same properties but in the lower dimensional subprojection spaces. This is necessary in order to capture potential interactions between the considered variables.

Among the existing methods, we can mention Standard Random Sampling strategies, i.e., Monte Carlo (Lemieux, 2009) ones. These algorithms search to randomly sample values from a considered distribution without establishing filling criteria for the considered space through (pseudo)random number generator algorithms. There exist several well established algorithms to achieve this goal, among which we can mention: Random number generators, Direct Sampling, Rejection Sampling or Importance Sampling Bishop (2006). Other sampling strategies have been developed in the same framework, such as Markov Chain Monte Carlo (MCMC) algorithms. Besides their simplicity one of the main advantages of Monte Carlo (MC) algorithms is that they also provide the convergence rates of estimated quantities of the outputs of the computer code (Lemieux, 2009), whose rate is $(\frac{1}{\sqrt{n}})$. If d is large, these rates can prove to be too slow and require an intractable amount of simulations (depending on the computational cost of the considered simulator). An improvement of the method is the use of Latin Hypercube designs, which guarantee a better coverage of the d-dimensional space, offering a better chance of no undersampling certain regions of the space.

The second main strategy is to follow space-filling designs that look to optimally (in the sense of a specific predefined criterion) sample the considered hypercube so as to guarantee an exploration as efficient as possible. In particular, we focus here on the so-called Latin Hypercubes Sampling (LHS from now on). Introduced by Mckay et al. (1979), these sampling strategy aim at providing a good exploration of the domain of each input variable of the computer code (taking into account their probability density functions).

In practice, in order to generate the basic version of a LHS, the generic $[0, 1]$ domain of each variable is divided into a number N of equally sized (probable) intervals: $\mathcal{I}_\nu = (\frac{\nu-1}{N}, \frac{\nu}{N}), \nu \in \{1, ..., N\}$. Let us also define d permutations π_j of the set $\{1, ..., N\}$ that will be randomly chosen such that the jth component x_j^l of the lth draw from the LHS can be obtained by randomly chosen vales of the domain partition $\mathcal{I}_{\pi_j^l}$ (Damblin et al., 2013).

Finally, since this basic form of LHS designs cannot ensure that the target input space will be appropriately sampled (Iooss et al., 2010), there exist optimized versions of the LHS sampling (Damblin et al., 2013) that will be presented when used in this manuscript.

To conclude this stage of the methodology, once an appropriate design of experiments has been sampled, the *CATHARE2* simulations will be launched and the corresponding outlyingness score θ_i of each simulations are estimated following the methodology presented in Chapter 2.

3.3.3 Target sensitivity analysis

In this section, Target sensitivity analysis through $HSIC$ measures based on permutation tests (de Lozzo and Marrel, 2016a) will be applied between the input variables in the design of experiments $(X_{i,j}), j \in \{1, ..., d\}; i \in \{1, ..., n\}$ and the corresponding values θ_i of each func-

tional output that corresponds to every input in the design of experiments. These measures are retained instead of more classical variance-based sensitivity indices such as the Sobol' indices 3.2 (Gamboa et al., 2014) since they are capable of capturing the dependence between the inputs and the scalar output of interest (in this case, θ_i) even when the total number of runs of *CATHARE2* is very limited.

This analysis will provide a set of inputs variables that present a quantifiable dependence with the outlyingness score, and that can be rightfully associated with anomalous or atypical behavior (in the sense of θ) in the outputs of the simulations.

3.3.4 Comparison between inlying and outlying samples

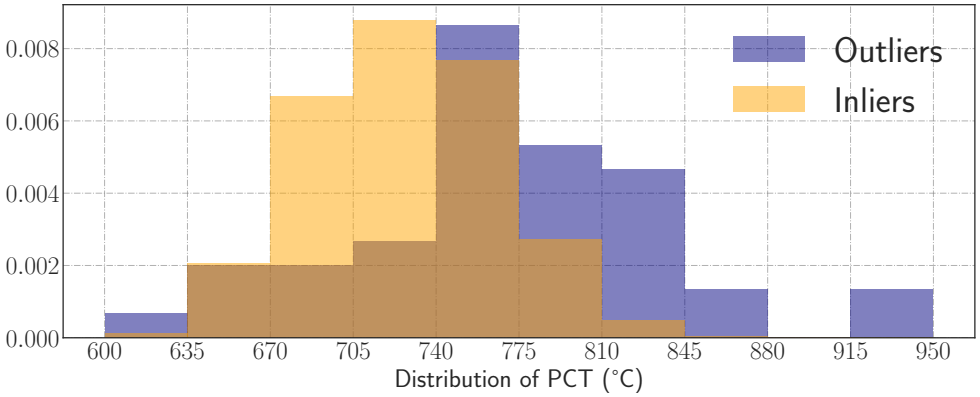

Figure 3.6: Differences of distributions between the inlying and outlying sample of PCT for a LOCA case.

Once all the aforementioned parameters are obtained, and three types of analysis are performed via several comparison techniques which, in essence, consist in comparing the distributions of the considered parameters between the inlying sample and the outlying one. The main objective of this final stage is the extensive characterization of the outlyingness and the detection of possible non-physical values or trends amongst the variables. Several comparison techniques (two graphical and one analytical) will be used.

1. For each considered subdomain $[t_k, t_{k+1}]$, compare the distributions of the samples of intermediate parameters through the Kruskal-Wallis test (See detailed explanation on Annex A). This step allows the detection of the most relevant time frames of the nuclear transient that explain the differences between the inlying and outlying samples. It is also useful in order to quantify which physical events present a higher impact on the progress of the transient.

2. Scatter plots between the relevant input parameters and the intermediate ones, showcasing the bivariate domain which present higher probabilities of being associated to outlying simulations. This provides considerable insight about the interactions between

the considered physical parameters and most of all, it allows the comparison of the trends of the inlying and outlying samples. If those two trends present opposing tendencies, it can be interpreted as considerable evidence for the existence of non-physical values in the simulations.

3. Graphical comparisons between the distributions of influential input variables and intermediate parameters in each considered time subdomain. This can be done through the use of classical histograms or violin plots (See Annex B or C). This is an important step in order to identify the subsets of values of the input variables that actually lead to the generation of outlying transients, which is closely linked to the physical phenomena that take place in said simulations.

3.4 Conclusions

This Chapter has been dedicated to the presentation of the main tool of nuclear transient analysis that has directed these Ph.D. works, the code *CATHARE2*. Firstly, we introduced the basic elements that constitute a Nuclear Power Plant (in particular, a Pressurized Water Reactor) and how its most important elements can be modeled through the already existing modules and submodules of *CATHARE2*. We also presented the basic workflow of the code and how steady-state calculations are achieved in order to solve the balance thermal-hydraulic equations of mass, momentum and energy amongst the possible meshes and modules of the code. We also mentioned how this code has been successfully used in industrial contexts in order to validate its calculations when compared to real experiments, and how can be used in uncertainty quantification contexts as a physical analysis tool.

Secondly, we introduced the domain of sensitivity analysis in simulation codes. This is a wide domain but we provided the essential notions that allow the quantification of the influence that specific sets of inputs have over a desired output of the considered code. We provided a systematic classification of the main methods that are used nowadays in the SA domain, in particular in what concerns the analysis of nuclear transients, mentioning their advantages and disadvantages, in order to justify the choice of methods that have been used in our context.

Finally, we provided a methodological analysis technique of nuclear transients aiming at increasing the comprehension of the physical phenomena that intervene during the simulation of accidental nuclear transients through black-box simulators. The methodology can be separated into four main stages that help characterize the outlyingness of specific sets of output simulations so as to provide an interpretation for them. This serves as a complement physical analysis tool that can also be useful in validation settings.

In the following chapters we shall showcase how the application of this methodology has been useful in real industrial applications.

4

Application of a Loss of Coolant Accident

Contents

In this chapter we will detail the main application that has directed the works presented in this manuscript. The application belongs to the domain of nuclear transient simulation. We focus here on accidental transients in NPP that result in an industrial risk for the system.

In particular, the analyzed transient belongs to one of the main failure modes of accidental nuclear transients, the Loss of Coolant Accident (LOCA). In this transient, a break in the primary system of the NPP decreases the amount of total coolant in the system, which hinders the evacuation of the thermal power produced by the nuclear core. This process can result in the fusion of the nuclear fuel, which characterizes a *severe* accident, if no countermeasures take place.

The chapter is divided as follows: firstly, we shall describe the generalities of the use-case, detailing the *CATHARE2* modeling of the transient, as well as the expected inputs and functional outputs of the code. Secondly, we will apply the generic methodology of analysis explained in the previous chapters, provide an interpretation of the results and an explanation for the existence of outliers in the simulation results. We will finish with the conclusions.

4.1 Presentation of the use-case

In this section we provide a detailed description of the analyzed transient, the main components of the NPP, its influence, the progress of the transient, as well as the main physical phenomena of interest and their modeling made with *CATHARE2*.

4.1.1 The Loss of Coolant Accident (LOCA)

The considered NPP is a Pressurized Water Reactor (PWR) of 900MW of nominal electrical power. In a general sense, a LOCA is defined as an accident in which some point of the primary system of PWR loses its integrity, most commonly due to a break in its piping. The main consequences (Tarride, 2013) of this event are: i) a mechanical stress on the internal structures of the Reactor Pressure Vessel (RPV), on the components of the primary circuit and support structures of its elements; ii) mechanical and thermal effects on the containment building ; iii) radiation consequences inside the building, and potentially to the environment and people in severe cases.

Generally speaking, a LOCA transient is caused by the apparition of a break in the primary circuit that provokes the depressurization of the primary through a loss of water (the coolant) inventory that cannot be compensated by the Chemical and Volume Control System (CVCS), which usually controls all the parameters linked to the state of the coolant in the primary circuit (chemical concentration of elements, total mass, level of water...). If this happens, the

reactor is automatically shutdown, the turbine is isolated from the Steam Generators (SG) and the Emergency FeedWater System (EFWS) guarantees the flow of coolant to the SG. The loss of coolant at the break must be compensated by the Safety Injection System (SIS) of the NPP so as to avoid an excessive increase in fuel temperature.

The actual effects of a LOCA transient on an NPP depend largely on the characteristics of the considered transient, such as the size of the break, the number of loops of the primary circuit, the nominal power of the NPP, or the available safety systems for instance.

In our particular use-case (provided by the EDF engineering division so as to penalize the consequences of the accident) the transient is characterized by the parameters presented in Table 4.1.

Table 4.1: Basic characteristics of the considered LOCA scenario.

Characteristic of scenario	**Physical value**
Break size	$15.4'' = 39.1$ cm
Location of break	Cold leg
Penalizing hypothesis	Loss Of Offsite Power (LOOP)
Aggravated scenario	Loss of Emergency Diesel Generators (EDG)

The break size corresponds to the equivalent diameter of the break (diameter of the circular break). Comparatively, the diameter of the corresponding cold leg is 89.46cm, allowing a section of passage of 6285.61cm^2 for the coolant. Regarding the position of the break, it is located between the annular collector and the safety injection system on a cold leg. This configuration is penalizing for water reactors with the safety injection system located in the cold leg (much of the cooling water from the SIS is lost at the beak before cooling the core). The LOOP (Table 4.1) implies the loss of redundant systems implicated in nuclear safety. This loss is partially or completely compensated by the EDG, which is the reason why the loss of one of diesel generators constitutes an aggravating factor.

The break size corresponds to an *intermediate break* according to Tarride (2013), although historically these breaks have sometimes been considered as *large* ones (U.S. Department of Energy, 1975). In practice, a break of 39cm of diameter in this specific NPP presents physical characteristics of both an intermediate and large break. On a side note, the consideration of the aggravated scenario in safety studies has lead to the implementation of redundancies (at least two independent trains for each one of them), where each one must be capable of ensuring the water injection individually and through independent activation and management systems, so as to avoid the possibility of a *Common Cause Failure (CCF)*, i.e., an event that may lead to the failure of all the redundancies of an ISS (Important System for Safety).

The management of this accidental transient requires the use of several specific systems important for nuclear safety. They are detailed in the following section.

4.1.1.1 Important systems for nuclear safety (in LOCA transients)

The main safety systems of protection and safeguards of a NPP are deemed *Important Systems for Safety (ISS)*, and constitute one the main lines of defense in the event of an accidental transient. They intervene automatically and their role is to lead the reactor to a safe state from the beginning of the transient, or at least to a manageable state by the operators of the NPP.

For these systems, the Single Failure Criterion (SFC) is applied. It means that these systems must remain available in the event of a nuclear transient even if one of its individual components fails to work. These failures can be *active* (e.g., a pump failure) or *passive* (e.g., a primary break).

There are several systems in the NPP susceptible of being relevant (intervene) during the nuclear transient. They are:

- **Automatic shutdown of the reactor (reactor trip)**. The system in charge of stopping the fission reactions in the core. It is formed by neutron absorbing control rods that are passively (without the need of external electric power) inserted into the core. It activates on the Low Pressure (LP) signal of the pressurizer.
- **Automatic shutdown of the primary reactor coolant pumps**. The pumps automatically stop if the LOOP hypothesis is considered.
- **Emergency Core Cooling System (ECCS)**. This system is charged with guaranteeing the cooling of the core if the primary pressure falls below a certain threshold. It consists of a high pressure train system, a low pressure one, and a set of accumulators. The latter are reservoirs of water with a discharge line that injects directly into the boiler.
- **The electrical components that allow the isolation of the SG**.
- **Aspersion system**. Its main function is to lower the pressure and temperature of the containment building in the case of an abnormal increase (such as in an accidental transient).
- **Emergency feedWater system of the SG**. Its role is to guarantee the flow of liquid water to the SG, which continues to evacuate the residual thermal power of the core. Including the LOOP assumption, one motopump and turbopump are available. The former activates on the signal of the activation of the ECCS, and the latter only intervenes on the Very Low Level (VLL) signal of the SG.
- **The steam generators relief valves**. They open if the pressure inside the SG reaches a certain pressure once they are isolated from the turbine. They ensure a minimal mass flow of 362 t/h, and their set pressure is taken as 77.6 bar.
- **Steam bypass system of the turbine to the atmosphere**. Its role is to evacuate the steam contained in the secondary circuit to the atmosphere, both in normal operation

conditions, incidental and in accidental ones. They ensure a minimal mass flow of 195 t/h at 70.3 bar. They open automatically if the pressure decreases below 72.7 bar.

- **Relief lines (pressurizer)**. They are formed by three tandems of relief valves, of which only one is available in the LOOP scenario.
- **Emergency Diesel Generators (EDG)**. Only one of the two is available in the assumed scenario. In order to further penalize the scenario, it is considered that the lost diesel is the one that leads to the loss of 2 out of 3 relief lines of the pressurizer.

4.1.1.2 Phases of the transient

An Intermediate Break LOCA (from now on, IBLOCA) transient with the intermediate break located in the cold leg of the primary of a PWR with instantaneous shutdown of the primary pumps due to a LOOP assumption could be decomposed into five main phases, which are summarized in Table 4.2.

Table 4.2: Main phases of the IBLOCA transient.

Phase	Description
I	Single-phase depressurization of the primary circuit
II	Void formation and stratification
III	Drop of water level due to differences of static pressure effects
IV	Drop of water level due to the loss of water inventory
V	Injection of water by the accumulators and reflood

In intermediate breaks of large size, or in large breaks, the duration of phases II and III is reduced in favor of phases IV and V. A brief description of these phases is provided below:

- **Phase I**: Single-phase depressurization. It is expected to last only several seconds in the case of large intermediate breaks. Signals for the ECCS and automatic shutdown of the core are sent during this phase. It lasts until the saturation conditions are reached in the primary circuit, which are governed by the single-phase flow at the break, i.e., the loss of coolant mass entails a fast decrease in the primary pressure. During this phase, the cooling of the fuel is guaranteed by the (still) single-phase coolant, or two-phase with very low void fraction ($\alpha = \frac{u_G}{u_{\text{Total}}} = \frac{u_G}{u_G+u_L}$, where u_G and u_L represent the volumes occupied by the gas and liquid phases in a considered component, respectively). For large breaks, the vaporization may begin even before the automatic shutdown.
- **Phase II**: Void formation and stratification. For the small or intermediate breaks, the generation of steam slows the depressurization of the primary circuit, and all the residual power that cannot be evacuated through the break is evacuated thanks to the SG. The

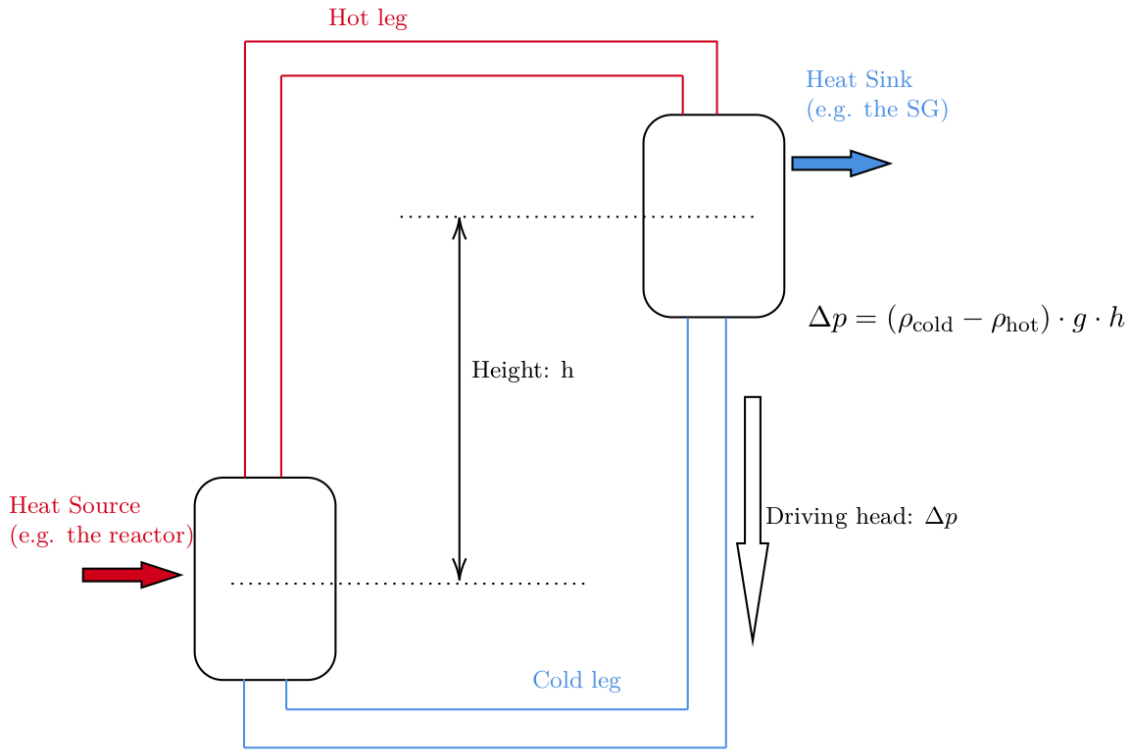

Figure 4.1: Example of a closed loop in which natural circulation may be created. In this case, the heat sink would correspond to the SG, whereas the heat source is the nuclear core, so the closed loop is composed by the elements in the boiler. ρ_{cold}: average density of the fluid in the cold leg; ρ_{hot}: average density of the coolant in the hot leg; g acceleration of gravity. Other head losses (friction with pipe walls, singular head losses, blocked tubes in the SG, etc.) exist in the circuit and must also be compensated.

ECCS trains of high and low pressure are activated, but they cannot compensate the flow of coolant at the break. Once the primary pumps stop, the natural circulation of the fluid in the primary begins, and a stratified regime starts (two-phase flow). In the case of large IB, the void is formed much faster and there is a risk of total uncovery of some fuel elements. A natural circulation (IAEA, 2005) regime in a closed loop (in this case, in the primary loops) can be formed when a heat sink located at higher elevation than the heat source (c.f. Figure 4.1), such that the considered fluid reduces its density when it is in contact to the heat source, and its density increases by circulating through the heat sink. This difference of density is acted upon by gravity over the elevation difference which, if it is sufficiently important, can compensate the head losses in the thermal-hydraulic circuit and naturally evacuate part of the residual thermal power.

- **Phase III**: During this phase, the decrease of the level of water is governed by differences of static pressures in the primary. The level decreases and reaches the U-legs, and if the level in the core continues to be reduced, the temperature of the fuel may increase notably, and a cross-flow may be established towards the hot leg from the vessel. If the

break is large enough, the evolution of the pressure in the primary circuit is independent from the pressure in the secondary, and the conditions of activation of the accumulators and the low pressure ECCS are reached earlier. In the uncovered parts of the core, the heat exchange is produced through steam convection and radiation, and the overheated steam, as well as the parts of the cladding that continue to increase their temperature, induce mechanical stresses on the fuel cladding, which might end up deforming. The exothermic oxidation of the Zr might also become relevant if the temperatures reach sufficiently high levels.

- **Phase IV**: This phase is characterized by the decrease in the level of the vessel by reduction of the total water mass. The liquid mass of the primary is the result of the injection flows and the flow at the break. For large IB, there is a large production of steam caused by the *flashing* phenomenon. Due to the rapid decrease in pressure in the primary at the beginning of the transient, saturation conditions are rapidly reached for the coolant, and therefore, the vessel might reach a wholly emptied state at the beginning of this phase. If this state is reached, there will be an excursion of temperature in the fuel even in the case of small and intermediate breaks.

- **Phase V**: Injection by the accumulators at the bottom of the RPV through the downcomer and reflood: the almost immediate reflood of the primary circuit implies that, despite the fast vaporization at the quenching front, the fluid around the fuel will reach saturation levels again. This means that the core is refilled with liquid water once again, and a steady (safe) state is expected to be reached.

An illustration of these phases can be found in Figure 4.2, where phases II and III are almost non-existent, and the passage between phases I and IV is done in less than a minute of physical time.

4.1.1.3 Physical phenomena of interest

It is clear that the studied nuclear transient entails a large number of physical phenomena that are susceptible of having an impact over its course. A common way of identifying which phenomena may have a major impact over the physical parameters of interest is to construct a PIRT (Phenomena Identification and Ranking Table, (NEA/CSNI/R, 2018)). This method is useful as a tool that provides insight over the variables of interest for an analyst, although it is generally constructed through the subjective analysis and judgment of experts of the domain. Nonetheless, it is a useful preliminary stage that allows to list the main physical phenomena, classify them by importance, knowledge and uncertainty. The classification of the phenomena that may potentially be relevant was made by an expert committee as an answer to the question: *Is this physical phenomenon that intervenes during this phase of the transient influential and well-known?*. The importance and the degree of knowledge of each phenomenon were quantified and evaluated giving each phenomenon a score between 1 and 5 according to a pre-established rating scale (Boyack et al., 1989).

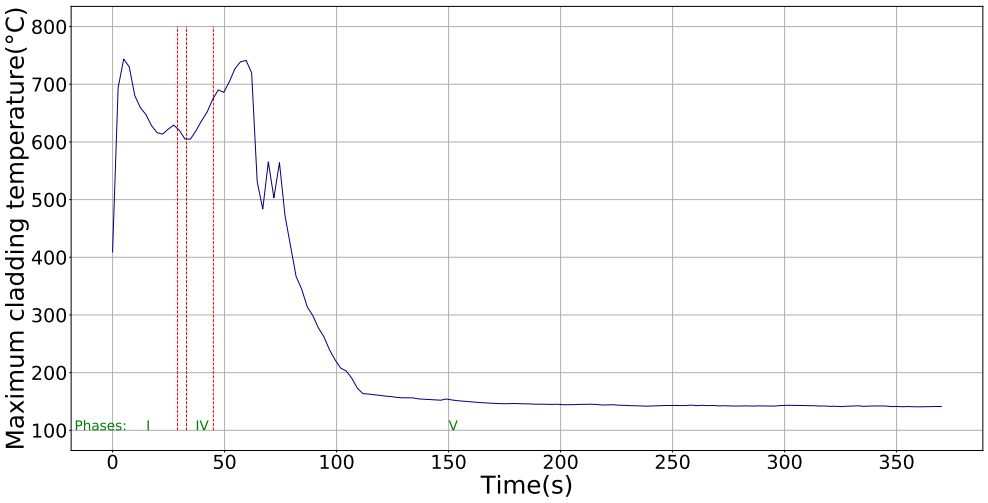

Figure 4.2: Evolution of the maximum cladding temperature during the nuclear transient. As it was explained, phases II and III are reduced in large intermediate breaks in favor of phases IV and V. Phases II and III take place in the interval $(29, 33)$ (in s) of the physical simulation.

The full PIRT of this use case is not shown here, but the main physical phenomena of interest and conclusions are listed in Table 4.3.

4.1.1.4 Safety criteria

In the context of a deterministic risk analysis, the safety requirements of a NPP translate into the respect of *safety criteria*. They constitute the threshold values of limiting characteristic physical phenomena that must be respected at all times, including accidental transients. In the case of an IBLOCA transient, the objective of the criteria is to avoid an important degradation of the nuclear core, aiming at limiting the radiological consequences for the environment. The safety criteria that must be respected are presented in Table 4.4.

The maximum cladding temperature is usually referred to as Peak Cladding Temperature (PCT from now on), and represents the maximum local temperature at any instant and any location of the core cladding of the nuclear fuel.

Regarding the oxidation of the cladding, this is a widely studied process in the nuclear industry (Baker and Just, 1962), and addresses the chemical interaction between the zirconium (Zr) present in the cladding of the nuclear fuel and the eventual surrounding steam during a nuclear accident. Zirconium oxidizes through the following reaction with steam:

$$\mathrm{Zr} + 2\,\mathrm{H_2O} \longrightarrow \mathrm{ZrO_2} + 2\,\mathrm{H_2}$$

Table 4.3: Dominant physical phenomena and elemental phenomena related to them in an IBLOCA transient (Martin and O'Dell, 2005)

Dominant phenomena	Elemental phenomena
Water inventory in the primary	Critical flow
	Phase at break
	Cold leg and downcomer condensation
	Condensation in SG tubes
	Heat exchange primary/secondary through the SG
Distribution of water mass	Degradation of pumps in two-phase regime
	Accumulators discharge
	Manometric effects
	3D effects and cross flows
Swollen level of water	Emptying/stock of water in Lower plenum
Reflood by accumulators	Interface friction core / higher plenum
	Counter flow from the SG
	Emptying and reflood of the downcomer
	Reflood of the core
Heat transfer in the core	3D effects: two-phase cross flows / Stack (chimney effect)
	Blocking pass section between fuel assemblies
Swelling of fuel rods	Heat transfer in the uncovered part
	Oxidation of cladding
	Mechanical deformation of fuel elements

This reaction is exothermic. Both the total hydrogen generation during the transient and the Effective Cladding Reacted (ECR) can be estimated thanks to the Baker-Just correlation (Baker and Just, 1962). According to this correlation, the mass/surface area of Zr consumed during steam oxidation (noted w) is given by the Arrhenius-type Equation (4.1):

$$w^2 = 33.3 \times 10^6 t \exp\Big(-\frac{45500}{RT}\Big), \qquad (\mathrm{mg/cm^2})^2 \tag{4.1}$$

where t is the time in seconds, T is the temperature in K and $R = 1.987$ (universal gas

Table 4.4: Safety criteria to be respected in an IBLOCA transient (Tarride, 2013).

Criterion	Description
Maximum cladding temperature	The maximum temperature attained by the fuel cladding at any point of the transient must remain below 1204°C.
Maximum hydrogen production	The total quantity of hydrogen produced by the chemical reaction between the cladding and the surrounding steam must not surpass 1% of the total quantity that would be produced if all the material that surrounds the fuel pellets had reacted.
Maximum oxidation of the cladding	The maximum cladding oxidation must remain below 17% of the original thickness of the cladding .
Core geometry	Any geometric core deformation must still allow the cooling of the fuel during the transient and afterwards.

constant). The equation is valid for an isothermal oxidation in a steam environment, and it is the implemented correlation in the *CATHARE2* code for the calculation of the ECR. The ECR (as a fraction) can be estimated by dividing w by the density of Zr ($\rho_{\mathrm{Zr}} = 6.5\mathrm{g/cm}^3$) and the reference cladding thickness h_{Zr} measured in cm:

$$\mathrm{ECR} = \frac{w}{\rho_{\mathrm{Zr}} h_{\mathrm{Zr}}} \tag{4.2}$$

This physical correlation overpredicts the total hydrogen produced and ECR during an accidental transient in high temperatures (USNRC, 1989), but this safety criterion is retained as a conservative hypothesis. Finally, the total allowed ECR also depends on the original concentration of hydrogen present in the cladding pre-accident. This is given by Table 4.5 (Tarride, 2013).

4.1.2 *CATHARE2* modeling

The *CATHARE2* modeling of the systems of the represented nuclear power plant (900MW and three loops) can be divided into three main parts: the modeling of the Reactor Pressure Vessel (RPV), the primary circuit and the secondary circuit. This model is based on the reference meshing for safety studies in IBLOCA transients, and has been validated on numerous applications (Charignon et al., 2016; Larget, 2018; Marrel and Chabridon, 2021).

Table 4.5: Maximum ECR (in %) allowed depending on the initial concentration of hydrogen (H) in the cladding.

H (ppm)	ECR max (%)
0	17.9
300	15.4
600	13.2
800	11.8
1040	10.2

4.1.2.5 The reactor pressure vessel

The modeling of the RPV can be divided into several individual parts as well:

- **Core and fuel**. They are represented by a 3D module in a cylindrical coordinate system, degenerated in the azimuthal component. It is then composed of one azimuthal mesh, three radial meshes and a series of equally spaced meshes along the vertical axis. The central radial mesh (representative of 9 fuel assemblies) gathers the *hot assembly* (HA, where the highest temperatures will be reached), the intermediate mesh (comprising 60 assemblies) is called the *Mean assembly* (MA, representative of the expected average behavior of the fuel) and the exterior mesh represents the remaining 88 fuel assemblies, which attain lower average temperatures during operation and the transient. In the longitudinal dimension, the core is formed by 50 vertical axial meshes. The physical characteristics of each assembly and their thermal power are considered uniform in the meshes.

- **Lower plenum**. It is formed by a sequence of three elements: 1 *volume* (0D) element, 1 *axial* (1D) element, and another *volume* element. The first volume represents the lower part of the RPV up until the supporting structure of the core; the axial element is representative of both the supporting structure of the core and the volume between this element and the lower part of the core. The final 0D element is used to connect the axial element to the core.

- **Upper plenum**. Formed by a volume element (0D), it represents the volume between the upper support structure of the core and the guiding tubes for the control rods. The junctions of the hot leg to the RPV are located in the upper plenum.

- **Bypass of the core**. This 1D element allows the modeling of the coolant flow through the guiding tubes for the control rods and the flow between the fuel assemblies and the core walls. It has the same height as the nuclear core and is parallel to it. It has junctions to the lower and upper plenums.

- **Downcomer**. It is the annular space between the walls of the core and the RPV walls. It is modeled through a 3D element that can be divided into: 1 radial mesh (the module degenerates to two dimensions), an axial mesh divided into 17 individual cells, and 6 azimuthal sectors. The junctions to the cold leg are connected to the upper part of this element.
- **Dome**. Modeled by a 0D module, it represents the volume between the vessel head and the supporting plaque of the rods. It is linked to the downcomer through 6 junctions (one for each azimuthal mesh).
- **Control rods guides**. Also modeled through a 0D module, they are connected to the dome and the upper plenum.

The modeling of the elements of the RPV is summarized in Figure 4.3.

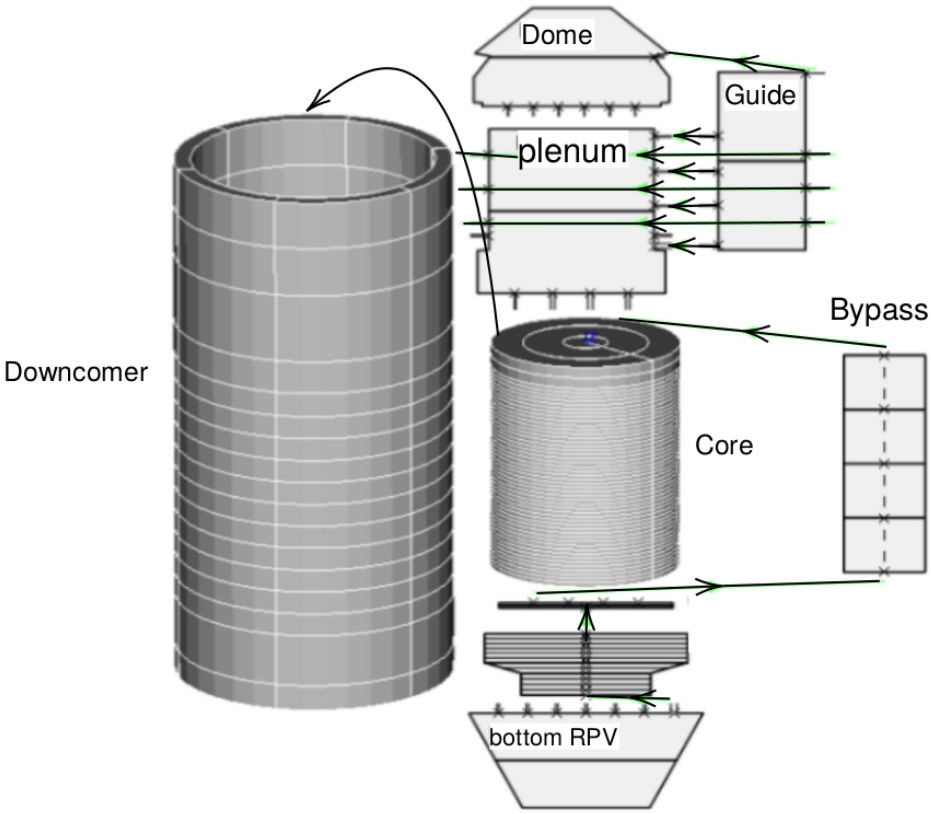

Figure 4.3: *CATHARE2* modeling of the reactor pressure vessel

4.1.2.6 The primary circuit

The primary circuit is composed by three different loops. The two intact loops are modeled by a unique axial element (1D), which represents the fluid volumes that flow sequentially through

the hot leg, the primary side of the SG, the U leg, and the cold leg, which is connected to the downcomer. Regarding the broken loop, we can distinguish four main parts in its modeling:

- **Primary pumps**. They are modeled thanks to the one-node pump submodule of *CATHARE2*. It describes the interaction between the pump and the one-phase or two-phase flow that can be located into a node of an axial 1D element. This model allows the calculation of the head of the pump, its rotation speed and the heating of the fluid that goes through it by means of its nominal head and torque, also taking into account a possible degradation due to a two-phase flow. It is located in the penultimate mesh of the U branches of the cold leg.
- **Pressurizer**. The pressurizer itself is modeled by means of a volume (0D) element and its discharge line by an axial element, which is itself connected to the axial that represents the broken loop.
- **Break**. The break is modeled by a 1D axial module in vertical position whose section corresponds to that of the break (39.1cm). It is connected to the generatrix of the axial module that represents the cold leg and its connection to the exterior of the primary circuit is made by a specific boundary condition of *CATHARE2* which imposes a pressure value and calculates the critical flow.
- **ECCS**. The accumulators are represented by a 0D volume, an axial module that represents the discharge line of the accumulators, plus the junctions between them and to the broken loop, plus the corresponding valves. Regarding the high pressure and low pressure injection pumps, they are modeled by a specific *CATHARE2* submodule.

The modeling of the aforementioned parts of the primary circuit is showcased in Figure 4.4.

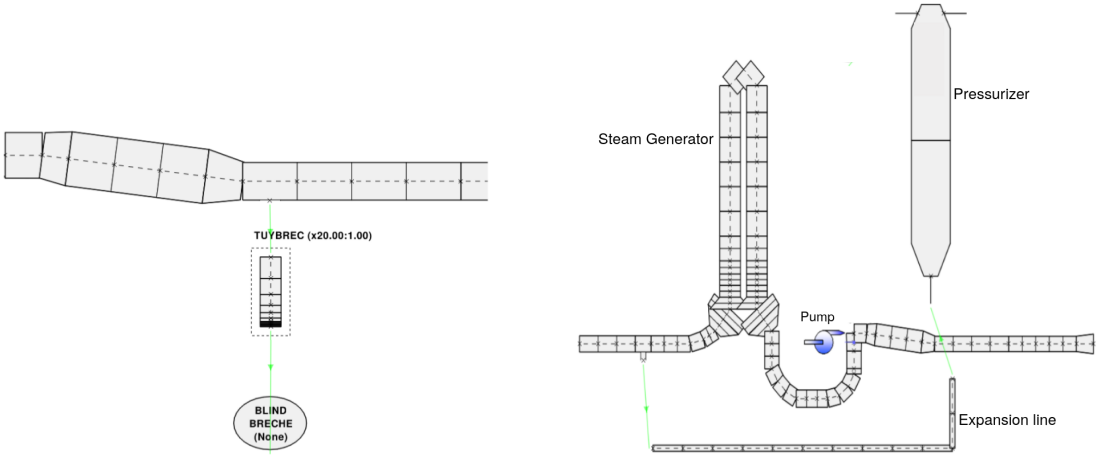

(a) Modeling of the break (b) Modeling of the primary circuit

Figure 4.4: *CATHARE2* modeling of the cold leg of the primary circuit presenting a break.

4.1.2.7 The secondary circuit

The *CATHARE2* modeling of the secondary circuit is divided into three main parts:

- **Secondary parts of the SG**. It is divided into three parts. Firstly, the injection by the EFWS is done through the use of two specific *CATHARE2* elements, which are connected to the axial (1D) module that represents the secondary part of the modeled steam generator. Finally, the upper part of the SG is modeled by a volume module that is connected to both the axial body of the SG and the steam line.
- **Steam line**. The steam produced in the SG through the thermal exchange between the primary and secondary circuits is evacuated through the steam lines. Each of the three SG possesses a steam line that links it to the steam drum, where the flows coming from each loop are mixed. These lines are modeled by means of an axial module with several nozzles and valves with imposed boundary conditions corresponding to the discharge lines to the surrounding environment.
- **Steam drum**. This volume element allows the mixture of the steam flows coming from the steam lines, i.e., the steam lines of each SG. It is connected to the turbine through a *CATHARE2* boundary condition that imposes the admission pressure to the turbine.

The secondary circuit is summarized in Figure 4.5.

4.1.3 Inputs and outputs of the code

The space defined by the input data of the *CATHARE2* code for this case is high-dimensional, with an original amount of 97 input variables. These variables can be separated into three main categories:

- **Type** 1: Initial conditions or limit conditions for the thermal-hydraulic circuits and the nuclear fuel. Some examples are the inertia of the primary pumps (RCP), the initial pressure of the accumulators, the initial primary pressure, the initial total thermal power produced by the core... .
- **Type** 2 Parameters for physical models and physical correlations. Some examples are the heat exchange coefficients between elements in different thermal-hydraulic conditions or the interfacial friction between phases. They can also be related to neutronic parameters, such as the fraction of delayed neutrons.
- **Type** 3: Scenario parameters. They define the main characteristics of the actual analyzed transient. Some examples can be: size of the break, the burn-up of the fuel at the beginning of the transient, the percentage of blocked tubes in each steam generator when the transient occurs...

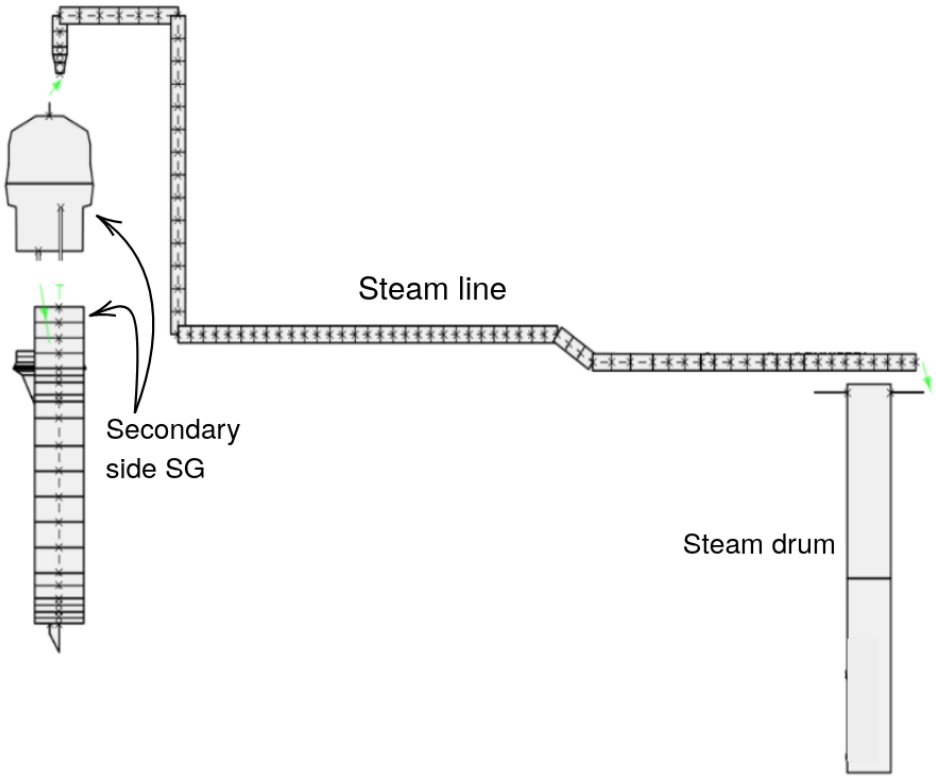

Figure 4.5: *CATHARE2* modeling of the secondary circuit

Again, these input variables correspond to a *CATHARE2* modeling commonly used in safety studies, and their probabilistic laws that model their corresponding uncertainty have been established (Larget, 2018). Each law is presented in Tables 4.6 to 4.10.

Table 4.6: Type 1 input parameters (a). **HS**: Hot Spot, **HR**: Hot Rod, **HA**: Hot Assembly, **MC**: Mean Core, **MA**: Mean Assembly, **MR**: Mean Rod, **ERF**: Enthalpy Rise Factor, **HTC**: Heat Transfer Coefficient, τ_i: Steam/water interface friction multiplicative coefficient, **CHF**: Critical Heat Flux.

Variable	Physical meaning	Units	Law
X_1	Total initial thermal power	MWth	$\mathcal{U}$
X_2	Life time of prompt neutrons	s	C
X_3	Fraction of delayed neutrons	-	C
X_4	Doppler coefficient of temperature	\$/K	C
X_5	Moderator coefficient parameter	\$/K	C
X_6	Residual power coefficient	-	$\mathcal{N}$
X_7	Initial primary pressure	Pa	$\mathcal{U}$
X_8	Average primary temperature	°C	C
X_9	Average temperature fuel pellets	°C	C
X_{10}	Primary flow per loop	m^3/h	$\mathcal{U}$
X_{11}	Pressurizer level of water	-	$\mathcal{U}$
X_{12}	Low pressure signal	Pa	$\mathcal{U}$
X_{13}	Very low pressure signal	Pa	$\mathcal{U}$
X_{14}	Multiplicative coefficient of head loss of the pressurizer expansion line	-	$\mathcal{U}$
X_{15}	Multiplicative coefficient of axial head loss of the HA	-	$\mathcal{U}$
X_{16}	Multiplicative coefficient of radial head loss between HA and MA	-	$\mathcal{S}$
X_{17}	Multiplicative coefficient of radial head loss between MA and outer radial mesh	-	$\mathcal{S}$
X_{18}	Multiplicative coefficient of head loss of the junction between downcomer and dome	-	$\mathcal{U}$
X_{19}	Multiplicative coefficient of nominal primary pump height multiplied by gravity acceleration	m^2/s^2	$\mathcal{U}$
X_{20}	Primary pumps inertia	$kg \cdot m^2$	$\mathcal{U}$
X_{21}	Pressure of the accumulators	Pa	$\mathcal{U}$
X_{22}	Initial volume of each accumulator	m^3	$\mathcal{U}$
X_{23}	Height of the connection between HR and HA	m	$\mathcal{U}$
X_{24}	Height of the connection between MR and HA	m	$\mathcal{U}$
X_{25}	Power axial offset in the core for MR	-	$\mathcal{U}$
X_{26}	Power axial offset in the core for HR	-	$\mathcal{U}$
X_{27}	HS: technological uncertainty of thermal deformation of the fuel	-	$\mathcal{N}$

Table 4.7: Type 1 input parameters (b). **HS**: Hot Spot, **HR**: Hot Rod, **HA**: Hot Assembly, **MC**: Mean Core, **MA**: Average Assembly, **AR**: Average Rod, **ERF**: Enthalpy Rise Factor, **HTC**: Heat Transfer Coefficient, τ_i: Steam/water interface friction multiplicative coefficient, **CHF**: Critical Heat Flux.

Variable	**Physical meaning**	**Units**	**Law**
X_{28}	HS: macroscopic fuel cross-section uncertainty of the fuel	-	$\mathcal{S}$
X_{29}	HS: microscopic fuel cross-section uncertainty of the fuel	-	$\mathcal{N}$
X_{30}	HS: modeling of the uncertainty on the grids	-	$\mathcal{N}$
X_{31}	ERF: technological uncertainty	-	$\mathcal{N}$
X_{32}	ERF: macroscopic uncertainty of the nuclear fuel	-	$\mathcal{S}$
X_{33}	ERF: microscopic uncertainty of the nuclear fuel	-	$\mathcal{N}$
X_{34}	Multiplicative factor of the internal pressure of the HR	-	$\mathcal{S}$
X_{35}	Multiplicative factor of the internal pressure of the HA	-	$\mathcal{S}$
X_{36}	Multiplicative factor of the internal pressure of the MC	-	$\mathcal{C}$
X_{37}	Modeling uncertainty for pellet temperature calculation of HR	-	$\mathcal{S}$
X_{38}	Modeling uncertainty for pellet temperature calculation of HA	-	$\mathcal{S}$
X_{39}	Uncertainties of fabrication for pellet mean temperature calculation of HR and HA	-	$\mathcal{N}$

Table 4.8: Type 2 input parameters (a). **HS**: Hot Spot, **HR**:Hot Rod, **HA**: Hot Assembly, **MC**: Mean Core, **MA**: Average Assembly, **MR**: Average Rod, **ERF**: Enthalpy Rise Factor, **HTC**: Heat Transfer Coefficient, τ_i: Steam/water interface friction multiplicative coefficient, **CHF**: Critical Heat Flux.

Variable	Physical meaning	Units	Law
X_{40}	Minimum film stable temperature HR, HA, MC	°C	$\mathcal{U}$
X_{41}	Multiplicative factor of HTC steam convection in HR	-	$\mathcal{LN}$
X_{42}	Multiplicative factor of HTC steam convection in HA	-	$\mathcal{LN}$
X_{43}	Multiplicative factor of HTC steam convection in MC	-	$\mathcal{LN}$
X_{44}	Multiplicative factor of HTC film boiling in HR	-	$\mathcal{N}$
X_{45}	Multiplicative factor of HTC film boiling in HA	-	$\mathcal{N}$
X_{46}	Multiplicative factor of HTC film boiling in MC	-	$\mathcal{N}$
X_{47}	Multiplicative factor of HTC steam-wall in HR	-	$\mathcal{LN}$
X_{48}	Multiplicative factor of HTC steam-wall in HA	-	$\mathcal{LN}$
X_{49}	Multiplicative factor of HTC steam-wall in MC	-	$\mathcal{LN}$
X_{50}	Multiplicative factor of HTC downstream of the quenching front of HR	-	$\mathcal{U}$
X_{51}	Multiplicative factor for HTC between fuel and coolant HA and MC downstream of the quenching front	-	$\mathcal{LN}$
X_{52}	τ_i in core during the reflood phase	J/m^3	$\mathcal{LN}$
X_{53}	HTC primary-secondary forced liquid convection in SG (primary side)	-	$\mathcal{U}$
X_{54}	HTC primary-secondary natural liquid convection in SG (primary side)	-	$\mathcal{LU}$
X_{55}	HTC primary-secondary nucleate boiling in SG (primary side)	-	$\mathcal{LU}$
X_{56}	HTC forced convection exchange wall- steam in SG (primary side)	-	$\mathcal{LU}$
X_{57}	HTC forced convection exchange wall- liquid in SG (primary side)	-	$\mathcal{LU}$
X_{58}	HTC wall-liquid at the interface (Chen correlation)	-	$\mathcal{N}$
X_{59}	HTC primary-secondary forced liquid convection in SG (secondary side)	-	$\mathcal{U}$
X_{60}	HTC primary-secondary natural liquid convection in SG (secondary side)	-	$\mathcal{LU}$
X_{61}	HTC primary-secondary nucleate boiling in SG (secondary side)	-	$\mathcal{LU}$
X_{62}	HTC interface between subvolumes in the accumulators	-	$\mathcal{LU}$
X_{63}	γ (heat capacity ratio) of nitrogen in the accumulators	-	$\mathcal{U}$
X_{64}	Wall-steam friction coefficient in the HA	-	$\mathcal{LU}$
X_{65}	Multiplicative coefficient on rupture stress	-	$\mathcal{S}$

Table 4.9: Type 2 input parameters (b). **HS**: Hot Spot, **HR**: Hot Rod, **HA**: Hot Assembly, **MC**: Mean Core, **MA**: Average Assembly, **MR**: Average Rod, **ERF**: Enthalpy Rise Factor, **HTC**: Heat Transfer Coefficient τ_i: Steam/water interface friction multiplicative coefficient, **CHF**: Critical Heat Flux.

Variable	Physical meaning	Units	Law
X_{66}	Creep velocity in HA, beginning of life	-	$\mathcal{S}$
X_{67}	Creep velocity in HR, beginning at life	-	$\mathcal{S}$
X_{68}	Creep acceleration factor of end at life in HA	-	$\mathcal{U}$
X_{69}	Creep acceleration factor of end of life in HR	-	$\mathcal{U}$
X_{70}	Multiplicative axial head loss coefficient due to fuel ballooning	-	$\mathcal{U}$
X_{71}	Balloon length	m	$\mathcal{U}$
X_{72}	Non coplanarity coefficient of fuel rupture in the assembly	-	$\mathcal{S}$
X_{73}	Fragment diameter for gap calculation of HA (relocation model)	mm	$\mathcal{S}$
X_{74}	Fragment diameter for pellet conductivity calculation of HA (relocation model)	mm	$\mathcal{S}$
X_{75}	Diameter of fragments for the calculation of the conductivity of the pellets of HA	mm	$\mathcal{S}$
X_{76}	Diameter of fragments for the calculation of the conductivity of the pellets of HR	mm	$\mathcal{S}$
X_{77}	Critical mass flow rate: flashing HTC between the phases (sub-cooled)		$\mathcal{LN}$
X_{78}	Critical mass flow rate: wall-liquid friction (subcooled)	-	$\mathcal{N}$
X_{79}	Critical mass flow rate: boiling delay (subcooled)	-	$\mathcal{N}$
X_{80}	Critical mass flow rate: HTC flashing (saturation)	-	$\mathcal{LN}$
X_{81}	Critical mass flow rate: steam-liquid interface friction	-	$\mathcal{N}$
X_{82}	τ_i in SG/U-branches during the decompression phase	J/m^3	$\mathcal{LN}$
X_{83}	τ_i in the hot leg during the decompression phase	J/m^3	$\mathcal{LN}$
X_{84}	τ_i in the hot leg elbow during the decompression phase	J/m^3	$\mathcal{LN}$
X_{85}	τ_i in the SG water chamber	J/m^3	$\mathcal{LN}$
X_{86}	τ_i in the downcomer during the reflood phase	J/m^3	$\mathcal{LN}$
X_{87}	τ_i in the core during the decompression phase	J/m^3	$\mathcal{N}$
X_{88}	Bubble rising velocity in the upper plenum	m/s	$\mathcal{LN}$
X_{89}	Bubble rising velocity in the lower plenum	m/s	$\mathcal{LN}$
X_{90}	Bubble rising velocity in the dome	m/s	$\mathcal{LN}$
X_{91}	HTC interface steam and liquid in the downcomer	-	$\mathcal{LN}$
X_{92}	Condensation in safety injection jet located in intact loops	-	$\mathcal{U}$
X_{93}	Condensation in stratified flow in intact loops	-	$\mathcal{S}$

Table 4.10: Type 3 input parameters (bis). **HS**: Hot Spot, **HR**: Hot Rod, **HA**: Hot Assembly, **MC**: Mean Core, **MA**: Average Assembly, **MR**: Average Rod, **ERF**: Enthalpy Rise Factor, **HTC**: Heat Transfer Coefficient τ_i: Steam/water interface friction multiplicative coefficient, **CHF**: Critical Heat Flux.

Variable	Physical meaning	Units	Law
X_{94}	Break size	cm	$\mathcal{U}$
X_{95}	Fuel Burn-up in the HR and HA	MWday/ton	$\mathcal{U}$
X_{96}	Axial offset of nuclear power in the MR	-	$\mathcal{U}$
X_{97}	k/A^2 (friction between water and pipe walls) in the discharge line of the accumulators	m^{-4}	$\mathcal{U}$
X_{98}	Liquid enthalpy of the water in the accumulators	J/kg	$\mathcal{U}$
X_{99}	Initial temperature of water in ECCS	°C	$\mathcal{U}$
X_{100}	Water flow rate of the ECCS	kg/s	$\mathcal{U}$
X_{101}	Rate of blocked tubes in the SG	-	$\mathcal{U}$
X_{102}	Multiplicative coefficient of water mass flow in the auxiliary water system	-	$\mathcal{U}$
X_{103}	Temperature of water in the Emergency FeedWater System of the SG	°C	$\mathcal{U}$
X_{104}	Initial temperature of liquid in the dome	°C	$\mathcal{U}$

The uncertainty of the input variables is modeled through their probability density laws, which will be Normal ($\mathcal{N}$), Log-Normal ($\mathcal{LN}$), Uniform ($\mathcal{U}$), Log-Uniform ($\mathcal{LU}$), Specific ($\mathcal{S}$) and Constant ($\mathcal{C}$), where the Normal and Log-Normal laws are truncated to the $[-3\sigma, +3\sigma]$ domain, where σ is the standard deviation of the law.

Amongst all these possible physical variables, several of them have been fixed to penalizing values in current safety analyses (Marrel and Chabridon, 2021) (values that lead to closer values of physical quantities of interest to the safety criteria). In particular, the scenario variables, especially those that present a higher impact over the PCT. The fixed variables are presented in Table 4.11.

Concerning the outputs of *CATHARE2*, the chosen functional outputs provided by the code are:

- Gas mass flow (kg/s) at the break.
- Liquid mass flow (kg/s) at the break
- Gas flow (kg/s) at the bottom of the core (MC)
- Gas flow (kg/s) at the top of the core (MC)
- Liquid flow (kg/s) at the bottom of the core (MC)

Table 4.11: Fixed penalized input variables for the IBLOCA transient.

Variable	Physical meaning	Units	Value
X_{94}	Break size	cm	39
X_{95}	Fuel Burn-up in the HR and HA	MWday/ton	34000
X_{96}	Axial offset of nuclear power in the AR	-	0
X_{98}	Liquid enthalpy of the water of the accumulators	J/kg	33500
X_{99}	Initial temperature of water in ECCS	°C	20.657
X_{102}	Multiplicative coefficient of water mass flow in the auxiliary water system	-	0.0409
X_{103}	Temperature of water in the emergency feedwater system of the SG	°C	17.410

- Liquid flow (kg/s) at the top of the core (MC)
- Primary pressure (Pa), measured in the pressurizer
- Total liquid mass in the Downcomer (kg)
- Total liquid mass in the core (kg)
- Swollen level of water in the core (m).

Examples of the evolution of parameters are provided in Figure 4.5.

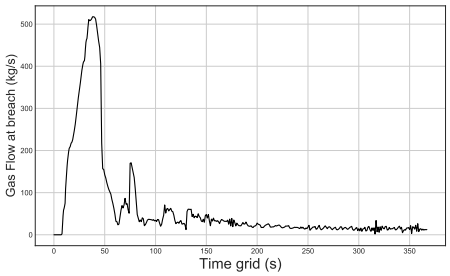

(a) Example of gas mass flow at the break

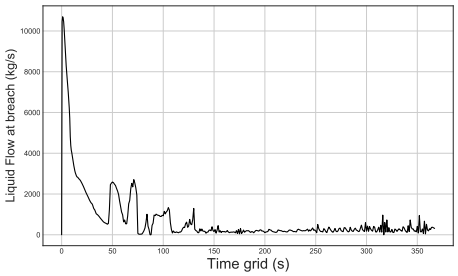

(b) Example of liquid mass flow at the break

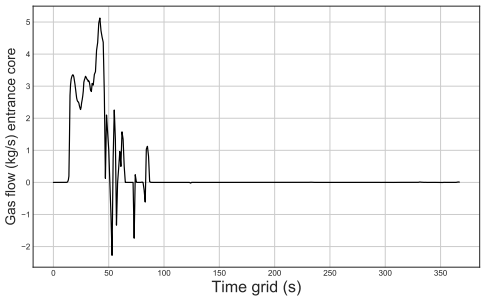

(c) Example of gas mass flow at the bottom of the core

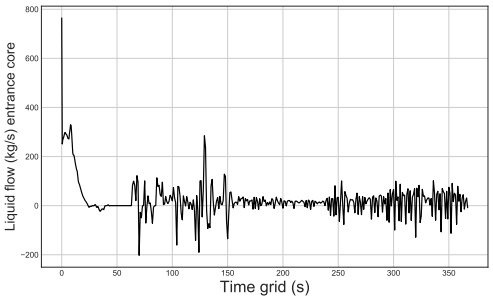

(d) Example of liquid mass flow at the bottom of the core

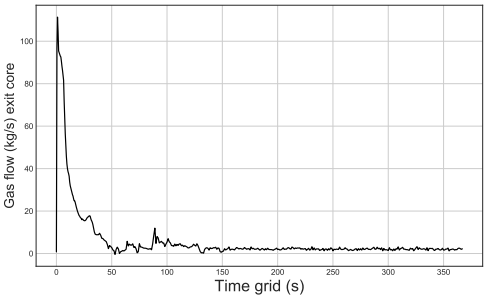

(e) Example of gas mass flow at the top of the core

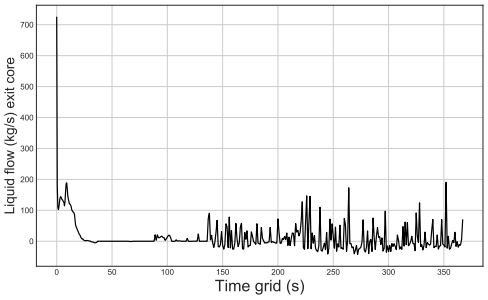

(f) Example of liquid mass flow at the top of the core

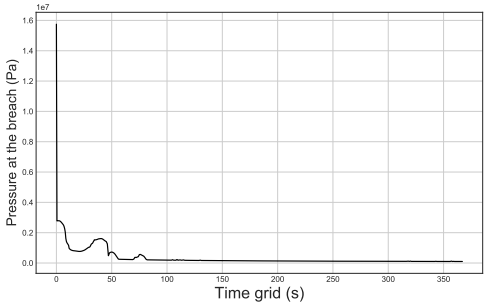

(g) Example of primary pressure

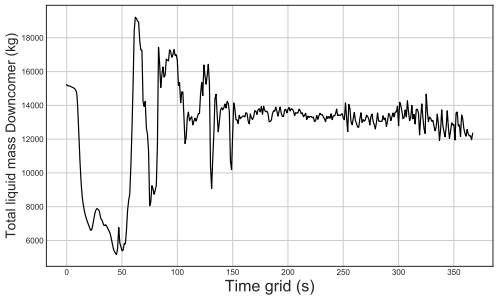

(h) Example of total liquid mass in the downcomer

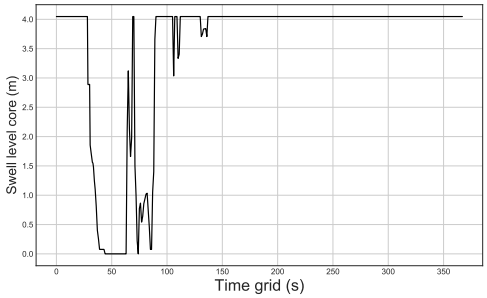

(i) Example of swollen level of water in the core

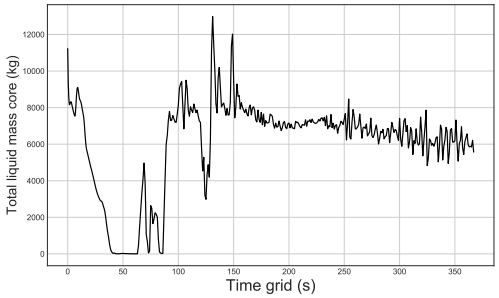

(j) Example of total liquid mass in the core

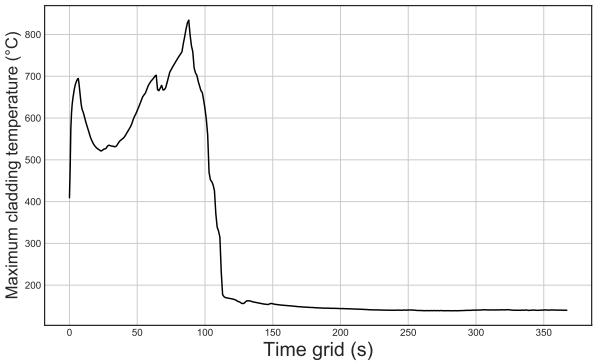

(k) Example of the evolution of the maximum cladding temperature

Figure 4.5: Examples of outputs provided by *CATHARE2*

4.2 Application of the methodology

In the following sections we will show how the functional outlier detection methodology presented in Chapter 2 can provide a set of outliers in this application that can be related to specific physical phenomena which provide their interpretation.

4.2.1 Preliminary considerations

Firstly, let us recall the physical phenomena of interest presented in Table 4.3. Amongst the six dominant phenomena, four of them are directly linked to the total water mass present in the core (water inventory in the primary circuit, distribution of water mass in the primary, swollen level of water in the core, and reflood dynamic by the accumulators), whereas the remaining two are related to the evacuation of the thermal power produced in the core and the maintaining of the geometry required for the long-term cooling of the core.

Within the perimeter of this study, we are interested in the short-term effects of the IBLOCA transient and the respect of the safety criteria. Amongst the 4 mentioned safety criteria in Section 4.4, we can show that the main criterion that must be respected in the short-term is the PCT threshold of 1204°C (Charignon et al., 2016). This short term transient is simulated during 367.00 s of physical time, so we are not focused on the long-term cooling safety criterion. Regarding the production of hydrogen safety criterion (second criterion in Table 4.4), it is less penalizing than the PCT in the considered time frame (IRSN, 2008). This means that the production of hydrogen may not be considered for the studied transient. A similar conclusion may be obtained regarding the oxidation of the cladding. A numerical application application for the estimation of the maximum ECR presented in Table 4.4 is given below. Since the ECR is a monotonically increasing function of the fuel temperature (see equations (4.1) and (4.2)), it is possible to define an envelope penalizing scenario in which, during the whole transient, the fuel temperature remains at 1477.15K. If the temperature were higher, the safety criterion of temperature would already not be respected and the transient would already be qualified as severe even without checking the ECR criterion. Let us therefore consider this envelope transient of a duration of 367.00 s, $R = 1.987\text{cal}/(\text{K} \cdot \text{mol})$ and 1204°C = 1477.15K:

$$\begin{aligned} w^2 = 33.3 \cdot 10^6 \cdot 360 \cdot \exp\Big(- \frac{45500}{1.987 \cdot 1477.15} \Big) = 2262.87 \qquad & (\text{mg/cm}^2)^2 \\ \implies w = 47.57 \qquad & (\text{mg/cm}^2) \end{aligned} \tag{4.3}$$

Therefore, considering a density for the Zr of 6.5 g/cm^3= 6500 mg/cm^3 and a reference thickness for the cladding of 4 mm (Deckers, 1985):

$$\text{ECR} = \frac{42.999}{6500 \cdot 0.4} = 0.018 \tag{4.4}$$

which is well below the maximum acceptable values of ECR shown in Table 4.5 for this penalized calculation. Therefore, we shall focus exclusively on the PCT as safety criterion for the analyzed transient, since it is the enveloping safety criterion in the framework of the use-case.

This also means that the natural set of functional outputs to which the FOD methodology will be applied to is restricted to the evolution of the maximum local cladding temperature (see Figure 4.5 (k)).

Finally, let us establish the breakpoint events of interest and the intermediate parameters that will be considered. We consider the activation of specific critical systems or signals (automatic shutdown of the core, ECCS, start of reflooding by the accumulators...) as well as the aforementioned phases in Section 4.2, which divide the transient into time intervals where differentiated physical phenomena take place or any combination of them.

In practice, due to the fast progression of the transient, there is an overlap between the frontiers of the phases I to V of the transient (see Table 4.2) and other important events that affect the phenomena showcased in Table 4.3. This is for instance the case for the activation of the accumulators, which demarcates the beginning of phase V, and whose activation strongly impacts the aforementioned phenomena.

A conservative approach is to retain as many events as possible, taking into account the events that will have an impact on the phenomena presented in Table 4.3.

Taking these elements into account, the selected breakpoint events in the transient are those displayed in Table 4.12.

Table 4.12: Considered breakpoint events for the IBLOCA transient. We provide orders of magnitude of their time of occurrence because they depend on each individual transient.

Event	**Order of magnitude** (s)	**Notation**
Automatic shutdown of the core	5	t_1
ECCS activation	32	t_2
Start of the accumulators discharge	48	t_3
First uncovery of the core	55	t_4
Second uncovery of the core	100	t_5

For the purposes of this chapter, we shall name $\mathcal{T} \subset \mathbb{R}$ the physical time interval in which the simulations take place, that is $\mathcal{T} := [0, T]$s, $T = 367$ (s). The set of breakpoint events is denoted $\tau_b \in \mathcal{T}, \tau_b = \{t_1, t_2, t_3, t_4, t_5\}$.

We shall focus on the *CATHARE2* outputs impacting the most the aforementioned physical phenomena of interest. These outputs are the evolution of the maximum cladding temperature, the swollen level of water in the core, as well as the masses of coolant in both the

core and the downcomer.

The considered intermediate parameters of interest through which the inlying and outlying samples will be compared are, for a given functional output z_s (see section 3.3.1): $h_1(z_s)|_{t_i}^{t_{i+1}} = \max(z_s)|_{t_i}^{t_{i+1}}, h_2(z_s)|_{t_i}^{t_{i+1}} = \min(z_s)|_{t_i}{}_{i+1}^{t}, h_3(z_s)|_{t_i}^{t_{i+1}} = \mathbb{E}[z_s]|_{t_i}^{t_{i+1}}$.

4.2.2 Design of experiments and functional outlier detection

Let us now consider the set of computer experiments to launch. The provided modeling of the IBLOCA in the considered NPP requires an input vector of $d = 97$ parameters, and the following step is to create a design of experiments, i.e., a set of scalar inputs $\{X_{i,1}, ..., X_{i,d}\}_{i=1}^{N}$ and functional outputs $\{z_{i,1}, ..., z_{i,S}\}_{i=1}^{N}$ (where N is the size of the considered sample, and S is the total number of available functional random variables).

In this application case, the inputs will be sampled through a random Monte Carlo design. There are two main reasons for doing this. Firstly, as it was mentioned in Chapter 2, the use of the HSIC indices as a screening tool requires independence between the considered experiments, and therefore a Monte Carlo design or LHS is appropriate. It is also to be noted that, for very large input spaces (namely, $d > 20$), even space-filling designs also rapidly struggle against the curse of dimensionality (Damblin et al., 2013). Another less important point, but relevant nonetheless, is the fact that we wish to explore how the application of this methodology can prove to be useful in real use cases with commonly used tools by engineers, and Monte Carlo designs of experiments remain a widely used sampling method.

Finally, the size N of the design of experiments must be established. As a general rule, the total number of required simulations depends on the purpose of the experiments (the statistical quantities that we wish to estimate), the total CPU time that is required for each individual simulation and the total number d of input parameters. Several heuristics that propose a value of N equal to ten times the dimension d of the input space (Loeppky et al., 2009) in the context of uncertainty propagation. For this particular use-case, we have chosen $N = 1000$.

As it was mentioned, the FOD method presented in Chapter 2 is applied to the subset of $N = 1000$ maximum local cladding temperature evolutions corresponding to each transient in the design of experiments that converged in their calculation.

The resulting set of outlyingness scores $\{\theta_i\}_{i=1}^{N}$, each one associated to its corresponding simulation, will be used as a tool for sensitivity analysis, and the results on the corresponding set of functional outputs is showcased in Figure 4.6.

The associated score θ_i to each curve (see Figure 4.6) has been calculated considering the h-mode depth and the DTW as detection features, with the outlying set of curves being formed by the $\alpha = 10\%$ more outlying transients, providing a total of 3.8% outlying transients. More restricting criteria would naturally provide smaller sets of outliers, but without large differences over the more outlying curves due to the shape of the distribution of θ_i values (see

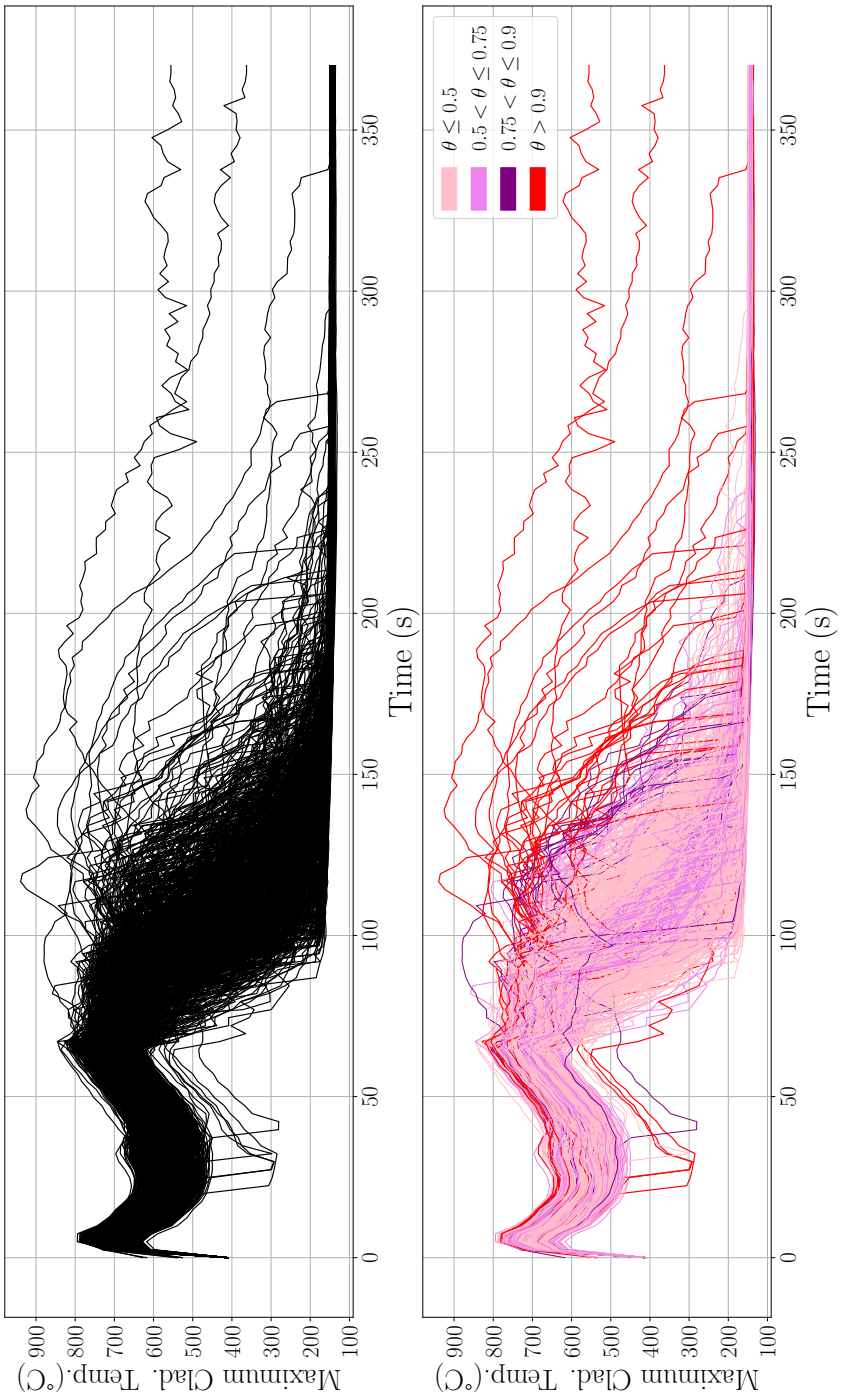

Figure 4.6: Results of the application of the FOD methodology to the set of maximum cladding temperatures in the design of experiments. Top: Raw set of functional outputs. Bottom: same set of curves but associated to four main groups, $\theta_i \in [0, 0.5]; \theta_i \in [0.5, 0.75]; \theta_i \in [0.75, 0.9]$ &$\theta_i \in [0.9, 1]$.

Figure 4.8). For $\alpha = 5\%$, the set of outliers is composed by the 3.1% more outlying curves, and for $\alpha = 1\%$, the set is reduced to 2.5%.

We showcase the histogram of PCT, i.e. the maximum value of temperature attained during the accidental transient for the maximum cladding temperature functional output, whose values range in the $[620.37, 939.31]$°C interval. The empirical estimator of the 90% quantile of PCT is shown in red in the Figure 4.7, and is equal to 779.59°C. No simulations surpass the threshold of temperature of the safety criterion (1204°C).

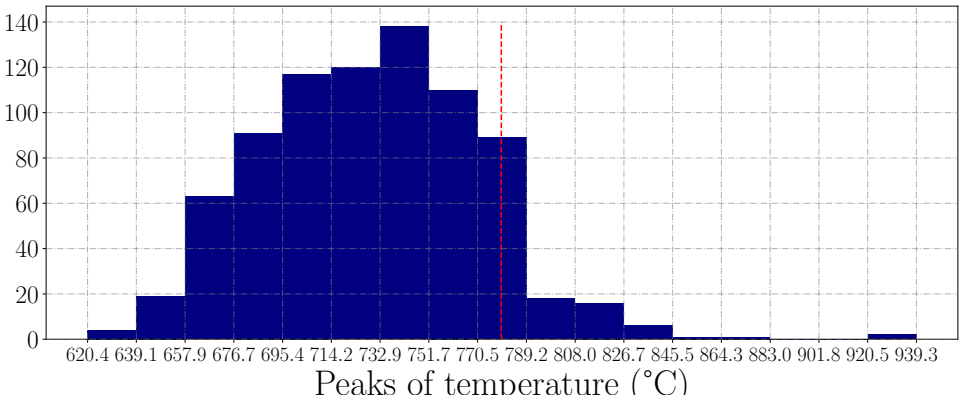

Figure 4.7: Distribution of local PCT across the design of experiments. Red: empirical 90% quantile of the distribution.

Finally, we showcase the corresponding histogram for the values of $\{\theta_i\}_{i=1}^N, \theta_i \in [0, 1]$ in Figure 4.8. The y-axis represents the total number of curves in the corresponding bin. There exists a set of simulations of with high associated values of outlyingness ($\theta_i \in [0.9, 1]$), which correspond to the strict outliers detected through the chosen criteria.

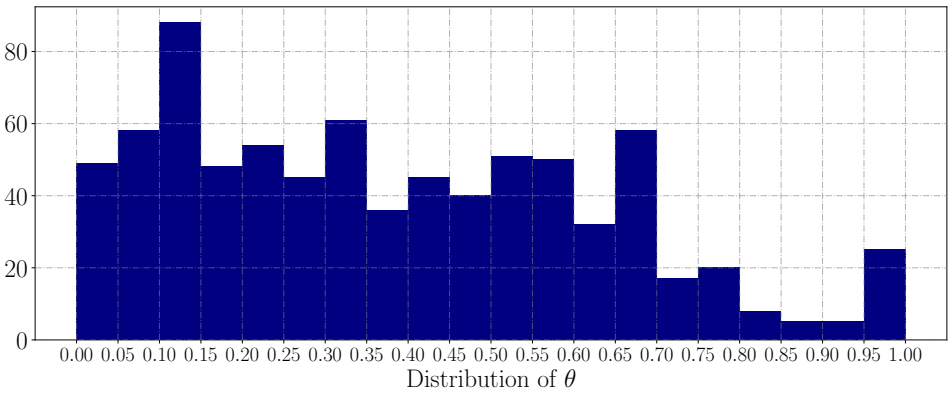

Figure 4.8: Distribution of θ_i across the design of experiments.

Although it will be explained in more detail afterwards, for the sake of clarity, we showcase here the distribution of local PCT for both the inlying and outlying samples (Figure 4.9). It can be appreciated how the automatic outlying detection procedure has been capable of extracting a sample of transients whose PCT significantly diverges from those in the inlying one. In particular, the distribution of outliers is skewed towards the more penalizing scenarios, with higher PCT values.

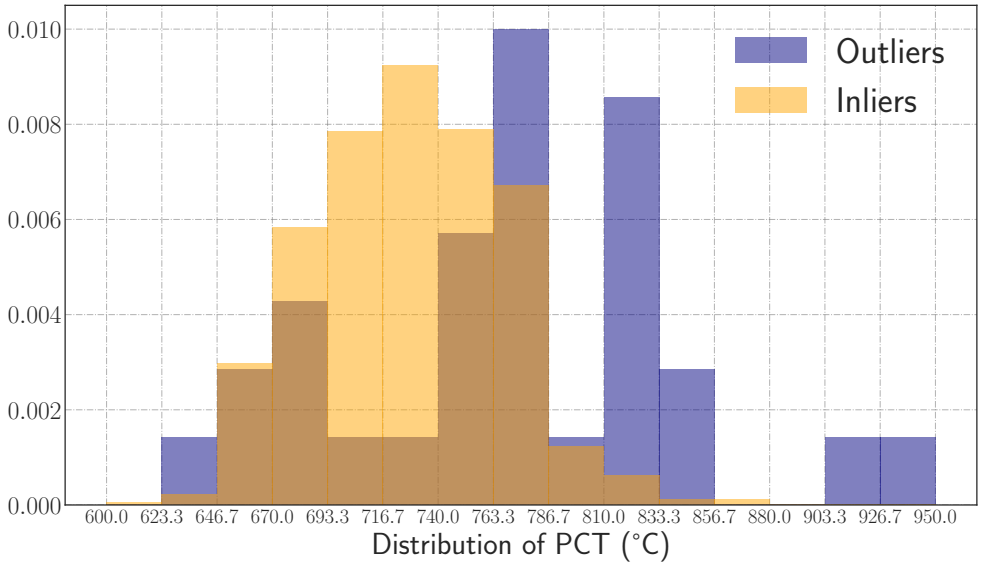

Figure 4.9: Distribution of PCT for both the inlying and outlying samples.

4.2.3 Sensitivity analysis

We perform now the Target Sensitivity Analysis (TSA, Marrel and Chabridon (2021), see Section 3.2) of the input parameters and the considered score of outlyingness $\theta \in \Theta, \Theta = [0, 1]$. We will consider the critical domain $\{\mathcal{S} \subset \Theta | \theta > 0.9\}$ and the TSA is performed through permutation tests (non-asymptotic framework) and HSIC measures.

The resulting influential variables are presented in Table 4.13.

Looking at Table 4.13, it is clear that, as it was intended, the variables that have been identified as influential over the extreme values of θ are closely related to the physical parameters of interest showcased in Table 4.3.

In the following, we provide a more detailed explanation of the corresponding physical meaning of these inputs, necessary for the interpretation of their impact during the transient.

- X_{51}: This parameter corresponds to the global heat transfer coefficient between the

Table 4.13: Identified influential variables according to the TSA through HSIC measures in the $\mathcal{S}$ domain.

Variable	Physical meaning	Units	Law	p-value independence test
X_{86}	τ_i in the downcomer during the reflood phase	J/m^3	$\mathcal{LN}$	0.0236
X_{51}	Multiplicative factor for HTC between fuel rods and coolant in HA and MC downstream of the quenching front	-	$\mathcal{LN}$	0.024
X_{70}	Multiplicative factor of axial head loss coefficient due to fuel ballooning	-	$\mathcal{U}$	0.0251
X_{91}	HTC interface steam and liquid in the downcomer	-	$\mathcal{LN}$	0.062
X_{52}	τ_i in core during the reflood phase	J/m^3	$\mathcal{LN}$	0.0623
X_{97}	k/A^2 (friction between water and pipe walls) in the discharge line of the accumulators	m^{-4}	$\mathcal{U}$	0.078

walls of the Zr cladding (the external oxide) and the surrounding coolant downstream of the quench front. A diagram of the intervening elements is presented in Figure 4.10. During the reflood phase, the quench front separates the gas and liquid phases, and the wall-fluid exchange may be done in film boiling, two-phase forced convection or natural convection regimes.

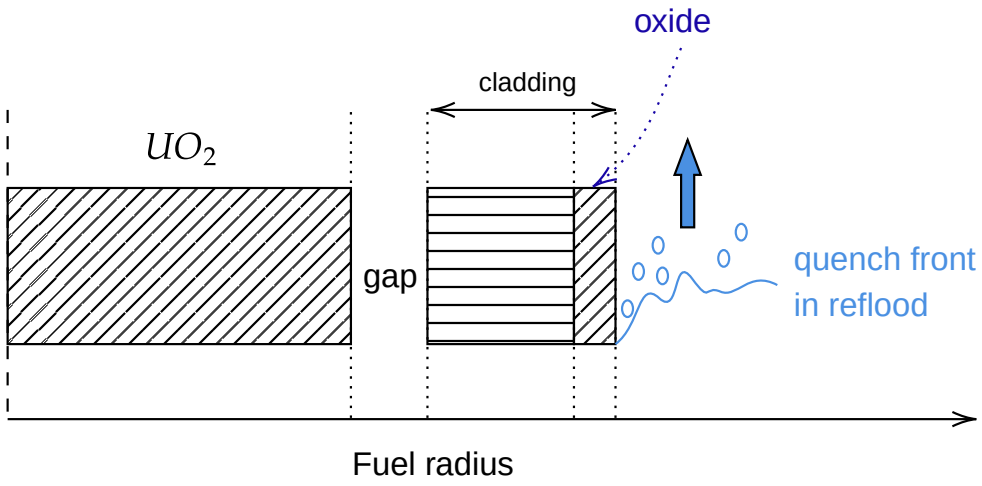

Figure 4.10: Cross-section of a fuel pellet

- X_{52}: for turbulent flows (such as during the reflood phase of the transient), the general form of the interfacial friction between the steam and liquid phases is:

$$\tau_i = \frac{1}{2} a_i f_i \rho \Delta V_2 k(\alpha) \tag{4.5}$$

where f_i is a friction coefficient; ΔV_2 is the square of a velocity difference; a_i represents the interfacial area; $k(\alpha)$ is a numerical smoothing function.

$$\Delta V_2 = \begin{cases} (\Delta V^2 + V_0^2) sign(\Delta V) & if |\Delta V| > V_0 \\ 2 V_0 \Delta V & if |\Delta V| \leq V_0 \end{cases}$$

During reflood, the value $V_0 = 0.2$m/s is used by *CATHARE2* for all geometries. Finally, the component $k(\alpha)$ is calculated differently depending on the side of the quench front that is taken into account:

  - Upstream of the quench front:

$$k(\alpha) = 1 + \frac{10^{-7}}{\alpha^3} + \frac{3 \cdot 10^{-15}}{(1-\alpha)^3}$$

  - Downstream of the quench front:

$$k(\alpha) = 1 + \frac{10^{-7}}{\alpha^3} + \frac{3 \cdot 10^{-18}}{(1-\alpha)^3}$$

The difference of velocities between the steam and liquid phases, ΔV, writes:

$$\Delta V = u_G - C_k u_L$$

where u_L and u_G correspond to the liquid and gas velocities at the interface, respectively. The coefficient C_k accounts for the effect of the distribution of void fraction. It derives from the Wallis Drift Flux model (Wallis, 2020), and writes:

$$C_k = 1 + 1.6 \alpha^{1.5} (1-\alpha)^{1.5}$$

The interfacial friction intervenes in the resolution of the momentum equations presented in Chapter 3, which corresponds to the force per unit volume arising from the action of tangential stresses between the phases in the core during the reflood phase.

- X_{70}: in this transient, the elevation of temperature of the fuel can induce the dilatation of the cladding in the hottest areas of the fuel in a process known as ballooning. *CATHARE2* is capable of modeling this effect and its thermal-mechanical influence on the thermal-hydraulic parameters during the transient. In particular, during the reflood phase, the code adds singular pressure drops at the locations of the balloons, and variable X_{70} represents a multiplicative coefficient to this axial head loss.

  The constrained flow also induces a modification in the heat transfer laws due to the increase of velocities of the phases. This translates into an increase in the wall-to-steam

heat transfer in the case of forced convection and an increase of the wall-to-fluid transfer in film boiling caused by droplet impacts.

$$K = -0.4026 + \frac{0.0779}{1-B} + \frac{0.4805}{(1-B)^2} \tag{4.6}$$

where B is a blockage correlation that was established on the basis of experiments on single-rod burst strains which were compared to the available NUREG database (Claude Grandjean, 2005). The correlation for the blockage writes:

$$B = \psi \cdot f(K_{nc} \cdot \epsilon)$$

where ψ is a coefficient that takes into account the presence of undeformable meshes (due to the presence of instrument tubes and structures), and K_{nv} is the parameter that takes into account the fact that the ballons are not coplanar. ϵ corresponds to the burst strain of the rods, and is calculated by *CATHARE2*.

- X_{86}: it represents the τ_i interfacial friction between steam and water in the downcomer, following equation (4.5). This variable is sampled independently from X_{52} and also follows a different distribution.

- X_{91}: it represents a multiplicative coefficient for the heat flux between the phases in the downcomer due to condensation. During the refill phase, the injected water from the ECCS provokes the condensation of the steam phase present in the downcomer before arriving to the core. In its most general form, the heat flux due to condensation is written:

$$q_{cond} = R \cdot q_{st} + (1-R)[C_S \cdot q_{\text{Chen}} + (1-C_S)q_{\text{Shah}} + E \cdot q_d]$$

This correlation integrates itself several different correlations that model the heat transfer depending on the flow regime in the downcomer. q_{st} represents the correlation of heat flux in the case of a stratified flow; q_d is the correlation for droplet flow; q_{Shah} is the Shah correlation (Shah, 1979) and q_{Chen} is the Chen correlation (Chen et al., 1987). R represents the rate of stratification in the downcomer and E is the entrainment fraction, i.e., the ratio of droplet flow rate to the total liquid flow rate. Finally, the coefficient C_S is a continuous function that ensures a smooth transition between the Chen and Shah correlations.

Originally, if the flow is non-stratified, the condensation heat flux was calculated thanks to the Shah correlation, but the results were not sufficiently satisfactory in the case of high steam quality and in the presence of non-condensible gases. The Chen correlation was implemented in *CATHARE2* as an improvement to better model the heat transfer.

- X_{97}: friction coefficient between the water and the pipe walls in the discharge line of the accumulator. The wall friction terms for the liquid phase (subindex L) can be written as:

$$\chi_f c_L f_L \frac{\rho}{2} u_L |u_L| \tag{4.7}$$

where u_l represents the longitudinal velocity along the pipe, and f_L is a friction coefficient which depends on the Reynolds number of the corresponding phase:

$$f_L = \max\left\{\frac{16}{Re_L}, \frac{0.079}{Re_L^{0.25}}, 0.003\right\} \tag{4.8}$$

and this Reynolds number (Re_L) is:

$$Re_L = \frac{\alpha_L \rho_L (|V_L| + 10^{-8}) D_h}{\mu_L} + 20$$

ρ_L is the corresponding density of the fluid, D_h is the hydraulic diameter, μ_L is the dynamic viscosity of the liquid. Finally, the function $g(\alpha)$ is a smoothing function that cancels the contribution of the liquid to the wall friction whenever the steam quality (the mass fraction of steam in the saturated mixture) is close to 1, and α_L is the liquid fraction.

c_L is a two-phase multiplier that depends on the flow regime in the discharge line and writes:

$$\begin{aligned} c_L &= [R \cdot c_{Lst} + (1-R) \cdot_{Lnst}] \cdot g(\alpha) \\ c_G &= R \cdot c_{Gst} + (1-R) \cdot c_{Gnst} \end{aligned} \tag{4.9}$$

where the multipliers $c_{Lst}, c_{Lnst}, c_{Gst}$ and c_{Gnst} serve to approximate the ratio of the perimeter in the pipe occupied by each phase, taking into account if the two-phase flow is stratified or not. For stratified flows, the multipliers simply take the form:

$$\begin{aligned} c_{Lst} &= \frac{1}{\pi} \cdot \arccos(2\alpha - 1) \\ c_{Gst} &= 1 - c_{Lst} \end{aligned} \tag{4.10}$$

In non-stratified flows, the coefficients c_{Lnst} and c_{Gnst} take more complex forms not specified here.

Although their impact will be explained in more detail in the following section, a brief explanation of how the identified variables impact the safety criterion is showcased in Table 4.14. Let us recall however that the selected variables have been chosen taking the outlyingness score into account, and not the PCT, which means that some of them may be related to other physical parameters and not have a direct link with the PCT.

In summary, it is expected that the multiplicative coefficients of the HTC both between the fuel and coolant, and the liquid-gas interface (variables X_{51} and X_{91}), help lower the

Table 4.14: Effect of increasing the values of the relevant inputs on the safety criterion, the peak cladding temperature.

Variable	Physical meaning	Trend	Impact on PCT
X_{86}	τ_i in the downcomer during the reflood phase	↑	↑
X_{51}	Multiplicative factor for HTC between fuel rods and coolant in HA and MC downstream of the quenching front	↑	↓
X_{70}	Multiplicative factor of axial head loss coefficient due to fuel ballooning	↑	↑
X_{91}	HTC interface steam and liquid in the downcomer	↑	↓
X_{52}	τ_i in core during the reflood phase	↑	↓
X_{97}	k/A^2 (friction between water and pipe walls) in the discharge line of the accumulators	↑	↑

PCT for their higher values. An increased heat transfer between the fuel and the surrounding coolant helps lower the cladding temperature, and a higher heat exchange between the phases in the downcomer helps to increase the amount of condensed steam, which will increase the amount of coolant entering the core in the bottom-up reflooding. Regarding variable X_{70}, the increase of head loss due to the ballooning of the fuel hinders the reflood of the core, globally increasing the PCT in the transient. Regarding the interface friction between the steam and liquid (τ_i) in the core (variable X_{52}), it is expected that higher values would increase the swollen level of water in the core, thanks to the rising bubbles generated through the contact between coolant and fuel in the reflood, which would help increase the surface of the core in contact with the injection water, lowering the PCT. Conversely, in the case of the interface friction but in the downcomer (variable X_{86}), the opposite effect is expected, and the rising steam in this part of the RPV should hinder the entrance of the liquid water in the core injected by the ECCS. The formed steam should then decrease the momentum of the injected water, hindering the reflood, and increasing the PCT. Finally, high values for variable X_{97} would also hinder the injection of liquid water through the reduction of momentum of the coolant in contact with the walls of the discharge line of the accumulators. High values of friction in this component are expected to increase the PCT values in the transient.

4.2.4 Comparison of samples

In this section we compare the obtained inlying and outlying samples with regard to the selected intermediate parameters and the influential inputs established in the previous section. The comparisons are made by means of the Kruskal-Wallis H-test (KW) (Kruskal and Wallis, 1952). This test is an efficient way of comparing if two samples can be objectively be consid-

ered to have been drawn from the same distribution. The test is non-parametric, and does not assume an underlying Gaussian distribution of the samples. Other reason that makes it practical in this context is the fact that it allows the comparison of statistical samples of different sizes, which is a basic requirement when comparing inlying and outlying samples, the second being always much smaller by definition. The details of the test can be found in Appendix A.

At this stage the available information is: a set of breakpoint events, a set of intermediate parameters over the relevant outputs of *CATHARE2* directly linked to the relevant phenomena, a scalar safety criterion and a set of outlying scores associated to the output transients of the numerical simulator.

The results of the comparisons can be found in Appendix B. In this appendix, we show which phases of the transient present quantifiable differences between the inlying and outlying sample, through Tables B.1 to B.9 for significance levels of $\alpha = 10\%$. These differences are visualized via their corresponding boxplots and violin plots from Figure B.1 to B.10. Visualizing the data not only helps to validate the objective conclusions of the KW test, but also help in the interpretation of the results, since the KW test only provides an objective test of the equality of distributions, but not of the reasons behind it or how these differences translate into a specific physical meaning.

We have found in the previous section that the most relevant inputs that explain the outlyingness are all related to the reflood of the core, through heat transfer coefficients, interfacial frictions between the steam and liquid phases, as well as the coolant in the discharge line of the accumulators. These variables intervene in three of the main components that influence the reflood, i.e., the core, the downcomer (which links the core with the ECCS systems and loops, including the one where the break is located) and the accumulators. As a complement to Figure 4.9, it is clear in Figure 4.11 how higher values of θ are related in most cases to more penalizing scenarios, which supports the analysis that is presented below.

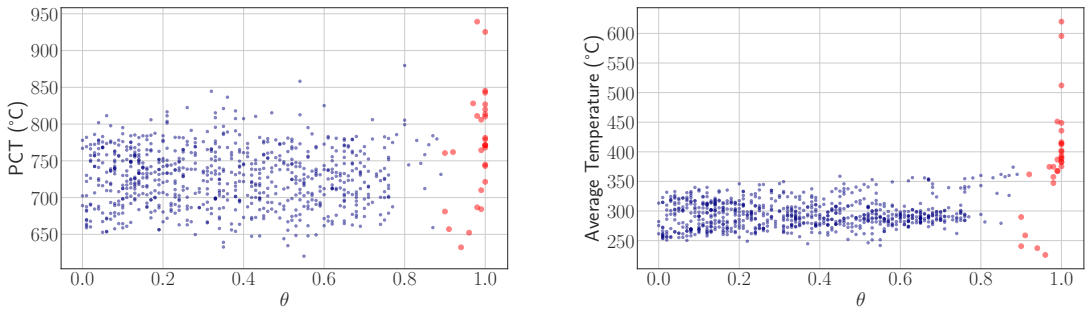

(a) Scatter plot between the PCT and θ

(b) Scatter plot between the average temperature of each transient and θ

Figure 4.11: Scatter plots showcasing the relationship between the PCT and the average temperature of each transient and θ.

The link between inputs and outlyingness score θ is complex, in the sense that their relationship is highly non-linear, and depends on more than a hundred parameters (all of the inputs plus the hyperparameters necessary for the FOD computation). It is however possible to analyze graphically the link between the subspace of of influential inputs (those deemed relevant during the TSA step) $\mathcal{X}_{\text{influential}} := \mathcal{X}_{51} \times \mathcal{X}_{52} \times \mathcal{X}_{70} \times \mathcal{X}_{86} \times \mathcal{X}_{91} \times \mathcal{X}_{97} \times, \mathcal{X}_{\text{influential}} \subset \mathcal{X}$ and Θ, as shown in Figure 4.12.

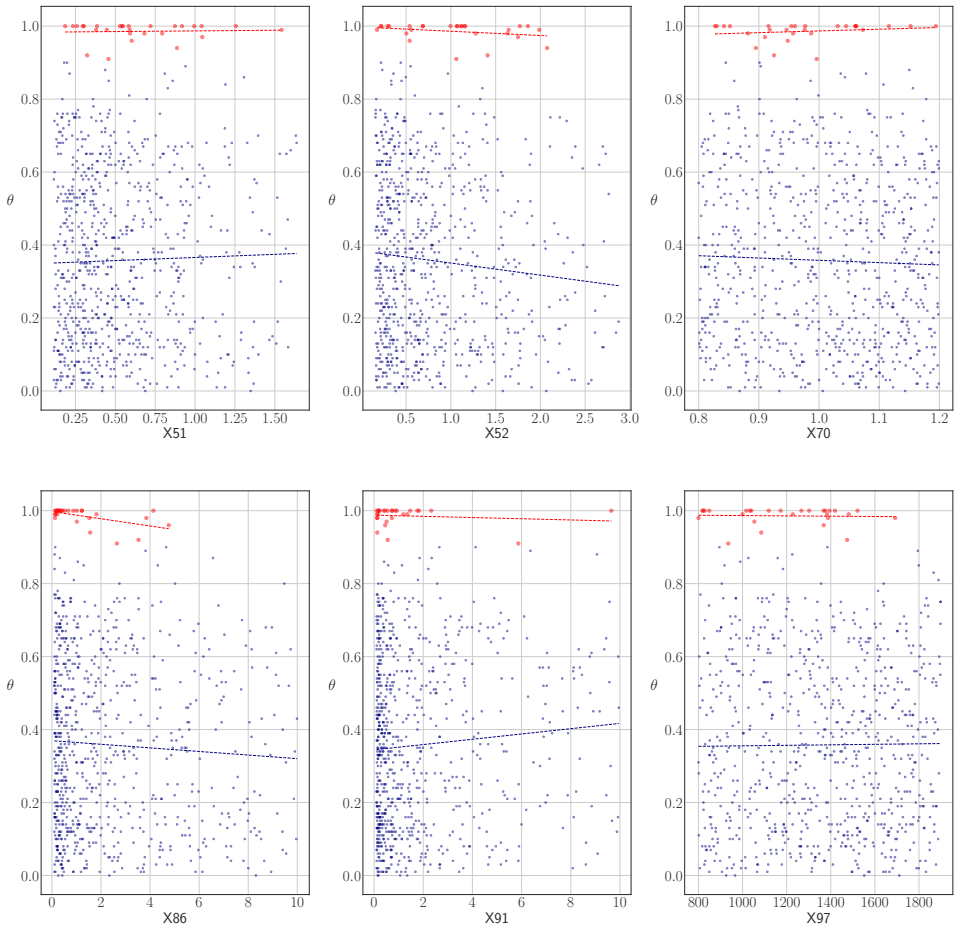

Figure 4.12: Scatter plots of the influential inputs and their corresponding values of θ during the reflood phase. The outliers are marked in red and the lines correspond to a polynomial regression model across the set of inliers and outliers. The outlying points are shown bigger to facilitate visibility.

The only two input variables that showcase a clear link between the outlyingness score θ

are X_{86} and X_{91}, which are the one related to the downcomer. We see that the outliers are mostly restricted to the subdomain where they present their lower values. Specifically, outliers have a higher chance to occur for $X_{86} \in [0, 5]$ and $X_{91} \in [0, 2]$, i.e., when moment transfer between steam and liquid in the downcomer and the heat exchange between the phases are minimized. Knowing that outlying transients are related to more penalizing scenarios, it makes sense that when the heat transfer between the phases is minimized, it will take longer to refill the core. The condensation of the steam present in the downcomer is minimized, and the bottom to top reflood of the core is delayed. It is however more difficult to justify how a lower interfacial friction between the phases could be related to more penalizing scenarios, since the ascending steam would hinder less the injection of water in the downcomer, and subsequently in the core.

A similar analysis may be performed between the inputs and the safety criterion, i.e., the maximum PCT of each transient (as a reminder, it must not surpass the threshold of 1204°C to avoid a severe accidental transient). This link is presented in Figure 4.13.

First of all, we can see that outlying transients present higher values of maximum PCT for their whole range of variation for all the variables in $\mathcal{X}_{\text{influential}}$. Again, it is difficult to establish a clear relationship between the inputs and the PCT due to the high dimensional dimension of the statistical problem and the fact that the sensitivity analysis is performed between $\mathcal{X}$ and Θ. The clearest trend is shown again for variable X_{86}. For the inlying sample, the general trend suggests that the observed influence of X_{86} over the reflood is as we expected. Higher friction values between the phases in the downcomer lead to higher maximum PCT since they hinder the injection of cold water into the core. Conversely, the outlying sample showcases a clear opposite trend, which is not consistent with the expected physical influence of the variable. In particular, whether or not they relate to outlying transients, it is clear that most of the outliers presenting the lowest values of X_{86} lead to the highest maximum PCT values. A similar conclusion is obtained when looking at variable X_{51}, i.e., the multiplicative factor of HTC downstream of the quench front during reflood in the core. This influence is expected, since we observe that lower HTC values lead to higher peaks of temperature due to the reduced heat evacuation in the core.

Figure 4.13 also shows how θ and the temperatures are linked. It is clear that the outlyingness score relates to higher average temperatures of the fuel during the transient, and therefore it is linked to more penalizing scenarios.

It is however clear that these relationships are not indisputable and that they are subject to interpretation, since there is a considerable overlap between the influential variables and the outlyingness score, although the trends are clearer for the parameters related to the downcomer.

However, as it was mentioned earlier in the chapter, another output of interest related to safety in this transient is the amount of coolant present in the core and the RPV, as well as the total uncovered height of fuel in the core during the injection.

Figures 4.14 and 4.15 illustrate the relationship between inputs, the (swollen) level of

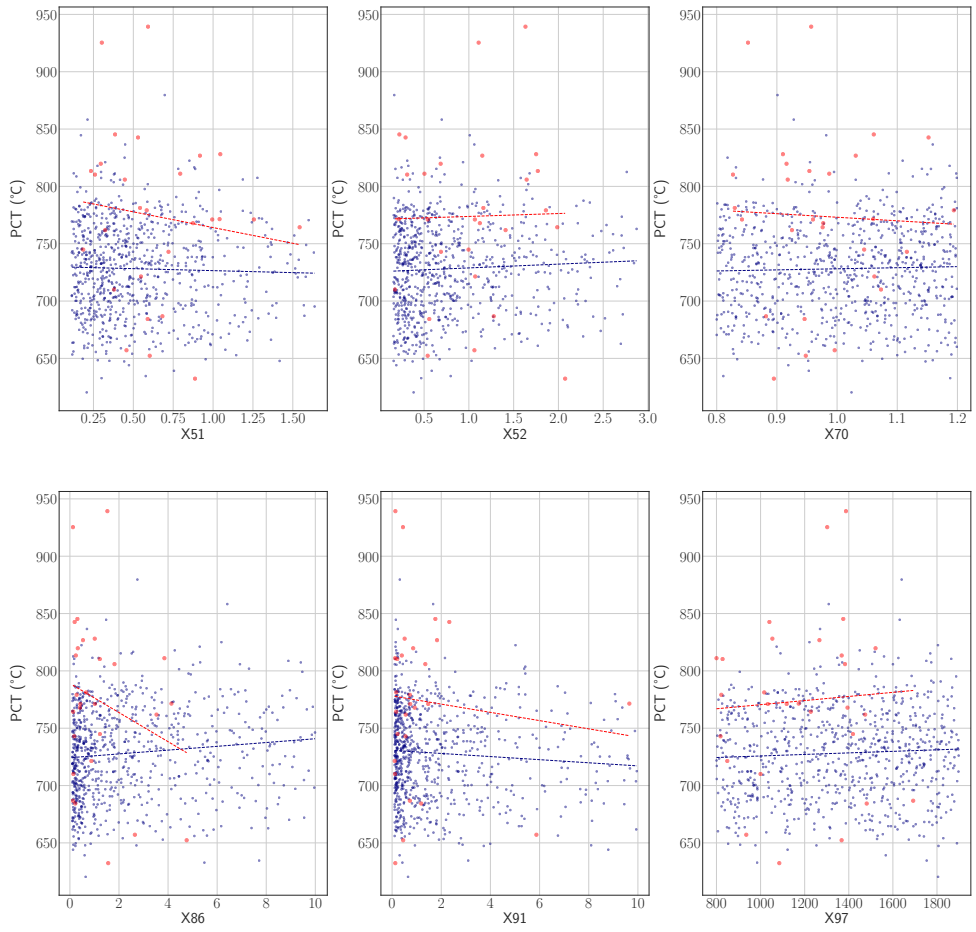

Figure 4.13: Scatter plots of the influential inputs and their corresponding values of PCT during the reflood phase. The outliers are marked in red and the lines correspond to a polynomial regression model across the set of inliers and outliers. The outlying points are shown bigger to facilitate visibility.

water in the core, the total mass of water in the downcomer and the points which correspond to the respective outlying transients.

The most noticeable difference between these figures and the previous ones is how the separation between inlying and outlying transients is much more apparent, suggesting that the physical parameters that better explain the outliers are more linked to the coolant mass in the core that to the fuel temperature. This comes as an advantage of the methodology, which, by taking into account the whole transients, and not only the safety criteria, is capable

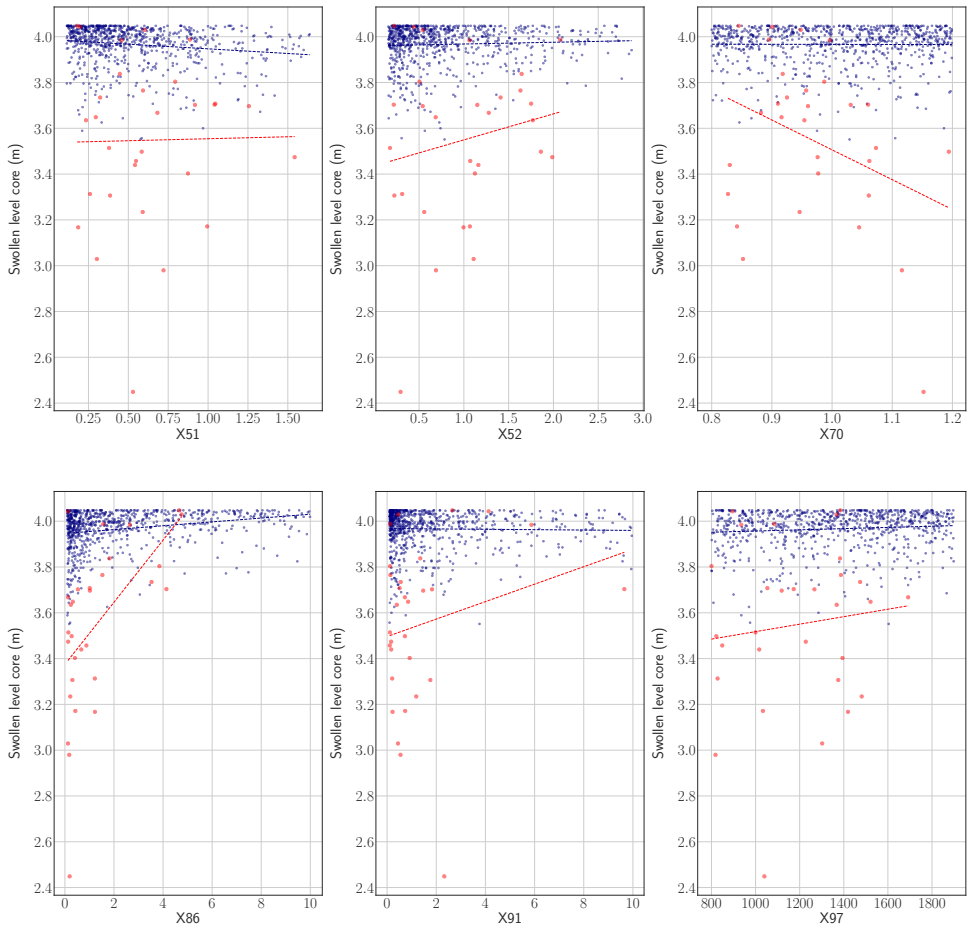

Figure 4.14: Scatter plots of the influential inputs and their corresponding values of swollen level during the reflood phase. The outliers are marked in red and the lines correspond to a polynomial regression model across the set of inliers and outliers. The outlying points are shown bigger to facilitate visibility.

of capturing deeper physical insights than scalar outputs. In this case, outliers found in the set of transients of temperature are better explained by the swollen level of coolant in phase V of the IBLOCA transient.

In the case of the swollen level, not only do inlying and outlying observations present a more clear separation, but the trends of the outlying samples are also more clearly displayed. In particular, variable X_{70}, i.e., the multiplicative coefficient of axial losses due to the ballooning of the fuel rods seems to present an expected behavior in outlying transients. The

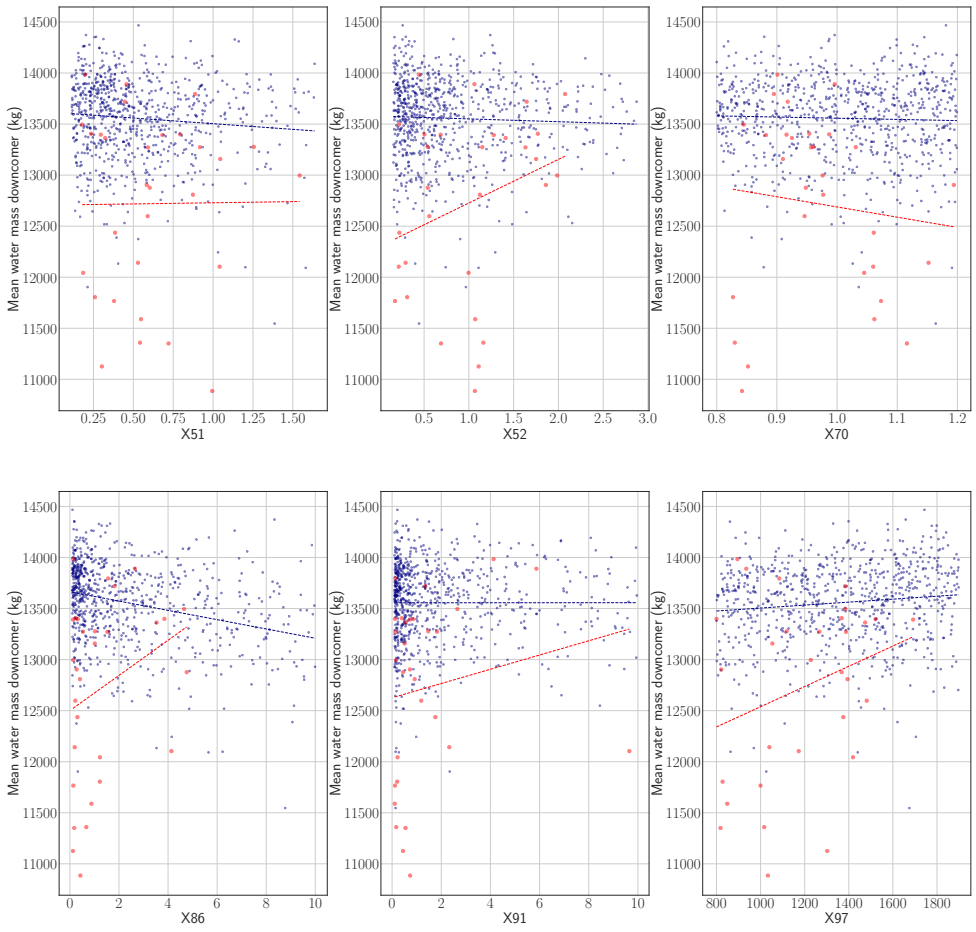

Figure 4.15: Scatter plots of the influential inputs and their corresponding values of water mass in the downcomer during the reflood phase. The outliers are marked in red and the lines correspond to a polynomial regression model across the set of inliers and outliers. The outlying points are shown bigger to facilitate visibility.

trend shows how higher values of head losses largely decrease the average level of water during phase V, hindering the reflood.

In the case of variables X_{86} and X_{91}, the interpretation of their influence is similar to that of their effect on the PCT. X_{91} presents a logical trend in which the increase in thermal transfer between the phases in the downcomer favors in the injection of cold coolant in the core, whereas X_{86} clearly correlates in its lower values ($X_{86} \in [0, 4]$) to larger average times of uncovery of the core during phase V, which is not consistent with the fact that the ascending

steam in the downcomer should hinder less the bottom-up reflood of the core for this set of values.

Finally, these interpretations become even more apparent when analyzing the evolution of mass in the downcomer during the transients (see Figure 4.15), where again the opposing trends between the inlying and outlying sample are even more obvious, with the inlying sample showcasing its expected physical behavior, and the outlying one presenting a non-expected, perhaps non-physical one, since its impact does not follow the expected one presented in Table 4.14.

Finding out which phases of the transient are more influential when analyzing the inlying and outlying transients is far from obvious, although a subsample of outliers are clear magnitude ones. However, the methodological analysis of the intervals through the KW test (see tables B.1 to B.10) clearly showcases that the intervals that better characterize the outliers are those between $[t_4, 367]$s, i.e., after the first uncovery of the core and not during phases I to IV of the transient. An example of these tables is given in Table 4.15 to illustrate this statement.

Table 4.15: KW tests for equality of distributions in each time interval defined by the breakpoint events between the samples of outlying transients and inlying ones for the $h_3(z_s)|_{t_i}^{t_{i+1}} = \mathbb{E}[z_s]|_{t_i}^{t_{i+1}}$ intermediate parameter applied to the maximum cladding temperature. S: same distributions, D: different distributions.

Interval	Statistic	p-value	Conclusion
$[t_1, t_2]$	1.27647	0.25855	S
$[t_2, t_3]$	0.90844	0.34052	S
$[t_3, t_4]$	0.876293	0.34921	S
$[t_4, t_5]$	**11.9712**	**0.00054**	**D**
$[t_5, \infty)$	**42.95961**	**0.00000**	**D**

This is however not always the case for all intermediate parameters, in particular in what concerns the water mass in the downcomer, where the statistical evidence of disparity between the inlying and outlying samples is mostly apparent in the early stages of the transient. In particular, this is the case in the interval between the activation of the ECCS and the first uncovery of the core, as shown in Tables B.8 and B.9. This is natural since it is during these stages that void is formed in the downcomer.

The other major difference is found not to be specifically linked to a particular time frame, but to a physical event. This is the case of the existence of a second uncovery of the nuclear core, as shown by Table B.10, or below in Table 4.16.

Finally, these results can be visualized through Figures B.1 to B.10. In particular, the approximate distributions (through violin plots) and boxplots of θ, as well as the existence of a second uncovery of the core during the transient are shown here (see Figure 4.16).

This figure shows how the existence of a second uncovery of the core is mostly an outlying

Table 4.16: KW tests for equality of distributions regarding the uncovery of the core. S: same distributions, D: different distributions.

Analyzed parameter	**Statistic**	p**-value**	**Conclusion**
Moment first uncovery	0.77815	0.37732	S
Existence of second uncovery	**7.62700**	**0.00575**	**D**

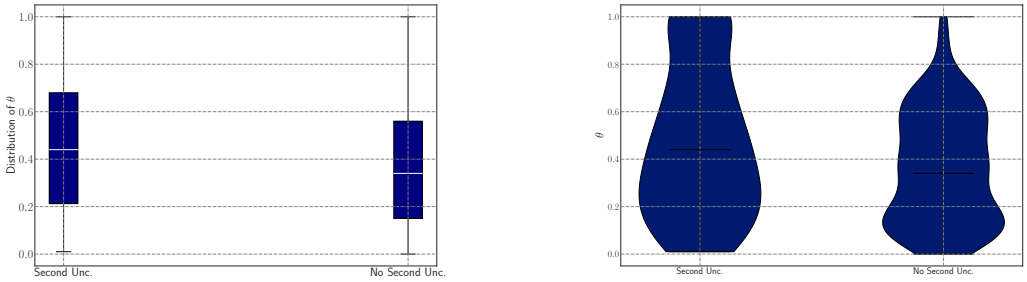

(a) Boxplot. (b) Violin plot.

Figure 4.16: Values of θ for the simulations that do or do not present a second uncovery of the nuclear core after the activation of the accumulators.

phenomenon or, in any case, for transients that present values of $\theta \in [0.8, 1]$. The accumulators are designed to be able to compensate the loss of coolant at the break during the reflood phase by injecting large amounts of pressurized water into the boiler, and therefore a second uncovery of the nuclear fuel during this phase is not supposed to occur.

More insights on the subject are provided in the following section.

4.2.5 Characterization of the outlying transients

Taking all of these parameters into account, we can characterize the outlying transients by specific physical phenomena and events that occur during the related transients.

Outlying transients correlate with higher temperatures of the nuclear fuel, both on average during the reflood phase and regarding the PCT (see Figure 4.11). This effect is related to smaller quantities of water in the nuclear core during reflood, as well as a lower swollen level of water in the core, and longer uncovery periods of time. We can also see that the outlying transients showcase a non-physical trend when comparing the effect that the interfacial friction between the phases has over the refill dynamic of the core. This is also showcased in Figure 4.16, where it is clear that the simulations presenting a second uncovery of the nuclear core systematically present higher values of the outlying score θ.

Explaining the second uncovery of the nuclear core and its outlying nature is far from

obvious. Indeed, this event occurs (in the outlying transients) during the phase V (reflood), and corresponds precisely to the time frame in which the core must be refilled thanks to the coolant injected by the accumulators. In Figure 4.17, we can appreciate the differences between two selected transients, an outlying one and an inlying one. Here we can clearly see how the outlying transient is characterized by a slower blowdown phase (the short stage in which there is a single-phase depressurization of the boiler), in which the emptying dynamic of the core is slower than in the inlying case, followed by a rapid reflood phase after the activation of the accumulators (see Figure 4.17 b). Initially, this could correspond to a non-penalizing scenario in which there is an efficient reflood phase by the accumulators. However, looking at phase V of the transient (which starts around 100s after the beginning), we can easily appreciate the almost instantaneous loss of liquid mass in the core that entails a second uncovery of the nuclear core.

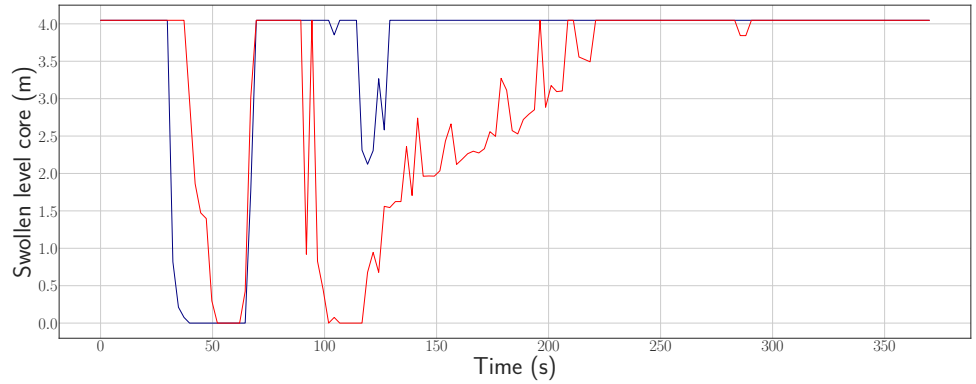

(a) Evolution of swollen level (m)

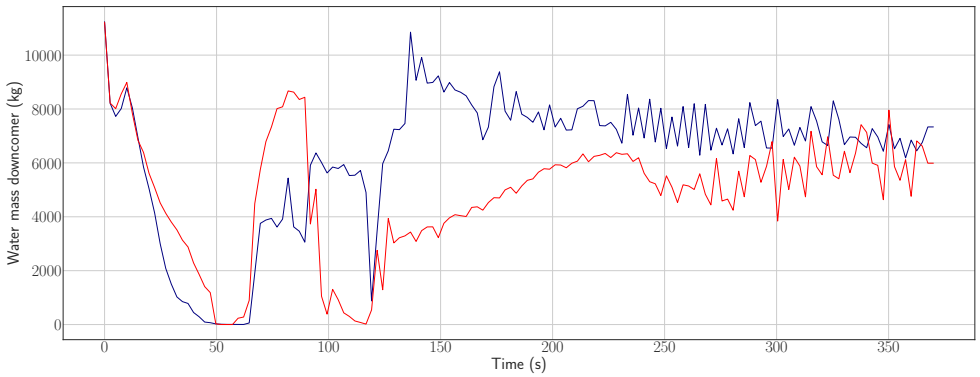

(b) Evolution of water mass in the core (kg)

This effect is not physically expected for two main reasons. Firstly, the accumulators continue injecting cold coolant after this outlying event (see for instance Figure 4.5 (f)), since there still exists a reflood phase in which the nuclear fuel in the core is rewetted, so it cannot be theorized that the accumulators have simply stopped injected water. Secondly, it is necessary

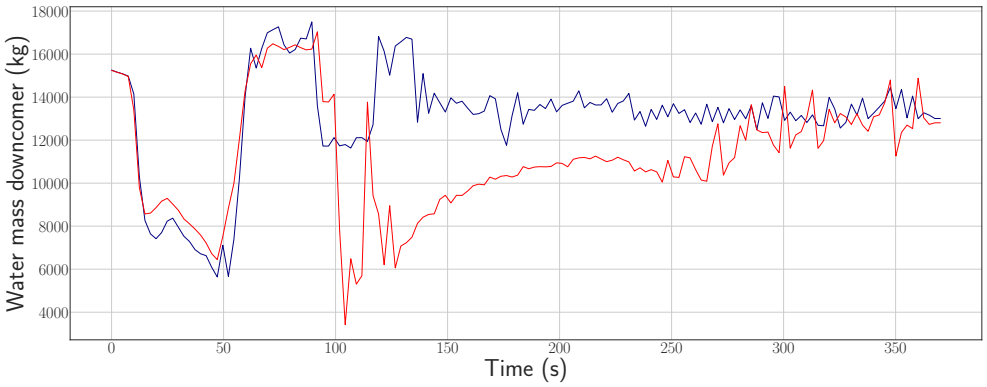

(c) Evolution of water mass in the downcomer (kg)

Figure 4.17: Examples inlying and an outlying transient. Red: Outlying transient. Blue: Inlying transient

to consider the dynamic of the event. This instantaneous vaporization of a large amount of water (around 7000 kg), which is much faster than during the blowdown phase, made at low pressure and with a slight spike of pressure (c.f. Figure 4.18) cannot have a physical origin, since there is no additional heat source, the temperature of the fuel is lowering at this stage, and the accumulators are still injecting cold coolant in the RPV.

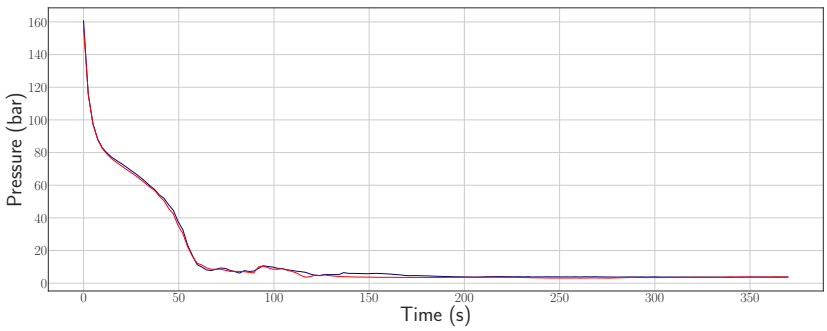

(a) Evolution of primary pressure (bar)

Figure 4.18: Examples of an inlying and an outlying transient. Red: Outlying transient. Blue: Inlying transient.

As a summary of these considerations, Figure 4.19 showcases the differences of distributions between the samples in a more visual way. We can appreciate the differences between the samples that have already been mentioned, and confirm that at least one of the main physical events that characterize the outlying transients is the existence of a second uncovery of the core. That is not to say that there exist no inlying transients that present a second uncovery as well, but their probability of occurrence is much lower.

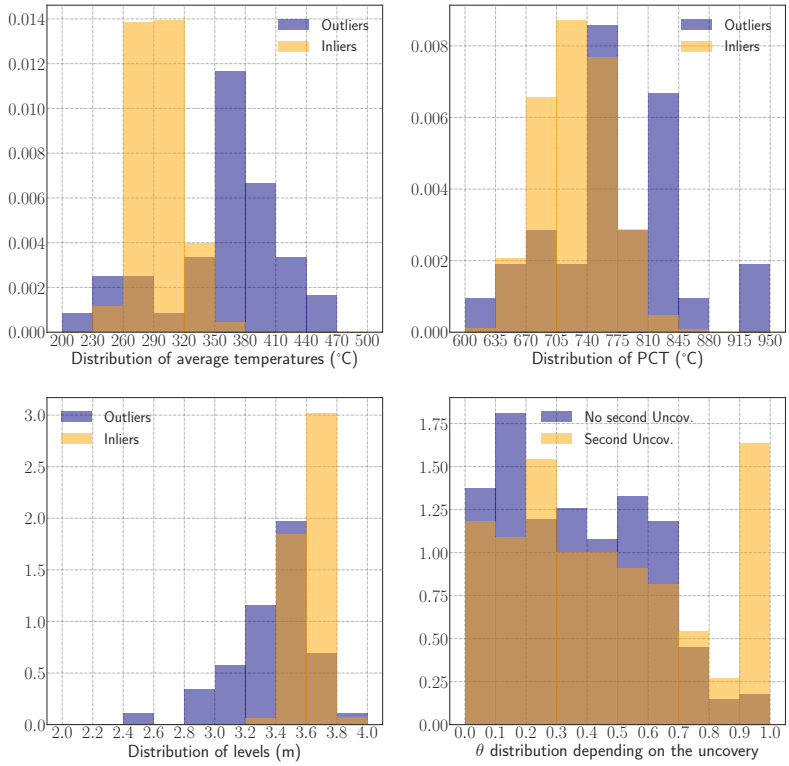

Figure 4.19: Examples of differences of distributions of intermediate parameters the inlying and outlying samples.

In the following section, we shall explain which was the origin of these outlying transients that present a second reflood phase.

4.3 Origin of outlying transients

In this application, the outlying event has been shown to be linked to the emptying and refilling dynamic of the core during the reflood phase. It has also been underlined that the origin of the outliers mainly lies in the reflood phase of the transient (phase V). The analysis of the *CATHARE2* modeling of the transient shows that the outlying simulations are actually caused by an incorrect activation of the *CATHARE2* submodule that manages the reflood phase of the transient.

4.3.1 Reflood modeling

The thermal-hydraulic modeling of the heat transfer during the reflood phase entails the intervention of complex physical phenomena that determine the total energy that is exchanged between the fuel walls and the two-phase fluid and its regime. Before the nuclear core is rewetted, the fuel attains high temperatures and rewetting the surfaces of the fuel rods requires the arrival of large quantities of coolant (Kelly et al., 1993). *CATHARE2* is capable of simulating this process (Lutsanych et al., 2015). The *CATHARE2* modeling of the reflood of the core occurs in several steps. Firstly, the core is cooled in gas convection conditions (core completely uncovered), and once the coolant water is injected, a film boiling (FB) transfer regime (Tong, 1972) is established. This heat transfer regime, inefficient compared to liquid convection or nucleate boiling, is characterized by the formation of a thin layer of steam between the walls and the coolant, which isolates the rods from the coolant and the thermal exchange is performed through conduction and convection. The heat transfer conditions in these situations is still a subject of extensive research and are not completely understood even today (Su et al., 2016). Finally, once the wall's temperature becomes lower than the minimum stable film temperature (T_{msf}), the liquid rewets the cladding, and the heat transfer increases.

In the case of large IBLOCA accidental transients or Large Break LOCA (LBLOCA) ones, the standard laws of *CATHARE2* don't predict accurately the quenching of the core in the bottom-up reflooding phase, which requires the use of a specific submodule of the code in order to compensate this underestimation. This is due to two main factors:

- The axial conduction within the fuel rods is non-negligible and helps the quenching. During the reflood phase, the cooler segments of the fuel rod can be found in the lower part of the core (they are the first to be reached by the injection of water), and the axial conduction of heat from the hotter zones in the upper zones of the fuel rods to the lower ones favors the evacuation of power and the rewetting temperature is reached earlier. This is not configured by default in the *CATHARE2* code and thus requires the use of this additional submodule.
- In the meshes located close to the quenching front, violent vaporization and droplet generation occur and the induced turbulence increases the total heat transfer. Much like in the previous process, this is not taken into account by default.

The impact of the activation the reflood submodule impacts the heat transfer laws through two main modifications:

- A local 2D mesh is superimposed to the considered original 1D mesh that progresses alongside the quench front in order to model the 2D conduction of heat.
- A specific heat flux is added to the heat transfer equation to model the augmented heat transfer thanks to the turbulent flow along the quench front. This term is taken

proportional to the axial wall gradient of temperature. It is then of the form $f = K\frac{T_W}{d_Z}$, where K is a constant, T_W represents the local wall temperature, and Z is the vertical axis that defined the axial meshes of the core.

The last term may be the preponderant term in the heat transfer alongside the quench front, inducing an accelerated cooling of the system when compared to the original transfer laws.

The aforementioned reflood submodule can be used in the following conditions:

- There exist vertical axial elements in the modeling. If the modeling of the system is 3D, then the submodule is only defined in a vertical zone.
- The temperature of the component is at least T_{msf}.
- The rewetting is sufficiently slow for the axial conduction of to play a role. In practice, this translates in a high initial temperature during the reflood, and a limited flowrate of water entering the considered element.
- The quenching is progressive.

4.3.2 Causes of outlyingness and correction

The conditions of the use of the submodule limit the range in which it might be used, and translate into specific physical conditions that must be verified at any point in the transient. For bottom-up reflooding transients, these physical conditions are:

1. Primary pressure. The pressure in the primary must remain below 6bar during the reflooding phase.
2. Liquid mass flux velocity. This condition ensures that the quenching is sufficiently slow for the axial conduction in the mesh to be relevant. The flowrate of the quenching front must remain below 200kg/m^2/s.
3. The power generated in the cladding must remain below 6W/cm^{-2}.

If these conditions are met, the submodule is activated, and the quenching front is defined in the mesh in which the wall is dry in one side and wet in the other. The origin of the outlying transients has been found to be an incorrect activation of the submodule due to an incorrect coding of the aforementioned conditions.

The main differences introduced between the original modeling of the transient and the corrected one are shown in Table 4.17.

Table 4.17: Differences in the activation conditions of the reflood submodule between the original and corrected modeling of the considered IBLOCA transient.

Original modeling	**Corrected modeling**
Not previously activated Primary pressure $<$ 6bar Physical time of simulation $>$ 30s	Not previously activated
	Primary pressure $<$ 6bar
	Physical time of simulation $>$ 30 s
	At least one accumulator has already started the injection of coolant
	The liquid mass flow in the lower mesh of the core is not null
	The void fraction in the lower part of the core is $>$ 0.9

An example of how the changes introduced regarding the activation conditions of the *CATHARE2* quenching modeling have impacted the outlying outputs is showcased in Figure 4.20.

As it can be seen, the beginning of the transient progresses in the exact same manner for both simulations, but they diverge slightly after the start of the reflood phase (at around 60s). The introduced modifications in the modeling have translated into the disappearance of the second uncovery of the core, the activation of the submodule only when the necessary physical conditions are met (most notably, when there is a quench front to model, and not when the core is fully filled), as well as lower PCT values attained during the transient due to the sudden loss of coolant in the core.

4.4 Conclusions

In this chapter we have presented how the developed methodology of analysis can be successfully applied to real industrial use-cases, and constitutes a systematic aid in the comprehension of the progress of nuclear transients. We have described how one of the most widely studied nuclear transients, an Intermediate Break Loss of Coolant Accident can be modeled through *CATHARE2*, and the main intervening physical phenomena of interest that affect nuclear safety beyond the safety margins for this transient.

Several points regarding the contributions of the study must be highlighted:

- The used modeling of the IBLOCA transient represents a real use-case used by EDF, but it was preliminary and did not constitute a basis for the development of safety reports up until after the identified problems with the modeling were corrected by the engineers.

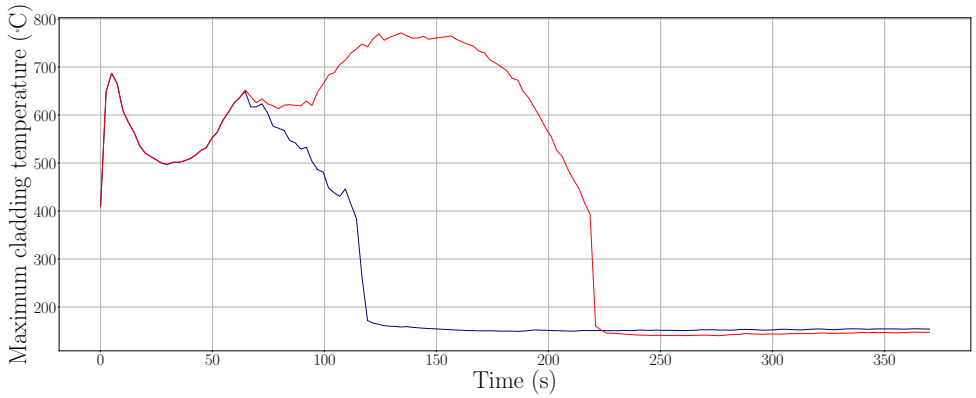

(a) Evolution of maximum cladding temperature (°C)

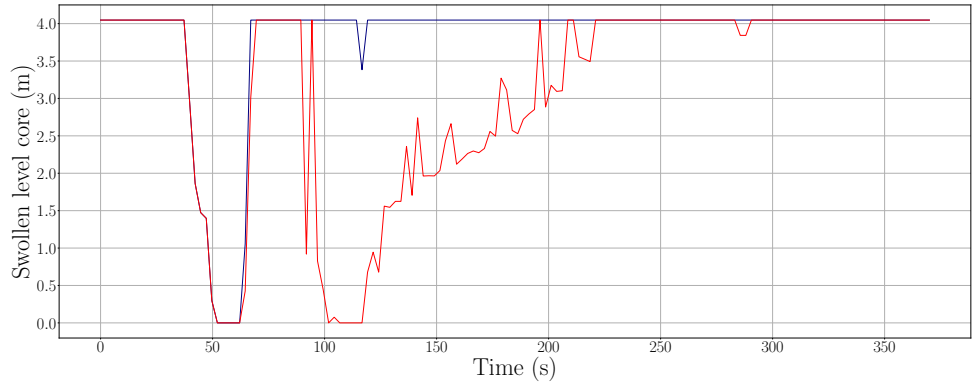

(b) Evolution swollen level of water in the core (m)

Figure 4.20: Examples of the original (Red) and modified (Blue) transients for a set of inputs that induced an outlying simulation in our first analysis.

Having said that, the whole research work presented in this study was performed with absolutely no prior knowledge about the validity of the modeling. We have proven how the presented methodology does not require any prior information about the analyzed transient and how it was capable of highlighting inconsistencies in the simulations.

- The conclusions that have been extracted could not have only been obtained through the close analysis of the safety criterion. Analyzing the safety criterion is the primary way of evaluating the respect of the safety margins in accidental nuclear transients. However, the simulator *CATHARE2* provides a much larger and richer amount of physical information that can be exploited and used in order to improve the knowledge of the analyzed transient.

- The outliers have been linked to both penalizing scenarios (in the sense of the safety criterion, the PCT in this case), and non-physical events in the set of simulations. Recalling the definitions provided in Chapter 2, the former is related to the outliers

understood as extreme events of an underlying stochastic process, whereas the second is related to the more strict definition, as realizations of a different underlying process. In real applications such as this one, both notions cannot be separated since the whole set of simulations is produced by the same numerical model. Nonetheless, this work showcases how both notions can be identified.

5

Analysis of the Pressurized Thermal Shock

Contents

In this chapter, we shall make use of the methodologies presented in previous chapters to analyze Pressurized Thermal Shock (PTS) transients. PTS studies aim to evaluate the risk of failure of some structures the primary circuit due to their sudden cooling by the safety injection water jet injected in the reactor pressure vessel. Although they are studied here for the same kind of initiating transient studied in 4, i.e., Loss of Coolant Accidents (LOCA), PTS events considerably differ from those referred to as IBLOCA in Chapter 4, both regarding the physical phenomena and timeframes at stake. As a consequence, they involve different safety criteria and modeling of the transient, leading to a specific engineering approach different from the one implicating IBLOCA transients. As such, PTS safety assessments offer a complementary illustration of the potential usefulness of the developed methods in this Ph.D.

The chapter is divided as follows: The first section is consecrated to the description of the origin of the transient, the main physical phenomena that impact the progression (and the existence) of the transient, and finally the modeling by *CATHARE2*. Section 5.2 presents the application of the analysis methodology, whereas Section 5.3 relates the found outliers to penalizing scenarios in relation to the safety margins presented in Section 5.1. Finally, the main conclusions are presented in Section 5.4.

Throughout this chapter, it is assumed that the reader is already familiar with the basic components of a PWR NPP, and therefore the main components of the installation (such as the steam generators or the downcomer of the reactor) are not explained once again. Any new element that had not been introduced before will be thoroughly described.

5.1 Presentation of the use-case

In this section the most important elements regarding the physics of the PTS transients are presented, including the main causes of the transient, how the nuclear installation manages the transients, and how it is modeled through *CATHARE2*.

5.1.1 Industrial issue

5.1.1.1 Nature of the risk in case of PTS

The PTS is a widely researched nuclear transient (Mukin et al., 2018; Ruan and Morishita, 2021; Trampus, 2018) since it affects one of the most important components of a NPP, the reactor pressure vessel (RPV). Apart from containing the nuclear fuel, thus being one of the main confinement barriers for radioactive material, it represents the main limiting factor in the lifespan of a nuclear power plant. This is due to the fact that it is the only element that

is impossible or economically infeasible to replace (IAEA, 2010). Therefore, it is subject to numerous studies aiming to understand its aging process better and preserve its mechanical properties. The analysis of the PTS is hence an essential part of the licensing of nuclear power plants, especially if they are to be operated beyond their design life limits.

The risk, in the case of a PTS event, comes from the fact that it corresponds to a situation in which the integrity of the RPV might not be guaranteed. It is caused by the existence of three specific physical conditions (shown in yellow in Figure 5.1). Regarding the thermal-hydraulic (TH) parameters, this accident is characterized by a rapid overcooling of the downcomer wall at high primary loop pressure. This situation may happen in several specific scenarios, including LOCAs, which is studied in the following. These TH conditions induce intense mechanical solicitations in the primary loop structures, among which the RPV is the critical one as it suffers an exposure to the radiation emitted by the nuclear core during the whole lifespan of the NPP. This exposure leads to a shift of the brittle-ductile transition temperature of the RPV steel and a subsequent embrittlement which reduces the component's capacity to withstand a thermal shock. Taking into consideration the potential presence in the RPV structure of undetected flaws generated at the component's manufacturing stage, a PTS event could lead to the initiation of a crack at a flaw tip if the mechanical solicitation comes to exceed the material's resistance. As part of the overall licensing process of PWR, PTS studies aim to justify the innocuity of flaws in the RPV wall by proving the existence of sufficient safety margins as regards the risk of crack initiation.

5.1.1.2 Objectives of PTS studies

When conducting safety studies, the role of the operator of nuclear facilities is not only to exhibit to authorities the numbers and calculation results justifying how these facilities comply with regulatory requirements. They must also show their understanding of the problem at study to prove that they have sufficient knowledge to manage and prevent risks with the highest possible standards in a continuous improvement process. This implies a fine comprehension of the behavior of nuclear systems, both in operation and for potential accidental situations. In the case of PTS studies, some assumptions are usually considered penalizing and thus commonly used in safety assessments. For example, the maximum possible flow rate of ECCS is often supposed to be part of a worst case PTS scenario as it maximizes the quantity of cold water injected. However, this simple reasoning does not take into account potential complex phenomena, including interaction with other parameters implicated in the transient dynamic, such as the effect of the injected flow rate on the depressurization pace during the transient. It is hence necessary, in order to support the line of arguments on which the safety demonstration is based, to support the influence of these assumptions on some key parameters of the scenario. This is even more essential when transient simulations use refined thermal-hydraulic modelings, allowing to represent many physical effects and potentially interacting ones.

Statistical methods allow to explore a whole domain of values for the physical thermal-hydraulic parameters considered uncertain and observe the influence of these parameters on

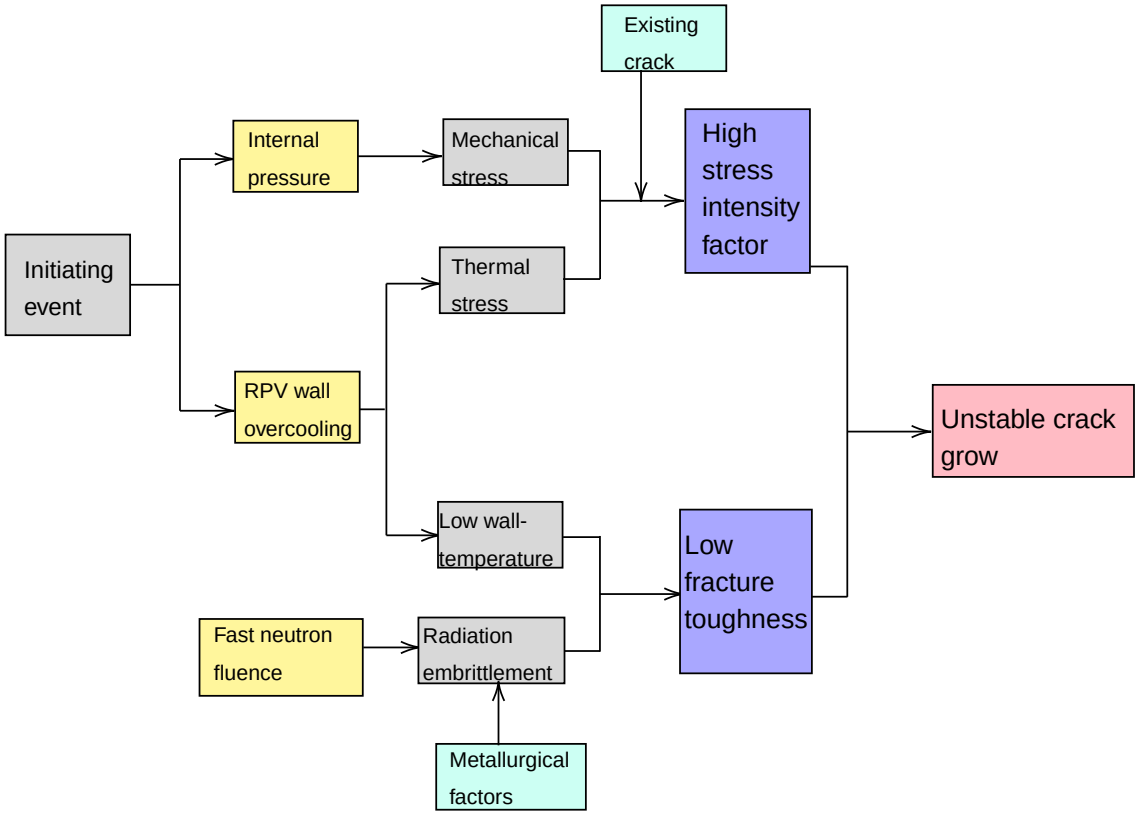

Figure 5.1: Diagram of the main physical phenomena and events leading to the propagation of a fissure on the RPV due to a PTS. Based on Trampus (2018).

the transients without postulating any prior penalizing values. As it will be shown, the outlier detection algorithm presented in Chapter 2 provides valuable insights to determine the actual effect of uncertain inputs of the model on the seriousness of the scenario and confirm the predominance of some variables over others.

5.1.2 PTS risk assessment methodology

The main elements leading to a PTS scenario can be seen on Figure 5.1, where the causes and the initial and final consequences of the accident are marked. These different elements are detailed in this section as well as the way they are modeled to perform PTS studies.

5.1.2.3 Transient leading to PTS events

The initiating events that may lead to a PTS can be classified into two main groups depending on the frequency of the events. The first group is includes scenarios called *anticipated transients*, e.g., those whose occurrence can be expected during the life in operation of the NPP (namely, with a frequency of more than 10^{-2} per reactor year), and which must not represent an actual danger for the safety of the NPP. These transients do not challenge the integrity of the RPV. Transients of the second type are the so-called *postulated transients*. These transients are not expected to happen during the whole lifespan of the installation (frequency below 10^{-2} per reactor year), but they are considered in the design, maintenance and operation of the NPP, or in the subsequent improvements in the safety of the nuclear power plant thanks to safety reassessment studies.

These transients, that may generate a PTS and that are to be examined in the licensing process, are the following (IAEA, 2006):

- **Loss of Coolant Accidents (LOCA)**. As it was shown in the previous chapter, these transients cause an activation of the ECCS systems, which are designed to inject large amounts of cold water in the boiler. Transients for different sizes of breaks and locations in the primary circuit can cause the walls of the RPV to overcool and initiate a PTS. In particular, scenarios that lead to a flow stagnation of the injected water (such as in the case of small breaks) can be penalizing due to the large plumes of cold coolant that originate in the downcomer.

- **Stuck open valves in the boiler**. There exist several valves in the primary circuit of a NPP. Specifically, those existing in the pressurizer may be particularly sensitive due to the steam-water two-phase equilibrium that exists in the component, which have been known to be able to cause opening and closing cycles of their relief valves as a way of regulating the primary pressure. If one of those valves is stuck open at some point, it will cause a pressurized overcooling of the system.

- **Primary to secondary leakage accidents** . These transients refer to those in which a number of tubes in the Steam Generators (SG) rupture, causing a rapid overcooling of the primary and a depressurization. In this case, there exists a risk of repressurization of the primary if the management of the transient requires the isolation of the damaged SG.

- **Large secondary leaks**. As with LOCA transients that affect the piping in the primary system, losses of coolant in the secondary can also represent a risk to the stability of pressure and temperature of the secondary, reducing the pressure in the secondary side of the SG and, consequently, the saturation temperature of the water-steam equilibrium. This can also cause an overcooling of the primary, since during the transient the total heat transfer between both systems will increase. A *common* cause for this transient can be the existence of a stuck-open valve in the secondary.

- **Actuation of high pressure injection systems**. This is a particular transient that can only arrive in nuclear power plants whose ECCS presents high pressure pumps that can inject cold water into the boiler at a higher pressure than the normal operation pressure of the system. Older NPP can possess this kind of pumps and, if they activate inadvertently, they can entail the injection of plumes of cold water in the walls of the downcomer during normal operation, also increasing the primary pressure in the process and the risk of a PTS.

- **Accidents resulting in a cooling of the RPV from outside**. Although unlikely, there exist some possible origins for a reactor cavity flooding, causing an overcooling of the RPV. For instance, through the activation of the containment spray system.

As it is one of the most critical scenarios regarding the integrity of the primary loop components, the LOCA transient is often the one studied the most in-depth. For this reason, we will focus on this particular scenario for the study of the PTS.

5.1.2.4 Mechanical loading

As already mentioned, a hypothetical PTS transient implies a risk for the irradiated areas of the RPV because of the potential presence of manufacturing defects. Several factors contribute to the formation of flaws in the vessel's steel, including the alloying elements content and values of physical parameters at the successive steps of the manufacturing process (casting, forging, cladding laying ...). In practice, calculations are performed for a semi-elliptical underclad flaw, which is a penalizing scenario (Leilei and Guoxing, 2014). This configuration is shown in Figure 5.2, where a and c represent the geometric parameters of the preexisting crack.

In case of a PTS event, the sudden cooling of the vessel by the ECCS generates a important temperature gradient in the radial direction which results in a transitory increase of tensile stress in the RPV wall. To provide a tentative visual representation of this thermal-mechanical phenomenon, one can imagine the downcomer of the RPV as two concentric cylinders, such that when the inner walls cool down due to the effect of the injected cold water by the ECCS, it contracts and pulls the outer wall, whereas the outer wall does the opposite, as illustrated in Figure 5.3. The induced stress tends to fracture the steel and open a crack at the flaw tip, as represented in Figure 5.4. The figure showcases the mode I failure in fracture mechanics caused by tensile forces only as it is the relevant one for the kind of flaw considered in this chapter. For the sake of completeness, other failure modes include Mode II, caused by shear stress parallel to the plane of the crack and perpendicular to the crack front, and Mode III, where the shear stress is parallel to the front.

The exact physical modeling of the phenomenon is inferred through the fracture mechanics theory (yun Fu et al., 2019), which allows to calculate the magnitude of the mechanical loading at the fault's location. The relevant quantity to represent this solicitation of the material is called *stress intensity factor*, noted K_I (Irwin, 1957).

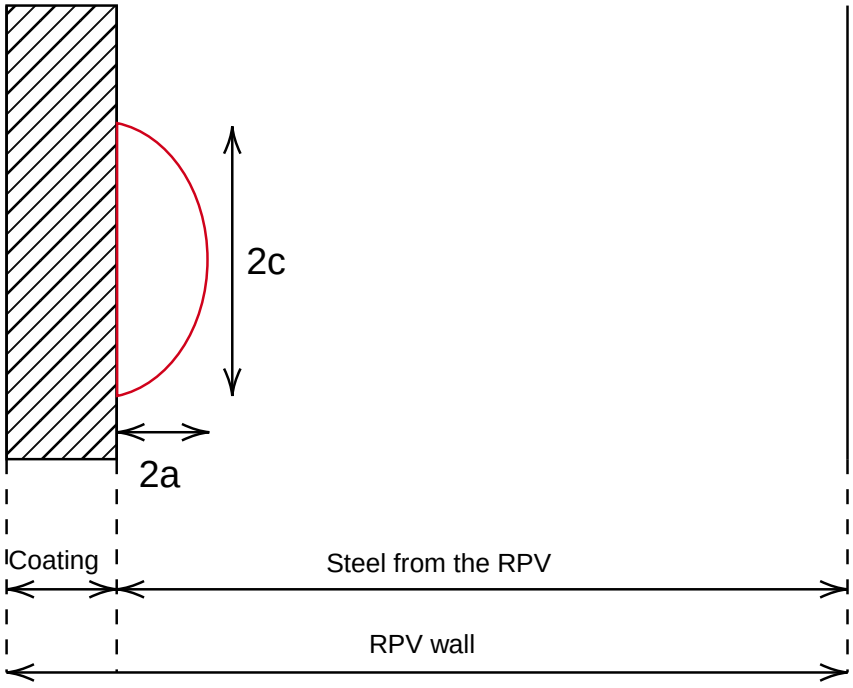

Figure 5.2: Preexisting semielliptical undercladding crack in a RPV.

The mathematical formulation of the stress intensity factor is not unique, and may be written in different forms depending on the modeling of the stress field surrounding the crack (Janssen et al., 2004). A typical approach (Jhung et al., 2008) is to consider the solution of the J-integral (a method of calculation of the energy release rate in a crak, see Cherepanov (1967) for reference) for the failure mode I:

$$K_I = \sqrt{\frac{JE}{1-\nu^2}} \tag{5.1}$$

where J represents the value of the integral, E is the Young's modulus of the material, and ν represents its Poisson ratio.

5.1.2.5 Resistance of the RPV material

To each thermal-hydraulic transient in the primary loop corresponds a K_I transient (an evolution of the K_I) in the vessel at the flaw tip, which also depends on the flaw dimensions and on the mechanical characteristics of the component's material. A RPV is mainly composed of ferritic iron that guarantees the necessary ductility in order to withstand the demanding conditions of the boiler (around 320°C and 155 bar), with the associated mechanical stresses involved in operation. The assessment of the risk of crack initiation consists in comparing

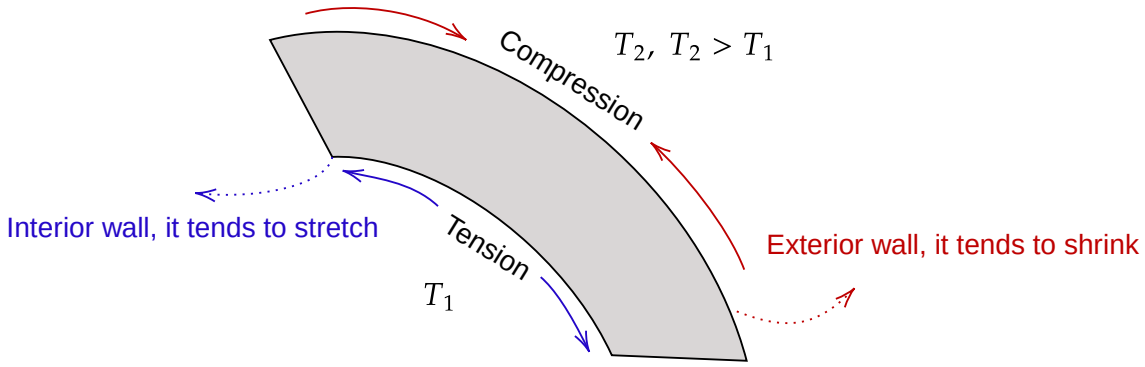

Figure 5.3: Illustration of the mechanical stresses in the event of an overcooling of the RPV.

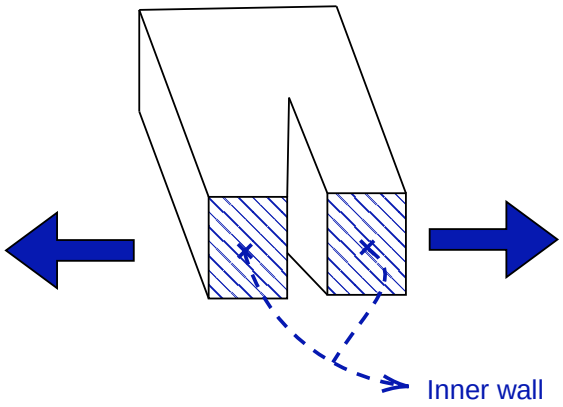

Figure 5.4: Tensile forces acting upon the inner wall that presents an already existing fracture.

this solicitation with the material resistance, the innocuity of the flaw being proved whenever the calculated loading remains below the resistance of the component's steel.

This resistance is given by the *fracture toughness* of the material, noted K_{IC}, which is defined as the critical value of stress intensity factor above which a fracture may occur. It can be experimentally established by applying a mechanical loading to a material sample with an increasing strength until a crack initiates at the notch tip. As an intrinsically aleatory phenomenon, the fracture may occur at different strength levels. However, the material's temperature during the experiments strongly impacts the observed K_{IC} value, so that K_{IC} can be modeled by an increasing function of T. For french facilities, the calculation methodology is based on K_{IC} curves provided by the ZG annex of the RCC-M code, which writes

$$\begin{cases} K_{IC}(T) = 40 + 0.09(T - T_{ref}) + 20\exp[0.038(T - T_{ref})] & \text{in the brittle domain} \\ 240.93\text{MPa} \cdot \sqrt{\text{m}} & \text{otherwise} \end{cases}$$

where T_{ref} corresponds to an experimental baseline temperature used in the definition of the law.

5.1.2.6 Embrittlement of the RPV material

Several degradation mechanisms can be postulated for the primary circuit structures due to the highly demanding physical conditions above mentioned, such as thermal aging or corrosion. However, as regards the specific risk arising from a potential PTS scenario, the predominant degradation effect comes from the high energy neutron (> 1 MeV) flux generated by the core. This exposure of the parts of the RPV surrounding the core causes several irradiation effects resulting in a global degradation of the steel's resistance to fracture.

As an example, some of the neutrons emitted by the core are absorbed by the iron crystal lattice of the RPV and transfer their kinetic energy to the atoms of the RPV steel. The absorption of a neutron may cause the displacement of an atom in the lattice (neutronic scattering), which will embed itself somewhere else in the crystal, normally in an interstitial site, creating a vacancy in the material where this atom used to be located. In practice, the kinetic energy of the initial neutron is sufficiently large to provoke a *cascade of displacement*, meaning that the initial atom displaced will likely displace other ones which will in turn displace more atoms and so on until a complete discharge of the kinetic energy.

This embrittlement results in a diminution of the fracture toughness at a given temperature of the material, which is reflected by a shift of the critical toughness curve in the transition domain. This temperature shift of the reference temperature to characterize the brittle-to-ductile transition hence summarizes the effect of irradiation as regards the component's ability to withstand a mechanical loading. For practical reasons, this temperature shift is measured through Charpy impact tests using V-notched specimens.

The Charpy V-notch (CVN) test is a standardized industrial procedure (Saba et al., 2019), commonly used because of its easiness to implement. The test measures the total energy needed to fracture a material (also called resilience) in standardized conditions. Charpy tests are done at different temperatures, showing a transition zone between brittle (low resilience) and ductile (higher resilience) behaviors. A reference energy level is then chosen to establish the temperature shift between unirradiated and irradiated materials. This procedure is illustrated in Figure 5.5, on which one can see an estimation of the results of a set of CVN experiments performed by the Oak Ridge National Laboratory (ORNL).

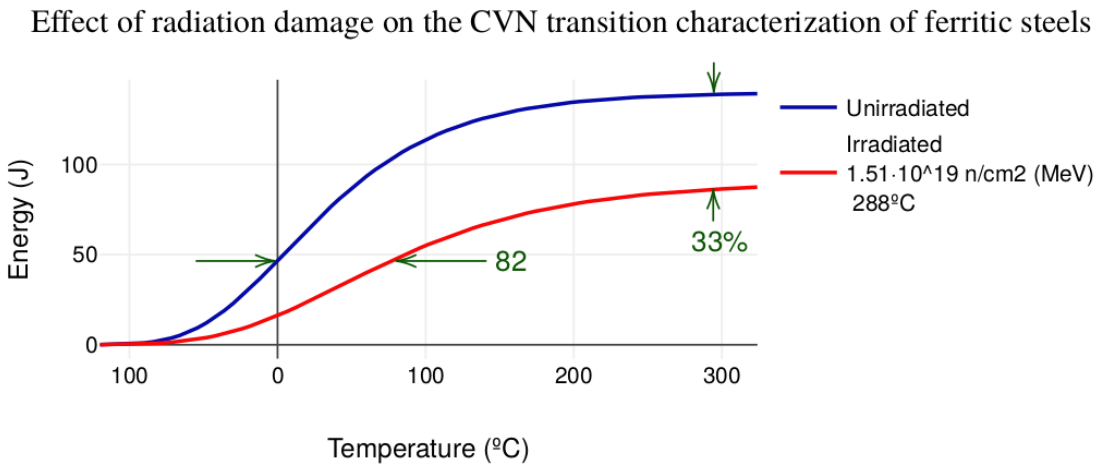

Figure 5.5: Schematic effect of radiation damage in a ferritic steel, such as the ones used in RPV. Results for Charpy Impact Test (CIT). Approximated curves from the experimental ones showcased in Araneo and D'Auria (2012).

5.1.2.7 Margins and safety criteria

The effect of the embrittlement phenomenon described in the previous section can be visualized on the fracture toughness (K_{IC}) curve in the (T,K) domain, where T is the temperature of the steel (in °C) and K the stress intensity factor (in MPa$\sqrt{\text{m}}$). On Figure 5.6, one can see the RCC-M curve for K_{IC} (see formula at the end of section 5.1.2.5) in this domain, as well as the effect of the embrittlement induced by the material irradiation. This irradiation causes a shift of the reference temperature, and hence of the K_{IC} curve, leading to a diminished resistance to mechanical solicitations.

As already exposed, the possibility of a crack initiation at the tip of the postulated flaw corresponds to transients for which the loading (stress intensity factor $K_I(t)$) comes to exceed the resistance of the RPV material (K_{IC}). In the same (T,K) space, we can represent the path followed by the steel during the transient (see Figure 5.7). It starts at a high temperature, before the thermal shock as such and the subsequent increase in K_I, and ends with the stabilization of the RPV structure temperature at a constant and low value. Throughout the transient and the progressive cooling of the steel, the stress intensity factor strongly increases until reaching one or several peaks, and might cross the K_{IC} curve at some point.

The risk criterion which is most commonly used in PTS studies to summarize the severity of a transient, which is called *margin factor* (MF), is the minimal value of the ratio $K_{IC}(t)/K_I(t)$ over the time frame of the simulation. The risk of a crack initiation is proved to be null whenever the MF value remains above 1, the *margin* being the smallest gap between K_{IC} and K_I during the transient, or more rarely the gap between the MF and the critical threshold 1.

An alternative criterion to the MF, which consists in comparing the loading to the resis-

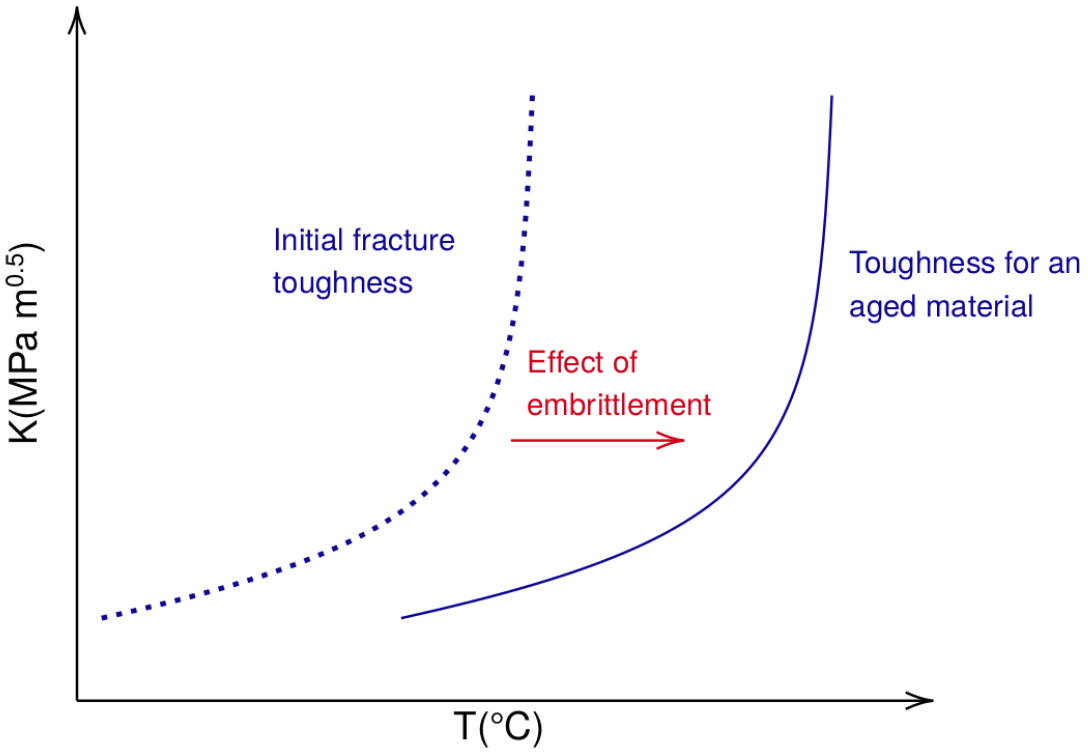

Figure 5.6: Effect of the embrittlement on the fracture toughness curve.

tance at each time step, is the *temperature margin* (TM), which is defined as the minimal value of the $T_{FT}(t) - T_C(t)$ difference, where T_{FT} is the temperature of the steel at the flaw tip and T_C is the (virtual) critical temperature for which K_{IC} would equal the $K_I(t)$ value at time t. The interest for this criterion comes from that it can be easily converted into a remaining operating time, as the aging of the RPV material, which is the main limiting factor of the reactor's lifespan, is directly linked to the reference temperature shift.

Now that the fundamentals of the physical origin of the PTS risk have been established, the following section will describe the transient itself.

5.1.3 Simulation of PTS transients

5.1.3.8 Thermal-hydraulic phenomenology

As it is natural, the main phases in which the transient may be divided largely depend on the initiating event that is considered among those presented in the previous section. In the present study, we consider a LOCA transient that largely differs from the one presented in Chapter 4. The interest of doing this is twofold. Firstly, there is an intrinsic interest in testing the methodology against a new application case whose physical phenomena are noticeably different, and second, in this case the safety criterion may not be directly calculated from the

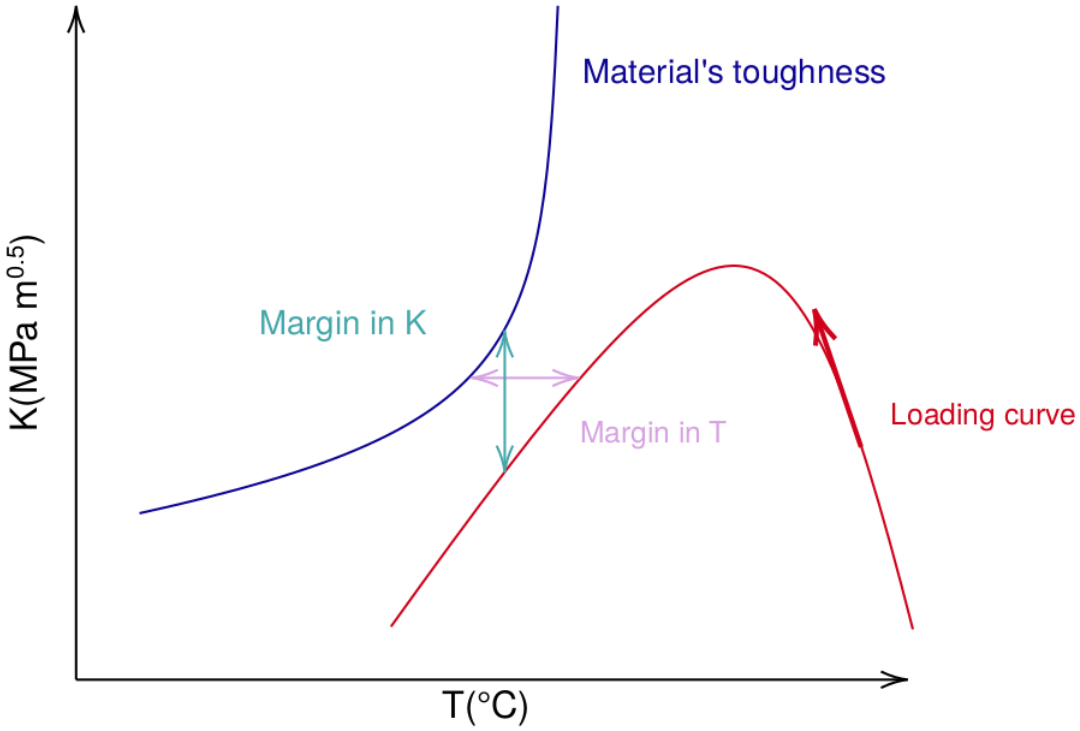

Figure 5.7: Representation of safety criteria and margins in K and in T in the (T,K) domain.

sample of output functional data.

The basic elements of the transient are presented in Table 5.1.

Table 5.1: Basic characteristics of the considered PTS scenario.

Characteristic of scenario	**Physical value**
Reactor	900MWe
Break size	$3'' = 7.62$ cm
Position of break	Hot leg
Penalizing hypothesis	Maximized residual power
Aggravated scenario	Loss of Emergency Diesel Generators (EDG)

Some comments can be made regarding these characteristics. Firstly, note that the 900MWe nuclear reactor corresponds to the oldest ones currently existing in the French nuclear fleet, and they are the ones which have been exposed to a higher neutron fluency during their years of operation. More recent systems (such as 1300MWe and 1450MWe reactors), have been exposed to the irradiation for a shorter period of time, and also have implemented systems that protect the RPV from neutron fluence in advance during their lifespan. The break size of 3 inches classifies this transient as an small break LOCA (SBLOCA), unlike the

one presented in Chapter 4. Therefore, we shall observe important differences in the progress of the transient, most notably in the depressurization rate of the boiler.

The other conditions (maximized residual power and break in the hot leg) are chosen since, in other exploratory studies (not referenced here due to confidentiality issues), they have shown to lead to the most penalizing scenarios. We will see how, conversely to the use-case of the previous chapter, a number of simulations do not respect the safety criterion in this chosen transient.

The transient may be divided into three main parts, showcased in Table 5.2.

Table 5.2: Main phases of the LOCA transient leading to a PTS risk.

Phase	Description
A	This phase covers the time frame between the opening of the break in the hot leg of one of the primary loops and the automatic shutdown of the reactor.
B	It corresponds to the period between the automatic shutdown of the reactor and the intervention of the operators of the NPP.
C	It comprises the instants after the intervention of the operators up until the reactor is led to a safe state.

The first main difference between this application case and the one presented in Chapter 4 is the fact that the automatic shutdown of the reactor is not as instantaneous after the opening of the break in the piping. The automatic shutdown occurs on the low pressure signal in the primary, which is reached close to 23 seconds after the beginning of the transient. The other main difference is the fact that the operators of the NPP can intervene in the progress of the transient, which was not possible in the previous case, where it had to be dealt with in the short term through the automatic mechanisms and systems of the plant. Operators are considered to begin their intervention so as to lead the reactor to a safe state exactly 20 minutes after the shutdown signal, and the whole phase C is influenced by their actions.

5.1.3.9 CATHARE modeling

The *CATHARE* modeling of the nuclear power plant used to simulate the LOCA that originates the PTS risk is similar to the one presented in Chapter 4, albeit one notable difference.

The modeling of the both the primary and secondary side of the NPP are showcased in Figures 5.8 and 5.9.

The *CATHARE2* modeling of the LOCA transient that originates the PTS is a somewhat simplified version of the one presented in the previous chapter. In essence, all systems present in both the primary and secondary circuits remain the same. The reader can find a detailed explanation in Section 4.1.2 of Chapter 4.

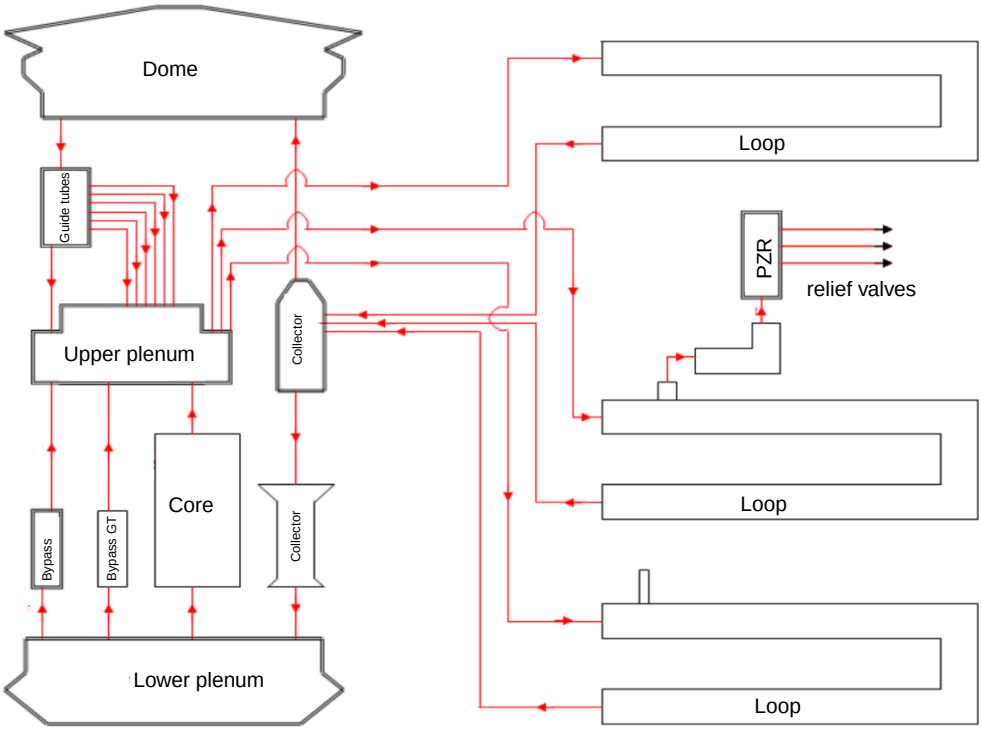

Figure 5.8: *CATHARE2* modeling of the primary circuit of the NPP for the PTS transient system-scale analysis

The main difference with respect to the aforementioned modeling is the treatment that is made of the nuclear core. In this application, the severity of the transient is characterized by the thermalhydraulic parameters in the downcomer, conversely to the previous use-case, in which the phenomena that took place in the nuclear core were the ones that established the boundaries of the safety margins through the peak cladding temperature of the fuel.

Here the nuclear core is simply modeled through a 1D axial element, such that possible 2D or 3D phenomena occurring in the core are not represented. This simplified version of the core still allows to simulate the general thermalhydraulic parameters and the thermal exchange between the fuel and the coolant thanks to corresponding *CATHARE2* modules.

The modeling of the downcomer is divided into two parts. Firstly, there exists a 0D *volume* element in the higher part of the downcomer modeling the annular collector in which the mixture of the coolant coming from the three loops is made. In particular, it is connected to the cold legs of the circuit. The junction between the loop in which the ECCS inject the cold water in case of accident is assumed to be the penalizing place of the circuit regarding the PTS, which is the reason why the mechanical calculation of margins is generally performed here, thus assuming that the preexisting flaw in the material is located precisely at this point.

The annular collector is connected to the annular space, which is modeled in the same way as the downcomer presented in the previous chapter. This cylindrical element receives the mixed coolant from the annular collector and links to the lower plenum of the RPV, from

which the coolant ascends to the nuclear fuel.

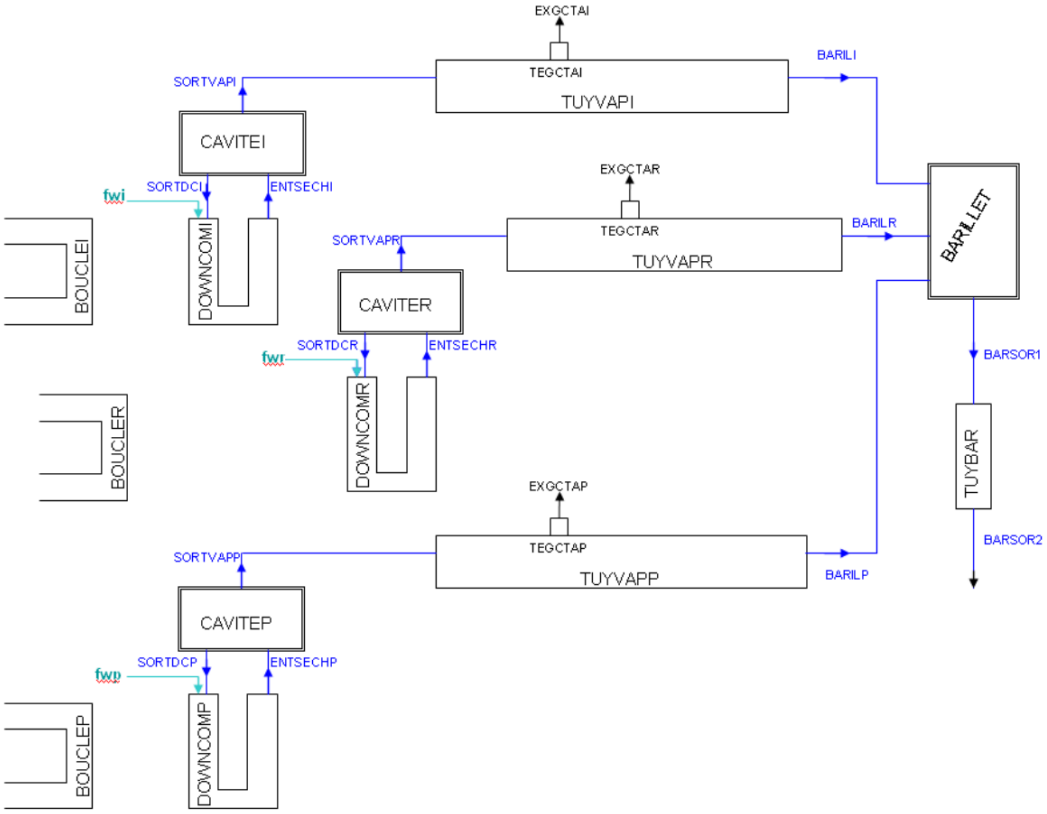

Figure 5.9: *CATHARE2* modeling of the secondary circuit of the NPP for the PTS transient system-scale analysis

5.1.3.10 Workflow of the transient simulation

The evaluation of the risk associated with a PTS transient involves two different calculation steps each one using a specific software. The first step consists in simulating the thermal-hydraulics of the reactor during the accident. This is done via the *CATHARE2* modeling presented in the previous section, which implements a 3 inch break LOCA. At the end of the transient simulation, the *CATHARE2* code provides the values of all the necessary thermal-hydraulic quantities for the ulterior computation of the safety criteria, namely the primary pressure, the water mass flow in the downcomer and the fluid temperature in the downcomer. Safety criteria are calculated through a thermal-mechanical model allowing to solve the heat equation within the RPV wall and the strain and stress fields, depending on the thermal-hydraulic conditions imposed to the structure during the transient as well as the characteristics of the flaw and the parameters of the RPV material. This part of the workflow is performed thanks to the *CUVE1D* code which also implements a calculation of the fracture toughness, to finally deliver the margin factor (MF) values.

Making use of the notations of previous chapters, the mathematical formulation of the

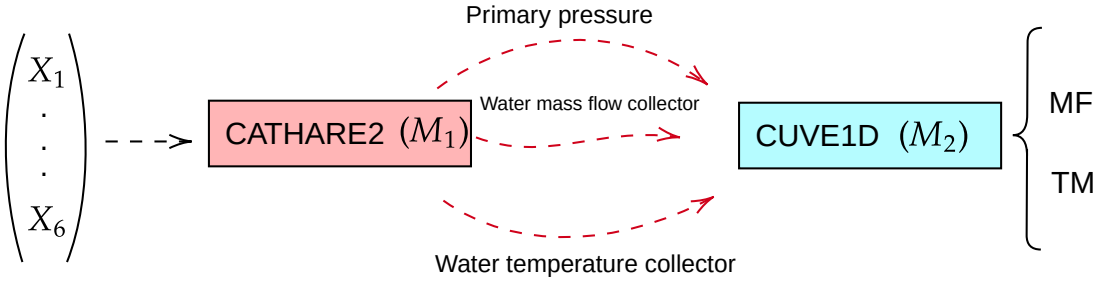

Figure 5.10: Workflow for the PTS margins calculation

chained codes can be written as it is seen in the expressions (5.2) and (5.3)

$$\begin{aligned} \mathcal{X} \subset \mathbb{R}^d &\mapsto \mathcal{F}^* \subset \mathcal{F} \\ X &\to Z = \mathcal{M}_1(X) \end{aligned} \tag{5.2}$$

$$\begin{aligned} \mathcal{F}^* \subset \mathcal{F} &\mapsto \mathcal{Y} \subset \mathbb{R}^q \\ Z &\to Y = \mathcal{M}_2(Z) \end{aligned} \tag{5.3}$$

where $\mathcal{X} = \prod_{j=1}^{d} \mathcal{X}_j$ represents the space of input parameters of the numerical simulator $\mathcal{M}_1$, i.e., *CATHARE2*, and the elements $Z \in \mathcal{F}$ correspond to the multivariate functional output belonging to the Hilbert space $\mathcal{F}$ that serves as input to the second simulator. This second simulator, i.e., *CUVE1D* and noted $\mathcal{M}_2$ is fed the multivariate functional sample Z and provides the corresponding safety criteria introduced in Section 5.1.2.7.

Specifically, for this exploratory study with a simplified *CATHARE2* modeling of the transient, we consider $d = 6$ input parameters for $\mathcal{M}_1$ (detailed the following section), 3 thermalhydraulic functional outputs of the simulator, and $q = 2$ outputs indicators of the transient severity. The overall calculation workflow is illustrated in Figure 5.10.

5.1.3.11 Uncertain inputs

The present modeling of the transient corresponds to a preliminary study that searches to analyze the effect of the safety injection systems on the severity of the thermal shock. The uncertain parameters considered are hence those concerning the characteristics of safety in-

jection pumps, the temperature of the injection water and the characteristics of accumulators.

The ECCS comprises two different safety injection systems. The first one is a bench of two high pressure pumps which is automatically started as soon as the reactor shutdown signal is triggered. High pressure pumps allow injecting water in the primary loop from the early instants of the LOCA transients when the primary pressure falls rapidly but is still close to its nominal value (155 bar). They deliver a rather constant flow rate - although increasing with the pressure decrease - until reaching the conditions allowing to switch from high pressure to low pressure injection means. Low pressure pumps present a rather different behavior as the flow rate they deliver strongly depends the pressure at the spouting point, such that flow rate increases steadily with the decrease in pressure.

The injection yield of the pumps, as a function of the output pressure, is inferred from design requirements of the ECCS and periodic tests realized on the pumps. However, the exact characteristics of both high pressure and low pressure injection systems cannot be accurately known and the flow rate of the pumps can be considered as one of the uncertain parameters of the scenario. To account for this uncertainty, for each injection configuration defined in operating the rules, *min* and *max* laws are set as lower and upper bounds for the ECCS injection flow rate (see Figure 5.11). Coefficients ranging from 0 to 1 are introduced, allowing the exploration of all intermediate laws between the envelope *min* and *max* ones. To account for the existence of two different injection systems (high and low pressure) two independent coefficients are used for the laws corresponding to each of the two systems. For each combination of values for these two coefficients (α_{HP} and α_{LP}), the corresponding laws are merged by a specific routine so as to obtain a physically realistic characteristic of the overall ECCS.

The injected water is taped from a water tank located outside the main nuclear building, which is connected to other hydraulic systems of the reactor. Consequently, its temperature is subject to constant variations depending on meteorological and operating conditions, within bounds defined by the design and licensing requirements of the reactor.

During the transient, the compensation of water leakage due to the break on the primary circuit is supported by the discharge of boroned water by accumulators. Accumulators are pressurized reservoirs from which this additional amount of water is pushed in the primary loop as soon as the primary pressure falls below the initial conditioning pressure in the accumulators. Both the initial enthalpy of the water contained by the accumulators and the pressure within are uncertain quantities. These accumulators are connected to the safety injection pipe through a discharge line in which the water is also subject to a pressure loss, which is itself uncertain. This last uncertainty is accounted for in the considered *CATHARE2* modeling through a friction coefficient in the discharge line of the accumulators.

The six uncertain input variables considered in the exploratory study are summarized in Table 5.3.

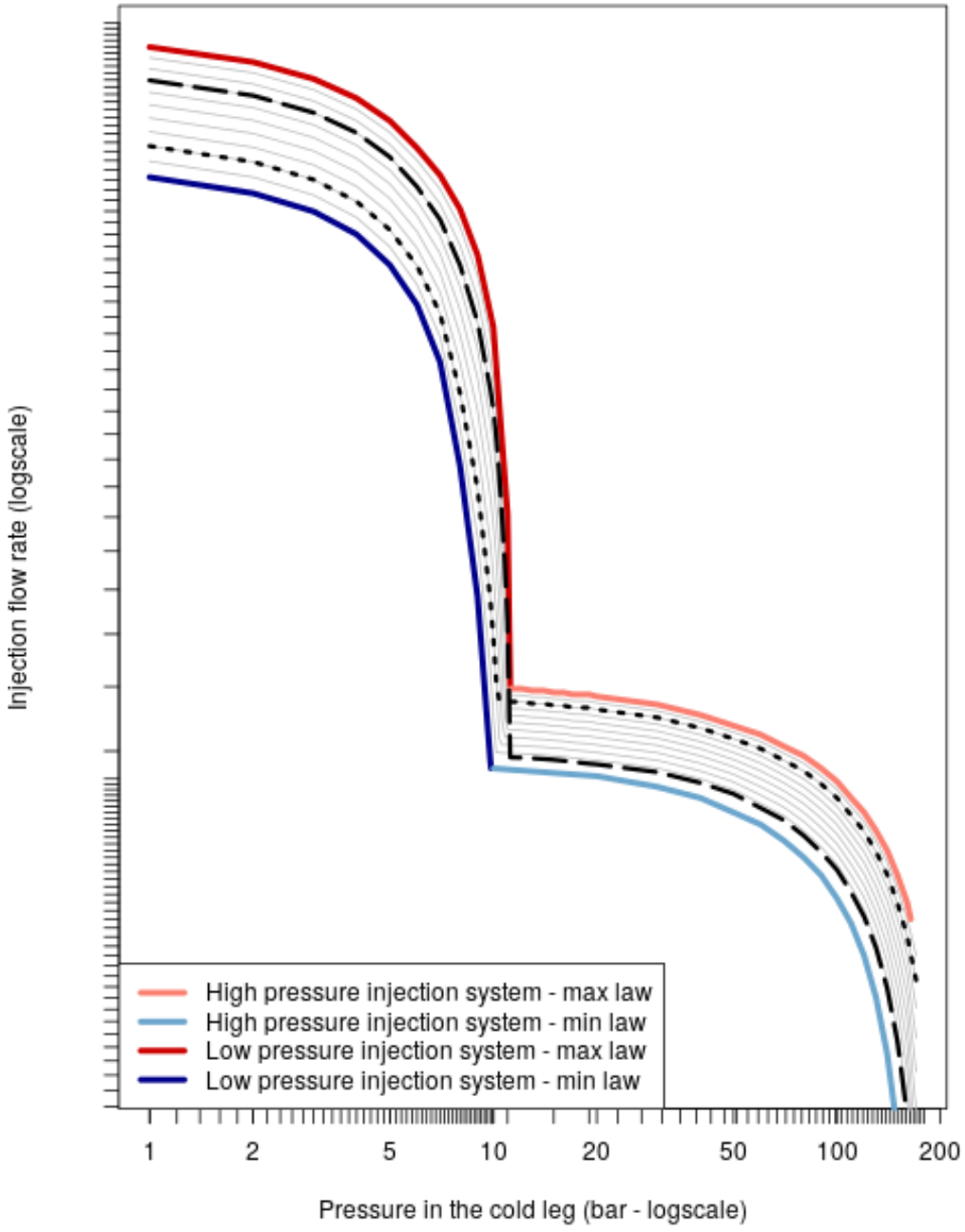

Figure 5.11: Min and Max laws for the ECCS with two instances of intermediate laws. Dashed line: $\alpha_{HP} = 0.15$ and $\alpha_{LP} = 0.7$; Dotted line: $\alpha_{HP} = 0.8$ $\alpha_{LP} = 0.2$.

5.2 Application of the methodology

In this section we shall make use of the developed methodologies presented in the document to the use-case presented in this chapter.

Table 5.3: Uncertain input parameters of the *CATHARE2* modeling of the LOCA transient susceptible of originating the PTS.

Variable	Physical meaning	Units	Law
X_1	Initial enthalpy of the accumulators' water	J/kg	$\mathcal{U}[33740, 108880]$
X_2	Initial pressure in the accumulators	bar	$\mathcal{U}[41.37, 43.85]$
X_3	K/A^2 friction in the discharge line of accumulators	m^{-4}	$\mathcal{U}[800, 1900]$
X_4	Initial temperature water reservoir for ECCS	°C	$\mathcal{U}[7, 60]$
X_5	Water flow coefficient high pressure ECCS (α_{HP})	-	$\mathcal{U}[0, 1]$
X_6	Water flow coefficient low pressure ECCS (α_{LP})	-	$\mathcal{U}[0, 1]$

5.2.1 Preliminary considerations

As with the previous chapter, some preliminary elements must be considered in the analysis. First of all, the functional outputs of interest in this case, and the ones more closely linked to the safety criteria (the margins), are the liquid temperature in the annular collector (in the downcomer), the water mass flow, and the primary pressure. These are the outputs that are taken as inputs of the code *CUVE1D* and which more closely impact the nature of the PTS.

Other essential elements in the analysis are selecting the breakpoint events in which we shall divide the transient. We can recall the phases of the initiating LOCA presented in Section 5.1.3.8, considering the reactor shutdown, as well as the starting instant of operator's actions. These events delimit the basic frontiers of the transient in engineering studies, but the phases present very different intervening physical phenomena. In order to retrieve more homogeneous time sub-domains regarding the thermalhydraulic parameters of interest (liquid temperature, mass flow and pressure), we shall add two breakpoint events to the analysis. They are the loss of natural circulation (LNC), which was introduced in Section 4.1.1.2 of Chapter 4, and the possible existence of a late PTS, which may occur in the late stages of the transient through a late overcooling while the boiler is still pressurized.

The breakpoint events are summarized in Table 5.4.

As before, we denote $\mathcal{T} \subset \mathbb{R}$ the physical time interval in which the simulations take place, that is $\mathcal{T} \coloneqq [0, T]$s, $T = 3700$ (s). The set of breakpoint events writes $\tau_b \in \mathcal{T}, \tau_b = \{t_1, t_2, t_3, t_4\}$. They are illustrated in Figure 5.12. Finally, similarly to the previous chapter, we consider the intermediate variables : $h_1(z_s)|_{t_i}^{t_{i+1}} = \max(z_s)|_{t_i}^{t_{i+1}}$, $h_2(z_s)|_{t_i}^{t_{i+1}} = \min(z_s)|_{t_i}^{t}{}_{i+1}$, $h_3(z_s)|_{t_i}^{t_{i+1}} = \mathbb{E}[z_s]|_{t_i}^{t_{i+1}}$.

Table 5.4: Considered breakpoint events for the LOCA transient leading up to a PTS. The provided times of occurrence are approximated and depend on the individual progression of the transient in each case.

Event	**Approximate moment of occurrence** (s)	**Notation**
Automatic shutdown of the core/Injection ECCS	30	t_1
LNC	300	t_2
Beginning of operators' actions	1200	t_3
Late PTS	2400	t_4

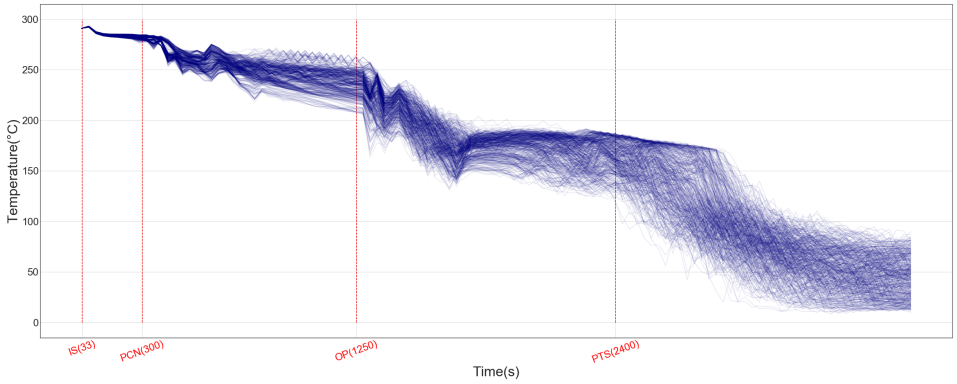

Figure 5.12: Illustration of the considered breakpoint events for the PTS transient over the liquid temperature in the collector of the downcomer.

5.2.2 Design of experiments and functional outlier detection

In this exploratory analysis, we aim at optimally exploring the space of input variables, $\mathcal{X}$, in order to better capture the space of possible functional outputs provided by *CATHARE2*. This is done through a LHS design (see section 3.3.2 of Chapter 3). The $d = 6$ input variables are sampled and considered to be independent in order to generate the design of experiments, $E = \{X_{i,1}, ..., X_{i,d}\}_{i=1}^{N}$, for $N = 1000$, as in the analyzed use-case of Chapter 4. We use the L_2 discrepancy (Damblin et al., 2013) as space-filling criterion, which allows to quantify how a given distribution associated to a set of points deviates from a perfectly uniform one. The centered L_2 discrepancy writes:

$$C_2(E) = \left(\frac{13}{12}\right)^2 - \frac{2}{N}\sum_{i=1}^{N}\prod_{k=1}^{d}\left(1 + \frac{1}{2}|X_k^{(i)} - 0.5| - \frac{1}{2}|X_k^{(i)} - 0.5|^2\right) + \frac{1}{N^2}\sum_{i,j=1}^{N}\prod_{k=1}^{d}\left(1 + \frac{1}{2}|X_k^{(i)} - 0.5| + \frac{1}{2}|X_k^{(j)} - 0.5| - \frac{1}{2}|X_k^{(i)} - X_k^{(j)}|\right) \tag{5.4}$$

which must be minimized in order to obtain the desired optimal design.

The quality of the exploration of the space can be seen through the pairwise 2D projections of E, which are illustrated in Figure 5.13. As we can see, there exists a good coverage of the input space without any appreciable spurious patterns in the design.

The application of the FOD methodology has been restricted to the set of outputs of *CATHARE2*. Since the temperature of the injected water is known to be the most influential with regard to the severity of the PTS transient, the methodology is applied to to the set of liquid temperature in the downcomer as outputs of the design of experiments, E. This yields the set of curves presented in Figure 5.14. We also obtain the set of estimators of $\theta \in \Theta, \Theta = [0, 1]$, represented as $\{\theta_i\}_{i=1}^N$.

It can be appreciated that, much more than in the IBLOCA case of Chapter 4, this application represents a true challenge of functional data interpretation and visualization. The preliminary inspection of Figure 5.14 (top) shows a set of curves difficult to analyze and interpret by itself. The detection of any potential outliers is impossible without dedicated tools for two reasons. Firstly, the curves are numerous and close to each other, restricting the possible outliers to purely shape ones, and preventing their detection through visual inspection. Secondly, the absence of any magnitude outliers does not allow the selection of a subsample amongst the curves that could be analyzed independently by experts on the transient that could provide insights that explains the outlyingness.

It will be shown how the transient may be analyzed and linked to the safety criteria through the use of the outlyingness score θ. The histogram of values of θ is shown in Figure 5.15. We can appreciate how it is skewed to the right, due to the calculation procedure, which subtracts the more outlying curves from the sample and will assign them a higher outlyingness value since they are not taken into account in the modeling of the underlying distribution.

5.2.3 Sensitivity Analysis

The TSA analysis (TSA, Marrel and Chabridon (2021) of the input parameters over the considered scalar output $\theta \in \Theta, \Theta = [0, 1]$ is performed through the permutation tests of the HSIC measures (Meynaoui, 2019) in the critical domain $\{\mathcal{S} \subset \Theta | \theta > 0.9\}$.

The influential variables are presented in Table 5.5.

There is a clear distinction here. We see that the variables related to the injection of cold

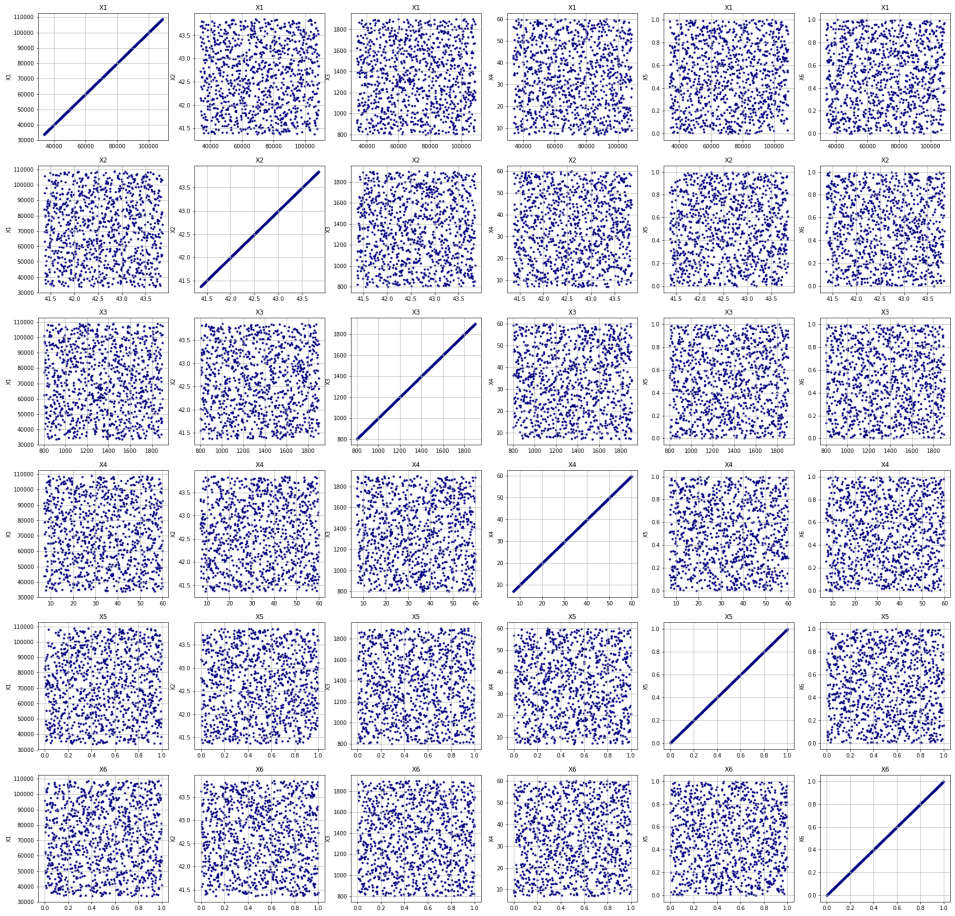

Figure 5.13: Pairwise bivariate projections of the $d = 6$ input variables.

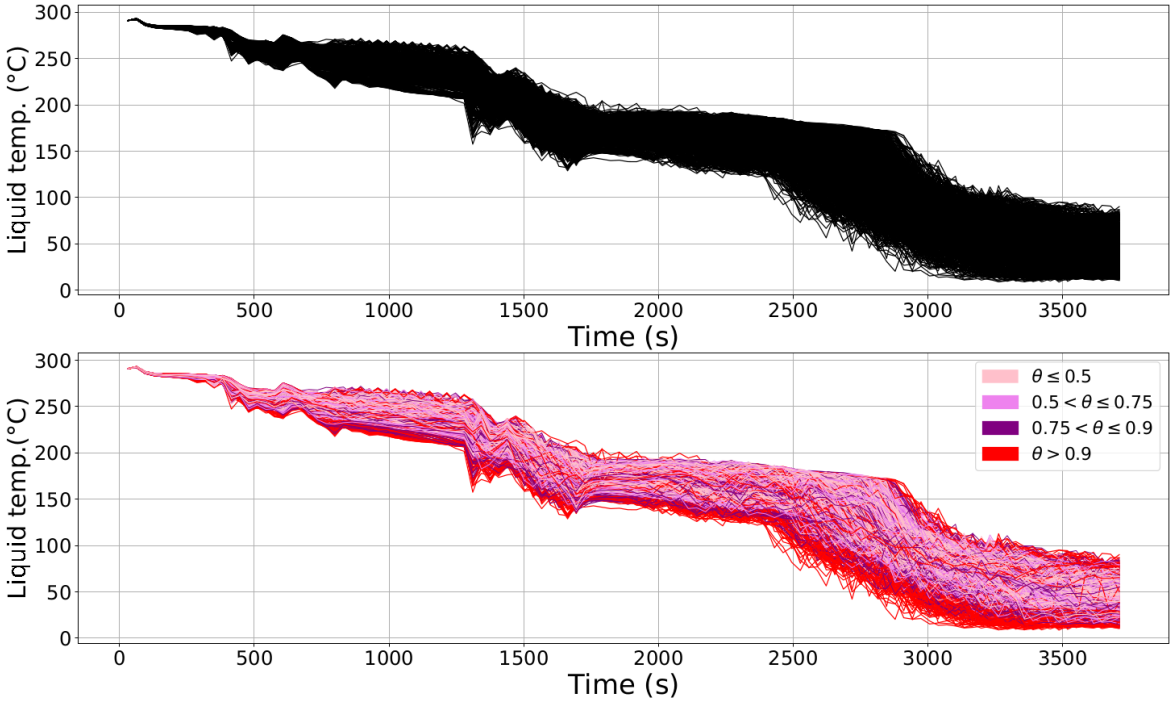

Figure 5.14: Top: set of outputs of liquid temperature in the collector for the design of experiments E. Bottom: Application of the FOD methodology to this set of functional outputs, showcasing different levels of outlyingness measured by θ.

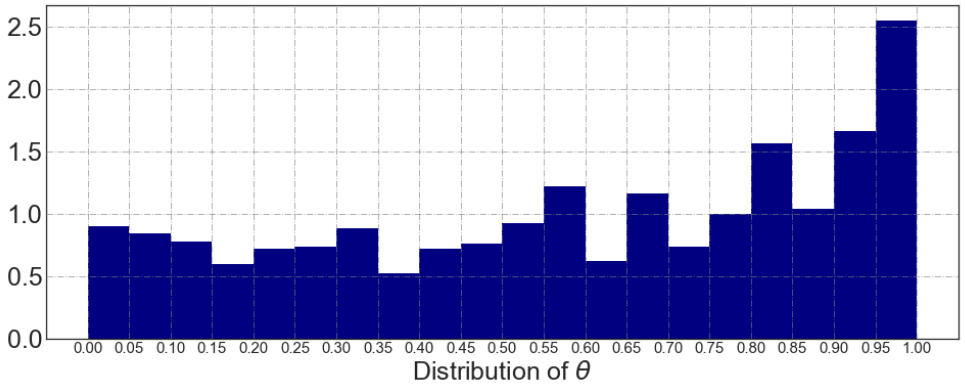

Figure 5.15: Histogram of $\{\theta_i\}_{i=1}^N$ for the PTS application.

Table 5.5: Identified influential variables according to the TSA through HSIC measures in the $\mathcal{S}$ domain. The influential variables are clearly distinguished, and do not depend on the choice of the significance level α for the test. Any standard choice of $\alpha = 0.01, 0.05$ or 0.1 yields the same set of influential variables.

Variable	**Physical meaning**	**Units**	***p*-value independence test**
X_1	Initial enthalpy of the accumulators' water	J/kg	0.68
X_2	Initial pressure in the accumulators	bar	0.32
X_3	K/A^2 friction in the discharge line of accumulators	m^{-4}	0.45
X_4	Initial temperature water reservoir for ECCS	°C	0.0000
X_5	Water flow coefficient high pressure ECCS	-	0.0000043
X_6	Water flow coefficient low pressure ECCS	-	3×10^{-11}

water by the accumulators do not present a relevant influence over the outlyingness of the transient. This is especially relevant if we consider that they were precisely the parameters related to this systems that lead to more outlying transients in the previous IBLOCA case. In fact, the variable X_1 had been fixed in the previous modeling of the transient to a penalizing value, since it was already known that it had an influence over the PCT (safety criterion).

In this case, the three parameters related to the ECCS system that inject cold water before the primary pressure falls below the threshold of the accumulators are the ones that lead to more outlying transients. All these variables, X_4, X_5 & X_6. define the cooling dynamic of the primary system (the boiler) during the majority of the transient, where X_4 describes the temperature of the tank of water that feed the pumps of high and low pressure ECCS. Naturally, this largely influence the temperature of the plumes of water that arrive to the downcomer before they are mixed in the collector and descend to the core. Variables X_5 and X_6 determine the regime of injection of the ECCS pumps, in that they fix the pressure and volumetric flow of both trains of pumps.

Finally, as showcased in Figure 5.16, it can be seen that there exists a clear separation between the inlying and outlying samples when considering their associated safety margins. There is a very clear correlation between the penalizing scenarios (those whose margin falls below 1) and the outlying transients. There also exists a minor number of simulations whose outlying nature is linked to particularly safe transients. This is due to the generality of the detection methodology, which is not designed to specifically identify penalizing situations, but outlying ones. Nonetheless, the link between outliers and penalized configurations is clear.

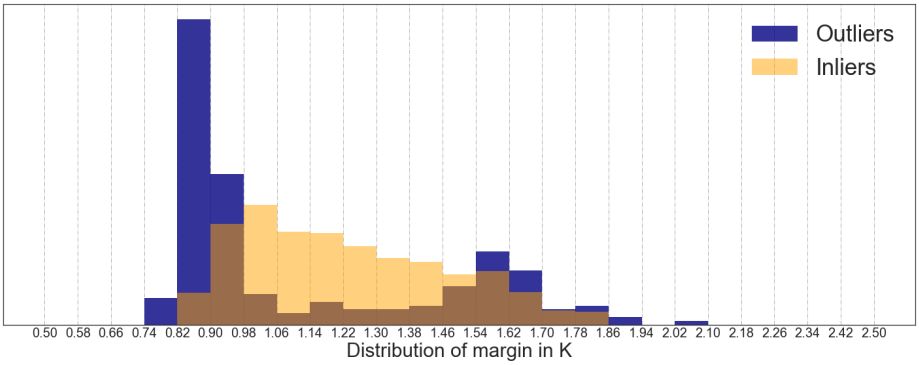

Figure 5.16: Distribution of margin factors for the inlying and outlying samples.

5.2.4 Comparison of samples

The results of the comparisons between inlying and outlying samples for the relevant functional outputs of *CATHARE2* can be found in Appendix C.

The first thing to notice is that the inlying and outlying samples for each physical parameter can be considered to present different distributions in each time interval considered after the reactor trip. This proves that the bulk of outlying thermalhydraulic transients (the initiating SBLOCA ones) are actually outlying in the whole time domain. This is coherent considering that the variables that have been shown to present the highest influence of all are those related to the activation of the ECCS (X_4, X_5 and X_6). This occurs approximately 30 seconds after the break in the primary opens in the hot leg, so their influence is felt throughout the whole transient. Another important remark concerning the outlying samples is their degree of outlyingness. In the KW test, the value of the test statistic (or, analogously its corresponding p-value), is representative of how much the samples differ, and therefore p-values that differ in several orders of magnitude imply that the compared samples are more different in certain cases. This question arises since most of the p-values in the compared samples are present values below 10^{-7}, and the differences may be judged to not be significant. However, looking for instance at Table C.3, we see that although the mean temperature of the outlying transients is significantly different from the inlying ones throughout the whole transient, it is in the late stages of the transient (most notably, after the eventual late PTS arrives), that these temperatures are shown to diverge the most. This is confirmed looking at the corresponding violin plots in Figure C.2, where it is clearly shown how around the 2400s of transient (approximate instant of the late PTS), the temperatures between the samples largely diverge, whereas the differences in $[t_1, t_4]$, although existing, are much less obvious.

This was simply an example of how even though the samples are quantitatively judged to differ during the whole transient for all the functional outputs and the intermediate parameters, they still showcase it in different degrees, which is important when analyzing the origin of the outlying samples.

For this application, we can quantitatively appreciate that outlying samples are characterized by lower minimum temperatures, especially in the range of time around the occurrence of the PTS (Figure C.1). This is penalizing from the overcooling point of view, but this factor also depends on the overcooling rates, not only the absolute values of temperature. Conversely, outlying transient showcase higher maximum and mean temperatures (Figure C.2) in the interval between the start of the operators' actions and the possible PTS. This translates to a higher risk of PTS due to the more rapid cooling rate necessary to attain these temperatures.

Regarding the primary pressure, higher values during the transient, and especially in the second half of the thermalhydraulic transient, when the PTS is more likely due to the overall temperature of the water in the primary and the plumes of cold water, are penalizing when considering the PTS. Higher primary pressures favor higher tension stresses over the RPV wall (see Figure 5.3), and Figure C.4 shows how these pressures are particularly higher in the outlying sample precisely in the time frame of the PTS.

Finally, we observe that outliers are related to higher rates of water flow in the collector (Figures C.5 and C.6). This element relates to higher convection coefficient between the coolant and the wall of the RPV, which can be penalizing if it occurs at the more sensitive point in the transient regarding the PTS (already low temperatures and sufficient pressure).

All in all, the results seem to indicate that the outlying samples present on average more penalizing physical values regarding the PTS, and that the most influential variables are those concerning the injection temperature of the water of the ECCS, as well as the flow regimes imposed by the high and low pressure pumps of the same system.

As a visual aid to help understand the influence of the variables over the analyzed functional outputs, we showcase in Figure 5.17 the relationship between the input variables of the *CATHARE2* modeling of the transient and the corresponding outputs.

On this figure the set of curves for the fluid temperature in the downcomer is plotted using a colormap related to input values. Each curve's color becomes closer to the red when the input value is closer to the postulated critical value. On the one hand, we can hardly observe any trend on this figure for the three upper graphs dedicated the three uncertain characteristics of accumulators (mass enthalpy of water within accumulators, X_1; initial pressure within accumulators, X_2 and friction coefficient in the discharge line, X_3). This suggests a weak influence of the accumulators on the phenomena at stake during the PTS. On the other hand, the three variables linked to the functioning of ECCS show some quite clear trends. First of all the injected water temperature seems to have a strong influence on the temperature of the primary fluid in the vessel as the lowest curves of the bundle are colored in red, e.g. are associated with the lowest values for the temperature in the water tank. Then, it can be seen that the highest values for the flow rate delivered by high pressure pumps, which are supposed to be penalizing regarding the PTS, lead to low temperatures of the fluid in the vessel up to the beginning of the late PTS phase, with little influence afterwards. The opposite can be observed for the influence of the flow rate coefficient of low pressure pumps, namely a null influence until approximately 2400 seconds of simulated time and a major influence after this

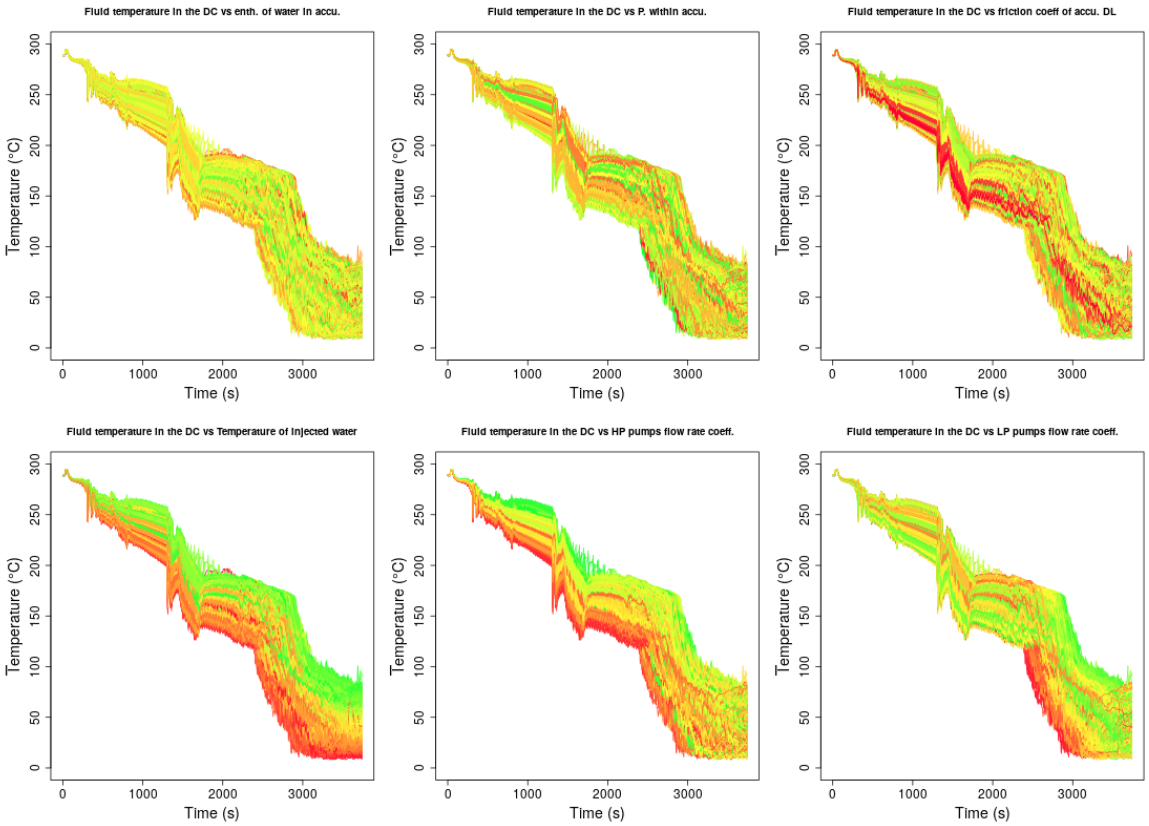

Figure 5.17: Graphical representation of the influence of the input parameters over the injected water in the downcomer through a colormap. **DL**: discharge line of the accumulators; **HP**: high pressure; **LP**: low pressure. The curves are showcased greener for the values of each input which would be postulated to lead to less penalizing scenarios, and the red ones correspond to values of the inputs which would be supposed to lead to more penalizing transients.

instant, with all the lowest curves for the fluid temperature colored in red (highest flow rate) on the graph at the bottom right. This is logical as the high pressure trains are in use from the early moments of the transient until reaching the pressure value that allows to switch over to the low pressure trains which allow a complete water refill of the primary circuit but in turn causes the late PTS event.

5.3 Characterization of outlyingness

Here, we will discuss the implications of the characteristics of the outlying transients and how they relate to specific physical phenomena and the severity of PTS transients.

On the Figure 5.17 in the previous section, we saw the curve bundle for the fluid temperature in the downcomer with curves colored in relationship with the outlyingness score of the corresponding simulation. On this graph, one can hardly infer any typical pattern for the outliers, which seem to be rather shape outliers than magnitude ones. This is confirmed by the examination of the primary pressure curves as well as the flow rate in the downcomer (Figure 5.19) which are the other two input quantities required for *CUVE1D* calculations, and as such, the most relevant variables for the physical analysis. On this figure, we see once again that outliers (in red) do not seem to present any typical characteristics that could clearly distinguish them from other cases. We can only notice that for most outliers, the primary loop pressure is among the lowest ones throughout the transient, especially around the beginning of operators actions (between 1000 s and 1500 s).

On the flow rates in the DC we also can hardly recognize any special pattern for outliers. Still, we can note that, for outlying transients, the flow rate in the DC are not the strongest ones but each sequence seem to be starting at an early instant in comparison with the rest of the curves, especially the triggering of low pressure injection pumps at the beginning of the late PTS phase ($\sim$ 2400 s). This shows anyways that the outlier detection algorithm, when applied to the fluid temperature curves in the DC, puts forward transients which dynamic cannot be detected with the naked eye by looking at the graphs of TH outputs of *CATHARE2*.

In spite of this acknowledgment, the observation of *CUVE1D* outputs, e.g. stress intensity factor and temperature of the RPV steel at the flaw tip, reveals that most outliers feature some penalizing aspects as regards the PTS. On Figure 5.20 (middle graph), we see that up to $\sim$ 2400 s the temperature of the steel for the outliers is never among the highest but rather in the middle of the bundle and sometimes lower. After this moment, the temperature of the RPV material falls more rapidly and with a higher intensity for most outliers than for the rest of the simulations. This leads to rather moderate mechanical loadings until reaching the late PTS phase, but with a main loading peak, provoked by the switching to low pressure injection means, starting at an early instant (before $t = 2500$ s vs. 2700 - 3000 s for the rest of the cases) and with a higher peak for outlying transients than for the other ones (see bottom graph of Figure 5.20). This is typically the kind of dynamic leading to severe PTS. Indeed, we see on the top graph of the same figure that critical cases are those showing a loading pattern in the temperature vs. loading domain with a peak of high intensity at a

low temperature of the steel, meaning close to the brittle domain of the material. Moreover, let us remind that the loading peak is caused by a strong temperature gradient within the RPV wall, which is maximized by a strong and fast temperature drop during the late PTS phase. It is however most critical when this peak is combined with a temperature of the steel (which is representative of its fracture toughness) which is already low at this time, thus minimizing the steel's resistance. Critical cases will hence be those combining a sufficiently low temperature value throughout the first stages of the transient, but with a temperature drop starting among the earliest and with a high intensity.

Another noticeable phenomenon which can be seen on loading curves, concerns the existence of a first thermal shock of a lower intensity than the main one. This occurs at around the same time as the beginning of operators' actions (1200s) and of the emptying of accumulators in the primary loop. This first rapid overcooling is clearly seen in Figure 5.12 after around 1250s, and actually benefits from higher pressures that slow down the injection, with a slower emptying dynamic of the accumulators due to the smaller difference of pressures between the boiler and them. In this case, one parameter (the higher pressure) favors the PTS, whereas the other two, i.e., the water flow and the liquid temperature can mitigate the PTS magnitude. On figure 5.20 we see that outlying transients show a rather small first peak at this point which confirms that a slow depressurization dynamic tends to prevent from a serious late PTS although leading to a stronger first one.

This raises the question of the influence of the residual power of the core, which uncertainty is not taken into account here but follows a max decay law. A maximized thermal residual power has several implications in the considered LOCA. Firstly, it slows the depressurization rate due to the maximized steam production of the primary. The stop of the natural circulation (which occurs after around 300s of transient) is also slowed by this factor, since the hydraulic force provided by the difference of densities will be larger (the steam has more time to overheat in contact with the fuel rods) due to the more important heat source.

All in all, when analyzing the outliers, the effect which can be expected from the uncertain inputs is coherent with the results displayed by the sensitivity analysis method (see 5.5 in the previous section). The penalizing flow rates for the high pressure pumps will be those weakest, leading to the fastest depressurization of the boiler by a weak compensation the water lost at the breach. This fact is of major importance since maximal flow rates for ECCS pumps are usually considered penalizing as they lead to a maximized cooling of the vessel, which is actually not critical at this stage of the transient. On the contrary, an early depressurization in comparison with average transients will lead to an early starting of the low pressure trains of the ECCS provoking the thermal shock itself which is maximized when the flow rate of low pressure pumps is maximized. Both phenomena are still maximized when the injected water temperature is low, as the cold water brought by the ECCS tends to contract the primary loop fluid and thus enhances the pressure decrease, in addition to favoring the cooling of the steel. Accumulators have a rather negligible role in this dynamic as their working principle consists in passively injecting water when the pressure is below a certain threshold. The injection time as well as the quantity injected is then controlled by the overall dynamic of the boiler.

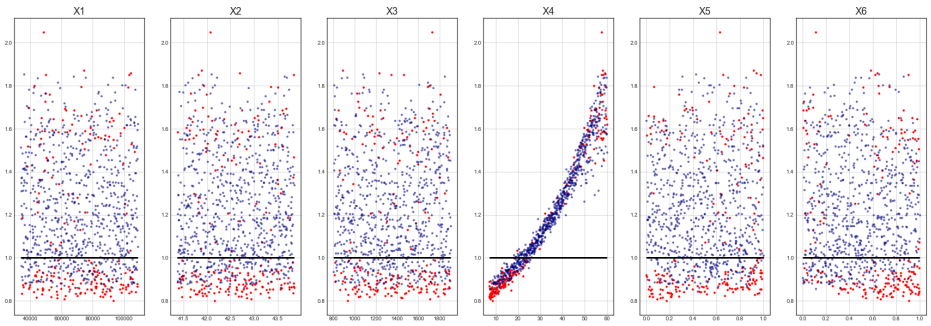

Figure 5.18: Scatter plots between the input parameters and the safety margins calculated conventionally with *CUVE1D*. Red: Outlying transients. Blue: Inlying transients.

These interpretations are validated when establishing the link between inputs parameters of *CATHARE2*, inlying and outlying samples, and the safety margin. This is illustrated in Figure 5.18.

Figure 5.18 shows how, indeed, the conclusions that we have extracted for this application case are correct. Firstly, the correlation between X_4, i.e., the injection temperature of the ECCS system is obvious, and shows how low values of the variable are penalizing regarding the PTS. This is logical since lower injection temperatures favor the overcooling.

The other major correlation is found between the low pressure ECCS and the margins, which characterizes the aforementioned late PTS, whereas we can see that, as expected, the variables concerning the accumulators are not so obviously related to the margins, even if a PTS would be possible after the injection at around 1200s of transient.

We also showcase how there is a clear correlation between the outlyingness score θ and the safety margins. We see that the score is capable of capturing the trend of penalizing scenarios.

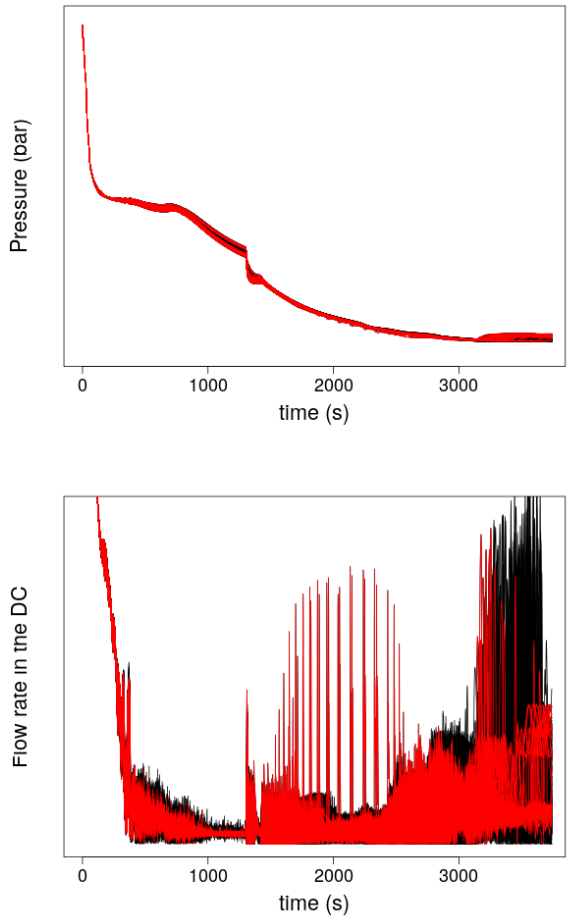

Figure 5.19: *CATHARE2* outputs: water flow in the downcomer and primary pressure. Red: Curves whose score of outlyingness surpasses the 0.9 threshold.

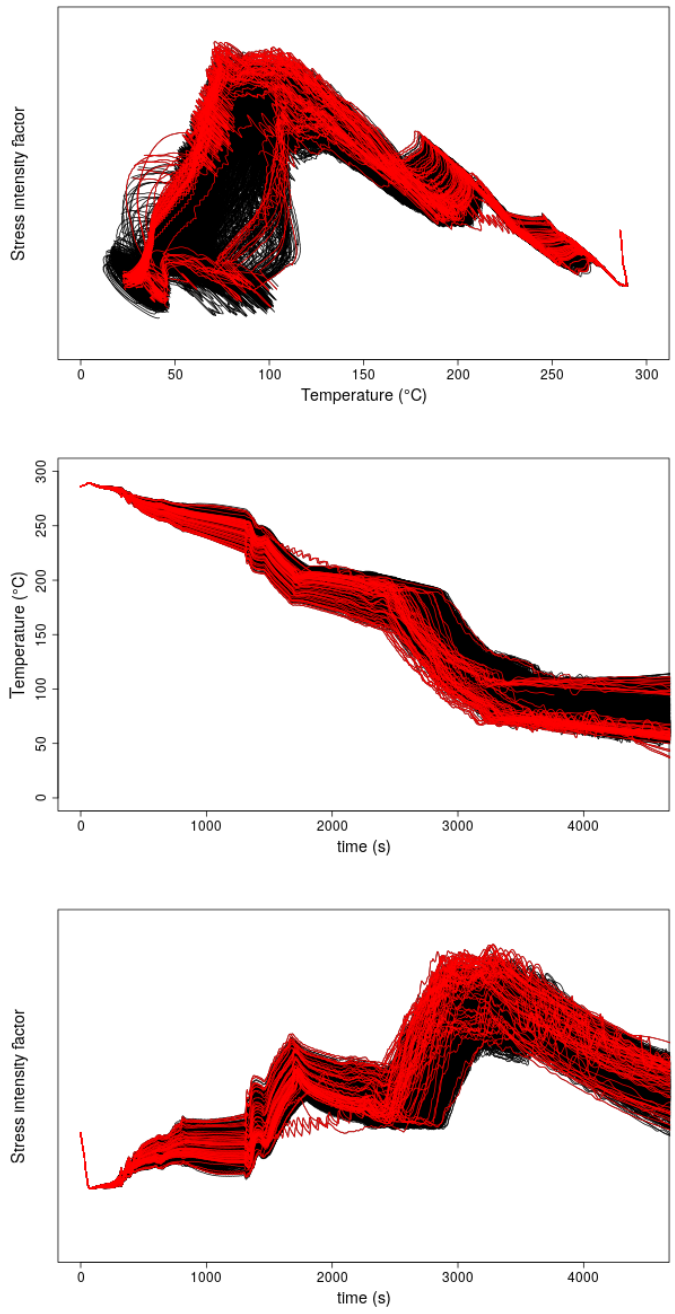

Figure 5.20: *CUVE1D* outputs: Stress intensity factor compared to the temperature and as a function of time with their corresponding temperature transients. Red: Curves whose score of outlyingness surpasses the 0.9 threshold.

5.4 Conclusions

This simpler application case has served to illustrate several aspects of our methodology complementary to those shown in Chapter 4. We verified that the score θ is capable of relating outlying transient identified as outputs of a computer code, *CATHARE2*, and the outputs of a chained mechanical code *CUVE1D*. Indeed, we observed that the θ score is strongly correlated with final safety criteria, most outliers being critical cases when it comes to the risk of PTS. In addition to this, the chapter shows how the sensitivity analysis method used in the study makes possible a robust screening of influential *versus* non-influential inputs, coherently with the postulated effects of uncertain variables, and through the use of the outlyingness score.

These two assets of the methodology allow several foreseeable benefits in its potential industrial use for PTS studies.

Firstly, as the methodology allows detecting shape outliers as well as magnitude ones, it is able to select atypical dynamics of fluid temperature combining low average temperature values during the whole transient, in comparison with other cases, with an early and strong temperature drop during the late PTS phase. This detection of atypical cases without any *a priori* selection criterion tends to rule out the hypothesis of a non anticipated specific behavior that might lead to a severe case with qualitatively different phenomena from those already known penalizing as regards the PTS. Conversely, this confirms, in a completely automated manner, the analysis which can be made with the conventional methodology based on expert knowledge, engineering physical reasoning and targeted simulations using only min and max values for uncertain inputs. This strengthens the line of arguments on which the safety demonstration is built.

Secondly, the methodology provides a reliable screening tool to select the most impactful uncertain parameters of the problem. This aspect is of significant interest for a potential broader exploration of physical uncertainties, e.g., studies including a larger number of input variables in the scope of uncertain ones. Some examples are the uncertainties on the residual power delivered by the core or those concerning the characteristics of the secondary loop. In such studies taking more uncertain inputs into account, it becomes very hard or even impossible to postulate or determine before looking at simulation results a worst-case scenario for the studied transient, since all inputs may interact with each other or involve feedback and mitigation effects, potentially modifying the influence of a quantity when considered isolated from the others. When the input dimension is large, it is also complex to exhibit the main effects of the most impactful inputs based on visual analysis with a graphical representation of results, especially when the design of experiments yields a set of functional outputs that do not showcase any obvious outliers to the naked eye. The sensitivity analysis method tested here, which is based on the outlyingness score, is a valuable alternative to already existing ones, as well as to the visual interpretation of the set of output curves, since it quantitatively exploits the available information of the functional outputs without restricting it to the sole final safety criterion.

A feasible perspective of these works would be to test how the methodology would perform

if the outliers were to be identified in the outputs of the final chained code (*CUVE1D*). These outputs also present a functional nature, and are directly related to the thermal-hydraulic aspects of the transient and the safety criteria, so they also represent good candidates on which to apply the methodology. Since one of the objectives of this application case to showcase how the methods remain useful even when applied to outputs that will act as inputs of another chained code, this perspective would be the next natural step of the research works.

6 Conclusions and perspectives

These Ph.D. works are contextualized in the intersection of several different scientific and industrial domains that are the object of profound research efforts by the main actors of the French nuclear R&D field. The increasing reliance of the nuclear industry on numerical system codes such as *CATHARE2* has allowed the development of pieces of research related to the analysis of nuclear transients, nuclear safety, and uncertainty quantification. These codes have also proved to be a valuable tool to complement safety studies in nuclear power plants.

In particular, in this document, we have developed a series of general methods that are applicable to the analysis of a wide variety of nuclear transients. The methods are concerned with the detection of outliers in sets of functional outputs of *CATHARE2*, as well as the analysis of accidental nuclear transients. Their industrial applicability has been showcased through two very different application cases.

The first contributions are related to the domain of functional data analysis. In particular, we have treated the domain of functional outlier detection, providing a systematic and general description of what constitutes an outlier in both a set of multivariate and functional data, the intrinsic difficulty in their definition, and how the problem is treated nowadays by the state of the art methods. We have justified and developed a description of the possible approaches to perform dimensionality reduction in sets of functional data, and how those measures can be useful descriptors of the considered samples. Finally, we have developed a functional outlier detection technique sensitive to the main types of considered outliers and which also deals with some of the most relevant challenges when tackling the subject of the modeling of the underlying structure that generates the data in a lower-dimensional space. The considered procedure allows the obtention of an outlyingness score for each observation of the considered

sample that provides both a unique detection criterion and a continuous measure that serves as a tool to perform sensitivity analysis in industrial applications.

The second contribution is related to the analysis of nuclear transient simulations. We propose a generic methodology that allows the interpretation of the functional outputs of a system computer code, a characterization of the outlying nature of specific observations in the sample according to a general detection criterion, and the detection of the most relevant breakpoint events according to the outlyingness measure. Nuclear transients involve a wide variety of physical phenomena that require specialized knowledge of the field, which is why the methodology relies on advanced statistical tools and integrates prior knowledge of the progression of the analyzed transient. The approach is valuable in the verification, validation, and uncertainty quantification fields and provides valuable insights regarding the detection of penalizing scenarios. This methodology makes use of the outlyingness score proposed in Chapter 2, which makes few assumptions about the nature of the analyzed data. On top of that, we propose visualization tools that help understand the origin of the outlyingness in functional data.

Finally, we have put into effect the proposed elements in a real industrial context. We have showcased how the explained methods have performed in a challenging setting. The code *CATHARE2* is an excellent example of an actual industrial code that models complex (non-linear) physical phenomena. The potential size of its input space represents a crucial challenge in determining which input parameters are relevant when analyzing specific output parameters, most notably, the safety margins related to particular safety criteria for each considered nuclear transient, as well as the introduced outlyingness score. Another major challenge is the quantification of the different types of uncertainties associated with this application, as well as their propagation over the considered output variables of interest and quantities of interest, also taking into account the computer cost that each simulation requires, and that severely limits the available methods in this context.

Two use-cases have been considered. Firstly, an Intermediate Break Loss of Coolant Accident (IBLOCA) was treated. This application entails a high-dimensional set of inputs, a very fast dynamic of physical phenomena (in the order of seconds), and complex modeling of the components of the NPP. The second application case, a Pressurized Thermal Shock (PTS), constitutes a very different application. This transient is simulated through the use of a simplified modeling of the nuclear core and relies on the chained code CUVE1D to perform the estimation of the safety margins for the transient by making use of the functional outputs provided by *CATHARE2*. Furthermore, the input space has a lower dimension in this case, with only six input parameters and a separated modeling of the laws of the high and low-pressure pumps of the ECCS.

The successful application of these works to the considered IBLOCA transient was a major objective of the Ph.D. . This document details all the main aspects of the transient, including its phases, the main events that occur during its progression, the systems that are activated, the dominant physical phenomena and its modeling. A design of experiments has been developed, and its corresponding functional outliers have been detected in a completely automatized manner. These outliers were interpreted and associated with specific physical

phenomena and events. We have identified how, in this application, they relate to faulty modeling of the progression of the transient, i.e., how these are *real* outliers, in the sense that they are generated by an incorrect modeling of the physics of the transient. Finally, we have also showcased how a different modeling of the transient that modifies the origin of the detected outliers allows its physically coherent simulation.

The other treated case, the PTS, aims at showing how the generality of the proposed methods proves its value in a wide variety of transients since this one is remarkably different from the IBLOCA. This case is related to the fact that the outliers are highly correlated to penalizing scenarios (those for which the safety margins surpass the considered thresholds), which is an argument in favor of the chosen score θ as an integrating measure that provides relevant insights into the physical analysis of transients.

It must also be highlighted that the computation of the outliers and their association with specific input parameters, the separation between the inlying and outlying samples, and the definition of the relevant breakpoint events can be computed in a reasonable amount of time (less than one minute).

Regarding the perspectives, several points of improvement can be mentioned. Since these works are separated into two main parts, the mathematical analysis of functional data and the physical analysis of nuclear transient simulations, the perspectives are also separated into two parts.

- Regarding the detection of functional outliers, it would be relevant to account for the uncertainty in the estimation of the underlying probability density function in the space of features. Accounting for this uncertainty will improve the quality of the estimators of the outlyingness score, robustifying them. Another issue, shared with other detection methodologies, is selecting an appropriate value of the significance level of the test of outlyingness. Indeed, this level plays a significant role in the total amount of outliers that will be identified. However, since simply increasing it will also increase the false positive rate, hindering the possible interpretations obtained in real applications, finding optimality criteria for its values would be helpful.

  Furthermore, an improved estimation scheme for the parameters in the GMM should be considered. The EM algorithm, although useful, still presents some drawbacks. Although the overfitting issue presented in Chapter 2 is dealt with in the outlier detection setting, there still exist open issues in the literature. One of them is the algorithm's sensitivity to the choice of initial values for the estimated parameters. Some recent propositions that tackle this problem are presented in Panić et al. (2020) through the so-called *REBMIX* algorithm.

  Another axis of research concerns the quality of the estimation of the corresponding minimum volume level sets in the case of the estimation of the associated θ value for each observation in the sample of functional data. This problem is well known, especially in the context of high-dimensional density estimation, and is related to other statistical problems. Firstly, the quality of the corresponding probability density function associated with the sample of data naturally adds to the uncertainty on any estimator coming

from it. Secondly, the research of the set that minimizes the volume of the level set associated to a given probability mass is a complex optimization problem that requires non-negligible computational time compared to the other stages of the detection algorithm. There exist faster plug-in estimators for level sets assuming mild assumptions on the underlying probability density functions (see Di Bernardino et al. (2013) for an example).

Finally, another possible improvement of the methodology would be to take into account the multivariate nature of the outputs provided by *CATHARE*. Although it is not guaranteed, detecting the desired outliers in a particular design of experiments could be a simplified task if a larger number of physical outputs is considered in the process. Some works related to this field can be found in Hubert et al. (2015); Lejeune et al. (2020); Dai and Genton (2018). This possibility must be studied with care since the addition of data not directly linked to the safety criterion might pollute the sample rather than adding useful information to characterize the outlyingness. Moreover, some of these methods have already been tested against rather *simple* toy examples but are yet to be validated more complex sets of data. Nonetheless, this can be an important path to be explored in complex physical systems.

- Incorporating prior knowledge about the transients' progression to interpret the outlyingness is both an advantage and a disadvantage. Including this information in the analysis' procedure allows a better definition of the actual events that take place during the transient and a more coherent division into intervals that share specific characteristics (such as the primary physical phenomena that occur or the activated systems). This largely facilitates the interpretation of the results and the association of the outlying samples to real events in the transients. However, the approach can be challenging if this prior knowledge is not available or is limited (for instance, in an exploratory study for which a PIRT is not available). The physical analysis of the transients could be more generally applied through the use of landmark registration techniques, aiming at detecting specific influential events without prior physical knowledge of the transient.

  It could be argued that imposing the subsets of time in which the outlyingness is characterized might not take into account all the possible combinations of physical events that occur in the different phases during a transient. A possible improvement of the methodology would be not to impose the analyzed subsets of time and consider all the possible permutations (within reasonable limits depending on the density of points in the mathematical support of all the functional outputs) of its elements. This might help characterize how events that occur at specific points in time can have a relevant impact much later in the transient. Nonetheless, the interpretation of the results would be more complex.

  Finally, analyzing the results provided in Chapter 4 demonstrates that taking the parameters of the numerical modeling of the transient can provide valuable information concerning transient analysis. In that case, it was shown that the outlying nature of specific transients was linked to the activation of a specific *CATHARE2* module. Adding the activation of particular modules of the simulators to the list of analyzed intermediate parameters should be considered as an axis of research to improve the physical

analysis methodology.

Appendix A

Kruskal-Wallis H-test

The H-test of Kruskal-Wallis (Kruskal and Wallis, 1952) aims at identifying two or more statistical samples have been generated by the same distribution. In order to tackle this problem, the authors propose to substitute the original data of the sample with their ranks, i.e., to sequentially assemble the data by order of magnitude and assign a value of 1 to the smallest, of 2 to the second smallest and so on. The largest value among the samples will a rank of N, where N corresponds to the size of the sample that combines the whole set of data.

Let us denote by C the total number of samples that are analyzed, and let $n_i, i \in \{1, ..., C\}$ be the number of observations in each one of those samples. The test writes:

$$\begin{aligned} \mathcal{H}_0 &: \textit{The } C \textit{ samples have been generated by the same distribution.} \\ \mathcal{H}_1 &: \textit{The samples come from different distributions.} \end{aligned} \tag{A.1}$$

The considered test is usually called the H-test, the Kruskal-Wallis test or the one-way analysis of variance. It relies upon the calculation of the following test statistic:

$$H = \frac{12}{N(N+1)} \sum_{i=1}^{C} \frac{R_i^2}{n_i} - 3(N+1) \tag{A.2}$$

where C is the number of samples, n_i corresponds to the number of observations in the ith sample, $N = \sum i = 1^C n_i$ the total number of observations, i.e., if all samples are combined, and R_i corresponds to the sum of the ranks in the ith sample.

Whenever the samples come from identical continuous distributions the test statistic follows a $\chi^2(C-1)$ distribution, and its values may be obtained through the use of the χ^2 tables.

In practice, if the samples differ by more factors than only their medians, this remains an approximation of the distribution, but the associated error is still small according to Kruskal and Wallis (1952) whenever the samples are not very small (namely, below 5 observations).

The null hypothesis is rejected for large values of H, i.e., it is rejected on the right-hand tail of the $\chi^2(C-1)$ distribution.

In the case where ties may exist between the observations, the authors propose a correction to the test. In this case, tied observations is given the mean of the ranks for which it is tied, and the test statistic H is divided by:

$$1 - \frac{\sum T}{N^3 - N} \tag{A.3}$$

where the summation is made over all the groups that present ties and $T = (t-1)t(t+1) = t^3 - t$ for every group of ties. The variable t represents the total number of tied observations in every group. The general form of the test statistic H is then written:

$$H = \frac{\frac{12}{N(N+1)} \sum_{i=1}^{C} \frac{R_i^2}{n_i} - 3(N+1)}{1 - \sum T/(N^3 - N)} \tag{A.4}$$

As we can see, in the case where there are no ties $T = 0$ and the expression in (A.4) becomes (A.2). In practice, whenever the compared samples do not actually follow the same distributions albeit they may present a shift or translation with respect to each other, then the test can only rightfully assume that the considered distributions are different, but not how, and care must be taken when analyzing the causes of these differences. In practice, knowledge about the nature of the samples is necessary to provide a deeper insight in that regard.

All in all, the H-test is a practical and useful way of analyzing if two or more samples of data haven generated by the same process for several reasons. Firstly, it does not make any strong assumptions over the nature of the analyzed data, such as normality, or equality of sizes of the samples. It does not require homogeneity of group variance either, thus making it a fast and flexible tool to tackle the presented problem.

Appendix B

Comparison of samples IBLOCA

Table B.1: KW tests for equality of distributions in each time interval defined by the breakpoint events between the samples of outlying transients and inlying ones for the $h_1(z_s)|_{t_i}^{t_{i+1}} = \min(z_s)|_{t_i}{}^{t}{}_{i+1}$ intermediate parameter applied to the maximum cladding temperature. S: same distributions, D: different distributions.

Interval	**Statistic**	p**-value**	**Conclusion**
$[t_1, t_2]$	0.74225	0.38894	S
$[t_2, t_3]$	1.40981	0.23509	S
$[t_3, t_4]$	0.89920	0.34299	S
$[t_4, t_5]$	**11.9712**	**0.00054**	**D**
$[t_5, \infty)$	**3.50820**	**0.06106**	**D**

Table B.2: KW tests for equality of distributions in each time interval defined by the breakpoint events between the samples of outlying transients and inlying ones for the $h_2(z_s)|_{t_i}^{t_{i+1}} = \max(z_s)|_{t_i}^{t_{i+1}}$ intermediate parameter applied to the maximum cladding temperature. S: same distributions, D: different distributions.

Interval	**Statistic**	p**-value**	**Conclusion**
$[t_1, t_2]$	1.13243	0.28725	S
$[t_2, t_3]$	1.33762	0.24745	S
$[t_3, t_4]$	0.88694	0.34630	S
$[t_4, t_5]$	**5.79816**	**0.016042**	**D**
$[t_5, \infty)$	**45.86510**	**0.00000**	**D**

Table B.3: KW tests for equality of distributions in each time interval defined by the breakpoint events between the samples of outlying transients and inlying ones for the $h_3(z_s)|_{t_i}^{t_{i+1}} = \mathbb{E}[z_s]|_{t_i}^{t_{i+1}}$ intermediate parameter applied to the maximum cladding temperature. S: same distributions, D: different distributions.

Interval	Statistic	p-value	Conclusion
$[t_1, t_2]$	1.27647	0.25855	S
$[t_2, t_3]$	0.90844	0.34052	S
$[t_3, t_4]$	0.876293	0.34921	S
$[t_4, t_5]$	**11.9712**	**0.00054**	**D**
$[t_5, \infty)$	**42.95961**	**0.00000**	**D**

Table B.4: KW tests for equality of distributions in each time interval defined by the breakpoint events between the samples of outlying transients and inlying ones for the $h_3(z_s)|_{t_i}^{t_{i+1}} = \mathbb{E}[z_s]|_{t_i}^{t_{i+1}}$ intermediate parameter applied to the swollen level of water in the core. S: same distributions, D: different distributions.

Interval	Statistic	p-value	Conclusion
$[t_1, t_2]$	**3.23287**	**0.07217**	**D**
$[t_2, t_3]$	0.87553	0.34942	S
$[t_3, t_4]$	0.42832	0.51281	S
$[t_4, t_5]$	0.14020	0.70807	S
$[t_5, \infty)$	**47.94558**	**0.00000**	**D**

Table B.5: KW tests for equality of distributions in each time interval defined by the breakpoint events between the samples of outlying transients and inlying ones for the $h_1(z_s)|_{t_i}^{t_{i+1}} = \min(z_s)|_{t_i}^{t_{i+1}}$ intermediate parameter applied to the total water mass in the core. S: same distributions, D: different distributions.

Interval	Statistic	p-value	Conclusion
$[t_1, t_2]$	0.32555	0.56828	S
$[t_2, t_3]$	**2.94392**	**0.08620**	**D**
$[t_3, t_4]$	0.30553	0.58043	S
$[t_4, t_5]$	**3.15621**	**0.07563**	**D**
$[t_5, \infty)$	**40.78851**	**0.00000**	**D**

Table B.6: KW tests for equality of distributions in each time interval defined by the breakpoint events between the samples of outlying transients and inlying ones for the $h_2(z_s)|_{t_i}^{t_{i+1}} = \max(z_s)|_{t_i}^{t_{i+1}}$ intermediate parameter applied to the total water mass in the core. S: same distributions, D: different distributions.

Interval	**Statistic**	p**-value**	**Conclusion**
$[t_1, t_2]$	0.00340	0.95346	S
$[t_2, t_3]$	0.00000	0.99935	S
$[t_3, t_4]$	1.10500	0.29316	S
$[t_4, t_5]$	0.17219	0.67816	S
$[t_5, \infty)$	**39.19967**	**0.00000**	**D**

Table B.7: KW tests for equality of distributions in each time interval defined by the breakpoint events between the samples of outlying transients and inlying ones for the $h_3(z_s)|_{t_i}^{t_{i+1}} = \mathbb{E}[z_s]|_{t_i}^{t_{i+1}}$ intermediate parameter applied to the total water mass in the core. S: same distributions, D: different distributions.

Interval	**Statistic**	p**-value**	**Conclusion**
$[t_1, t_2]$	0.418303	0.51778	S
$[t_2, t_3]$	0.00945	0.92252	S
$[t_3, t_4]$	0.71732	0.39702	S
$[t_4, t_5]$	0.76902	0.38051	S
$[t_5, \infty)$	**38.07125**	**0.00000**	**D**

Table B.8: KW tests for equality of distributions in each time interval defined by the breakpoint events between the samples of outlying transients and inlying ones for the $h_2(z_s)|_{t_i}^{t_{i+1}} = \max(z_s)|_{t_i}^{t_{i+1}}$ intermediate parameter applied to the total water mass in the downcomer. S: same distributions, D: different distributions.

Interval	**Statistic**	p**-value**	**Conclusion**
$[t_1, t_2]$	0.00696	0.93347	S
$[t_2, t_3]$	**8.00085**	**0.00467**	**D**
$[t_3, t_4]$	**6.84467**	**0.00889**	**D**
$[t_4, t_5]$	1.00838	0.31528	S
$[t_5, \infty)$	2.26033	0.13272	S

Table B.9: KW tests for equality of distributions in each time interval defined by the breakpoint events between the samples of outlying transients and inlying ones for the $h_3(z_s)|_{t_i}^{t_{i+1}} = \mathbb{E}[z_s]|_{t_i}^{t_{i+1}}$ intermediate parameter applied to the total water mass in the Downcomer. S: same distributions, D: different distributions.

Interval	**Statistic**	p**-value**	**Conclusion**
$[t_1, t_2]$	**7.60245**	**0.00582**	**D**
$[t_2, t_3]$	**7.25784**	**0.00705**	**D**
$[t_3, t_4]$	**4.64432**	**0.03115**	D
$[t_4, t_5]$	1.35266	0.24481	S
$[t_5, \infty)$	**31.30121**	**0.00000**	**D**

Table B.10: KW tests for equality of distributions regarding the uncovery of the core. S: same distributions, D: different distributions.

Analyzed parameter	**Statistic**	p**-value**	**Conclusion**
Moment first uncovery	0.77815	0.37732	S
Existence of second uncovery	**7.62700**	**0.00575**	**D**

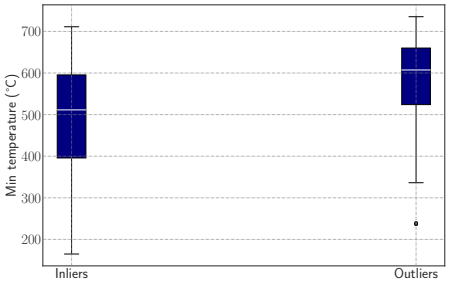

(a) Boxplot. Minimum cladding temperature in $[t_4, t_5]$.

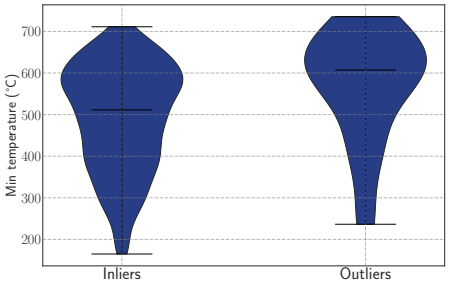

(b) Violin plot. Minimum cladding temperature in $[t_4, t_5]$.

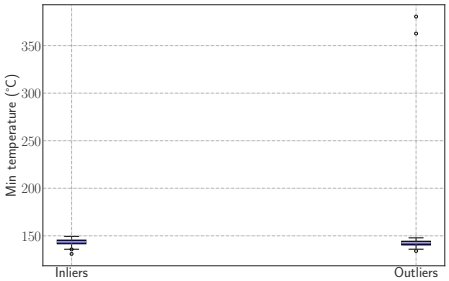

(c) Boxplot. Minimum cladding temperature in $[t_5, \infty)$.

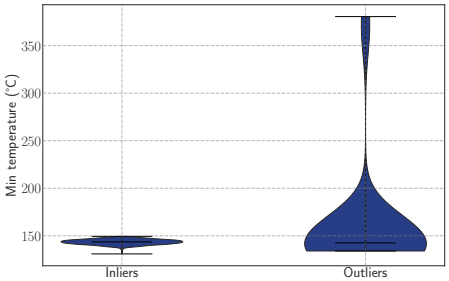

(d) Violin plot. Minimum cladding temperature in $[t_5, \infty)$.

Figure B.1: Minimum cladding temperature. Comparison between inlying and outlying samples for the $h_1(z_s)|_{t_i}^{t_{i+1}} = \min(z_s)|_{t_i}^{t_{i+1}}$ intermediate parameter.

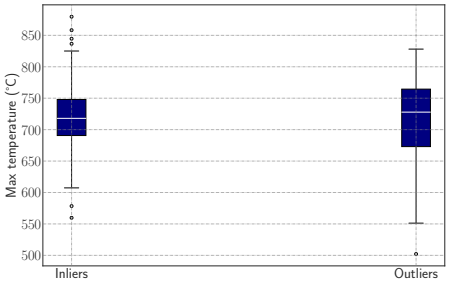

(a) Boxplot. Maximum cladding temperature in $[t_4, t_5]$.

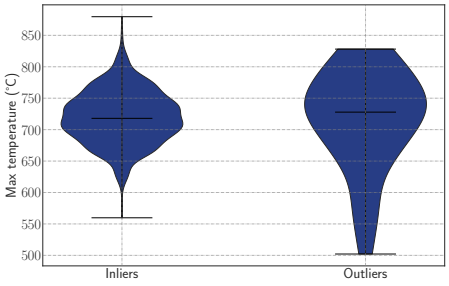

(b) Violin plot. Maximum cladding temperature in $[t_4, t_5]$.

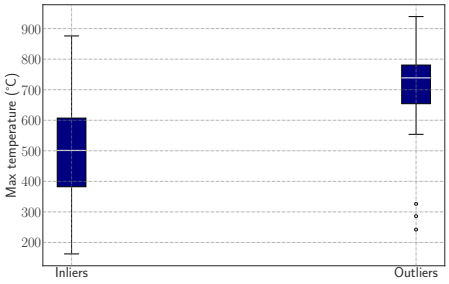

(c) Boxplot. Maximum cladding temperature in $[t_5, \infty)$.

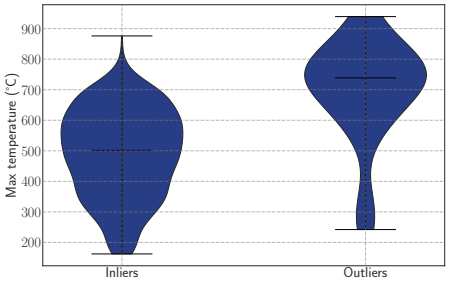

(d) Violin plot. Maximum cladding temperature in $[t_5, \infty)$.

Figure B.2: Maximum cladding temperature. Comparison between inlying and outlying samples for the $h_2(z_s)|_{t_i}^{t_{i+1}} = \max(z_s)|_{t_i}^{t_{i+1}}$ intermediate parameter.

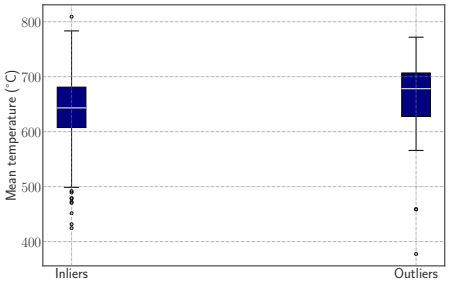

(a) Boxplot. Mean cladding temperature in $[t_4, t_5]$.

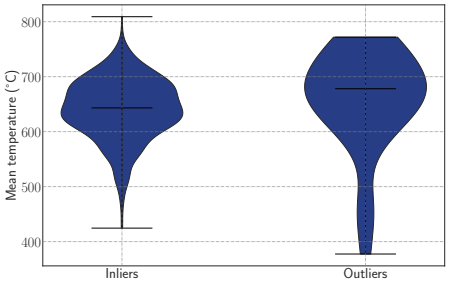

(b) Violin plot. Mean cladding temperature in $[t_4, t_5]$.

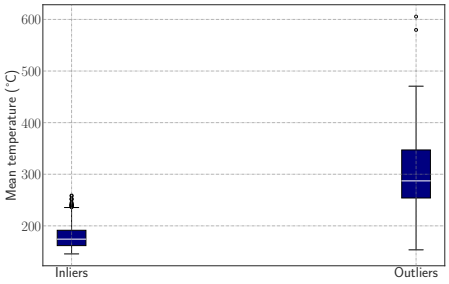

(c) Boxplot. Mean cladding temperature in $[t_5, \infty)$.

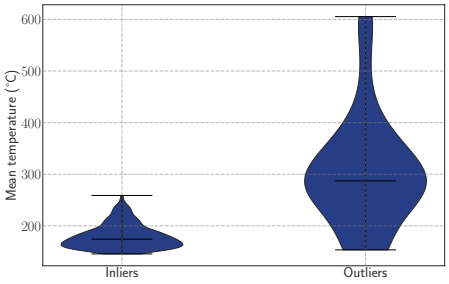

(d) Violin plot. Mean cladding temperature in $[t_5, \infty)$.

Figure B.3: Average cladding temperature. Comparison between inlying and outlying samples for the $h_3(z_s)|_{t_i}^{t_{i+1}} = \mathbb{E}[z_s]|_{t_i}^{t_{i+1}}$ intermediate parameter.

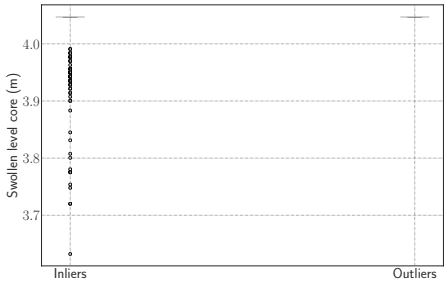

(a) Boxplot. Mean swollen level of water in the core in $[t_1, t_2]$.

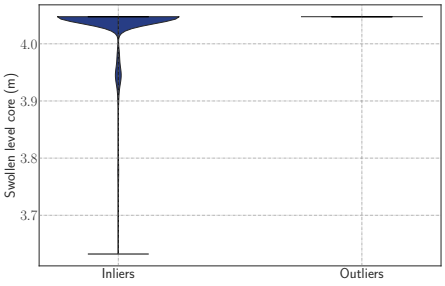

(b) Violin plot. Mean swollen level of water in the core in $[t_1, t_2]$.

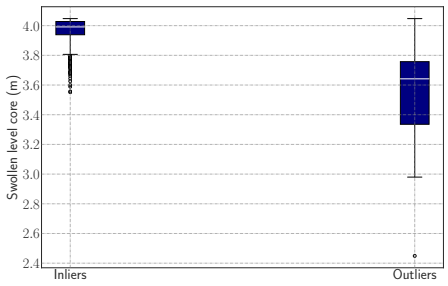

(c) Boxplot. Mean swollen level of water in the core in $[t_5, \infty)$.

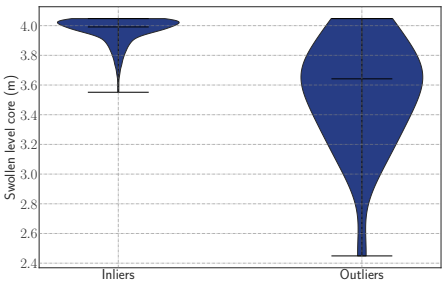

(d) Violin plot. Mean swollen level of water in the core in $[t_5, \infty)$.

Figure B.4: Swollen level of water in the core. Comparison between inlying and outlying samples for the $h_3(z_s)|_{t_i}^{t_{i+1}} = \mathbb{E}[z_s]|_{t_i}^{t_{i+1}}$ intermediate parameter.

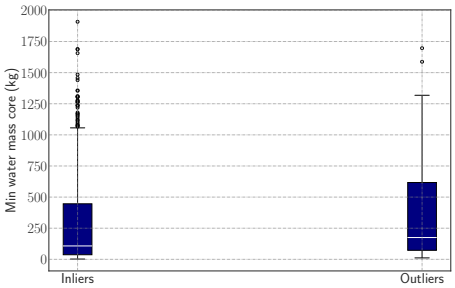

(a) Boxplot. Minimum mass of water in the core in $[t_2, t_3]$.

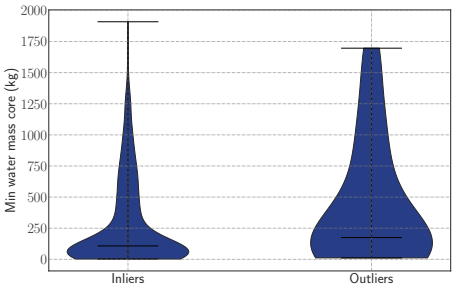

(b) Violin plot. Minimum mass of water in the core in $[t_2, t_3]$.

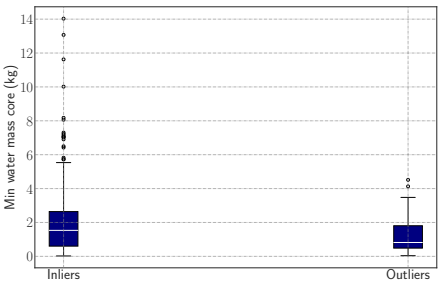

(c) Boxplot. Minimum mass of water in the core in $[t_4, t_5]$.

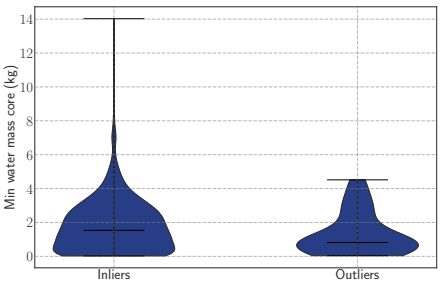

(d) Violin plot. Minimum mass of water in the core in $[t_4, t_5]$.

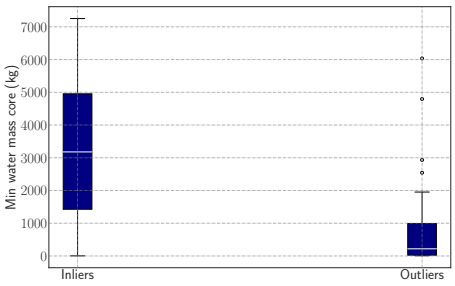

(e) Boxplot. Minimum mass of water in the core in $[t_5, \infty)$.

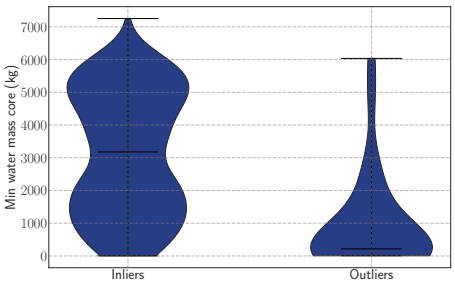

(f) Violin plot.Minimum mass of water in the core in $[t_5, \infty)$.

Figure B.5: Minimum mass of water in the core. Comparison between inlying and outlying samples for the $h_1(z_s)|_{t_i}^{t_{i+1}} = \min(z_s)|_{t_i}{}_{i+1}^{t}$ intermediate parameter.

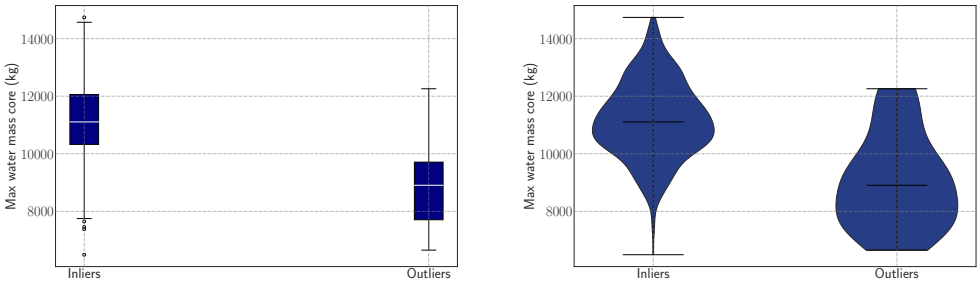

(a) Boxplot. (b) Violin plot.

Figure B.6: Mass of water in the core. Comparison between inlying and outlying samples for the $h_2(z_s)|_{t_i}^{t_{i+1}} = \max(z_s)|_{t_i}^{t_{i+1}}$intermediate parameter in the $[t_5, \infty)$ interval.

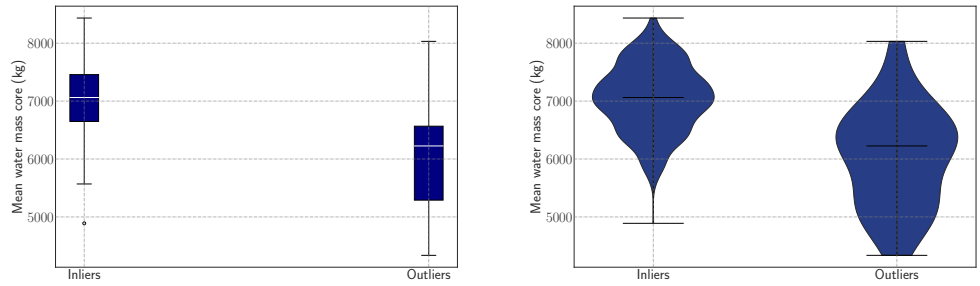

(a) Boxplot. (b) Violin plot.

Figure B.7: Mass of water in the core. Comparison between inlying and outlying samples for the $h_3(z_s)|_{t_i}^{t_{i+1}} = \mathbb{E}[z_s]|_{t_i}^{t_{i+1}}$ intermediate parameter in the $[t_5, \infty)$ interval.

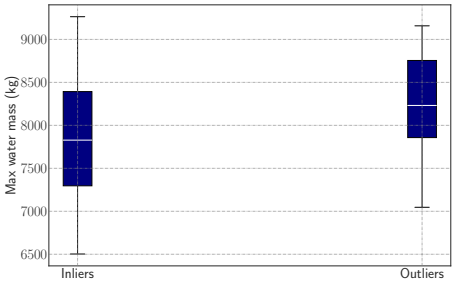

(a) Boxplot. Maximum mass of water in the downcomer in $[t_2, t_3]$.

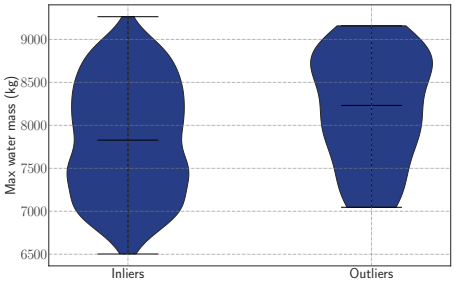

(b) Violin plot. Maximum mass of water in the downcomer in $[t_2, t_3]$.

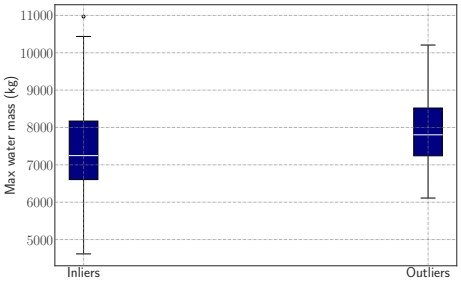

(c) Boxplot. Maximum mass of water in the downcomer in $[t_3, t_4]$.

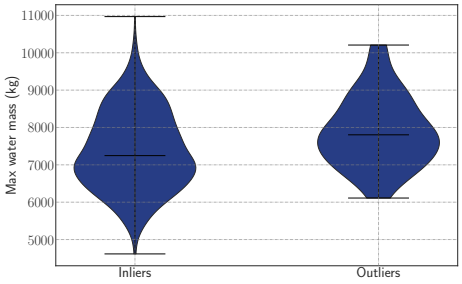

(d) Violin plot. Maximum mass of water in the downcomer in $[t_3, t_4]$.

Figure B.8: Mass of water in the core. Comparison between inlying and outlying samples for the $h_2(z_s)|_{t_i}^{t_{i+1}} = \max(z_s)|_{t_i}^{t_{i+1}}$intermediate parameter

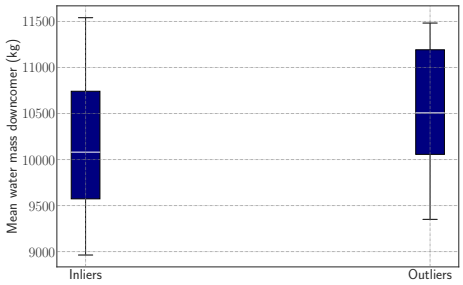

(a) Boxplot. Mean mass of water in the downcomer in $[t_1, t_2]$.

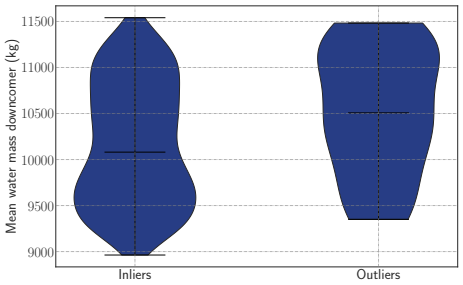

(b) Violin plot. Mean mass of water in the downcomer in $[t_1, t_2]$.

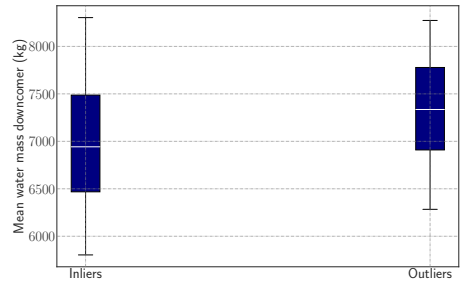

(c) Boxplot. Mean mass of water in the downcomer in $[t_2, t_3]$.

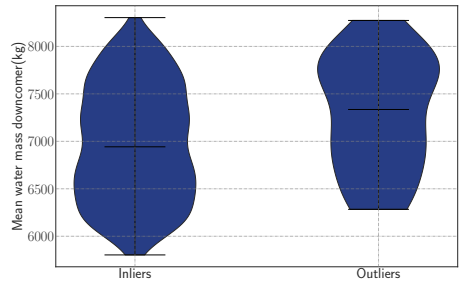

(d) Violin plot. Mean mass of water in the downcomer in $[t_2, t_3]$.

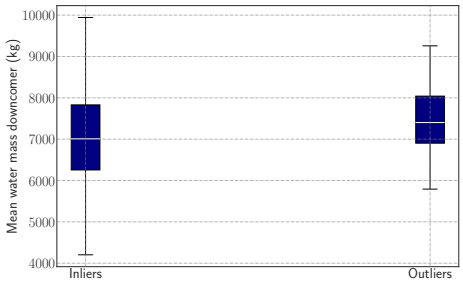

(e) Boxplot. Mean mass of water in the downcomer in $[t_3, t_4]$.

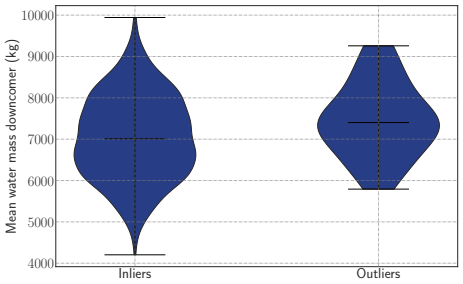

(f) Violin plot. Mean mass of water in the downcomer in $[t_3, t_4]$.

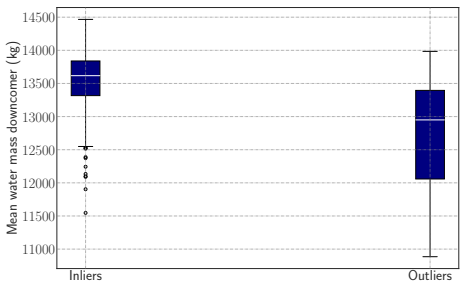

(g) Boxplot. Mean mass of water in the downcomer in $[t_5, \infty)$.

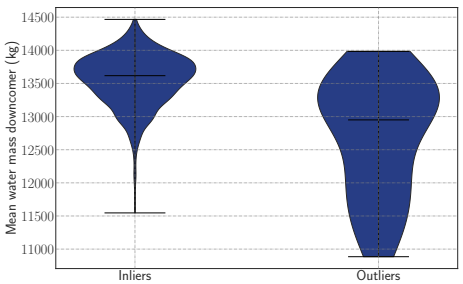

(h) Violin plot. Mean mass of water in the downcomer in $[t_5, \infty)$.

Figure B.9: Mass of water in the core. Comparison between inlying and outlying samples for the $h_3(z_s)|_{t_i}^{t_{i+1}} = \mathbb{E}[z_s]|_{t_i}^{t_{i+1}}$ intermediate parameter

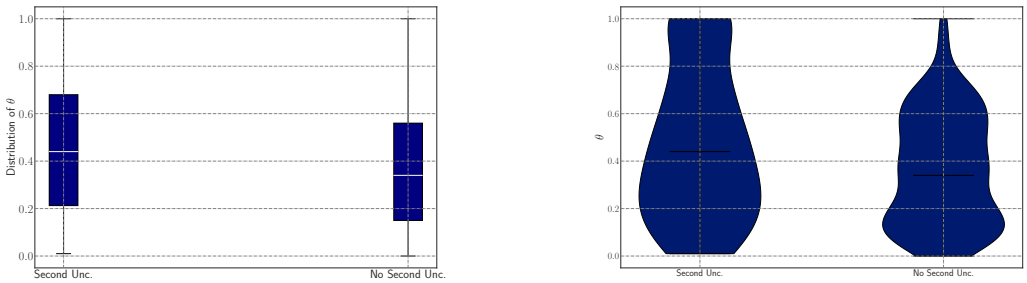

(a) Boxplot.

(b) Violin plot.

Figure B.10: Values of θ for the simulations that do not present a second uncovery of the nuclear core after the activation of the accumulators.

Appendix C

Comparison of samples PTS

Table C.1: KW tests for equality of distributions in each time interval defined by the breakpoint events between the samples of outlying transients and inlying ones for the $h_1(z_s)|_{t_i}^{t_{i+1}} = \min(z_s)|_{t_i}{}_{i+1}^{t}$ intermediate parameter applied to the liquid temperature in the collector. S: same distributions, D: different distributions.

Interval	**Statistic**	***p*-value**	**Conclusion**
$[t_1, t_2]$	25.06476	5.54365×10^{-7}	D
$[t_2, t_3]$	31.23626	2.28458×10^{-8}	D
$[t_3, t_4]$	36.22641	1.75672×10^{-9}	D
$[t_4, \infty)$	51.52518	7.06845×10^{-11}	D

Table C.2: KW tests for equality of distributions in each time interval defined by the breakpoint events between the samples of outlying transients and inlying ones for the $h_2(z_s)|_{t_i}^{t_{i+1}} = \max(z_s)|_{t_i}{}_{i+1}^{t}$ intermediate parameter applied to the liquid temperature in the collector. S: same distributions, D: different distributions.

Interval	**Statistic**	***p*-value**	**Conclusion**
$[t_1, t_2]$	28.84936	7.82314×10^{-8}	D
$[t_2, t_3]$	27.622552	1.47449×10^{-7}	D
$[t_3, t_4]$	29.83075	4.71453×10^{-8}	D
$[t_4, \infty)$	34.49552	4.27232×10^{-9}	D

Table C.3: KW tests for equality of distributions in each time interval defined by the breakpoint events between the samples of outlying transients and inlying ones for the $h_3(z_s)|_{t_i}^{t_{i+1}} = \mathbb{E}[z_s]|_{t_i}^{t_{i+1}}$ intermediate parameter applied to the liquid temperature in the collector. S: same distributions, D: different distributions.

Interval	**Statistic**	***p*-value**	**Conclusion**
$[t_1, t_2]$	28.81307	7.97111×10^{-8}	D
$[t_2, t_3]$	31.17290	2.36037×10^{-8}	D
$[t_3, t_4]$	33.12639	8.63584×10^{-9}	D
$[t_4, \infty)$	86.46078	1.42535×10^{-20}	D

Table C.4: KW tests for equality of distributions in each time interval defined by the breakpoint events between the samples of outlying transients and inlying ones for the $h_1(z_s)|_{t_i}^{t_{i+1}} = \min(z_s)|_{t_i}{}_{i+1}^{t}$ intermediate parameter applied to the primary pressure. S: same distributions, D: different distributions.

Interval	**Statistic**	***p*-value**	**Conclusion**
$[t_1, t_2]$	27.40726	1.6481×10^{-7}	D
$[t_2, t_3]$	48.7868	2.8534×10^{-12}	D
$[t_3, t_4]$	47.23391	6.30008×10^{-12}	D
$[t_4, \infty)$	4.97092	0.02577	D

Table C.5: KW tests for equality of distributions in each time interval defined by the breakpoint events between the samples of outlying transients and inlying ones for the $h_2(z_s)|_{t_i}^{t_{i+1}} = \max(z_s)|_{t_i}{}_{i+1}^{t}$ intermediate parameter applied to the primary pressure. S: same distributions, D: different distributions.

Interval	**Statistic**	***p*-value**	**Conclusion**
$[t_1, t_2]$	0.01780	0.89384	S
$[t_2, t_3]$	23.89051	1.019729×10^{-6}	D
$[t_3, t_4]$	48.76799	2.88103×10^{-12}	D
$[t_4, \infty)$	47.34161	5.96325×10^{-12}	D

Table C.6: KW tests for equality of distributions in each time interval defined by the breakpoint events between the samples of outlying transients and inlying ones for the $h_3(z_s)|_{t_i}^{t_{i+1}} = \mathbb{E}[z_s]|_{t_i}^{t_{i+1}}$ intermediate parameter applied to the primary pressure. S: same distributions, D: different distributions.

Interval	**Statistic**	***p*-value**	**Conclusion**
$[t_1, t_2]$	34.48283	4.30026×10^{-9}	D
$[t_2, t_3]$	46.02064	1.17013×10^{-11}	D
$[t_3, t_4]$	53.80216	2.21728×10^{-13}	D
$[t_4, \infty)$	11.84469	0.00057	D

Table C.7: KW tests for equality of distributions in each time interval defined by the breakpoint events between the samples of outlying transients and inlying ones for the $h_2(z_s)|_{t_i}^{t_{i+1}} = \max(z_s)|_{t_i}{}^{t}{}_{i+1}$ intermediate parameter applied to the mass flow of water in the collector of the downcomer. S: same distributions, D: different distributions.

Interval	**Statistic**	***p*-value**	**Conclusion**
$[t_1, t_2]$	14.96037	0.00011	D
$[t_2, t_3]$	23.28591	1.39618×10^{-6}	D
$[t_3, t_4]$	42.11727	8.59606×10^{-11}	D
$[t_4, \infty)$	4.25183	0.03920	D

Table C.8: KW tests for equality of distributions in each time interval defined by the breakpoint events between the samples of outlying transients and inlying ones for the $h_3(z_s)|_{t_i}^{t_{i+1}} = \mathbb{E}[z_s]|_{t_i}^{t_{i+1}}$ intermediate parameter applied to the mass flow of water in the collector of the downcomer. S: same distributions, D: different distributions.

Interval	**Statistic**	***p*-value**	**Conclusion**
$[t_1, t_2]$	33.44733	7.32200×10^{-9}	D
$[t_2, t_3]$	10.78052	0.00102	D
$[t_3, t_4]$	10.461955	0.0012188	D
$[t_4, \infty)$	24.20434	8.663664×10^{-11}	D

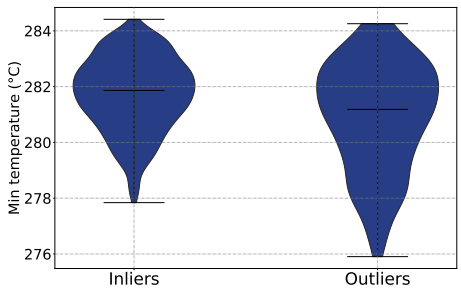

(a) Minimum water temperature in the collector in $[t_1, t_2]$.

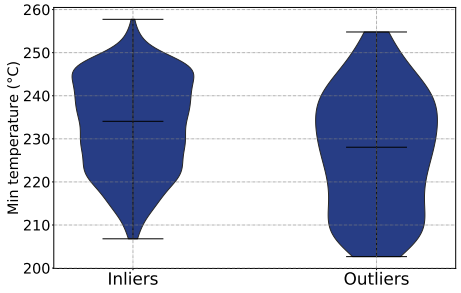

(b) Minimum water temperature in the collector in $[t_2, t_3]$.

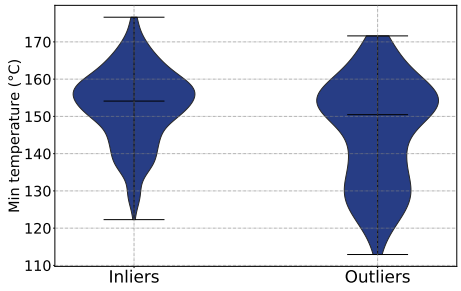

(c) Minimum water temperature in the collector in $[t_3, t_4]$.

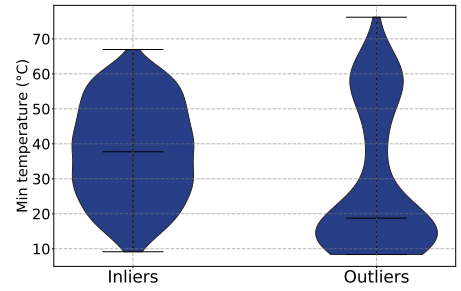

(d) Minimum water temperature in the collector in $[t_4, \infty)$.

(e) Maximum water temperature in the collector in $[t_1, t_2]$.

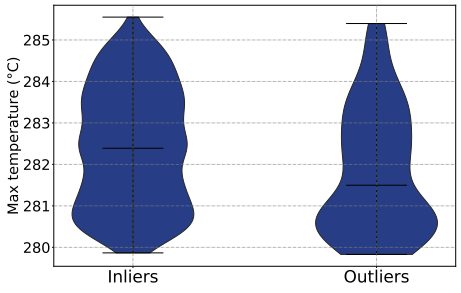

(f) Maximum water temperature in the collector in $[t_2, t_3]$.

Figure C.1: Water temperature in the collector for the $h_1(z_s)|_{t_i}^{t_{i+1}} = \min(z_s)|_{t_i}^{t_{i+1}}$ and $h_2(z_s)|_{t_i}^{t_{i+1}} = \max(z_s)|_{t_i}^{t_{i+1}}$ intermediate parameter.

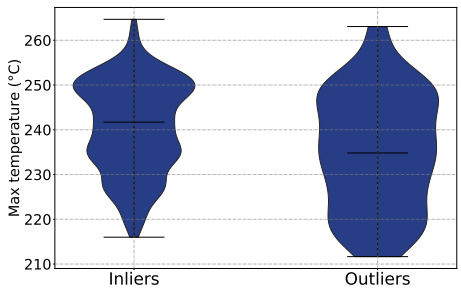

(a) Maximum water temperature in the collector in $[t_3, t_4]$.

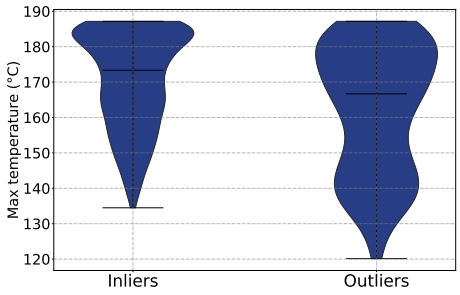

(b) Maximum water temperature in the collector in $[t_4, \infty)$.

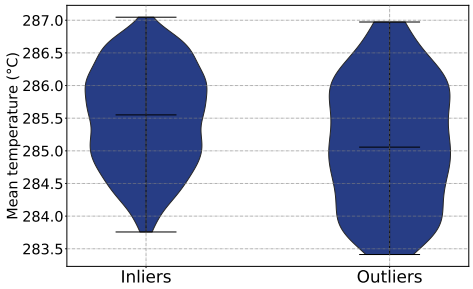

(c) Mean water temperature in the collector in $[t_1, t_2]$.

(d) Mean water temperature in the collector in $[t_2, t_3$.

(e) Mean water temperature in the collector in $[t_3, t_4]$.

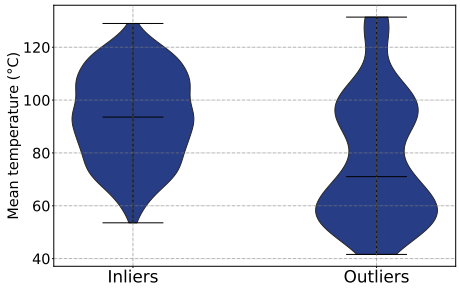

(f) Mean water temperature in the collector in $[t_4, \infty)$.

Figure C.2: Water temperature in the collector for the $h_3(z_s)|_{t_i}^{t_{i+1}} = \mathbb{E}[z_s]|_{t_i}^{t_{i+1}}$ and $h_2(z_s)|_{t_i}^{t_{i+1}} = \max(z_s)|_{t_i}^{t_{i+1}}$ intermediate parameter.

(a) Minimum primary pressure in $[t_1, t_2]$.

(b) Minimum primary pressure in $[t_2, t_3]$.

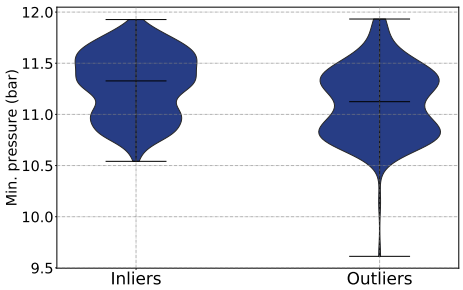

(c) Minimum primary pressure in $[t_3, t_4]$.

(d) Minimum primary pressure in $[t_4, \infty)$.

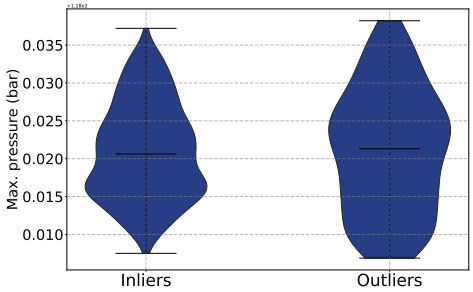

(e) Maximum primary pressure in in $[t_1, t_2]$.

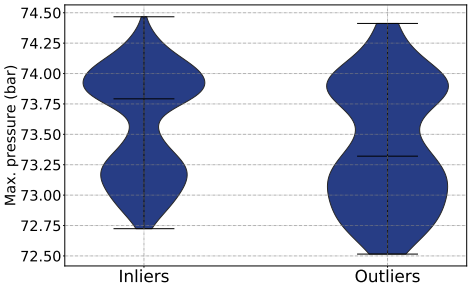

(f) Maximum primary pressure in in $[t_2, t_3]$.

Figure C.3: Primary pressure for the $h_1(z_s)|_{t_i}^{t_{i+1}} = \min(z_s)|_{t_i}^{t_{i+1}}$ and $h_2(z_s)|_{t_i}^{t_{i+1}} = \max(z_s)|_{t_i}^{t_{i+1}}$ intermediate parameter.

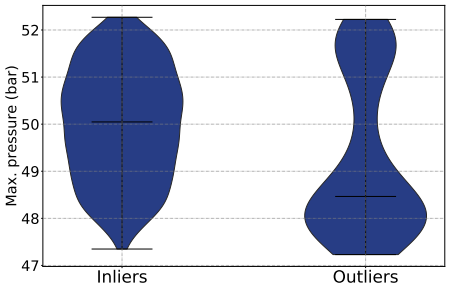

(a) Maximum primary pressure in $[t_3, t_4]$.

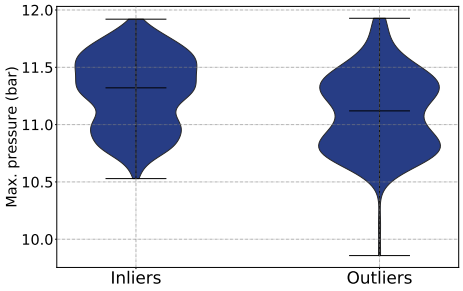

(b) Maximum primary pressure in $[t_4, \infty)$.

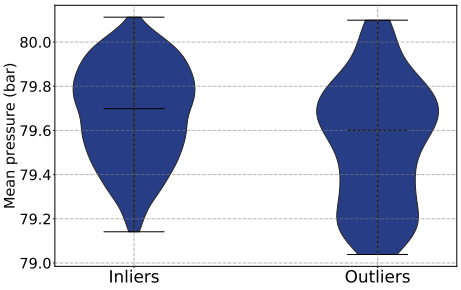

(c) Mean primary pressure in $[t_1, t_2]$.

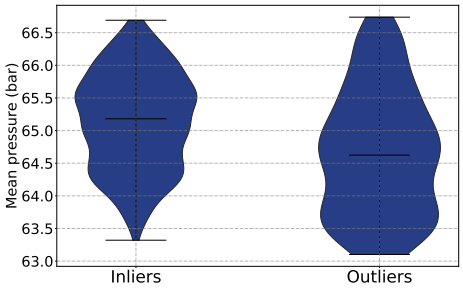

(d) Mean primary pressure in $[t_2, t_3]$.

(e) Mean primary pressure in $[t_3, t_4]$.

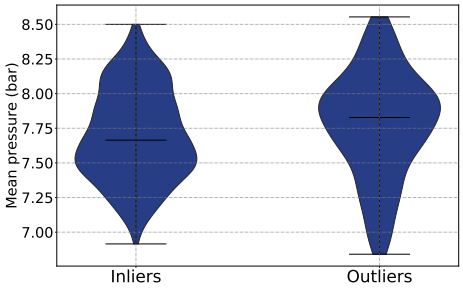

(f) Mean primary pressure in $[t_4, \infty)$.

Figure C.4: Primary pressure for the $h_3(z_s)|_{t_i}^{t_{i+1}} = \mathbb{E}[z_s]|_{t_i}^{t_{i+1}}$ and $h_2(z_s)|_{t_i}^{t_{i+1}} = \max(z_s)|_{t_i}^{t_{i+1}}$ intermediate parameter.

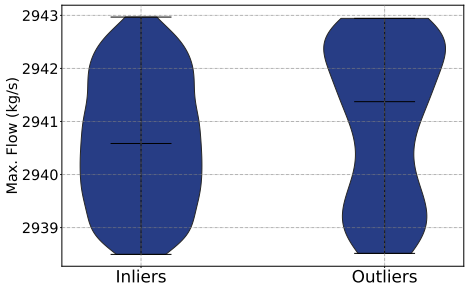

(a) Maximum water flow in the collector in $[t_1, t_2]$.

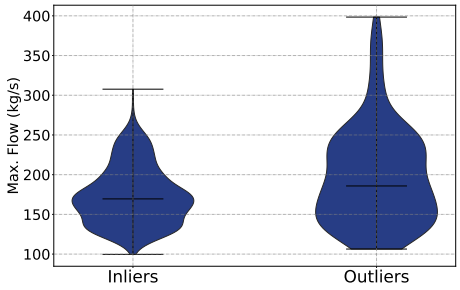

(b) Maximum water flow in the collector in $[t_2, t_3]$.

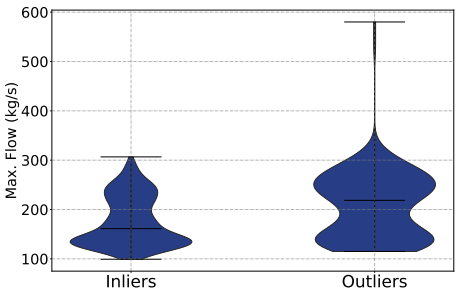

(c) Maximum water flow in the collector in $[t_3, t_4]$.

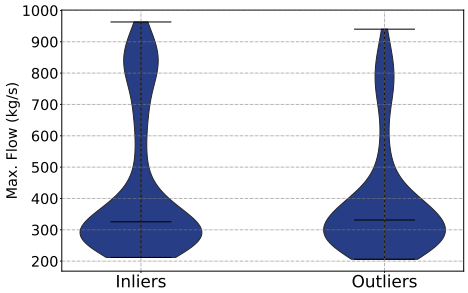

(d) Maximum water flow in the collector in $[t_4, \infty)$.

Figure C.5: Water flow in the collector for the $h_2(z_s)|_{t_i}^{t_{i+1}} = \max(z_s)|_{t_i}^{t_{i+1}}$ intermediate parameter.

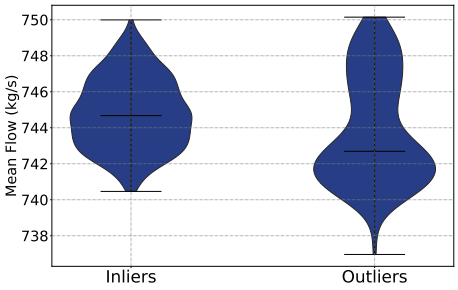

(a) Mean water flow in the collector in $[t_1, t_2]$.

(b) Mean water flow in the collector in $[t_2, t_3]$.

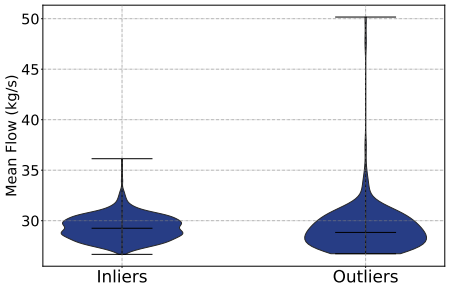

(c) Mean water flow in the collector in $[t_3, t_4]$.

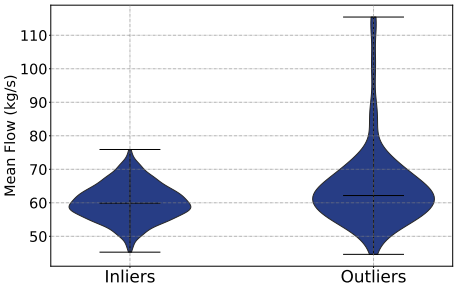

(d) Mean water flow in the collector in $[t_4, \infty)$.

Figure C.6: Water flow in the collector for the $h_3(z_s)|_{t_i}^{t_{i+1}} = \mathbb{E}[z_s]|_{t_i}^{t_{i+1}}$ intermediate parameter.

Bibliography

1. Abraham, C., Cornillon, P., Matzner-Løber, E., and Molinari, N. (2003). Unsupervised curve clustering using B-splines. *Scandinavian Journal of Statistics*, 30:581–595. [Cited on page(s) 28.]

2. Aggarwal, C. (2017). *Outlier Analysis*. Springer International Publishing, 2 edition. [Cited on page(s) 23, 25, 49, and 59.]

3. Aggarwal, C. C. and Yu, P. S. (2001). Outlier detection for high dimensional data. In *Proceedings of the 2001 ACM SIGMOD International Conference on Management of Data*, SIGMOD 01, page 37–46, New York, NY, USA. Association for Computing Machinery. [Cited on page(s) 23.]

4. Alam, F. M., McNaught, K. R., and Ringrose, T. J. (2004). Using Morris' randomized OAT designs a factor screening method for developing simulation metamodels. In *Proceedings of the 36th conference on Winter simulation*, pages 949–957, Washington, D.C. [Cited on page(s) 76.]

5. Amano, Y. (2018). Going long term: US nuclear power plants could extend operating life to 80 years. Technical report, IAEA, International Atomic Energy Agency (IAEA). [Cited on page(s) 11.]

6. Araneo, D. A. and D'Auria, F. (2012). Methodology for pressurized thermal shock analysis in nuclear power plant. *INTECH Open Access Publisher*. [Cited on page(s) xiv and 154.]

7. Arkhangel'skii, A. and Pontryagin, L. (1990). *General Topology I: Basic Concepts and Constructions Dimension Theory*. Encyclopaedia of Mathematical Sciences. Springer-Verlag Berlin Heidelberg, 1st edition. [Cited on page(s) 29.]

8. Aronszajn, N. (1950). Theory of reproducing kernels. *Transactions of the American mathematical society*, 68:337–404. [Cited on page(s) 80.]

9. Arribas-Gil, A. and Romo, J. (2014). Shape outlier detection and visualization for functional data: The outliergram. *Biostatistics*, 15(4):603–619. [Cited on page(s) 13, 38, 41, and 44.]

10. Au, S. and Beck, J. (2001). Estimation of small failure probabilities in high dimensions by subset simulation. *Probabilistic Engineering Mechanics*, 16:263–277. [Cited on page(s) 85.]

11. Auder, B. (2011). *Classification and modelling of computer codes functional outputs: application to accidental thermo-hydraulic computations in pressurized water reactors (PWR)*. PhD thesis, Paris 6 University. [Cited on page(s) 13, 27, and 70.]

12. Baker, Jr., L. and Just, L. C. (1962). Studies Of Metal-Water Reactions At High Temperatures III. Experimental And Theoretical Studies Of The Zirconium-Water Reaction. [Cited on page(s) 102 and 103.]

13. Barreyre, C., Laurent, B., Loubes, J.-M., Boussouf, L., and Cabon, B. (2019). Multiple testing for outlier detection in space telemetries. *IEEE Transactions on Big Data*, 6(3):443–451. [Cited on page(s) 21, 28, and 39.]

14. Baucells, M. and Borgonovo, E. (2013). Invariant probabilistic sensitivity analysis. *Management Science*, 59(11):2536–2549. [Cited on page(s) 79.]

15. Bentivoglio, F., Tauveron, N., Geffraye, G., and Gentner, H. (2008). Validation of the CATHARE2 code against experimental data from Brayton-cycle plants. *Nuclear Engineering and Design*, 238:3145–3159. [Cited on page(s) 70.]

16. Bertrand, E. and Mauger, G. (2015). Transient analysis of the ASTRID demonstrator including a gas nitrogen power conversion system with the CATHARE2 code. In *Proceedings of NURETH-16, The 16th International Topical Meeting on Nuclear Reactor Thermal Hydraulics*, Chicago, IL. [Cited on page(s) 70.]

17. Bestion, D. (1990). The physical closure laws in the CATHARE code. *Nuclear Engineering and Design*, 124(3):229–245. [Cited on page(s) 72 and 73.]

18. Biernacki, C., Celeux, G., and Govaert, G. (2000). Assessing a mixture model for clustering with the integrated completed likelihood. *Pattern Analysis and Machine Intelligence, IEEE Transactions on Pattern Analysis and Machine Intelligence*, 22:719–725. [Cited on page(s) 53.]

19. Bishop, C. M. (2006). *Pattern Recognition and Machine Learning*. Information Science and Statistics. Springer-Verlag New York. [Cited on page(s) 47 and 92.]

20. Bouveyron, C. and Brunet, C. (2013). Model-based clustering of high-dimensional data: A review. *Computational Statistics and Data Analysis*, 71:1–27. [Cited on page(s) 28.]

21. Boyack, B., Duffey, R., Wilson, G., Griffith, P., Lellouche, G., Levy, S., Rohatgi, U., Wulff, W., and Zuber, N. (1989). Quantifying reactor safety margins: Application of code scaling, applicability, and uncertainty evaluation methodology to a large-break, Loss-Of-Coolant Accident. Technical report, United States. NUREG/CR–5249. [Cited on page(s) 101.]

22. Cacuci, D. G. (1981). Sensitivity theory for nonlinear systems I. Nonlinear functional analysis approach . *Journal of Mathematical Physics*, 22:2794–2802. [Cited on page(s) 76.]

23. Campbell, K., McKay, M., and Williams, B. (2006). Sensitivity analysis when model outputs are functions. *Reliability Engineering & System Safety*, 91:1468–1472. [Cited on page(s) 87.]

24. Cardot, H., Ferraty, F., and Sarda, P. (1999). Functional linear model. *Statistics & Probability Letters*, 45:11–22. [Cited on page(s) 30.]

25. Carnevali, S. and Bazin, P. (2015). Validation of cathare code on the 3d ROSA-LSTF pressure vessel. In *Proceedings of the NURETH 16- 16th International Topical Meeting on Nuclear Reactor Thermal Hydraulics*. [Cited on page(s) 69.]

26. Carnevali, S. and Bazin, P. (2016). Comparison of CATHARE code using a 3D Reactor Pressure Vessel modelling approach and experimental results on intermediate break LOCAs of ROSA 2 program. In *Proceedings of the NUTHOS-11, The 11th International Topical Meeting of Nuclear Reactor Thermal Hydraulics, Operation and Safety*, Gyeongju, Korea. [Cited on page(s) 70.]

27. Castro, P. E., Lawton, W. H., and Sylvestre, E. A. (1986). Principal modes of variation for processes with continuous sample curves. *Technometrics*, 28(4):329–337. [Cited on page(s) 30.]

28. Chagny, G., Comte, F., and Roche, A. (2017). Adaptive estimation of the hazard rate with multiplicative censoring. *Journal of Statistical Planning and Inference*, 184:25–47. [Cited on page(s) 18.]

29. Charignon, C., Lecoy, J.-C., and Sauvage, J.-Y. (2016). CathSBI, a new methodology for the revised French LOCA rules. In *Proceedings of the 11th International Topical Meeting on Nuclear Reactor Thermal-Hydraulics, Operation and Safety (NUTHOS-11)*. [Cited on page(s) 104 and 118.]

30. Chen, S. L., Gerner, F. M., and Tien, C. L. (1987). General film condensation correlations. *Experimental Heat Transfer*, 1(2):93–107. [Cited on page(s) 126.]

31. Cherepanov, G. (1967). Crack propagation in continuous media. *Journal of Applied Mathematics and Mechanics*, 31(3):503–512. [Cited on page(s) 151.]

32. Claude Grandjean (2005). A State-of-the-Art Review of past programs devoted to fuel behavior under LOCA conditions. *Technical Report SEMCA-2005-313*. [Cited on page(s) 126.]

33. Csiszár, I. (1967). Information-type measures of difference of probability distributions and indirect observations. *Studia Scientiarum Mathematicarum Hungarica*, 2:299–318. [Cited on page(s) 80.]

34. Cuesta-Albertos, J. and Nieto-Reyes, A. (2008). The random Tukey depth. *Computational Statistics & Data Analysis*, 52(11):4979–4988. [Cited on page(s) 32.]

35. Cuevas, A. (2014). A partial overview of the theory of statistics with functional data. *Journal of Statistical Planning and Inference*, 147:1–23. [Cited on page(s) 17.]

36. Cuevas, A., Febrero-Bande, M., and Fraiman, R. (2007). Robust estimation and classification for functional data via projection-based depth notions. *Computational Statistics*, 22:481–496. [Cited on page(s) 13 and 33.]

37. Cuevas, A. and Fraiman, R. (2009). On depth measures and dual statistics. A methodology for dealing with general data. *Journal of Multivariate Analysis*, 100:753–766. [Cited on page(s) 32.]

38. Cukier, H., Levine, R., and Shuler, K. (1978). Nonlinear sensitivity analysis of multiparameter model systems. *Journal of Computational Physics*, 26:1–42. [Cited on page(s) 79.]

39. da Veiga, S., Gamboa, F., Iooss, B., and Prieur, C. (2021). *Basics and Trends in Sensitivity Analysis*. SIAM. [Cited on page(s) 79, 87, and 91.]

40. da Veiga, Sébastien (2015). Global sensitivity analysis with dependence measures. *Journal of Statistical Computation and Simulation*, 85(7):1283–1305. [Cited on page(s) 80, 82, and 87.]

41. Dai, W. and Genton, M. G. (2018). Multivariate functional data visualization and outlier detection. *Journal of Computational and Graphical Statistics*, 27(4):923–934. [Cited on page(s) 13, 26, 38, 42, and 182.]

42. Dai, W. and Genton, M. G. (2019). Directional outlyingness for multivariate functional data. *Computational Statistics & Data Analysis*, 131:50–65. High-dimensional and functional data analysis. [Cited on page(s) 38 and 42.]

43. Dai, W., Mrkvicka, T., Sun, Y., and Genton, M. (2020). Functional outlier detection and taxonomy by sequential transformations. *Computational Statistics and Data Analysis*, 149:106960. [Cited on page(s) 26, 39, 43, 44, and 53.]

44. Damblin, G., Couplet, M., and Iooss, B. (2013). Numerical studies of space-filling designs: Optimization of Latin Hypercube Samples and subprojection properties. *Journal of Simulation*, 7:276–289. [Cited on page(s) 92, 120, and 164.]

45. Daubechies, I. (1992). Ten lectures on wavelets. In *CBMS-NSF Regional Conference Series in Applied Mathematics*, volume 61 of *Lecture Notes in Computer Science*. Society for Industrial and Applied Mathematics (SIAM). [Cited on page(s) 22.]

46. de Lozzo, M. and Marrel, A. (2016a). New improvements in the use of dependence measures for sensitivity analysis and screening. *Journal of Statistical Computation and Simulation*, 86:3038–3058. [Cited on page(s) 80, 84, and 92.]

47. de Lozzo, M. and Marrel, A. (2016b). Sensitivity analysis with dependence and variance-based measures for spatio-temporal numerical simulators. *Stochastic Environmental Research and Risk Assessment*, 31:1437–1453. [Cited on page(s) 87.]

48. de Rocquigny, E., Devictor, N., and Tarantola, S. (2008). *Uncertainty in Industrial Practice: A Guide to Quantitative Uncertainty Management.* John Wiley & Sons. [Cited on page(s) 6.]

49. Deckers, J. (1985). Minimum cladding thickness of material test reactor fuel plates. Technical report, International Atomic Energy Agency (IAEA). INIS-XA-C–054. [Cited on page(s) 118.]

50. Delaigle, A. and Hall, P. (2010). Defining probability density for a distribution of random functions. *The Annals of Statistics*, 38(2):1171–1193. [Cited on page(s) 8.]

51. Dempster, A. P., Laird, N. M., and Rubin, D. B. (1977). Maximum likelihood from incomplete data via the EM algorithm. *Journal of the Royal Statistical Society. Series B (Methodological)*, 39(1):1–38. [Cited on page(s) 47.]

52. Di Bernardino, E., Laloë, T., Maume-Deschamps, V., and Prieur, C. (2013). Plug-in estimation of level sets in a non-compact setting with applications in multivariate risk theory. *ESAIM: Probability and Statistics*, 17. [Cited on page(s) 182.]

53. Dunford, N. and Schwartz, J. T. (1988). *Linear operators, Part 1, General Theory.* Wiley. [Cited on page(s) 19.]

54. Efron, B. and Tibshirani, R. (1994). *An Introduction to the Bootstrap.* Macmillan Publishers Limited. All rights reserved. [Cited on page(s) 52.]

55. Eliason, S. (1993). *Maximum Likelihood Estimation: Logic and Practice (Quantitative Applications in the Social Sciences).* Newbury Park, California. [Cited on page(s) 7.]

56. Febrero-Bande, M., Galeano, P., and González-Manteiga, W. (2008). Outlier detection in functional data by depth measures, with application to identify abnormal NOx levels. *Environmetrics*, 19:331 – 345. [Cited on page(s) 13, 26, 27, 38, and 44.]

57. Ferraty, F. and Vieu, P. (2006). *Nonparametric Functional Data Analysis: Theory and Practice*, volume 51. Springer. [Cited on page(s) 4, 8, 13, 17, 18, 28, 29, 31, and 87.]

58. Fort, J.-C., Klein, T., and Rachdi, N. (2016). New sensitivity analysis subordinated to a contrast. *Communications in Statistics-Theory and Methods*, 45(15):4349–4364. [Cited on page(s) 85.]

59. Forum, U. . T. G. I. I. (2002). A technology roadmap for Generation IV Nuclear Energy Systems. Technical report. [Cited on page(s) 70.]

60. Fraiman, R. and Muniz, G. (2001). Trimmed means for functional data. *TEST: An Official Journal of the Spanish Society of Statistics and Operations Research*, 10:419–440. [Cited on page(s) 26.]

61. Francom, D., Sansó, B., Kupresanin, A., and Jóhannesson, G. (2018). Sensitivity analysis and emulation for functional data using bayesian adaptive splines. *Statistica Sinica*, 28(2):791–816. [Cited on page(s) 87.]

62. Frank, I. E. and Friedman, J. H. (1993). A statistical view of some chemometrics regression tools. *Technometrics*, 35(2):109–135. [Cited on page(s) 30.]

63. Gamboa, F., Janon, A., Klein, T., and Lagnoux, A. (2014). Sensitivity analysis for multidimensional and functional outputs. *Electronic Journal of Statistics*, 8(1):575–603. [Cited on page(s) 87 and 93.]

64. Gasser, T., Hall, P., and Presnell, B. (1998). Nonparametric estimation of the mode of a distribution of random curves. *Journal of the Royal Statistical Society. Series B (Statistical Methodology)*, 60(4):681–691. [Cited on page(s) 8.]

65. Gauchy, C., Stenger, J., Sueur, R., and Iooss, B. (2021). An Information Geometry Approach to Robustness Analysis for the Uncertainty Quantification of Computer Codes. *Technometrics*, 64(1):80–91. [Cited on page(s) 13.]

66. Geffraye, G., Antoni, O., Farvacque, M., Kadri, D., Lavialle, G., Rameau, B., and Ruby, A. (2011). CATHARE 2 V2.5_2: A single version for various applications. *Nuclear Engineering and Design*, 241:4456–4463. [Cited on page(s) 16 and 69.]

67. Geffraye, G., Kalitvianski, V., Maas, L., Meloni, P., Polidori, M., Tauveron, N., and Cochemé, F. (2012). Cathare 2 code validation on HE-FUS3 loop. *Nuclear Engineering and Design*, 249:237–247. [Cited on page(s) 3 and 70.]

68. Gervini, D. (2012). Outlier detection and trimmed estimation for general functional data. *Statistica Sinica*, 22(4):1639–1660. [Cited on page(s) 38.]

69. Gijbels, I. and Nagy, S. (2017). On a General Definition of Depth for Functional Data. *Statistical Science*, 32(4):630–639. [Cited on page(s) 33 and 39.]

70. Goia, A. and Vieu, P. (2016). An introduction to recent advances in high/infinite dimensional statistics. *Journal of Multivariate Analysis*, 146:1–6. Special Issue on Statistical Models and Methods for High or Infinite Dimensional Spaces. [Cited on page(s) 17.]

71. Grenander, U. (1950). Stochastic processes and statistical inference. *Arkiv for Matematik*, 1(3):195–277. [Cited on page(s) 4 and 17.]

72. Gretton, A. (2015). A simpler condition for consistency of a kernel independence test. *arXiv: Machine Learning*. [Cited on page(s) 81.]

73. Gretton, A., Fukumizu, K., Teo, C. H., Song, L., Schölkopf, B., and Smola, A. (2008). A Kernel Statistical Test of Independence. page 585–592. MIT press. [Cited on page(s) 84.]

74. Gretton, A., Herbrich, R., Smola, A. J., Bousquet, O., and Schölkopf, B. (2005). Kernel methods for measuring independence. *Journal of Machine Learning Research*, 6:2075–2129. [Cited on page(s) 80 and 82.]

75. Gusak, D., Kukush, A., Kulik, A., Mishura, Y., and Pilipenko, A. (2010). *Theory of Stochastic Processes With Applications fo Financial Mathematics and Risk Theory*. Number 30. Springer, Vienna. [Cited on page(s) 18.]

76. Hamilton, J. D. (1994). *Time Series Analysis*. Princeton University Press. [Cited on page(s) 18.]

77. Hawkins, D. (1980). *Identification of Outliers*. Monographs on applied probability and statistics. Chapman and Hall. [Cited on page(s) 23.]

78. Helland, I. S. (1990). Partial least squares regression and statistical models. *Scandinavian Journal of Statistics*, 17(2):97–114. [Cited on page(s) 30.]

79. Hellinger, E. (1909). Neue Begründung der Theorie quadratischer Formen von unendlichvielen Veränderliche. *Journal für die reine und angewandte Mathematik (in German)*, 1:210–271. [Cited on page(s) 80.]

80. Hoeffding, W. (1948). Class of statistics with asymptotically normal distributions. *Annals of Mathematical Statistics*, 19:293–325. [Cited on page(s) 77.]

81. Horváth, L. and Kokoszka, P. (2012). *Inference for functional data with applications*, volume 200 of *Springer Series in Statistics*. Springer-Verlag New York. [Cited on page(s) 4 and 17.]

82. Hotelling, H. (1933). Analysis of a complex of statistical variables into principal components. *Journal of Educational Psychology*, 24:417–441. [Cited on page(s) 22.]

83. Hsieh, I.-C. and Huang, Y. (2021). Sensitivity analysis and visualization for functional data. *Journal of Statistical Computation and Simulation*, 91(8):1593–1615. [Cited on page(s) 86 and 88.]

84. Hubert, M., Rousseeuw, P. J., and Segaert, P. (2015). Multivariate functional outlier detection. *Statistical Methods & Applications*, 24(2):177–202. [Cited on page(s) 13, 26, 38, and 182.]

85. Hyndman, R. J. (2009). Rainbow plots , bagplots and boxplots for functional data. *Journal of Computational and Graphical Statistics*, 19:29–45. [Cited on page(s) 13, 26, 28, 38, 40, 44, and 60.]

86. Härdle, W., Kerkyacharian, G., Picard, D., and Tsybakov, A. (1998). *Wavelets, Approximation, and Statistical Applications*, volume 129 of *Lecture Notes in Statistics*. Springer-Verlag New York. [Cited on page(s) 22.]

87. IAEA (2001). *Safety Assessment and Verification for Nuclear Power Plants*. Number NS-G-1.2 in Safety Standards Series. International Atomic Energy Agency, Vienna. [Cited on page(s) 3 and 68.]

88. IAEA (2005). *Natural Circulation in Water Cooled Nuclear Power Plants*. Number 1474 in TECDOC Series. International Atomic Energy Agency, Vienna. [Cited on page(s) 100.]

89. IAEA (2006). *Guidelines on Pressurized Thermal Shock Analysis for WWER Nuclear Power Plants*. Number 8 (Rev.1) in IAEA-EBP-WWER. International Atomic Energy Agency, Vienna. [Cited on page(s) 149.]

90. IAEA (2008). *Best Estimate Safety Analysis for Nuclear Power Plants: Uncertainty Evaluation*. Number 52 in Safety Reports Series. International Atomic Energy Agency, Vienna. [Cited on page(s) 69.]

91. IAEA (2009). *Integrity of Reactor Pressure Vessels in Nuclear Power Plants: Assessment of Irradiation Embrittlement Effects in Reactor Pressure Vessel Steels*. Number NP-T-3.11 in Reactor Concepts Manual. Vienna. [Cited on page(s) 66.]

92. IAEA (2010). *Pressurized Thermal Shock in Nuclear Power Plants: Good Practices for Assessment*. Number 1627 in TECDOC Series. International Atomic Energy Agency, Vienna. [Cited on page(s) 147.]

93. IAEA (2014). *Accident Analysis for Nuclear Power Plants with Pressurized Water Reactors*. Number SSG-30 in Safety Guide Series. International Atomic Energy Agency, Vienna. [Cited on page(s) 91.]

94. Ieva, F., Paganoni, A. M., Pigoli, D., and Vitelli, V. (2013). Multivariate functional clustering for the morphological analysis of electrocardiograph curves. *Journal of the Royal Statistical Society. Series C (Applied Statistics)*, 62(3):401–418. [Cited on page(s) 28.]

95. Iooss, B. (2018). Sensitivity analysis of model outputs: methods and issues for BEPU methodology. In *Proceedings of ANS Best Estimate Plus Uncertainty International Conference (BEPU2018)*, Lucca, Italy. [Cited on page(s) 70.]

96. Iooss, B., Boussouf, L., Feuillard, V., and Marrel, A. (2010). Numerical studies of the metamodel fitting and validation processes. *International Journal of Advances in Systems and Measurements*, 3:11–21. [Cited on page(s) 92.]

97. Iooss, B. and Lemaître, P. (2015). *A Review on Global Sensitivity Analysis Methods*, pages 101–122. Springer US, Boston, MA. [Cited on page(s) 16, 75, and 85.]

98. Iooss, B. and Marrel, A. (2019). Advanced methodology for uncertainty propagation in computer experiments with large number of inputs. *Nuclear Technology*, 205(12):1588–1606. [Cited on page(s) 13, 16, and 70.]

99. Iooss, B. and Saltelli, A. (2017). Introduction: Sensitivity analysis. In Ghanem, R., Higdon, D., and Owhadi, H., editors, *Handbook of uncertainty quantification*, pages 1–20. Springer International Publishing. [Cited on page(s) xii and 76.]

100. Iooss, B., Vergès, V., and Larget, V. (2021). BEPU robustness analysis via perturbed law-based sensitivity indices. *Proceedings of the Institution of Mechanical Engineers, Part O: Journal of Risk and Reliability*, 0(0):1748006X211036569. [Cited on page(s) 13.]

101. IRSN (2008). A state-of-the-art review of past programmes devoted to fuel behaviour under Loss-of-Coolant conditions. Part 3. Cladding oxidation. Resistance to quench and post-quench loads. Technical report, France. Direction de la prévention des accidents majeurs. [Cited on page(s) 118.]

102. Irwin, G. R. (1957). Analysis of Stresses and Strains Near the End of a Crack Traversing a Plate. *Journal of Applied Mechanics*, 24(3):361–364. [Cited on page(s) 150.]

103. Jacques, J. and Preda, C. (2014). Functional data clustering: a survey. *Advances in Data Analysis and Classification*, 8(3):231–255. [Cited on page(s) 27 and 28.]

104. Janon, A., Klein, T., Lagnoux, A., Nodet, M., and Prieur, C. (2014). Asymptotic normality and efficiency of two sobol index estimators. *ESAIM: Probability and Statistics*, 18:342–364. [Cited on page(s) 79.]

105. Janssen, M., Zuidema, J., and Wanhill, R. (2004). *Fracture Mechanics - 2nd Edition*. Spon Press. [Cited on page(s) 151.]

106. Jhung, M., Kim, S., Choi, Y., Jung, S., Kim, J., Kim, J., Kim, J., Jang, C., Chang, Y., and Kang, K. (2008). Structural integrity assessment of reactor pressure vessels during pressurized thermal shock. *Journal of Mechanical Science and Technology*, 22:1451–1459. [Cited on page(s) 151.]

107. Joyce, M. (2018). Chapter 14 - Nuclear Safety and Regulation. In Joyce, M., editor, *Nuclear Engineering*, pages 323–355. Butterworth-Heinemann. [Cited on page(s) 10.]

108. Kelly, J., Bartaz, J., and Janicot, A. (1993). Reflood modelling under oscillatory flow conditions with CATHARE. In *Proceedings of NURETH-6, The 6th International Topical Meeting on Nuclear Reactor Thermal Hydraulics (NURETH-6) Grenoble*, Grenoble, France. [Cited on page(s) 140.]

109. Kiureghian, A. D. and Ditlevsen, O. (2009). Aleatory or epistemic? Does it matter? *Structural Safety*, 31(2):105–112. Risk Acceptance and Risk Communication. [Cited on page(s) 5.]

110. Knorr, E. M. and Ng, R. T. (1999). Finding intensional knowledge of distance-based outliers. In *Proceedings of the 25th VLDB Conference*, pages 211–222. [Cited on page(s) 23.]

111. Kruskal, W. H. and Wallis, W. A. (1952). Use of ranks in one-criterion variance analysis. *Journal of the American Statistical Association*, 47(260):583–621. [Cited on page(s) 128, 185, and 186.]

112. Kuhnt, S. and Rehage, A. (2016). An angle-based multivariate functional pseudo-depth for shape outlier detection. *Journal of Multivariate Analysis*, 146:325–340. Special Issue on Statistical Models and Methods for High or Infinite Dimensional Spaces. [Cited on page(s) 38.]

113. Kullback, S. and Leibler, R. A. (1951). On Information and Sufficiency. *The Annals of Mathematical Statistics*, 22(1):79 – 86. [Cited on page(s) 80.]

114. Lamboni, M., Monod, H., and Makowski, D. (2011). Multivariate sensitivity analysis to measure global contribution of input factors in dynamic models. *Reliability Engineering & System Safety*, 96:450–459. [Cited on page(s) 87.]

115. Larget, V. (2018). How to bring conservatism to a BEPU analysis. In *Proceedings of the 18th International Topical Meeting on Nuclear Reactor Thermal Hydraulics (NURETH 2019)*, pages 343–354. [Cited on page(s) 104 and 109.]

116. Leilei, X. and Guoxing, L. (2014). Fracture mechanics analysis for reactor pressure vessel under pressurized thermal shock. *Atomic Energy Science and Technology*, 48(11):2078–2084. [Cited on page(s) 150.]

117. Lejeune, C., Mothe, J., Soubki, A., and Teste, O. (2020). Shape-based outlier detection in multivariate functional data. *Knowledge-Based Systems*, 198:105960. [Cited on page(s) 182.]

118. Lemaître, P. (2014). *Analyse de sensibilité en fiabilité des structures (In French)*. PhD thesis, Université de Bordeaux. [Cited on page(s) 85.]

119. Lemieux, C. (2009). *Monte Carlo and Quasi-Monte Carlo Sampling*. Springer Series in Statistics. Springer-Verlag New York. [Cited on page(s) 92.]

120. Little, R. J. A. and Rubin, D. B. (2019). *Statistical Analysis with Missing Data*. Wiley. [Cited on page(s) 20.]

121. Liu, R. Y., Parelius, J. M., and Singh, K. (1999). Multivariate analysis by data depth: descriptive statistics, graphics and inference, (with discussion and a rejoinder by Liu and Singh). *The Annals of Statistics*, 27(3):783–858. [Cited on page(s) 39.]

122. Loeppky, J. L., Sacks, J., and Welch, W. J. (2009). Choosing the sample size of a computer experiment: A practical guide. *Technometrics*, 51(4):366–376. [Cited on page(s) 120.]

123. Long, J. P. and Huang, J. Z. (2015). A study of functional depths. *Preprint, arXiv:1506.01332*. [Cited on page(s) 53.]

124. López Pintado, S. and Romo, J. (2011). A half-region depth for functional data. *Computational Statistics & Data Analysis*, 55:1679–1695. [Cited on page(s) 34, 38, and 41.]

125. Lutsanych, S., Moretti, F., and D'Auria, F. (2015). Validation of CATHARE TH-SYS code against experimental reflood tests. In *Proceedings of NURETH-16, The 16th International Topical Meeting on Nuclear Reactor Thermal Hydraulics*, Chicago, IL. [Cited on page(s) 140.]

126. López-Pintado, S. and Romo, J. (2009). On the concept of depth for functional data. *Journal of the American Statistical Association*, 104(486):718–734. [Cited on page(s) 13, 32, 33, 38, and 53.]

127. Marrel, A. and Chabridon, V. (2021). Statistical developments for target and conditional sensitivity analysis: Application on safety studies for nuclear reactor. *Reliability Engineering & System Safety*, 214:107711. [Cited on page(s) 13, 81, 85, 86, 104, 114, 123, and 165.]

128. Martin, R. and O'Dell, L. (2005). AREVA's realistic large break LOCA analysis methodology. *Nuclear Engineering and Design*, 235:1713–1725. [Cited on page(s) xvii and 103.]

129. Mazgaj, P., Vacher, J.-L., and Carnevali, S. (2016). Comparison of CATHARE results with the experimental results of cold leg intermediate break LOCA obtained during ROSA-2/LSTF test 7. *Nuclear Sciences & Technologies*, 2(1). [Cited on page(s) 70.]

130. Mckay, M., Beckman, R., and Conover, W. (1979). A comparison of three methods for selecting vales of input variables in the analysis of output from a computer code. *Technometrics*, 21:239–245. [Cited on page(s) 92.]

131. Meynaoui, A. (2019). *New developments around dependence measures for sensitivity analysis : application to severe accident studies for generation IV reactors*. PhD thesis. [Cited on page(s) 82, 85, and 165.]

132. Mitteilung, E. (1910). Zur theorie der orthogonalen funktionensysteme. *Mathematische Annalen (In German)*, 69:331–371. [Cited on page(s) 22.]

133. Monod, H., Naud, C., and Makowski, D. (2006). Uncertainty and sensitivity analysis for crop models. *Working with Dynamic Crop Models*, pages 55–100. [Cited on page(s) 79.]

134. Mozharovskyi, P. (2016). Tukey depth: linear programming and applications. *Preprint, arXiv:1603.00069*. [Cited on page(s) 26 and 31.]

135. Mukin, R., Clifford, I., Ferroukhi, H., and Niffenegger, M. (2018). Pressurized Thermal Shock (PTS) Transient Scenarios Screening Analysis With TRACE. International Conference on Nuclear Engineering. [Cited on page(s) 146.]

136. Müller, M. (2007). Dynamic Time Warping. *Information Retrieval for Music and Motion*, 2:69–84. [Cited on page(s) 34 and 35.]

137. Nagy, S. (2016). *Statistical Depth for Functional Data*. PhD thesis, KU Leuven. [Cited on page(s) 13 and 33.]

138. Nagy, S., Gijbels, I., and Hlubinka, D. (2017). Depth-based recognition of shape outlying functions. *Journal of Computational and Graphical Statistics*, 26(4):883–893. [Cited on page(s) 38 and 44.]

139. Nanty, S. (2015). *Stochastic methods for uncertainty treatment of functional variables in computer codes: application to safety studies*. PhD thesis, Université Grenoble Alpes. [Cited on page(s) 13.]

140. NEA/CSNI/R (2018). *PIRT: R&D priorities for Loss-Of-Cooling and Loss-Of-Coolant Accidents in Spent Nuclear Fuel Pools.* [Cited on page(s) 101.]

141. Nieto-Reyes, A. and Battey, H. (2016). A Topologically Valid Definition of Depth for Functional Data. *Statistical Science*, 31(1):61–79. [Cited on page(s) 32 and 39.]

142. NRC (2004). *Pressurized Water Reactor (PWR) Systems.* Number 0603 in USNRC Technical Training Center. [Cited on page(s) 66.]

143. Nuclear Regulatory Commision (NRC) (2015). Typical pressurized-water reactor. [Online; accessed June, 2021]. [Cited on page(s) xii and 65.]

144. Oja, H. (1983). Descriptive statistics for multivariate distributions. *Statistics & Probability Letters*, 1(6):327–332. [Cited on page(s) 26.]

145. Ordóñez, C., Martínez, J., Rodríguez-Pérez, J. R., and Reyes, A. (2011). Detection of outliers in GPS measurements by using functional-data analysis. *Journal of Surveying Engineering*, 137:150–155. [Cited on page(s) 18.]

146. Panić, B., Klemenc, J., and Nagode, M. (2020). Improved Initialization of the EM Algorithm for Mixture Model Parameter Estimation. *Mathematics*, 8(3). [Cited on page(s) 181.]

147. Pearson, K. (1901). On lines and planes of closest fit to systems of points in space. *Philosophical Magazine Series 1*, 2:559–572. [Cited on page(s) 22.]

148. Peng, J. and Müller, H.-G. (2008). Distance-based clustering of sparsely observed stochastic processes, with applications to online auctions. *The Annals of Applied Statistics*, 2(3):1056–1077. [Cited on page(s) 28.]

149. Perret, G., Wicaksono, D., Clifford, I. D., and Ferroukhi, H. (2019). Global sensitivity and registration strategy for temperature profile of reflood experiment simulations. *Nuclear Technology*, 205(12):1638–1651. [Cited on page(s) 87.]

150. Perrin, G. and Defaux, G. (2019). Efficient evaluation of reliability-oriented sensitivity indices. *Journal of Scientific Computing*, 79:1433–1455. [Cited on page(s) 85.]

151. Polonik, W. (1997). Minimum volume sets and generalized quantile processes. *Stochastic Processes and their Applications*, 69(1):1–24. [Cited on page(s) 45.]

152. Ramsay, J. and Silverman, B. (2005). *Functional Data Analysis.* Springer series in statistics. Springer. [Cited on page(s) 4, 8, 17, and 23.]

153. Ramsay, J. O. (1982). When the data are functions. *Psychometrika*, 47:379–396. [Cited on page(s) 16, 17, and 86.]

154. Ramsay, J. O. and Dalzell, C. J. (1991). Some tools for functional data analysis. *Journal of the Royal Statistical Society. Series B (Methodological)*, 53(3):539–572. [Cited on page(s) 17.]

155. Rao, C. R. (1958). Some statistical methods for comparison of growth curves. *Biometrics*, 14(1):1–17. [Cited on page(s) 17.]

156. Ratanamahatana, C. and Keogh, E. (2004). Everything you know about Dynamic Time Warping is wrong. In *Third Workshop on Mining Temporal and Sequential Data*. [Cited on page(s) 34.]

157. Reynolds, D. (2009). *Gaussian Mixture Models*, pages 659–663. Springer US, Boston, MA. [Cited on page(s) 46.]

158. Ribés, A., Pouderoux, J., and Iooss, B. (2020). A visual sensitivity analysis for parameter-augmented ensembles of curves. *Journal of Verification, Validation and Uncertainty Quantification*, 4(4):041007. [Cited on page(s) 87.]

159. Rollón de Pinedo, A., Couplet, M., Iooss, B., Marie, N., Marrel, A., Merle, E., and Sueur, R. (2021). Functional outlier detection by means of h-mode depth and dynamic time warping. *Applied Sciences*, 11(23). [Cited on page(s) 44.]

160. RTE (2019). Rte. bilan électrique 2019. Technical report, France. [Cited on page(s) 2.]

161. Ruan, X. and Morishita, K. (2021). Pressurized thermal shock analysis of a reactor pressure vessel for optimizing the maintenance strategy: Effect of asymmetric reactor cooling. *Nuclear Engineering and Design*, 373:111021. [Cited on page(s) 146.]

162. Saba, N., Jawaid, M., and Sultan, M. (2019). An overview of mechanical and physical testing of composite materials. In Jawaid, M., Thariq, M., and Saba, N., editors, *Mechanical and Physical Testing of Biocomposites, Fibre-Reinforced Composites and Hybrid Composites*, Woodhead Publishing Series in Composites Science and Engineering, pages 1–12. Woodhead Publishing. [Cited on page(s) 153.]

163. Saltelli, A., Ratto, M., Andres, T., Campolongo, F., Cariboni, J., Gatelli, D., Saisana, M., and Tarantola, S. (2008). *Global Sensitivity Analysis: The Primer*. Wiley. [Cited on page(s) 13, 75, and 77.]

164. Savage, L. J., Barnard, G., Cornfield, J., Bross, I., Box, G. E. P., Good, I. J., Lindley, D. V., Clunies-Ross, C. W., Pratt, J. W., Levene, H., Goldman, T., Dempster, A. P., Kempthorne, O., and Birnbaum, A. (1962). On the foundations of statistical inference: Discussion. *Journal of the American Statistical Association*, 57(298):307–326. [Cited on page(s) 24.]

165. Schwarz, G. (1978). Estimating the dimension of a model. *The Annals of Statistics*, 6:461–464. [Cited on page(s) 53.]

166. Shah, M. (1979). A general correlation for heat transfer during film condensation inside pipes. *International Journal of Heat and Mass Transfer*, 22(4):547–556. [Cited on page(s) 126.]

167. Shannon, C. (1948). A mathematical theory of communication. *Bell System Technical Journal*, 27:379–423. [Cited on page(s) 80.]

168. Sobol, I. M. (1993). Sensitivity estimates for nonlinear mathematical models. *MMCE*, 1:407–414. [Cited on page(s) 77, 78, and 79.]

169. Spear, R. and Hornberger, G. (1980). Eutrophication in peel inlet—II. Identification of critical uncertainties via generalized sensitivity analysis. *Water Research*, 14(1):43–49. [Cited on page(s) 38 and 85.]

170. Sriperumbudur, B., Gretton, A., Fukumizu, K., Schölkopt, B., and Lanckriet, G. (2010). Hilbert space embeddings and metrics on probability measures. *Journal of Machine Learning Research*, 11:1517–1561. [Cited on page(s) 80.]

171. Stenger, J. (2020). *Optimal uncertainty quantification of a risk measurement from a computer code*. PhD thesis, Institut de Mathématiques de Toulouse. [Cited on page(s) 13 and 70.]

172. Stenger, J., Gamboa, F., Keller, M., and Iooss, B. (2020). Optimal uncertainty quantification of a risk measurement from a thermal-hydraulic code using canonical moments. *International Journal for Uncertainty Quantification*, 10:35–53. [Cited on page(s) 16 and 70.]

173. Su, G.-Y., Bucci, M., McKrell, T., and Buongiorno, J. (2016). Transient boiling of water under exponentially escalating heat inputs. Part II: Flow boiling. *International Journal of Heat and Mass Transfer*, 96(C):685–698. [Cited on page(s) 140.]

174. Sueur, R., Iooss, B., and Delage, T. (2017). Sensitivity analysis using perturbed-law based indices for quantiles and application to an industrial case. *arXiv preprint arXiv:1707.01296*. [Cited on page(s) 13.]

175. Sugiyama, M. and Yamada, M. (2012). On kernel parameter selection in Hilbert-Schmidt Independence Criterion. *IEICE Trans. Inf. Syst.*, 95-D:2564–2567. [Cited on page(s) 82.]

176. Sullivan, T. (2015). *Introduction to Uncertainty Quantification*, volume 63. Springer International Publishing. [Cited on page(s) 6.]

177. Sun, Y. and Genton, M. G. (2011). Functional boxplots. *Journal of Computational and Graphical Statistics*, 20(2):316–334. [Cited on page(s) 38, 39, and 44.]

178. Szabo, Z. and Sriperumbudur, B. (2018). Characteristic and universal tensor product kernels. *Journal of Machine Learning Research*, 18:1–29. [Cited on page(s) 81.]

179. Székely, G., Rizzo, M., and Bakirov, N. (2007). Measuring and testing dependence bycorrelation of distances. *The annals of statistics*, 35:2769–2794. [Cited on page(s) 80.]

180. Tarride, B. (2013). *Physique, fonctionnement et sûreté des REP. Maîtrise des situations accidentelles du système réacteur*. EDP Sciences: Génie Atomique. [Cited on page(s) xvii, 10, 96, 97, and 104.]

181. Tissot, J.-Y. and Prieur, C. (2015). A randomized orthogonal array-based procedure for the estimation of first- and second-order sobol' indices. *Journal of Statistical Computation and Simulation*, 85(7):1358–1381. [Cited on page(s) 79.]

182. Tokushige, S., Yadohisa, H., and Inada, K. (2007). Crisp and fuzzy k-means clustering algorithms for multivariate functional data. *Computational Statistics*, 22(1):1–16. [Cited on page(s) 28.]

183. Tong, L. (1972). Heat-transfer mechanisms in nucleate and film boiling. *Nuclear Engineering and Design*, 21(1):1–25. [Cited on page(s) 140.]

184. Trampus, P. (2018). Pressurized thermal shock analysis of the reactor pressure vessel. *Procedia Structural Integrity*, 13:2083–2088. ECF22 - Loading and Environmental effects on Structural Integrity. [Cited on page(s) xiii, 146, and 148.]

185. U.S. Department of Energy (1975). Reactor safety study. An assessment of accident risks in U. S. commercial nuclear power plants. Executive summary: main report. PWR & BWR. *Technical Report*. [Cited on page(s) 97.]

186. USNRC (1989). Best-estimate calculations of emergency core cooling system performance. Technical report, United States. REGULATORY GUIDE 1.157. [Cited on page(s) 104.]

187. Wallis, G. B. (2020). *One-dimensional two-phase flow*. Courier Dover Publications. [Cited on page(s) 125.]

188. Wang, J.-L., Chiou, J.-M., and Müller, H.-G. (2016). Functional data analysis. *Annual Review of Statistics and Its Application*, 3(1):257–295. [Cited on page(s) 20.]

189. Wicaksono, D., Zerkak, O., and Pautz, A. (2015). A methodology for global sensitivity analysis of transient code output applied toa reflood experiment model using TRACE. In *Proceedings of NURETH-16: The 16th International Topical Meeting on Nuclear Reactor Thermal Hydraulics*, Chicago, IL. [Cited on page(s) 87.]

190. Wold, H. (1966). Estimation of principal components and related models by iterative least squares. In Krishnaiaah, P., editor, *Multivariate Analysis.*, chapter 10, pages 391–420. Academic Press, New York. [Cited on page(s) 30.]

191. Yamanishi, Y. and Tanaka, Y. (2005). Sensitivity analysis in functional principal component analysis. *Computational Statistics*, 20:311–326. [Cited on page(s) 87.]

192. yun Fu, S., Lauke, B., and wing Mai, Y. (2019). Chapter 11 - fracture mechanics. In Fu, S.-Y., Lauke, B., and wing Mai, Y., editors, *Science and Engineering of Short Fibre-Reinforced Polymer Composites (Second Edition)*, Woodhead Publishing Series in Composites Science and Engineering, pages 301–409. Woodhead Publishing, second edition edition. [Cited on page(s) 150.]

193. Zhang, X. and Wang, J.-L. (2016). From sparse to dense functional data and beyond. *The Annals of Statistics*, 44(5):2281 – 2321. [Cited on page(s) 20.]

194. Zuo, Y. and Sering, R. (2000). General notions of statistical depth function. *Annals of Statistics*, 28. [Cited on page(s) 31.]

Analyse statistique des résultats de simulations numériques de situations accidentelles sur les réacteurs à eau pressurisée

Résumé — Les études de sûreté nucléaire reposent de plus en plus sur l'utilisation de simulateurs numériques (notamment le code français thermohydraulique *CATHARE2*) capables de fournir la meilleure estimation possible des grandeurs physiques pertinentes pour l'évaluation de la sûreté des centrales nucléaires. Dans ce contexte, l'utilisation de ces codes présente des défis scientifiques liés au coût de calcul de chaque simulation, aux phénomènes physiques complexes (non linéaires) qui interviennent dans les transitoires nucléaires accidentels, ainsi qu'à l'incertitude associée des données d'entrée, des modèles physiques du code et de ses sorties. Dans l'ensemble, l'analyse approfondie des transitoires nucléaires accidentels nécessite une connaissance du domaine par des ingénieurs spécialisés, et l'estimation des Quantités d'Intérêt (QoI) statistiques pertinentes liées à la sûreté nucléaire dépend d'outils avancés de Quantification des Incertitudes (UQ). Cette thèse développe des méthodes statistiques d'analyse des sorties de simulations d'accident nucléaires. La recherche d'*outliers* dans les ensembles de données de sortie disponibles fournit des informations concernant la détection de configurations pénalisantes dans les accidents nucléaires. Elle permet également d'effectuer des études de validation et facilite la tâche d'analyse des transitoires les plus pertinents. La première contribution principale de ces travaux est liée au domaine de la détection d'*outliers* fonctionnels. Nous présentons une méthodologie permettant la détection d'*outliers* fonctionnels de différents types (magnitude, forme), sans hypothèses préalables sur le processus de génération des données. Cette méthode est comparée à d'autres techniques existantes afin de justifier son utilisation dans l'analyse des sorties complexes fournies par le code *CATHARE2*. Nous proposons une méthodologie d'analyse physique systématique basée sur des outils avancés d'analyse de sensibilité (SA), simplifiant l'analyse des transitoires nucléaires en comparant les échantillons de sortie *outlier* et *inlier*. Enfin, les méthodologies développées sont appliquées avec succès à deux cas d'application de transitoires nucléaires accidentels. D'une part, nous analysons un Accident de Perte de Réfrigérant Primaire (APRP), démontrant comment les méthodologies proposées ont été capables d'identifier les incohérences physiques dans l'ensemble des sorties du code. D'autre part, une étude sur un transitoire nucléaire pouvant conduire à un choc thermique préssurisé (PTS) montre l'intérêt de la méthodologie dans les cas où les marges de sécurité sont obtenues comme résultat d'un chaînage de codes thermo-hydraulique et mécanique.

Mots clés : Données fonctionnelles, Détection d'outliers fonctionnels, Sûreté nucléaire, Simulations de transitoires nucléaires.

Statistical Analysis of the results of numerical simulations of accidental situations in Pressurized Water Reactors

Abstract — Nuclear safety studies rely increasingly upon the use of numerical simulators (namely, the French thermal-hydraulic code *CATHARE2*) capable of providing the best possible estimation of the physical variables relevant in the safety assessment of nuclear power plants. In this context, the use of these codes presents scientific challenges related to the computational cost of each simulation, the complex (non-linear) physical phenomena that intervene in accidental nuclear transients, as well as the associated uncertainty of the inputs, the physical models of the code, and its outputs. All in all, the in-depth analysis of accidental nuclear transients requires advanced knowledge of the domain by specialized engineers, and the estimation of relevant statistical Quantities of Interest (QoI) related to nuclear safety depends upon advanced Uncertainty Quantification (UQ) tools. We propose to extend the methodology to improve the existing knowledge related to the analysis of nuclear accident simulations. Since the considered numerical simulator outputs take the form of functional objects, usually a one-dimensional mathematical field, they provide rich information when performing safety studies. Finding outliers in the available sets of outputs provides insights regarding the detection of penalizing configurations in nuclear accidents, allows to perform validation studies, and facilitates the task of analyzing the most relevant transients. The first main contribution of these works is related to the functional outlier detection domain. We present a methodology allowing the detection of functional outliers of different types (magnitude, shape), with no prior assumptions of the generating process of the data. This method is compared to available state-of-the-art techniques in order to justify its use when analyzing the complex outputs provided by the *CATHARE2* code. Secondly, we propose a systematic physical analysis methodology based on advanced Sensitivity Analysis (SA) tools, simplifying the analysis of nuclear transients by comparing the inlying and outlying samples of outputs. Finally, the developed methodologies are successfully applied to two use-cases of accidental nuclear transients. On the one hand, we analyze a reactor-scale Intermediate Break Loss of Coolant Accident (IBLOCA), fully showcasing how the proposed methodologies have been capable of identifying physical inconsistencies in the set of outputs of the code. On the other hand, an exploratory use-case of Pressurized Thermal Shock (PTS) transients demonstrates how the methodology remains helpful in cases where the safety margins are obtained as the result of a sequence of chained thermal-hydraulic and mechanical computer codes.

Keywords: Functional data, Functional outlier detection, Nuclear safety, Nuclear transient simulation.

Análisis estadístico de los resultados de simulaciones numéricas de situaciones accidentales en reactores de agua a presión

Resumen — Los estudios de seguridad nuclear se basan cada vez más en el uso de simuladores numéricos (por ejemplo, el código termohidráulico francés *CATHARE2*) capaces de proporcionar la mejor estimación posible de las variables físicas relevantes en la evaluación de la seguridad de las centrales nucleares. La utilización de dichos códigos presenta retos científicos relacionados con el coste computacional de cada simulación, los complejos fenómenos físicos (no lineales) que intervienen en los transitorios nucleares accidentales, así como la incertidumbre asociada de las variables de entrada, los modelos físicos del código y sus salidas. En definitiva, el análisis en profundidad de los transitorios nucleares accidentales requiere un conocimiento avanzado del dominio por parte de ingenieros especializados, y la estimación de las Cantidades de Interés (QoI) estadísticas relevantes relacionadas con la seguridad nuclear depende de herramientas avanzadas de Cuantificación de la Incertidumbre (UQ). La presente tesis propone ampliar las metodologías para mejorar los conocimientos existentes relacionados con el análisis de simulaciones de accidentes nucleares. Dado que los resultados de los simuladores numéricos considerados adoptan la forma de objetos funcionales, normalmente un cuerpo matemático unidimensional, ellos proporcionan una gran cantidad de información a la hora de realizar estudios de seguridad. La identificación de *outliers* en los conjuntos de salidas disponibles proporciona información sobre la detección de configuraciones penalizadoras en accidentes nucleares, permite realizar estudios de validación y facilita la tarea de analizar los transitorios más relevantes. La primera contribución principal de este trabajo está relacionada con el ámbito de la detección de *outliers* funcionales. Presentamos una metodología que permite la detección de *outliers* funcionales de diferentes tipos (magnitud, forma), sin suposiciones previas sobre proceso de generación de los datos. Este método es comparado con las técnicas disponibles en el estado del arte con el fin de justificar su uso al analizar las complejas salidas proporcionadas por el código *CATHARE2*. En segundo lugar, proponemos una metodología sistemática de análisis físico basada en herramientas avanzadas de Análisis de Sensibilidad (SA), simplificando el análisis de los transitorios nucleares mediante la comparación de las muestras de salidas *inlier* y *outlier*. Por último, las metodologías desarrolladas se aplican con éxito a dos casos de aplicación de transitorios nucleares accidentales. Por un lado, analizamos un transitorio de Pérdida Accidental de Refrigerante (IBLOCA) a escala de reactor, mostrando cómo las metodologías propuestas han sido capaces de identificar inconsistencias físicas en el conjunto de salidas del código. Por otro lado, un caso de uso exploratorio de los transitorios de Choque Térmico Presurizado (PTS) demuestra cómo la metodología sigue siendo útil en los casos en que los márgenes de seguridad se obtienen como resultado de una secuencia de códigos informáticos termohidráulicos y mecánicos encadenados.

Palabras clave: Datos funcionales, Detección de outliers funcionales, Seguridad nuclear, Simulaciones de transitorios nucleares.